Dilip Chalissery

Fused Filament Fabrication to Manufacture Three-and Four-Dimensional Objects made of Shape Memory Polymers

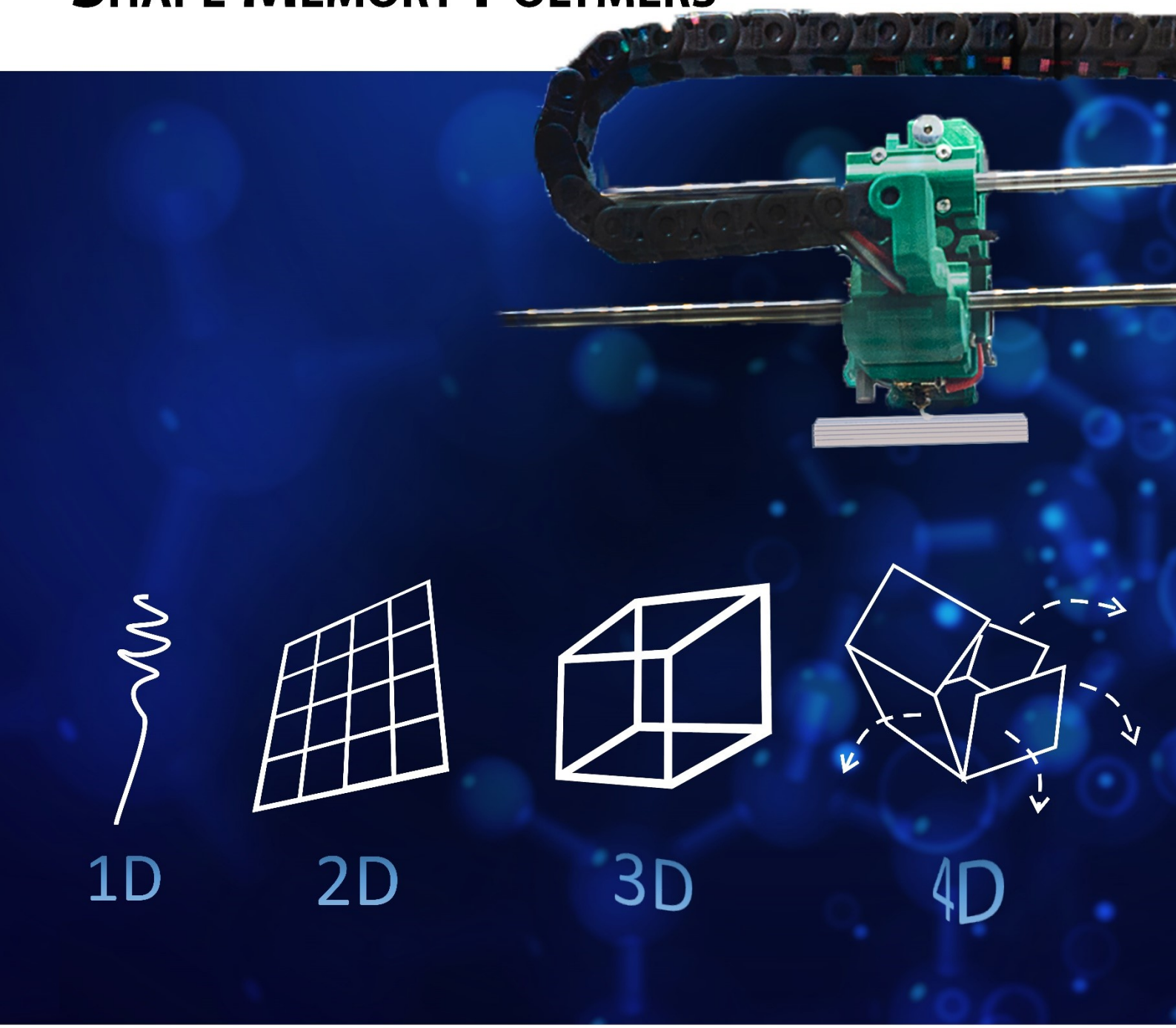

Fraunhofer IAP

TU berlin

FUSED FILAMENT FABRICATION TO MANUFACTURE THREE- AND FOUR-DIMENSIONAL OBJECTS MADE OF SHAPE MEMORY POLYMERS

vorgelegt von

M. Sc.

Dilip Chalissery

ORCID: 0000-0001-7152-6438

an der Fakultät III - Prozesswissenschaften

der Technischen Universität Berlin

zur Erlangung des akademischen Grades

Doktor der Ingenieurwissenschaften

– Dr.-Ing. –

genehmigte Dissertation

Promotionsausschuss:

Vorsitzender: Prof. Dr. Alexander Gurlo

Gutachter: Prof. Dr. -Ing. Dietmar Auhl

Gutachter: Prof. Dr. rer. nat. Alexander Böker

Gutachter: Dr. rer. nat. Thorsten Pretsch

Tag der wissenschaftlichen Aussprache: 24. Januar 2023

Berlin 2023

Enjoy each step, for in every step there is something to learn.

-John P Strelecky

There are things to do that no one has attempted before
and things to create that no one has created before.
With the new findings and technology,
one may not set out to change the world,
but we change the world one step at a time.

... to my loved ones and family

Abstract

Abstract

Programmable materials can perform specific tasks with the function of stimuli, like temperature, where the programming of material is understood as the programming of a functionality. The internal structure of the programmable materials enables reversible material properties, behavior, or shape changes according to a program. As the programmable materials require neither control electronics nor technical devices or cables, the self-sufficient behavior makes them fulfill sensor and actuator functionality. Shape memory polymers (SMPs) are smart materials that qualify as functional base materials to design programmable materials. SMPs can retain an imposed, temporary shape after thermomechanical treatment, also called programming. The initial, permanent shape can be recovered when applying an external stimulus like heat. In the last decade, thermoplastic polyurethanes (TPUs) belonged to the most researched SMPs. The thermoplastic nature of TPUs permits them to be molded using classical melt-based processing techniques like extrusion, injection molding, etc. Additive manufacturing (AM), alias three-dimensional (3D) printing, is an effective layer-by-layer technique to process thermoplastic polymers into 3D objects. Amidst various AM technologies, fused filament fabrication (FFF) is a hot-melt extrusion-based 3D printing process and is widely prevalent. The doctoral thesis aims to utilize self-synthesized and commercially available TPUs for FFF and to specifically influence the printing technology to produce either non-thermoresponsive or thermoresponsive objects or structures and open up new material and system functionalities.

The primary hurdle of this doctoral study was to process SMPs using a standard commercially available FFF machine. Motivated by the fact that previously presented manufacturing processes of thermoresponsive quick response (QR) codes were too time-consuming for production, QR codes were initially developed as anti-counterfeiting technology. The work introduces a novel manufacturing method for the same, thereby also addressing the AM of TPU-based SMP using standard FFF machines. Following this, the layer deposition pattern of tensile bars of TPU with shape memory properties was modified to achieve printing either in vertical or horizontal orientation. After processing commercially available polyester urethane and characterization, the mechanical and shape memory properties of the 3D printed samples were studied, and the results were compared to its injection-molded analogs and other materials manufactured via FFF. The results showed that the direction of loading and printing pattern orientation could be utilized to control the shape recovery stress and mechanical properties. Subsequently, the filigree printing and the smallest structure that can be obtained from FFF were explored by printing Arial fonts of the letter “A” in different sizes. Afterward, the potential application of SMP as thermally activatable and de-activatable gears and innovative smart keyboard keys was developed by utilizing the one-way (1W) shape memory effect (SME).

The second part of the work concentrates on four-dimensional (4D) printing employing FFF that enables the production of thermoresponsive objects directly in AM process. The work

presents a facile FFF printing strategy for commercially available polylactic acid (PLA) material and an in-house synthesized thermoplastic polyether urethane to obtain highly shrinkable objects, which allowed to show how to achieve precise control over the shapes after printing and heating. Later, the thermoresponsiveness after 4D printing of other objects in the form of solid cuboid, hollow cuboid, and hollow cylinder, with heights along the z-axis bigger than 30 mm, was explored. One of the applications of the developed highly shrinkable objects is active assembly. The concept is demonstrated by developing a lightweight, hands-free door opener for healthcare applications to counteract the spread of smear infections. After triggering the 4D effect for assembly, the device can be disassembled by heating the TPU over its glass transition temperature once it reaches its end-of-use. After removal from the door handle, the device can be mechanically recycled, and the material can be reused for 4D-printing. Successively, the know-how of 4D-printing was applied to address novel applications in active assembly, disassembly, programming tools, and as thermally deactivating gear.

Thirdly, FFF was utilized to produce elements that can undergo thermomechanical treatment to develop thermoresponsive two-way (2W) actuating objects that can bridge the gap toward manufacturing programmable materials. After developing a poly(1,10-decylene adipate) (PDA) based polyester urethane, processing it via FFF and thermomechanical treatment, a novel approach was developed to identify the ideal actuating temperature conditions using dynamic mechanical analysis. Once characterized, the polymer was found to actuate reliably under stress-free conditions by expanding on cooling and shrinking on heating with a maximum thermoreversible strain of ~16%. Later, allowing the 2W programmed TPU-based SMP to actuate in its ideal actuating temperature range between 15 °C and 64 °C for 100 heating-cooling cycles revealed that the reversible strain change stabilizes after about 25 cycles at 12%. The developed actuating elements were then integrated into a mechanical linkage system to form a thermally activatable gripper. This way, a hen's egg could be picked up, safely transported, and deposited, qualifying for soft robotic purposes. Further, actuating elements were combined with two types of unit cells to obtain programmable materials that can actuate on temperature variation. Afterward, the development of programmable actuating structures using TPU with a 2W-SME was studied. The primary aim was to enable a better actuation for physically crosslinked SMPs under stress-free conditions. Therefore, a novel gear design was first developed and processed using PDA-based TPU as functional base material. After thermomechanical treatment, the programmable gear actuated efficiently between two metastable states with a reversibility length change of ~42%. In order to prove that the thermoreversible actuation can be reproduced in other structural motifs, another actuating element was developed and programmed similarly. Once allowed to actuate under the same condition as the programmable gear, the element showed a reversible length change of ~44%.

Lastly, the work develops a novel FFF approach for semicrystalline SMPs to directly obtain objects in their thermoresponsive state, which can arbitrarily actuate between two metastable states by varying the temperature. Here, evidence is shown of how semicrystalline TPU is suitable for 4D-printing. During FFF, a cold air stream was used to cool

the SMP strongly. Upon its removal from the build platform, it can be activated under stress-free conditions by shrinking on heating to 62 °C and expanding on cooling to 15 °C with a maximum thermoreversible strain of 7%. Later, a 4D printed actuator was integrated into a lever mechanism qualified to witness highly complex shape changes. Subsequently, self-sufficient actuators in the form of a cylinder were fabricated, and their actuation behavior was studied. The work concludes that the functional integration of SMP via FFF to achieve 2W-SME by an "*in-situ*" programming method is a promising step to produce inherent thermoresponsive programmable materials.

Zusammenfassung

Programmierbare Materialien können bestimmte Funktionen in Reaktion auf Stimuli, wie z. B. die Temperatur ausführen können, wobei die Programmierung eines Materials als Programmierung einer Funktion angesehen wird. Die interne Struktur der programmierbaren Materialien ermöglicht reversible Materialeigenschaften, Verhaltens- oder Formänderungen nach einem Programm. Aufgrund der Tatsache, dass die programmierbaren Materialien weder Steuerelektronik noch technische Geräte oder Kabel benötigen, erfüllen sie durch ihr autarkes Verhalten sowohl Sensor- als auch Aktorfunktionen. Formgedächtnispolymere (FGP) sind smarte Materialien, die sich als funktionelle Basismaterialien für die Entwicklung programmierbarer Materialien eignen. FGPs können nach einer thermomechanischen Behandlung, auch Programmierung bezeichnet, eine vorgegebene, temporäre Form beibehalten. Die ursprüngliche, permanente Form kann wiederhergestellt werden, wenn ein externer Stimulus, wie z. B. Wärme, angewendet wird. In den letzten zehn Jahren gehörten thermoplastische Polyurethane (TPUs) zu den am meisten erforschten FGPs. Die thermoplastische Natur von TPUs ermöglicht ihre Verarbeitung mit klassischen schmelzbasierten Verfahren wie Extrusion, Spritzguss usw. Die additive Fertigung (AM), auch als dreidimensionaler Druck (3D) bezeichnet, ist eine effektive Technik zur Verarbeitung thermoplastischer Polymere zu 3D-Objekten. Unter den verschiedenen AM-Technologien ist die die am häufigsten verwendete Fused Filament Fabrication (FFF), ein 3D-Druckverfahren, das auf der Schmelzextrusion basiert. Ziel der Dissertation ist es, selbst synthetisierte und kommerziell erhältliche TPUs mittels FFF für die Herstellung von nicht-thermoresponsiven oder thermoresponsiven Objekten oder Strukturen zu nutzen, um neue Material- und Systemfunktionalitäten zu erschließen.

Die erste Herausforderung dieser Dissertation bestand darin, FGP mit einer kommerziellen FFF-Maschine zu verarbeiten. Motiviert durch die Tatsache, dass die bisher vorgestellten Herstellungsverfahren für thermoresponsive Quick-Response-Codes (QR-Codes) zu zeitaufwendig für die Produktion waren, wo sie ursprünglich als Fälschungsschutztechnologie entwickelt wurden. Die Arbeit beginnt mit der Einführung eines neuartigen Herstellungsprozesses für QR-codeträger, der sich auch mit dem AM von TPU-basierten FGP auf Standard-FFF-Maschinen befasst. Anschließend wurde das Schichtablagemuster der Zugstäbe aus TPU mit Formgedächtniseigenschaften so modifiziert, dass sie sowohl in vertikaler als auch in horizontaler Orientierung gedruckt werden können. Nach der Verarbeitung von kommerziell verfügbarem Polyester-Urethan und der Charakterisierung wurden die mechanischen und Formgedächtniseigenschaften der 3D-gedruckten Proben untersucht und die Ergebnisse mit ihren spritzgegossenen Analoga und anderen mit FFF hergestellten Materialien verglichen. Die Ergebnisse zeigten, dass die Belastungsrichtung und die Orientierung des Druckablagemusters zur Steuerung der Formrückstellungsspannung und der mechanischen Eigenschaften verwendet werden können. Anschließend wurden der filigrane Druck und die kleinste Struktur, die mit FFF hergestellt werden kann, durch den Druck

von Arial-Schriften des Buchstabens "A" in verschiedenen Größen untersucht. Danach wurde die potenzielle Anwendung von FGP als thermisch aktivierbare und deaktivierbare Zahnräder und innovative smarte Tastaturtasten durch Nutzung des Ein-Weg (1W) Formgedächtniseffekts (FGE) entwickelt.

Der zweite Teil der Arbeit befasst sich mit dem vierdimensionalen (4D) Druck mittels FFF, der die Herstellung von thermoresponsiven Objekten direkt im AM-Prozess ermöglicht. Diese Arbeit stellt eine einfache FFF-Druckstrategie für kommerziell verfügbares Polymilchsäure (PLA)-Material und ein in-house synthetisiertes thermoplastisches Polyether-Urethan vor, um hoch schrumpfbare Objekte zu erhalten. Dadurch wird gezeigt, wie man die Formen sowohl nach dem Druck als auch nach dem Erhitzen genau kontrollieren kann. Anschließend wurde die Thermorepsonsivität nach dem 4D-Druck von anderen Objekten in Form von Vollquadern, Hohlquadern und Hohlzylindern mit Höhen von mehr als 30 mm entlang der z-Achse untersucht. Eine der Anwendungen der entwickelten hochschrumpfbaren Objekte ist die aktive Montage. Das Konzept wird anhand der Entwicklung eines leichten, handfreien Türöffners für Anwendungen im Gesundheitswesen demonstriert, um die Verbreitung von Schmierinfektionen zu verhindern. Nach dem Auslösen des 4D Effekts für den Zusammenbau kann das Gerät zerlegt werden, indem das TPU über seine Glasübergangstemperatur erhitzt wird, sobald es sein End-of-Use erreicht hat. Nach dem Entfernen des Türgriffs kann das Produkt mechanisch recycelt und das Material für den 4D-Druck wiederverwendet werden. Das Know-how des 4D-Drucks wurde anschließend für neuartige Anwendungen in den Bereichen aktive Montage, Demontage, Programmierwerkzeuge und thermische Deaktivierung von Zahnrädern eingesetzt.

Drittens wurden mit Hilfe der FFF Elemente hergestellt, die einer thermomechanischen Behandlung unterzogen werden können, um thermoresponsiv aktivierende Zwei-Wege (2W) Objekte zu entwickeln, die die Lücke zur Herstellung programmierbarer Materialien schließen können. Nach der Entwicklung eines Poly(1,10-decylenadipat)-basierten Polyester-Urethans (PDA), dessen Verarbeitung durch FFF und thermomechanische Behandlung, wird ein neuer Ansatz entwickelt, um die idealen Aktivierungstemperaturen mittels dynamisch-mechanischer Analyse zu bestimmen. Die Charakterisierung des Polymers ergab, dass es sich unter spannungsfreien Bedingungen zuverlässig aktiviert, indem es sich beim Abkühlen ausdehnt und beim Erwärmen schrumpft, wobei die maximale thermoreversible Dehnung ~16% beträgt. Dann wurde das 2W programmierte TPU-basierte FGP in seinem idealen Temperaturbereich zwischen 15 °C und 64 °C für 100 Heiz-Kühl-Zyklen aktiviert und die reversible Dehnungsänderung stabilisierte sich nach etwa 25 Zyklen bei 12 %. Die entwickelten Aktorelemente wurden dann in ein mechanisches Gelenksystem integriert, um ein thermisch aktivierbares Greifersystem zu realisieren. Auf diese Weise könnte ein Hühnerei aufgenommen, sicher transportiert und abgelegt werden, so dass es sich für den Einsatz in der Soft-Robotik eignet. Die Aktuatoren wurden mit zwei verschiedenen Einheitszellen kombiniert, um programmierbare Materialien zu schaffen, die abhängig von Temperaturänderungen aktiviert werden können. Daraufhin wurde die Entwicklung programmierbarer Aktorstrukturen unter Verwendung von TPU mit einer 2W-FGE erforscht.

Das Hauptziel bestand darin, eine bessere Aktivierung von physikalisch vernetztem FGP unter spannungsfreien Bedingungen zu ermöglichen. Daher wurde zunächst ein neuartiges Zahnraddesign entwickelt und unter Verwendung von PDA-basiertem TPU als funktionellem Basismaterial hergestellt. Nach der thermomechanischen Behandlung konnte das programmierbare Zahnrad effizient zwischen zwei metastabilen Zuständen mit einer reversiblen Längenänderung von ~42% aktiviert werden. Um zu beweisen, dass die thermoreversible Aktivierung auch in anderen Strukturmotiven reproduzierbar ist, wurde ein weiteres Aktorelement entwickelt und in ähnlicher Weise programmiert. Bei Aktivierung unter den gleichen Bedingungen wie das programmierbare Zahnrad zeigte das Element eine reversible Längenänderung von ~44%.

Schließlich wurde in der Arbeit ein neuartiger FFF-Ansatz für teilkristalline FGPs entwickelt, um Objekte direkt in ihrem thermoresponsiven Zustand zu erzeugen, die durch Variation der Temperatur beliebig zwischen zwei metastabilen Zuständen umschalten können. Hier wurde der Beweis erbracht, wie teilkristallines TPU für den 4D-Druck verwendet werden kann. Während der FFF wurde Luft verwendet, um das FGP stark zu kühlen. Nach der Entnahme aus der Bauplattform kann es unter spannungsfreien Bedingungen zuverlässig aktiviert werden, indem es sich bei Erwärmung auf 62 °C zusammenzieht und bei Abkühlung auf 15 °C ausdehnt, mit einer maximalen thermoreversiblen Dehnung von~7 %. Danach wurde ein 4D-gedruckter Aktor in einen Hebelmechanismus integriert, der sich für hochkomplexe Formänderungen qualifiziert. Nachfolgend wurden autarke Aktoren in Form eines Zylinders hergestellt und deren Aktivierungsverhalten untersucht. Die Arbeit kommt zu dem Schluss, dass die funktionale Integration von FGP über FFF zur Erreichung von 2W-FGE durch eine "*in-situ*"-Programmiermethode ein vielversprechender Schritt zur Herstellung inhärent thermoresponsiver programmierbarer Materialien ist.

Acknowledgment

Acknowledgment

This thesis has been made possible by the support, mentoring, and friendship of several people to whom I would like to express my gratitude.

First, I express my most profound appreciation to my supervisor Dr. Thorsten Pretsch for offering me the position to pursue my doctoral work in his group at Fraunhofer-Institut für Angewandte Polymerforschung (IAP). Also, for the continuous support, never-ending help, invaluable feedback, and advice on all concerns. I am immensely grateful for his professional and scientific support.

Furthermore, I would like to thank Prof. Dr. Alexander Böker, Prof. Dr. Dietmar Auhl, and Prof. Dr. André Laschewsky for reviewing my thesis. My deepest gratitude goes to Prof. Dr. Alexander Böker and Prof. Dr. Dietmar Auhl for undertaking this thesis's academic responsibility, encouragement, and support.

I am also grateful to the Fraunhofer High-Performance Center for Functional Integration in Materials (project 630039), Fraunhofer Cluster of Excellence "Programmable Materials" (projects 63500, 630527, 630507, PSP elements 40-01922-2500-00002 and 40-03420-2500-00003), and future cluster candidate Additive Manufacturing Cluster Berlin-Brandenburg (AMBER, 03ZK102AC) for funding my research projects. I am thankful to Covestro Deutschland AG for kindly providing Desmopan® DP 2795A SMP, as it was used as the model material for various contexts in this work.

My thanks and appreciations also go to my colleagues, ex-colleagues, and students of the Shape Memory Polymer group of Fraunhofer IAP. First, I express my gratitude to my officemate Dennis Schönfeld, for lively chats on SMPs in general, visions, suggestions, opinions, and ideas of products and mechanisms, and for synthesizing many SMPs on demand. A special mention goes to Tobias Rümmler, who could transform any ideas and models into reality, also for his continuous support in carrying out the extrusion of SMPs and other polymers, conducting dynamic mechanical analysis, and for his constant support for the last five years. I want to thank Dr. Mario Walter for his support, the lively talks on SMPs, and his capability to synthesize novel SMPs, as this was the functional base material for developing new shape memory effects. Further, I wish to thank the ex-colleagues, Dr. Fabian Friess and Dr. Benjamin Heyne, and all the interns and students who accompanied me during my Ph.D. work and provided me with various time-consuming measurements: Nishith Puvati, Yu Yu Chen, Yim Yam Chan, Vincent Scholz, Julia Friederike Kubitz, Saskia Wendland, Nour Adilien, Fernanda Alvarado Galindo, and Harish Babu Eppa.

Additionally, I would like to thank all the colleagues and students of Fraunhofer IAP for their daily support, coffee talks, and many entertaining conversations over lunch -as simple as that- their company and for making my time in Fraunhofer IAP a lot lighter, easier, and lively. Furthermore, I would like to extend my thanks to the colleagues of the division of Synthesis- and Polymer Technology and the team members of Strategy and Marketing of Fraunhofer IAP for their immense support on many occasions. Additionally, I would like to

thank the other doctoral students, group leaders, scientific researchers, and lab assistants for their general support, helpful scientific discussions, and for making my working time enjoyable.

Last but not least, I want to thank my family and friends for supporting me throughout my Ph.D. thesis, particularly my parents, brother, sister-in-law, and parents-in-law for the extended support, encouragement, and understanding. Also, my cats Finnchen and Mickey, for their effective distractions when further work on the manuscript was pointless anyway and for offering the lovely environment. Above all, my wife Anne-Kathrin for her love, patience, trust, faithful support, and continuous encouragement.

Preface

Preface

This dissertation is a cumulative work based on four peer-reviewed published articles and four sub-chapters (non-published). The articles are presented separately as independent sub-chapters with their own introduction, experimental section, results, discussion, conclusions, and references. The formatting of already published manuscripts was modified to ensure consistency throughout the dissertation. The thesis also contains a general abstract, introduction, motivation, discussion, and conclusion. The following four published articles and sub-chapters are enclosed in this thesis:

Chapter 3: One-Way Shape Memory Effect of Objects Programmed After Fused Filament Fabrication

Chapter 3.1: Additive Manufacturing of Information Carriers Based on Shape Memory Polyester Urethane. Chalissery, D.; Pretsch, T.; Staub, S.; Andrä, H. Polymers 2019, 11, 1005. https://doi.org/10.3390/polym11061005

Chapter 3.2: Influence of Print Orientation on Shape Memory- and Mechanical-Properties After Fused Filament Fabrication

Chapter 3.3: Fused Filament Fabrication of Filigree Objects With Shape Memory Properties

Chapter 4: Four-Dimensional (4D) Printing Via Fused Filament Fabrication

Chapter 4.1: Highly Shrinkable Objects as Obtained from 4D-printing. Chalissery, D., Schönfeld, D., Walter, M., Shklyar, I., Andrae, H., Schwörer, C., Amann, T., Weisheit, L. and Pretsch, T. (2022). Macromol. Mater. Eng., 307: 2100619. https://doi.org/10.1002/mame.202100619

Chapter 4.2: Potential Applications of 4D-Printed Objects

Chapter 5: *Ex-Situ* Programming of Objects Manufactured via Fused Filament Fabrication to Attain Two-Way Shape Memory Effect

Chapter 5.1: Actuating Shape Memory Polymer for Thermoresponsive Soft Robotic Gripper and Programmable Materials. Schönfeld, D.; Chalissery, D.; Wenz, F.; Specht, M.; Eberl, C.; Pretsch, T.. Molecules 2021, 26, 522. https://doi.org/10.3390/molecules26030522.

Chapter 5.2: Programmable Materials

Chapter 6: Fused Filament Fabrication of Actuating Objects. Chalissery, D., Schönfeld, D., Walter, M., Ziervogel, F., Pretsch, T., *Macromol. Mater. Eng.* 2022, 2200214. https://doi.org/10.1002/mame.202200214.

Table of Contents

Table of Contents

TITLE PAGE ..... **III**

ABSTRACT ..... **I**

ZUSAMMENFASSUNG ..... **V**

ACKNOWLEDGMENT ..... **IX**

PREFACE ..... **XIII**

TABLE OF CONTENTS .....

CHAPTER 1: INTRODUCTION **1**

1.1. POLYMERS **2**

1.1.1. Molecular Architecture of Polymers *2*

1.1.2. States of Matter and Thermal Transitions *3*

1.1.3. Thermoplastics *5*

1.1.4. Shape Memory Polymers *11*

1.1.5. Molecular Mechanism of Shape Memory Effect *12*

1.2. SHAPE MEMORY EFFECT OF OBJECTS MANUFACTURED VIA FUSED FILAMENT FABRICATION **13**

1.2.1. One-Way Shape Memory Effect *14*

1.2.2. Two-Way Shape Memory Effect *15*

1.2.3. Four Dimensional (4D)-Printing *16*

1.2.4. Two-Way Four-Dimensional Printing *18*

1.3. REFERENCES **19**

CHAPTER 2: MOTIVATION **29**

REFERENCES **32**

CHAPTER 3: ONE-WAY SHAPE MEMORY EFFECT OF OBJECTS PROGRAMMED AFTER FUSED FILAMENT FABRICATION **35**

CHAPTER 3.1: ADDITIVE MANUFACTURING OF INFORMATION CARRIERS BASED ON SHAPE MEMORY POLYESTER URETHANE **36**

CHAPTER 3.2: INFLUENCE OF PRINT ORIENTATION ON SHAPE MEMORY- AND MECHANICAL- PROPERTIES AFTER FUSED FILAMENT FABRICATION **61**

CHAPTER 3.3: FUSED FILAMENT FABRICATION OF FILIGREE OBJECTS WITH SHAPE MEMORY PROPERTIES **72**

CHAPTER 4: FOUR-DIMENSIONAL (4D) PRINTING VIA FUSED FILAMENT FABRICATION **85**

CHAPTER 4.1: HIGHLY SHRINKABLE OBJECTS AS OBTAINED FROM 4D-PRINTING **86**

CHAPTER 4.2: POTENTIAL APPLICATIONS OF 4D-PRINTED OBJECTS **117**

CHAPTER 5: *EX-SITU* PROGRAMMING OF OBJECTS MANUFACTURED VIA FUSED FILAMENT FABRICATION TO ATTAIN TWO-WAY SHAPE MEMORY EFFECT **131**

CHAPTER 5.1: ACTUATING SHAPE MEMORY POLYMER FOR THERMORESPONSIVE SOFT ROBOTIC GRIPPER AND PROGRAMMABLE MATERIALS **132**

CHAPTER 5.2: PROGRAMMABLE MATERIALS **159**

CHAPTER 6: FUSED FILAMENT FABRICATION OF ACTUATING OBJECTS **172**

6.1. Introduction *175*

6.2. Results and discussion *177*

6.3. Conclusions *187*

6.4. Experimental Section *188*
6.5. References *192*

CHAPTER 7: DISCUSSION **194**

References *201*

CHAPTER 8: CONCLUSION AND OUTLOOK **205**

APPENDIX **209**

Journals *210*
Patents *210*
Presentations *211*
Permanent Database: *212*

LIST OF ABBREVIATIONS AND SYMBOLS **214**

Chapter 1:
Introduction

Chapter 1: Introduction

1.1. Polymers

Polymers have gained wide popularity in the last decades. They are multifaceted materials employed in diverse areas of our daily lives, like car key housing, credit cards, clothing made from synthetic fibers, and car parts like bumpers, wheel caps, instrument panels, and dashboards. Polymers are materials made from repeating building blocks called monomers. [1–4]. Polymers can be categorized into two groups based on their origin: natural and synthetic. Natural polymers are found in nature [5,6], like silk, wool, DNA, cellulose, and proteins. In turn, synthetic polymers, such as high-density polyethylene (HDPE), are used in the manufacture of bottles and are produced in the synthesis process by scientists or engineers [7–9].

Polymers can be classified into thermoplastics, elastomers, and thermosets, depending on the structure and nature of cross-links. In the case of thermoplastic polymers and elastomers, the physical cross-linking gives thermoplastic material properties. In contrast, elastomers and thermosets consist of extensive cross-linking between polymer chains to produce an infusible and insoluble polymer network. The thermoplastics can be further subdivided into amorphous and semicrystalline polymers based on bulk state, and the polymer can be again subcategorized as homopolymer and copolymer based on monomer composition.

1.1.1. Molecular Architecture of Polymers

Polymers composed of one monomer species are called homopolymers [10]. Examples include polypropylene [11], polyvinyl acetate [12], and polystyrene [12,13]. On the other hand, polymers whose backbone chain is built up by more than one monomer species are called copolymers [10]. Here, varying the monomer fractions is an appropriate tool to control the material's physical, chemical, and processing properties. According to the arrangement of the monomers, the skeletal structure of polymers is divided into linear, branched, and network structures [4,14–16] (**Figure 1.1**).

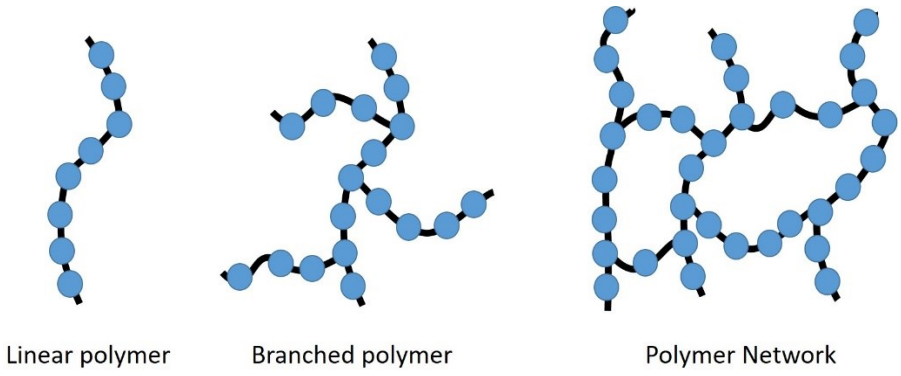

Figure 1.1. Schematic representation of the different types of polymers.

The macromolecules in linear polymers form a long chain in which the monomers are attached end to end. The chains are neither straight nor stiff but flexible. Thus, the macromolecules can twist, bend and become entangled [17]. Generally, the degree of entanglement impacts the physical properties of a polymer, and the higher the number of entanglements per chain, the higher the polymer toughness, strength, and glass transition temperature (T_g). In branched polymers, the macromolecules have several short or long branched side chains attached to the main chain [18]. The ability of chains to slide past one another is affected by branching, thereby influencing chain entanglement. While for network-structured polymers, the macromolecules form three-dimensional (3D) structures. These polymers consist of a network macromolecule or an assembly of interacting macromolecules. Such polymers are usually chemically cross-linked, where the polymer's phase transition temperatures, rigidity, and crystallinity are adjusted using the chain length, cross-link density, degree of cross-linking, and nature of the cross-links [3,18]. The network polymers containing long, flexible branches connected to only a few sites along the chains exhibit elastic properties, while the network polymers which contain dense networks are generally rigid.

1.1.2. States of Matter and Thermal Transitions

Polymers' bulk state, sometimes called the condensed or solid state, can include crystalline and amorphous domains [19,20]. Semicrystalline polymers are often opaque because the crystallites may scatter light, while amorphous polymers are generally glass-like or transparent.

Polymers like linear homopolymers and block-copolymers may crystallize when their chain adapts to regular arrangements. This behavior is mainly observed for macromolecules with lower molecular weight. On the contrary, branched and long-chain polymers have a low tendency to crystallize because of their high degree of entanglement. This is particularly evident when the polymer melt is very viscous, and the individual chains do not flow easily. Polymers typically do not form flawless crystalline materials, whereas they form semicrystalline polymers consisting of amorphous regions and crystalline domains. Due to the strong intermolecular interaction forces associated with close chain packing of the crystallites, semicrystalline polymers generally exhibit high toughness. X-radiation (X-ray) diffraction [21,22], density measurements [16], and differential scanning calorimetry (DSC) [20] are usually used to determine the degree of crystallinity.

In a DSC measurement, the crystallites melt when heated and are formed when cooled. Thus, they exhibit a so-called first-order transition. The melting of crystallites and the crystallization of amorphous segments can be observed with discontinuity, especially in the heat flow-temperature diagram. The melting is an endothermic process, while the crystallization is an exothermic process. The associated heat transitions represent the melting enthalpy ΔH_m and the crystallization enthalpy ΔH_c. In contrast, the respective transition temperatures are the T_m when the polymer is heated and the crystallization temperature T_c when it is cooled (**Figure 1.2**). Crystallization can also be induced by severe deformation such

as stretching or compression, also known as strain-induced crystallization [23–25]. Here, the chains line up to crystallize on deformation. Such crystallites are usually harder to break because of their pronounced reinforcing effects.

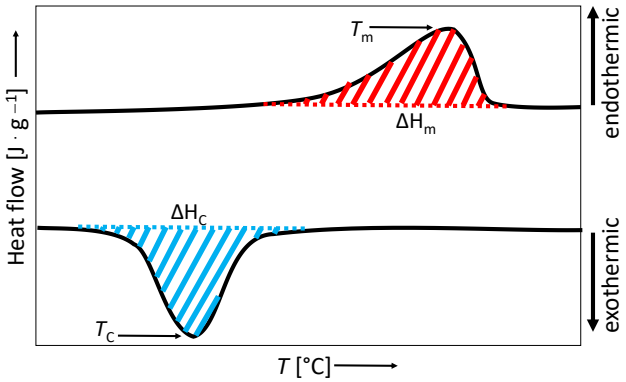

Figure 1.2. A typical DSC thermogram of a semicrystalline polymer showing a crystalline melting transition on heating (red region) and the associated crystallization transition on cooling (blue region).

Branched and long-chain linear macromolecules often tend to be amorphous, where the atoms rotate around the axis of the covalent bond, and the polymer chain adapts to diverse configurations. Generally, a randomly coiled and entangled state is the most likely arrangement observed for a single macromolecule [17]. Due to entropic forces, disordered chains are more probable than stretched, ordered ones. The glass transition, also called glass-fluid or glass-rubber transition, is considered the thermal transition for amorphous polymers. The amorphous domains of the polymer become rigid and brittle on vitrification caused by the transition from the viscous liquid state into the glassy state on supercooling. Vitrification reduces the micro-Brownian motion of the (network) chains [26,27], and the polymer is in a permanent non-equilibrium state. The phase transition of polymers is commonly determined by dynamic mechanical analysis (DMA) and DSC. In a DMA measurement, the loss modulus E'' is a measure of the viscous response of a polymer, and the storage modulus is the energy stored in the material. In other words, it measures the sample's elastic behavior. The transition of the polymer's bulk from a glassy to rubbery state is often determined by the ratio between loss modulus E'' and storage modulus E', where the temperature at the peak of the tanδ curve is frequently used to determine the T_g [28–30]. As the temperature rises above the glass transition temperature, the viscosity of the polymer increases uniformly, and Young's modulus decreases significantly [20,31]. This is particularly visible in a stepwise decrease in the evolution of the storage modulus E' (**Figure 1.3**).

Differential scanning calorimetry is used to study the thermal properties of a polymer. In the DSC experiment, the T_g of the polymer can be seen by the drastic shift of the baseline, indicating a change in the heat capacity C_p (**Figure 1.4**). The midpoint of the transition temperature from the glassy to the rubbery state is often considered the T_g [20].

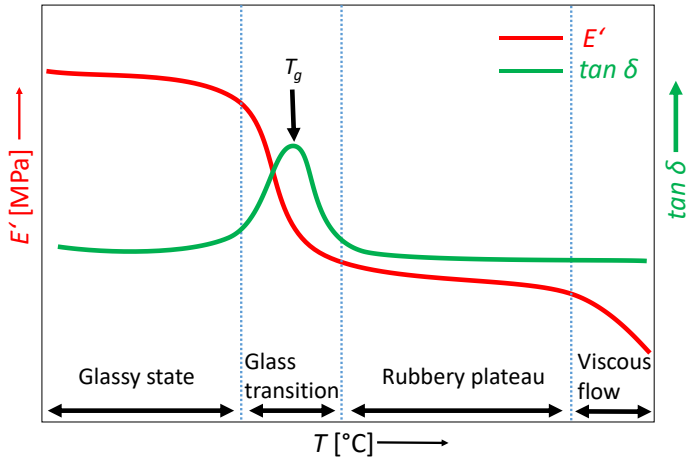

Figure 1.3. A typical DMA measurement of an amorphous polymer is measured during heating from a lower temperature. The evolution of the storage modulus (*E´*) is represented with the red line and the tanδ with the green line.

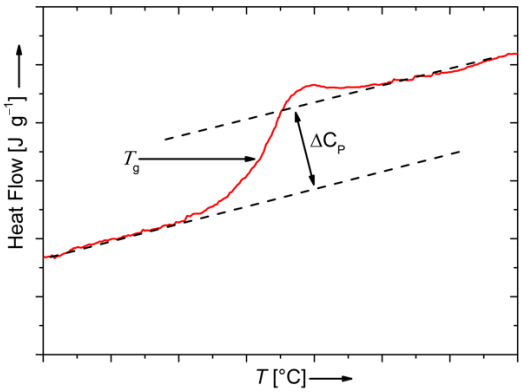

Figure 1.4. A typical DSC measurement of an amorphous polymer shows a second-order glass transition during heating.

Although the DSC and DMA methods can be used to determine the phase transition temperature of a polymer, the latter is considered to be the more sensitive method for determining the T_g, since the accuracy for determining the T_g using DMA is higher by a factor of about 1000 than the DSC technique [32,33].

1.1.3. Thermoplastics

Thermoplastic polymers consist of linear or branched macromolecules forming physically cross-linked polymers. Physical cross-linking occurs through interchain hydrogen bonding, dipole-dipole interactions, entanglements, and van der Waals forces. [17]. Such interactions support the crystal structure formation and hold the polymer segments together [34]. Processing techniques like extrusion [35–37], injection molding [38–40], additive manufacturing [41], and blow molding [42,43] help to mold and remold thermoplastics into virtually any shape.

In the case of thermoplastic elastomers, the netpoints are formed by reversible cross-links [44,45]. These get molten on heating and reform the cross-links on successive cooling. Systems like these exhibit a phase-segregated microstructure as they are typically composed of thermodynamically incompatible blocks [46–48]. The netpoints, also known as hard segments, have the highest thermal transition temperature (T_{perm}) and serve as physical cross-links and reinforcing fillers. Thereby, they supply the mechanical strength to the polymer. Above T_{perm}, the polymer behaves as a homogenous viscous melt and can be processed as described above. The so-called soft segment has a lower thermal transition temperature and acts as a mobile (switching) phase. It supplies elastic properties to the polymer.

Thermoplastics' and thermoplastic elastomers' thermal properties and functional performance can be tailored by varying polymer synthesis and manufacturing strategies. The vital parameters of the polymers depend on polymer architecture, including the molecular weight of the segments [49–52], cross-link density [53], and microphase separation [54,55].

Thermoplastic polyurethanes (TPUs) are a well-known example of phase-segregated polymers. TPUs are commonly synthesized from three building blocks: polyisocyanates, polyols, and chain extenders (**Figure 1.5**) [44,45,56].

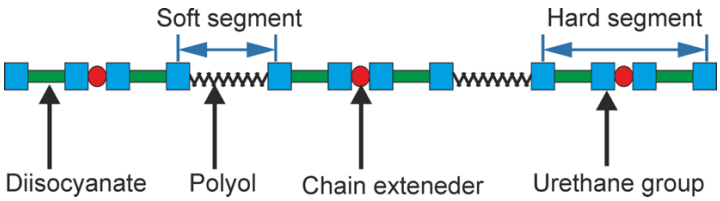

Figure 1.5. Schematic representation of a repeated hard segment and soft segment of a typical TPU.

The chain extender is made up of a short-chain low mol mass diol or diamines such as ethylene diamine [57], 1,4-butanediol (1,4-BD) [58], 1,6-hexanediol [59], or ethylene glycol [60]. In turn, the hard segment is made from chain extender and aromatic or aliphatic diisocyanate such as 2,4-toluene diisocyanate [61], 4,4'-methylene diphenyl diisocyanate (MDI) [62], 1,4-cyclohexane diisocyanate [63], or hexamethylene diisocyanate [64]. Finally, the polyol, which makes up the soft segment, is usually a long-chain difunctional, hydroxy-terminated oligoester or -ether. Some examples of polyester polyols are poly(1,10-decylene adipate) [65], poly(1,4-butylene adipate) (PBA) [66], while polypropylene glycol (PPG) is an example of a polyether polyol [67].

Thermoplastic polyurethanes are synthesized either by the prepolymer [68–72] or the one-shot method [71–77]. In the case of the prepolymer method, the polymerization is initiated by the reaction of a stoichiometric excess of a diisocyanate with linear polyols with a molecular weight of 50 to 5000 g mol^{-1}, thereby forming an intermediate polymer called prepolymer [76] (**Figure 1.6**). Next, the final high mol mass polymer is formed by the reaction of the prepolymer with a diol chain extender. **Figure 1.6** shows an example of the synthesis of a polyester-based TPU, while for the synthesis of polyether-based TPU, a hydroxy-terminated oligoether would be used instead of the oligoester.

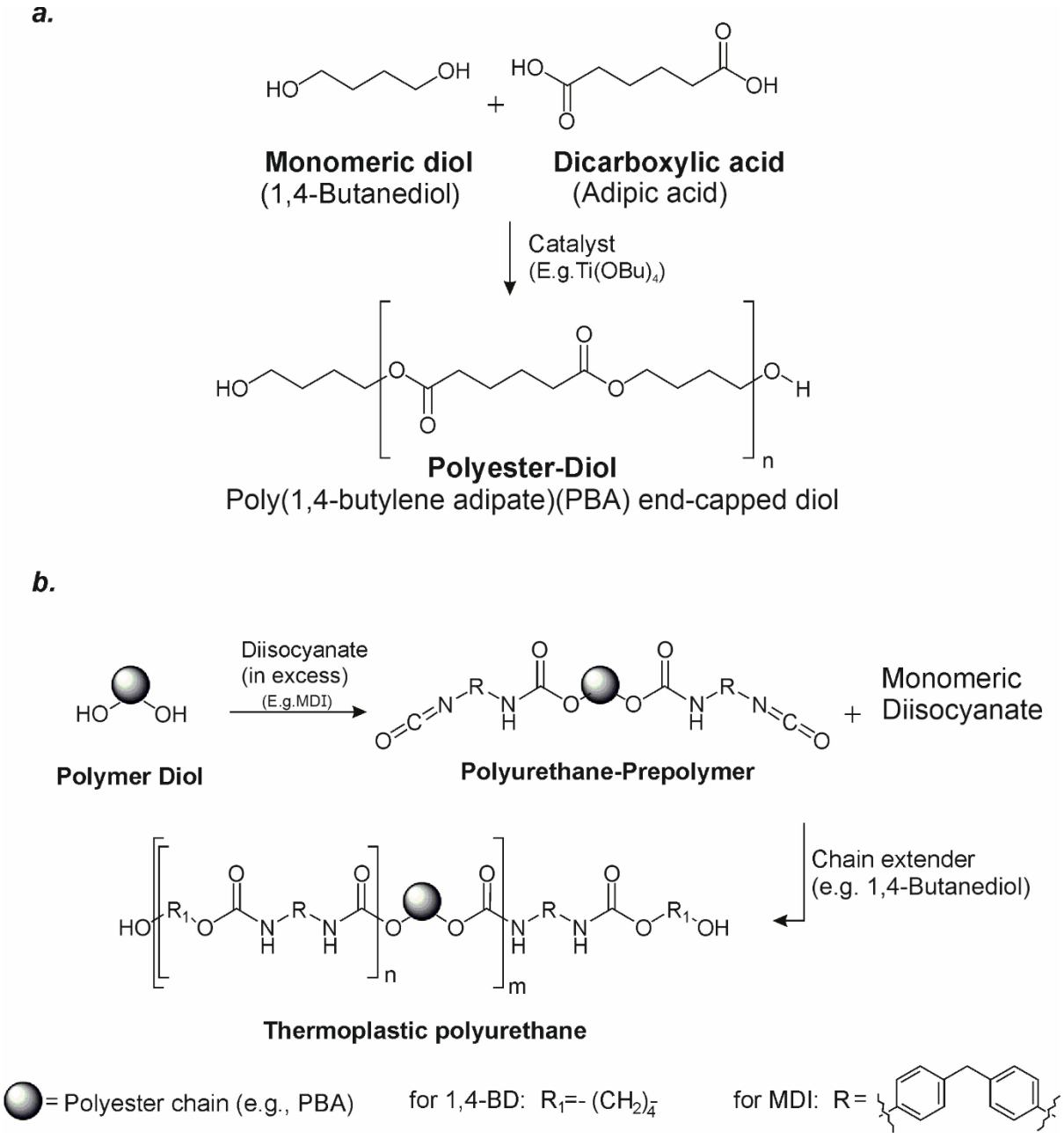

Figure 1.6. Synthesis of a TPU in the form of a polyester urethane via prepolymer method using (a) polycondensation reaction and (b) polyaddition reaction.

In the case of the one-shot method, the polymer is synthesized in a single step, where the three building blocks are added simultaneously. In both methods, other substances like additives or components can be supplied during the processing, such as flame retardants [78–80], dyes [81–83], pigments [84,85], stabilizers against hydrolysis [86], and radiation [87,88] or reinforcing fibers [89–91]. The urethane bonds connected through the chain extender molecules show high polarity because of significant hydrogen bonding. Due to this strong intermolecular interaction, the hard segments are formed and embedded in the amorphous or semicrystalline matrix of the elastic soft segments. After polymer synthesis, the TPUs can be processed into final or intermediate products, as described above.

1.1.3.1. Extrusion

Polymer extrusion is a high-profile manufacturing process. Extrusion processing is a technique for continuously shaping a fluidized polymer through an appropriately shaped die, followed by the solidification of the extrudate [92,93]. The main parts of an extruder are the plasticator (screw), barrel, motor, and nozzle (**Figure 1.7**).

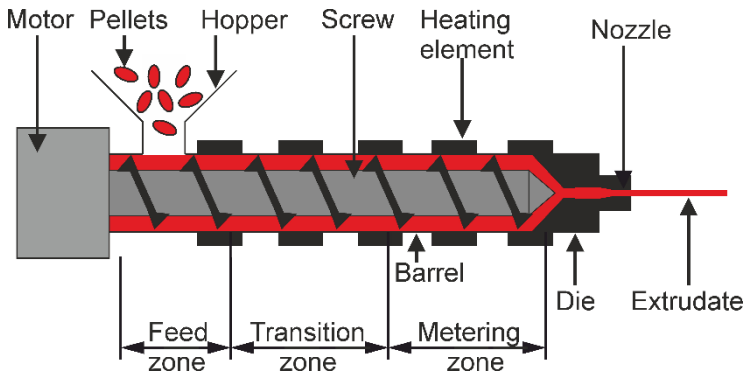

Figure 1.7. Schematic diagram of an extruder machine, showing individual parts.

The raw thermoplastic polymer in pellets, granules, flakes, powders, or a combination is used for extrusion. Additional to the raw material, additives such as pigments, dyes, reinforced materials, or other materials, either in liquid or pellet form, are often used to achieve specific characteristics or properties for the final product. The raw material and additives are fed to the hopper with or without a feeding mechanism. The feeding can be achieved using different feeding techniques, like starvation or flood feed techniques. As the material enters the feed throat through the hopper near the rear end of the barrel, it comes in contact with the screw. The rotating screw forces the plastic resin forward through the barrel. The screw system is typically categorized by three zones: the feed zone, where solid pellets are loaded; the transition zone, where mechanical working and heating fluidize the polymer; and the melt-metering zone, where the molten polymer is driven to the extrusion die. Each barrel section has a heating element with an independent PID controller (proportional-integral-derivative) to control the heating according to the temperature profile precisely. The extra heat is provided to the polymer via intense pressure and friction generated within the barrel and the screw rotation as the raw material moves forward. The plastic resin is gradually melted as it is pushed through the barrel, lowering the risk of overheating, which may cause degradation of the polymer. The molten polymer is then forced into a die, which imposes the intended final geometry on the extruded material and allows it to solidify through cooling to maintain the shape. A crucial challenge for extrusion systems is the phenomenon of die swell, which refers to the increase in the cross-section area observed when the extrudate leaves the restriction of the die. For a given polymer choice, this effect is a function of flow resistance, thereof, the melt temperature. Typical design measures used to stabilize the geometry of the extruded material include the manipulation of the extrusion-die geometry and associated material, as well as active cooling by forced air convection or water

quenching. Extrusion processing is customarily used to produce pipe/tubing [94], filaments [65,95,96], window frames [94], plastic films and sheeting [97], thermoplastic coatings [98,99], etc.

1.1.3.2. Injection Molding

Injection molding is another polymer processing technique used to produce parts by injecting material into a mold cavity [100–102]. The injection molding process starts with feeding polymers with or without additives in the form of granulates through a hopper to a barrel heated to a sufficient temperature for melting the polymer. The molten polymer is mixed and carried to the nozzle using a screw. Then the molten polymer will be injected with high pressure into a mold cavity. Later, the product is set to cool, which helps the solidification process while adapting to the cavity configuration. Subsequently, the plates are moved apart, and the product is ejected or removed from the mold, primarily using an ejection pin. Injection molding is a helpful technique for the cost-effective production of complex three-dimensional parts. The primary advantage of the processing technique is that the mold cavity can be so designed that there are a specific number of cavities to enable the production of a maximum number of products simultaneously out of the same mold in one cycle and therefore used for mass production.

1.1.3.3. Additive Manufacturing

Additive manufacturing (AM), alias 3D printing, is a rapid prototyping technique [103–107]. The 3D printing technique is a computer numerical controlled (CNC) operation in which a computer controls the parameters for each layer to form a 3D object by adding layer by layer. This way, 3D printed objects are created by adding material layers one after the other. Almost any shape or geometry of the object can be produced from a digital model or other electronic data files, such as standard triangle language (STL) or an additive manufacturing file (AMF).

In 1981, Hideo Kodama of Nagoya Municipal Industrial Research Institute published the first account of a working photopolymer-based rapid prototyping system [108]. Since then, it has marked the development of 3D printing machines. Additive manufacturing has been successfully applied in various fields, like aerospace and biomedical fields [103]. Due to its high customizability and design-on-demand, it has shown its importance in product development for developing visual and functional prototypes and modeling [109–111]. 3D printing technology is also widely used for small or medium-scale production [112,113].

The process of 3D printing is discussed in the following. The initial step of the 3D printing process is modeling. Here, the 3D model is designed with computer-aided designing (CAD) or 3D modeling software; a 3D scanner, digital camera, or photogrammetry software can also be used to develop 3D models. The models created with the CAD software generally have the least possible errors and are the best source for modeling. Once the model is created, it is exported into specific file extensions like .STL or .AMF.

The second step of the process is carried out with slicing software. The software converts the 3D model with predefined parameters, such as printing or movement speed, layer height, geometrical coordinates, nozzle-, bed temperature, and other variables with which the object should be manufactured. The information is then exported into a file with a 3D printer-compatible file extension like ".gcode" for fabricating the 3D model. The resulting file is a plain-text file with a series of GCODE and MCODE commands with a list of the complete *X*-, *Y*- , and *Z*-axis coordinates and machine parameters required for printing the 3D model.

The final step of the 3D printing process is carried out by transferring the GCODE file to the 3D printer. The 3D printer reads and processes the file accordingly and creates the 3D object layer by layer.

1.1.3.4. Fused Filament Fabrication

Fused filament fabrication (FFF) is a widely popular and most used technique among different AM techniques [109,114–118], like stereolithography (SLA), multi-jet fusion (MJF), selective laser sintering (SLS), and big area additive manufacturing (BAAM). The FFF uses the raw material in the form of a filament. Commercially available standard FFF printers prerequisite the filaments in diameter of either 2.85 mm or 1.75 mm with significantly lower tolerances, depending upon manufacturing requirements. **Figure 1.8** shows a typical FFF printer.

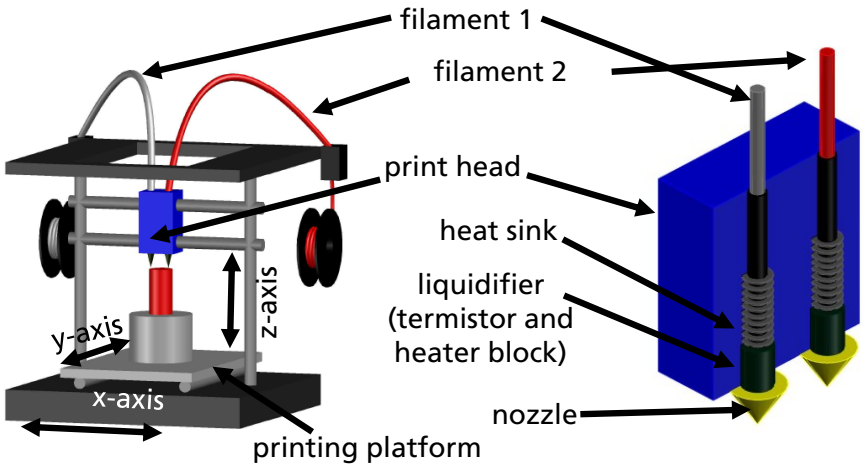

Figure 1.8. The schematic representation of a 3D printer that works according to the principle of FFF and the individual parts of the print head (blue color).

During the printing process, the material is unwounded from the spool to fabricate the part. A torque and pinch system is typically used to feed the filament to the printer's extruder precisely. The filament from the feeding system is pushed to the printer's extruder head directly or through a Bowden tube. A typical FFF 3D printer's extruder head consists of a heat sink, a heater block with a thermistor, a heating cartridge, and a nozzle (**Figure 1.8**). The filament enters the heater block via the heat sink from the cold end to ensure that the

filament gets molten only at the region of the heater block (hot end). This helps maintain a constant printing pressure and uniform polymer extrusion throughout the printing process. Once the material enters the heater block, the block heats and melts the filament to a usable temperature. The molten filament is then forced out through the nozzle opening and extrudes the material into thin strands. The extruded material is laid over the model or builds platform as predetermined by the slicer program, where the print head and/or build platform are moved to the exact location (X, Y, or Z) for placing the molten material. The 3D printer then builds the model by layer-by-layer addition of material and thereby builds the physical object [109,114–118].

1.1.4. Shape Memory Polymers

Shape memory polymers (SMPs) are smart materials that can retain a temporary shape attained through a thermomechanical treatment called "programming." The SMP recovers its permanent shape once exposed to an external stimulus by triggering the shape memory effect (SME) [119–123] (**Figure 1.9**). The external stimuli can be temperature [123], light [124], infrared radiation or laser light [125–128], magnetic field [129–132], electric field [133,134], or others [123,135–138].

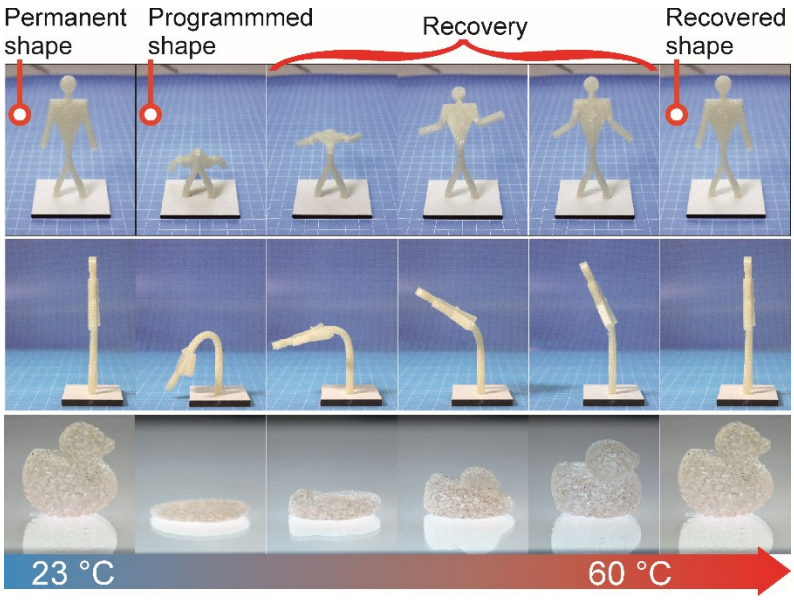

Figure 1.9. Permanent shape, programmed shape, triggering of the SME when heated above the T_m of the soft segments (switching temperature) and recovered shape of an additively manufactured man (top and middle row, front and left view respectively) and duck (bottom row).

The SME is independent of a specific material property of single polymers but results from a combination of the polymer's morphology and structure in cooperation with the applied programming and processing technology. Among different SMPs, thermally switchable SMPs are the most common and studied polymers [135,139,140]. Based on the network structure, SMPs can be categorized as physically [119,120,141–143] and chemically cross-linked

SMPs [119,120,144,145]. While, according to the thermal transition temperature (T_{trans}) of the particular switching segments, the SMPs T_{trans} can be either the T_m or T_g. The thermoresponsive SMEs of SMPs may be triggered either via direct or indirect heating. For indirect heating, the polymer is doped with suitable fillers, which enable selective heating of the polymer by irradiation with light [146,147], magnetic fields [132,148–150], or electric current [151–153].

Amidst other SMPs, TPUs have proven their potential [51,86,154–165], primarily due to their adjustable phase separation, strong deformability, reprocessing capability, and recyclability. The TPUs exhibiting shape memory properties consist of switching segments, also known as soft segments, and crosslinks or netpoints, making the hard segments. The former is used to maintain the temporary shape, while the latter determines the permanent shape and is used to recover its initial shape. A typical programming procedure of thermoresponsive SMPs includes either applying a deformation above the phase transition temperature (T_{trans}), so-called "hot programming," or deforming the sample at a low temperature, known as the "cold programming." Subsequently, for the hot programming scenario, while holding the deformed shape, the SMP would be cooled below the fixation temperature (T_{fix}), i.e., below its T_g or offset of crystallization transition temperature (T_c) of the soft segment. After a sufficient cooling time, the external load would be removed, and the temperature would be raised to room temperature to complete the programming steps. Afterward, the new temporary shape remains stable until the ambient temperature of the polymer is raised over T_{trans}. Consequently, the SME is triggered, and the polymer recovers its original shape. The SMP can be brought into a subsequent temporary shape by performing the programming step again. This new temporary shape need not be the first temporary shape.

1.1.5. Molecular Mechanism of Shape Memory Effect

The polymer chains of thermoplastic SMPs always prefer a randomly coiled arrangement in their permanent shape. In the case of semicrystalline SMPs, heating above the T_{trans} of the soft segment makes them elastic during programming. Later, stretching the polymer increases the distance between the netpoints of the hard segment and orients the network structure. The new temporary shape is fixed by introducing reversible physical cross-links in the form of crystallites by cooling below the T_{fix}. The freshly formed crystals stabilize the new shape and restrict the macromolecules from spontaneously returning to the random coil structure. The temporary shape remains stable until the SME is triggered. Heating the material above T_{trans} again cleaves the physical cross-links by melting the crystallites in the switching phase. The associated gain in entropy is the thermodynamic reason for the polymer to recover its random coiled structure, enabling the SMP to recover its permanent shape (**Figure 1.10**).

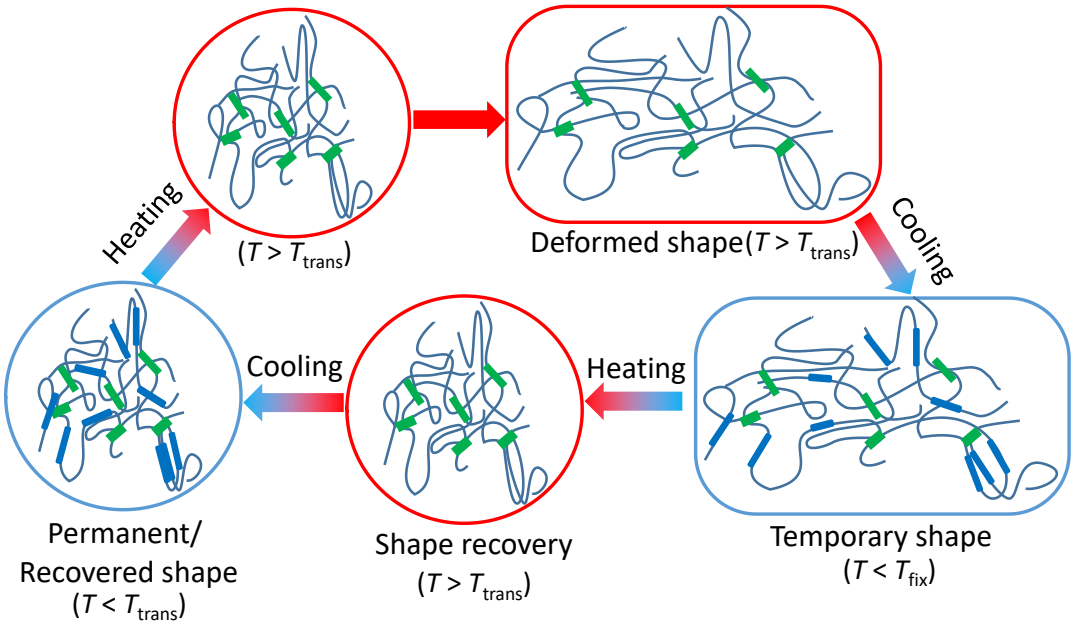

Figure 1.10. Molecular mechanism of a physically cross-linked SMP representing permanent shape, programming of a temporary shape, and shape recovery. Green blocks represent the netpoints formed by hard segments, and blue lines represent soft segments.

In the case of amorphous SMPs, the polymer can be easily deformed elastically in its rubbery state once heated above its T_g. Later, the fixation of the temporary shape is accomplished by kinetically freezing the motion of the polymer chains by cooling below its T_g. The programmed shape remains stable as the polymeric chains do not possess sufficient thermal energy to retract to their preferred orientation in the glassy state. The almost permanent shape is later recovered when thermal energy is brought into the system via heating above T_g.

1.2. Shape Memory Effect of Objects Manufactured via Fused Filament Fabrication

Fused filament fabrication (FFF) with polymers can be subdivided into five categories based on the SMEs that can be harnessed from the additively manufactured object (**Figure 1.11**).

Additive manufacturing with polymers generally creates non-responsive objects that are static. However, the FFF with thermoresponsive SMPs helps to produce 3D objects that can exhibit dual shape one-way (1W) SME, one-way 1W-SME (four-dimensional (4D) printing), two-way (2W)-SME, and 2W-4D SME. The different thermoresponsive SMEs achieved employing FFF will be described in more detail in the following.

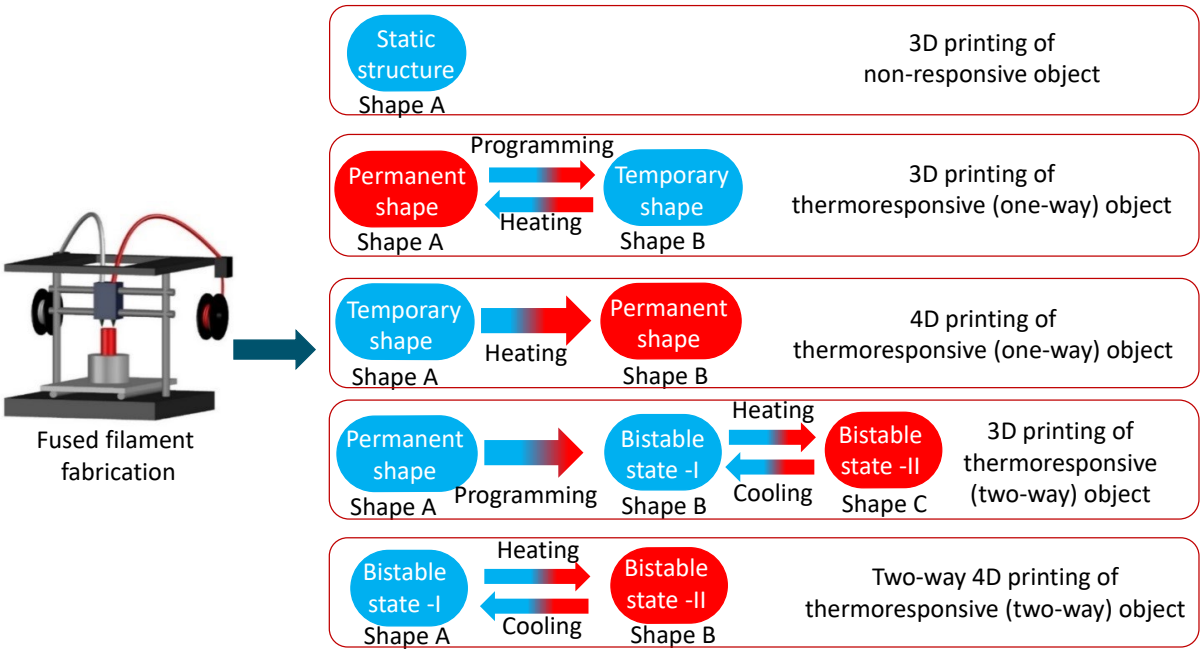

Figure 1.11. Classification of the fused filament fabrication (FFF) process based on the responsiveness of the printed object.

1.2.1. One-Way Shape Memory Effect

Dual-shape 1W-SME is the most prominent and widely employed SME. Following a programming step, the SMP can take a temporary shape and remain stable at room temperature [95,166–169]. The permanent shape of the SMP is recovered under stress-free conditions once the SMP is heated above its T_{trans} of the soft segment [95,167,170] (**Figure 1.12**). An additional programming step has to be undergone after each triggering of the 1W-SME to restore the thermoresponsive state for enabling the next shape memory cycle.

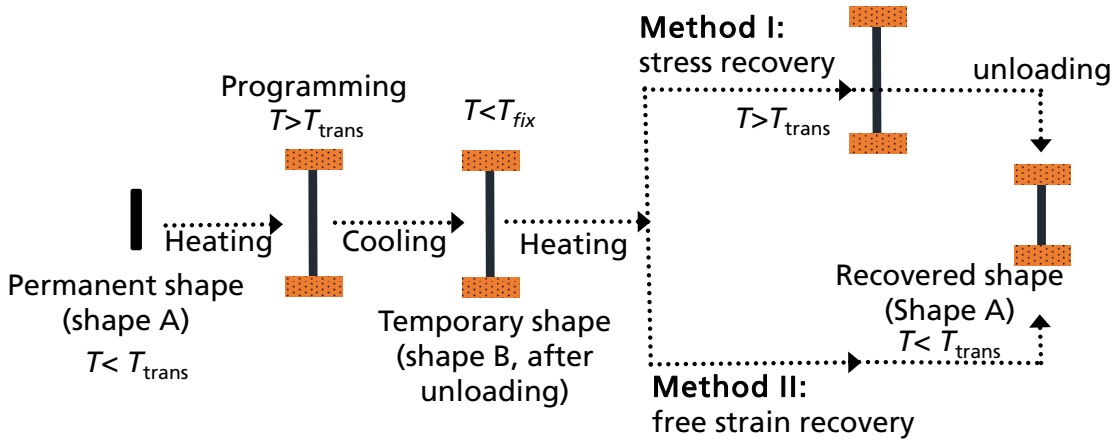

Figure 1.12. Programming and recovery step of an additively manufactured object to achieve 1W-SME.

The shape memory properties of a polymer are generally quantified in cyclic thermo-mechanical measurements (CTMs) [119,123,171]. The measurements are carried out using a

tensile testing machine equipped with an environmental chamber. During a CTM study, the temperature (T), strain (ε), and stress (σ) are generally closely watched. At the same time, the respective heating or cooling rates, deformation, and loading or unloading rates can be adjusted to develop different programming procedures. Generally, a dog-bone-shaped tensile bar (EN ISO 527-2:1996) [172] is used to perform CTMs.

Additive manufacturing is an established method to produce 3D objects from SMPs [95,166–170,173,174]. The SMPs processed utilizing FFF can be programmed as described in **sections 1.1.4** and **1.1.5** to show 1W shape memory properties. Among other AM techniques, FFF has shown its significance in processing SMPs, primarily due to the adjustable horizontal and vertical resolution, good printing results [95,169], and the ability to adjust mechanically and shape memory properties by varying geometrical parameters like print orientation and infill percentage [167,168].

1.2.2. Two-Way Shape Memory Effect

Without further programming steps, the SMPs cannot return to their temporary shape on heating or cooling after triggering their 1W-SME and the complete recovery of their original shape (1W-SME). On the other hand, the 2W-SME using SMP can actuate between two programmable metastable states [65,175–181]. Generally, some semicrystalline SMPs like TPU have shown this switching behavior for single-material systems. The 2W-SME was initially observed in chemically cross-linked poly(cyclooctene) [175] and was later transferred to physically cross-linked polymers. However, the initially discovered 2W-SME was achieved while applying an external load permanently. It was recently shown that it is possible to actuate a semicrystalline SMP just by heating and cooling without needing any external load [66,182,183].

The programming of a reversible 2W-SME is almost identical to a 1W-SME. After heating the polymer to a temperature of $T > T_m$, the soft segment becomes completely amorphous. The material is then deformed from its permanent form (shape A) into a predetermined form, shape B, using an external force (**Figure 1.13**). This deformation induces the polymer chains to achieve a highly oriented molecular structure within the polymer network of the soft segment. Subsequently, the fixation of the temporary shape is achieved by cooling under stress to a temperature of T_c, below the offset of the soft segmental crystallization temperature, thereby storing the temporary shape (shape B). The applied stress can be removed after crystallization without causing the chain segments to recoil. The macromolecular alignment is inextricably linked to the macroscale deformation of the material, and thus, bespoke geometries can be realized by simply varying the applied force during programming.

The hard segments are responsible for determining the shape-shifting geometry during actuation. Here, the soft segments provide the driving force for actuation because their chain segments undergo conformational dis- and reorientation on heating and cooling, respectively. In detail, on heating to an intermediate temperature T_{max} (maximum actuation

temperature) < T_m, which is between the onset and offset of the melt transition temperature, the melting-induced contraction (MIC) of the actuation domains generates a first bistable state- I (shape C). The soft segmental chains responsible for actuation remain in a partially oriented conformation, constrained by the deformed crystalline geometry determining units. Upon cooling to T_c, the recrystallization of the soft segments drives in achieving the second bistable state-II (shape D). Cycling between T_c and T_{max} allows to switch between the two metastable states (shape C and shape D) reversibly and can be repeated hundreds of times [65]. Moreover, the SMP can be further reprogrammed by heating to T_m. The original shape of the material is recovered, and later, a completely new shape can be defined by repeating the programming procedure.

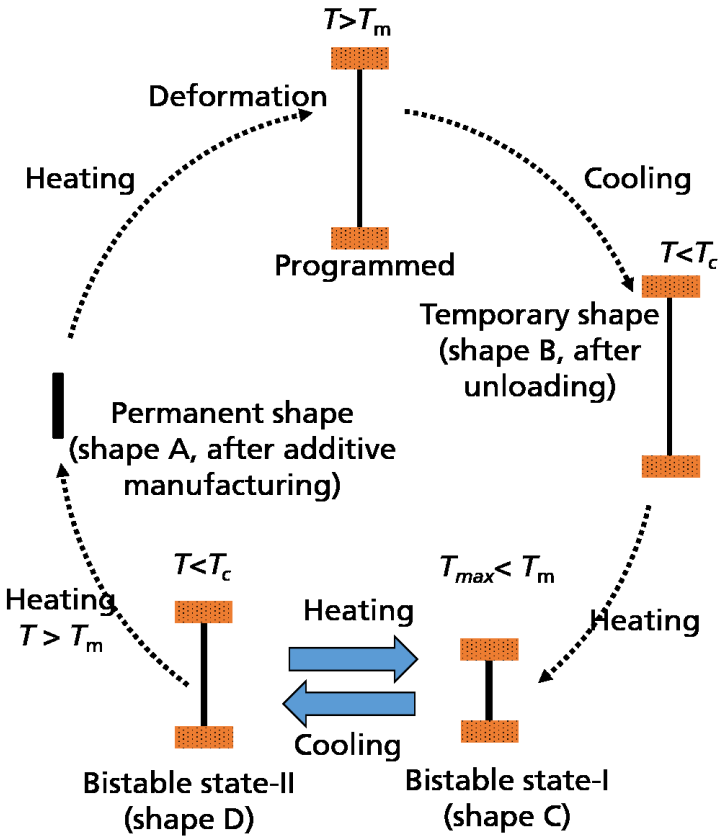

Figure 1.13. Schematic representation of programming and actuation of an additively manufactured object to achieve 2W-SME.

1.2.3. Four Dimensional (4D)-Printing

3D printing with SMPs produces non-responsive objects, which always requires an additional programming step to make them thermoresponsive. In the case of 4D-printing, the printed objects are obtained directly in their temporary shape and determine the shape after heating above the switching temperature [67]. In 2013, Skylar Tibbits first introduced the concept of 4D-printing, where the printed objects can transform their shape directly after removal from the print platform when appropriate stimuli are applied, without needing a

further post-treatment step [184]. To demonstrate the 4D-printing concept, Skylar Tibbits utilized a multi-material combinational approach, where a hydrogel was used as an active material and a static, rigid polymer as a passive material to achieve different degrees of bending or shape transformations [184,185]. Later, the 4D-printing technology was transferred to the FFF and was achieved using a single SMP [67,186–194]. It is worth mentioning that on using 4D-printing, the objects are manufactured directly in their thermoresponsive state and are thus available for immediate use [67,186,188,190,191,193,194] (**Figure 1.14**). This way, the need for classical 1W-SME programming can be eliminated for certain SMPs.

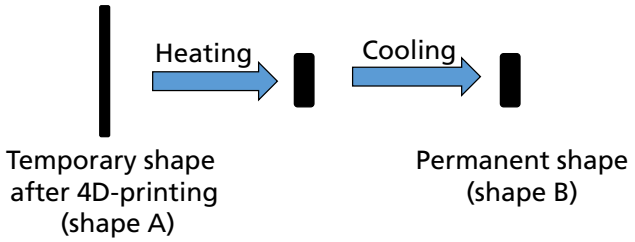

Figure 1.14. Schematic representation of 4D-printing and shape transformation of an additively manufactured object to achieve one-time thermoresponsiveness.

In the case of 4D-printing via FFF with SMPs, specific printing parameters like nozzle temperature, printing pressure, and speed are precisely selected for attaining individual polymer chains to assume a highly oriented state. At the same time, the printing pattern is adjusted to achieve specific bending or shrinkage behavior [67,186,195]. The basic idea behind the 4D-printing technique is that an extruded polymer strand laid on the printing platform or a top polymer layer is rapidly cooled below the polymer's glass transition temperature so that the individual polymer chains are oriented in the direction of nozzle movement. Later, they are not allowed to relax on quick vitrification, thus storing the highly oriented states efficiently.

Figure 1.15 shows an illustration of the 4D-printing process. In detail, the polymer filament is first heated to a melt temperature (T_{perm}) above the material's T_g. The molten filament is then extruded through the nozzle and laid on the print platform, also denoted as the print bed. The selection of specific printing parameters causes the polymer chains to orientate in the direction of nozzle movement [186]. The SMP is then allowed to cool quickly below its T_g once laid on the printing platform or the previous layer (below) [67,196,197]. The vitrification freezes the oriented chain formation caused by the printing to be stored in the material. The printed shape (Shape A) remains stable until the ambient temperature is raised above the switching temperature of the SMP, most commonly the glass transition temperature [67]. Once heated, the polymer releases internal stresses by molecular motion to gain an entropically more favorable random coil chain conformation, culminating in shrinkage along the direction of nozzle movement to achieve its permanent shape (Shape B) [196,197].

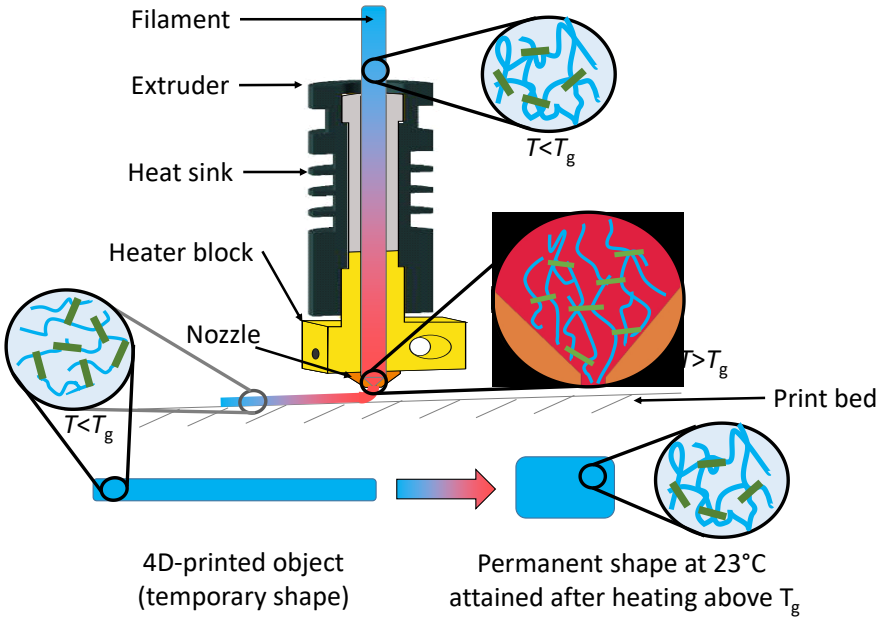

Figure 1.15. Schematic representation of the 4D-printing process and thermal triggering of the 4D effect on a printed object.

1.2.4. Two-Way Four-Dimensional Printing

The 4D-printing of actuating objects is a novel area of research. The underlying concept was developed to eliminate the time-consuming classical programming of SMPs to witness 2W-SMEs, directly after the 4D-printing. In other words, an object is fabricated/ additively manufactured directly in a first bistable state-I after printing, from which the shape can be switched to a second bistable state-II only by applying an appropriate stimulus. The whole process is reversible (**Figure 1.16**).

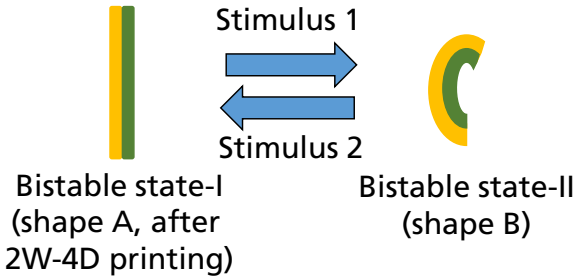

Figure 1.16. Schematic representation of 2W-4D-printing of an actuating object.

The development and innovation of materials and AM technology has led to objects that actuate immediately after printing. The 2W-4D-printing technique can be achieved through gradient- or bilayer-structures or core-shell embedded structures [198]. The bilayer- or gradient- structure exploits composite AM technology [199–205]. Here, the fabricated composite layers consist of materials with antagonistic or reversible physical properties, like shape changes associated with water absorption/desorption or temperature changes, to

induce stimulus-governed shape changes. On the contrary, the core-shell embedded structure focuses on manufacturing elastomeric material composites containing magnetic particles [206–209]. When applying a specific magnetic field, their shape can be changed in a controllable manner; as soon as the magnetic field is switched off, the initial shape is recovered due to the elastomeric properties of the matrix material.

1.3. References

1. Cowie, J.M.G.; Arrighi, V. *Polymers*: *Chemistry and physics of modern material* CRC Press: Boca Raton, 2008, ISBN 9780849398131.
2. Stevens, M.P. *Polymer chemistry*: *An introduction / Malcolm P. Stevens*, 2nd ed.; Oxford University Press: New York, 1990, ISBN 0195057597.
3. Painter, P.C.; Coleman, M.M. *Fundamentals of polymer science*: *An introductory text / Paul C. Painter, Michael M. Coleman*, 2nd ed.; Technomic: Lancaster, Pa., 1997, ISBN 1566765595.
4. Young, R.J.; Lovell, P.A. *Introduction to polymers*, 3rd ed. / Robert J. Young, Peter A. Lovell; CRC: Boca Raton, Fla., 2011, ISBN 9780849339295.
5. Mohanty, A.K.; Misra, M.; Drzal, L.T. *Natural fibers, biopolymers, and biocomposites;* Taylor & Francis: Boca Raton, FL, 2005, ISBN 0203508203.
6. *Natural polymers*: *Perspectives and applications for a green approach;* Jacob, J.; Gomes, F.; Haponiuk, J.T.; Kalarikkal, N.; Thomas, S., Eds., First edition; Apple Academic Press: Palm Bay FL, 2022, ISBN 9781771889605.
7. Freitag, R. *Synthetic polymers for biotechnology and medicine;* Landes Bioscience; Austin: Georgetown, Tex., 2003, ISBN 1587060272.
8. Yagci, Y.; Mishra, M.K.; Nuyken, O.; Ito, K.; Wnek, G. *Tailored polymers & applications;* CRC Press: Boca Raton, 2000, ISBN 9067643262.
9. Chamas, A.; Moon, H.; Zheng, J.; Qiu, Y.; Tabassum, T.; Jang, J.H.; Abu-Omar, M.; Scott, S.L.; Suh, S. Degradation Rates of Plastics in the Environment. *ACS Sustainable Chem. Eng.* **2020**, *8*, 3494–3511, doi:10.1021/acssuschemeng.9b06635.
10. Jones, R.G.; Kitayama, T.; Hellwich, K.-H.; Hess, M.; Jenkins, A.D.; Kahovec, J.; Kratochvíl, P.; Mita, I.; Mormann, W.; Ober, C.K.; et al. Source-based nomenclature for single-strand homopolymers and copolymers (IUPAC Recommendations 2016). *Pure and Applied Chemistry* **2016**, *88*, 1073–1100, doi:10.1515/pac-2015-0702.
11. KUMAR, R.; SINGH, V.P.; PRAJAPATI, M.; A, A.; SINGH, P.; SAMANTA, S.; BANERJEE, S. Performance Evaluation of Nucleating Agents in Polypropylene Homopolymer. *JPM* **2020**, *36*, 323–335, doi:10.32381/JPM.2019.36.04.3.
12. Shi, B.; Peng, P.; Jia, L. Relationship Between Total Surface Tension of Monomer and Its Homopolymer. *Journal of Macromolecular Science, Part B* **2011**, *50*, 952–955, doi:10.1080/00222348.2010.497092.
13. Feldman, D.; Barbalata, A. *Synthetic polymers*: *Technology, properties, applications / Dorel Feldman and Alla Barbalata;* Chapman & Hall: London, 1996, ISBN 0412710404.
14. Askadskiĭ, A.A. *Physical properties of polymers*: *Prediction and control / Andrey A. Askadskii;* Gordon and Breach: Amsterdam, United Kingdom, 1996, ISBN 2884491554.
15. Daniels, C.A. *Polymers*: *Structure and properties;* Technomic Publishing: Basel, 1989, ISBN 0877625522.
16. Mark, J.E. *Physical properties of polymer handbook*, 2nd ed.; Springer: New York, London, 2007, ISBN 9780387312354.
17. Mandelkern, L. *Crystallization of polymers*, 2nd ed.; Cambridge University Press: Cambridge, 2002-, ISBN 0521816815.
18. Painter, P.C.; Coleman, M.M. *Essentials of polymer science and engineering;* DEStech Publications: Lancaster, Pa., 2009, ISBN 9781932078756.
19. Brown, R. *Handbook of Polymer Testing;* CRC Press, 1999, ISBN 9780429177446.
20. Sperling, L.H. *Introduction to physical polymer science*, 4th ed.; Wiley: New York, Chichester, 2006, ISBN 9780471706069.
21. Katz, L. X-ray diffraction in crystals, imperfect crystals, and amorphous bodies (Guinier, A.). *J. Chem. Educ.* **1964**, *41*, 292, doi:10.1021/ed041p292.2.

22. Suryanarayana, C. *X-Ray Diffraction*: *A Practical Approach*, 1st ed.; Springer: New York, NY, 1998, ISBN 9781489901484.
23. Mark, J.E. The effect of strain-induced crystallization on the ultimate properties of an elastomeric polymer network. *Polym. Eng. Sci.* **1979**, *19*, 409–413, doi:10.1002/pen.760190608.
24. Sakurai, K.; Takahashi, T. Strain-induced crystallization in polynorbornene. *J. Appl. Polym. Sci.* **1989**, *38*, 1191–1194, doi:10.1002/app.1989.070380616.
25. Rao, I.J.; Rajagopal, K.R. A study of strain-induced crystallization of polymers. *International Journal of Solids and Structures* **2001**, *38*, 1149–1167, doi:10.1016/S0020-7683(00)00079-2.
26. Sasabe, H.; Saito, S. Effects of Temperature and Pressure on the Micro-Brownian Motion in Poly(vinyl chloride). *Polym J* **1972**, *3*, 631–639, doi:10.1295/polymj.3.631.
27. JELČIĆ, Ž.; RANOGAJEC, F. Relaxation properties and glass transition by radiation crosslinking of unsaturated polyester resins. *Polimeri : časopis za plastiku i gumu* **2010**, *31*, 113–126.
28. Fritzsche, N.; Pretsch, T. Programming of Temperature-Memory Onsets in a Semicrystalline Polyurethane Elastomer. *Macromolecules* **2014**, *47*, 5952–5959, doi:10.1021/ma501171p.
29. Rocco, J.A.F.F.; Lima, J.E.S.; Lourenço, V.L.; Batista, N.L.; Botelho, E.C.; Iha, K. Dynamic mechanical properties for polyurethane elastomers applied in elastomeric mortar. *J. Appl. Polym. Sci.* **2012**, *126*, 1461–1467, doi:10.1002/app.36847.
30. Li, J.; Kan, Q.; Chen, K.; Liang, Z.; Kang, G. In Situ Observation on Rate-Dependent Strain Localization of Thermo-Induced Shape Memory Polyurethane. *Polymers* **2019**, *11*, doi:10.3390/polym11060982.
31. Ferry, J.D. *Viscoelastic properties of polymers*, 3rd ed.; Wiley: New York, Chichester, 1980, ISBN 0471048941.
32. GROENEWOUD, W.M. CHAPTER 4 - DYNAMIC MECHANICAL ANALYSIS. In *Characterisation of polymers by thermal analysis*; GROENEWOUD, W.M., Ed.; Elsevier: Amsterdam, London, 2001; pp 94–122, ISBN 978-0-444-50604-7.
33. Hagen, R.; Salmén, L.; Lavebratt, H.; Stenberg, B. Comparison of dynamic mechanical measurements and Tg determinations with two different instruments. *Polymer Testing* **1994**, *13*, 113–128, doi:10.1016/0142-9418(94)90020-5.
34. Zhu, Y.; Hu, J.; Yeung, K. Effect of soft segment crystallization and hard segment physical crosslink on shape memory function in antibacterial segmented polyurethane ionomers. *Acta Biomater.* **2009**, *5*, 3346–3357, doi:10.1016/j.actbio.2009.05.014.
35. Rauwendaal, C. *Polymer extrusion*, 5th edition; Hanser Publications; Hanser Publication: Munich, Cincinnati, 2014, ISBN 9781569905166.
36. *Polymer extrusion;* Lafleur, P.G.; Vergnes, B.; Reveley, Z., Eds., 1., Auflage; ISTE: London, 2014, ISBN 9781118827000.
37. Cassagnau, P.; Bounor-Legaré, V.; Fenouillot, F. Reactive Processing of Thermoplastic Polymers: A Review of the Fundamental Aspects. *International Polymer Processing* **2007**, *22*, 218–258, doi:10.3139/217.2032.
38. Kelleher, P.G. Advances in injection molding of fiber-reinforced thermoplastics during 1991—Part II: Processing, design, and manufacture. *Adv. Polym. Technol.* **1993**, *12*, 297–311, doi:10.1002/adv.1993.060120308.
39. Kamal, M.R.; Kenig, S. The injection molding of thermoplastics part I: Theoretical model. *Polym. Eng. Sci.* **1972**, *12*, 294–301, doi:10.1002/pen.760120408.
40. *Injection Molding*: *Technology and Fundamentals;* Kamal, M.R.; Isayev, A.I., Eds.; Hanser: München, 2012, ISBN 9783446433731.
41. Celik, E. *Additive manufacturing*: *Science and technology;* Walter de Gruyter GmbH: Berlin, Boston, 2020, ISBN 9781501518775.
42. Belcher, S.L. *Practical guide to injection blow molding;* Taylor & Francis: Boca Raton, Fla., 2006, ISBN 9781420014815.
43. Thielen, M. *EXTRUSION BLOW MOLDING;* Hanser Publications: [S.l.], 2021, ISBN 9781569908402.
44. Kricheldorf, H.R.; Quirk, R.P.; Holden, G. *Thermoplastic elastomers*, 3rd ed.; Hanser Gardner Publications: Cincinnati, 2004, ISBN 1569903646.
45. Holden, G. Thermoplastic Elastomers. In *Rubber Technology*; Morton, M., Ed.; Springer US: Boston, MA, 1987; pp 465–481, ISBN 978-1-4615-7825-3.
46. Bonart, R.; Müller, E.H. Phase separation in urethane elastomers as judged by low-angle X-ray scattering. I. Fundamentals. *Journal of Macromolecular Science, Part B* **1974**, *10*, 177–189, doi:10.1080/00222347408219403.
47. Lee, H.S.; Wang, Y.K.; Hsu, S.L. Spectroscopic analysis of phase separation behavior of model polyurethanes. *Macromolecules* **1987**, *20*, 2089–2095, doi:10.1021/ma00175a008.

48. Xu, Y.; Petrovic, Z.; Das, S.; Wilkes, G.L. Morphology and properties of thermoplastic polyurethanes with dangling chains in ricinoleate-based soft segments. *Polymer* **2008**, *49*, 4248–4258, doi:10.1016/j.polymer.2008.07.027.
49. Ping, P.; Wang, W.; Chen, X.; Jing, X. Poly(epsilon-caprolactone) polyurethane and its shape-memory property. *Biomacromolecules* **2005**, *6*, 587–592, doi:10.1021/bm049477j.
50. Chen, S.; Hu, J.; Liu, Y.; Liem, H.; Zhu, Y.; Meng, Q. Effect of molecular weight on shape memory behavior in polyurethane films. *Polymer International* **2007**, *56*, 1128–1134, doi:10.1002/pi.2248.
51. Bothe, M.; Emmerling, F.; Pretsch, T. Poly(ester urethane) with Varying Polyester Chain Length: Polymorphism and Shape-Memory Behavior. *Macromolecular Chemistry and Physics* **2013**, *214*, 2683–2693, doi:10.1002/macp.201300464.
52. Momtaz, M.; Razavi-Nouri, M.; Barikani, M. Effect of block ratio and strain amplitude on thermal, structural, and shape memory properties of segmented polycaprolactone-based polyurethanes. *J Mater Sci* **2014**, *49*, 7575–7584, doi:10.1007/s10853-014-8466-y.
53. Mondal, S.; Hu, J.L. Studies of Shape Memory Property on Thermoplastic Segmented Polyurethanes: Influence of PEG 3400. *Journal of Elastomers & Plastics* **2007**, *39*, 81–91, doi:10.1177/0095244307067423.
54. Chen, W.-P.; Kenney, D.J.; Frisch, K.C.; Wong, S.-W.; Moore, R. Study of phase separation in polyurethane using paramagnetic labels. Effect of soft segment molecular weight, structure, and thermal history. *J. Polym. Sci. B Polym. Phys.* **1991**, *29*, 1513–1524, doi:10.1002/polb.1991.090291208.
55. Pereira, I.M.; Oréfice, R.L. morphology and phase mixing studies on poly(ester–urethane) during shape memory cycle. *Journal of materials science* **2010**.
56. Oertel, G. *Kunststoff-Handbuch*, 3rd ed.; Hanser: München, Wien, 1993, ISBN 9783446162631.
57. Touchet, T.J.; Cosgriff-Hernandez, E.M. 1 - Hierarchal structure–property relationships of segmented polyurethanes. In *Advances in polyurethane biomaterials*; Cooper, S.L., Guan, J., Eds.; Woodhead Publishing: Duxford, 2016; pp 3–22, ISBN 978-0-08-100614-6.
58. Walter, M.; Friess, F.; Krus, M.; Zolanvari, S.M.H.; Grün, G.; Kröber, H.; Pretsch, T. Shape Memory Polymer Foam with Programmable Apertures. *Polymers* **2020**, *12*, doi:10.3390/polym12091914.
59. Xian, W.; Song, L.; Liu, B.; Ding, H.; Li, Z.; Cheng, M.; Le Ma. Rheological and mechanical properties of thermoplastic polyurethane elastomer derived from CO 2 copolymer diol. *J. Appl. Polym. Sci.* **2018**, *135*, 45974, doi:10.1002/app.45974.
60. Azzam, R.A.; Mohamed, S.K.; Tol, R.; Everaert, V.; Reynaers, H.; Goderis, B. Synthesis and thermo-mechanical characterization of high performance polyurethane elastomers based on heterocyclic and aromatic diamine chain extenders. *Polymer Degradation and Stability* **2007**, *92*, 1316–1325, doi:10.1016/j.polymdegradstab.2007.03.017.
61. Kausar, A. Physical properties and shape memory behavior of thermoplastic polyurethane/poly(ethylene-alt-maleic anhydride) blends and graphene nanoplatelet composite. *Iran Polym J* **2016**, *25*, 945–955, doi:10.1007/s13726-016-0481-1.
62. Behniafar, H.; Azadeh, S. Transparent and Flexible Films of Thermoplastic Polyurethanes Incorporated by Nano-SiO 2 Modified With 4,4'-Methylene Diphenyl Diisocyanate. *International Journal of Polymeric Materials and Polymeric Biomaterials* **2015**, *64*, 1–6, doi:10.1080/00914037.2014.886237.
63. Riehle, N.; Athanasopulu, K.; Kutuzova, L.; Götz, T.; Kandelbauer, A.; Tovar, G.E.M.; Lorenz, G. Influence of Hard Segment Content and Diisocyanate Structure on the Transparency and Mechanical Properties of Poly(dimethylsiloxane)-Based Urea Elastomers for Biomedical Applications. *Polymers* **2021**, *13*, doi:10.3390/polym13020212.
64. Głowińska, E.; Wolak, W.; Datta, J. Eco-friendly Route for Thermoplastic Polyurethane Elastomers with Bio-based Hard Segments Composed of Bio-glycol and Mixtures of Aromatic-Aliphatic and Aliphatic-Aliphatic Diisocyanate. *J Polym Environ* **2021**, 1–10, doi:10.1007/s10924-020-01992-5.
65. Schönfeld, D.; Chalissery, D.; Wenz, F.; Specht, M.; Eberl, C.; Pretsch, T. Actuating Shape Memory Polymer for Thermoresponsive Soft Robotic Gripper and Programmable Materials. *Molecules* **2021**, *26*, doi:10.3390/molecules26030522.
66. Bothe, M.; Pretsch, T. Bidirectional actuation of a thermoplastic polyurethane elastomer. *J. Mater. Chem. A* **2013**, *1*, 14491–14497, doi:10.1039/C3TA13414H.
67. Chalissery, D.; Schönfeld, D.; Walter, M.; Shklyar, I.; Andrae, H.; Schwörer, C.; Amann, T.; Weisheit, L.; Pretsch, T. Highly Shrinkable Objects as Obtained from 4D Printing. *Macro Materials & Eng* **2022**, *307*, 2100619, doi:10.1002/mame.202100619.
68. Sánchez-Calderón, I.; Bernardo, V.; Santiago-Calvo, M.; Naji, H.; Saiani, A.; Rodríguez-Pérez, M.Á. Effect of the Molecular Structure of TPU on the Cellular Structure of Nanocellular Polymers Based on PMMA/TPU Blends. *Polymers* **2021**, *13*, doi:10.3390/polym13183055.

69. Sánchez–Adsuar, M.S.; Papon, E.; Villenave, J.-J. Influence of the prepolymerization on the properties of thermoplastic polyurethane elastomers. Part II. Relationship between the prepolymer and polyurethane properties. *J. Appl. Polym. Sci.* **2000**, *76*, 1602, doi:10.1002/(SICI)1097-4628(20000606)76:10<1602:AID-APP16>3.3.CO;2-B.
70. Snchez-Adsuar, M.S.; Papon, E.; Villenave, J.-J. Influence of the synthesis conditions on the properties of thermoplastic polyurethane elastomers. *J. Appl. Polym. Sci.* **2000**, *76*, 1590–1595, doi:10.1002/(SICI)1097-4628(20000606)76:10<1590:AID-APP14>3.0.CO;2-2.
71. Król, P. *Linear polyurethanes*: *Synthesis methods, chemical structures, properties and applications / by Piotr Król;* VSP: Leiden, Boston, 2008, ISBN 9004161244.
72. Wong, C.S.; Badri, K.H. Chemical Analyses of Palm Kernel Oil-Based Polyurethane Prepolymer. *MSA* **2012**, *03*, 78–86, doi:10.4236/msa.2012.32012.
73. Zhu, Q.; Feng, S.; Zhang, C. Synthesis and thermal properties of polyurethane-polysiloxane crosslinked polymer networks. *J. Appl. Polym. Sci.* **2003**, *90*, 310–315, doi:10.1002/app.12790.
74. Renault, B.; Tassaing, T.; Cloutet, E.; Cramail, H. One-shot synthesis of high molar mass polyurethane in supercritical carbon dioxide. *J. Polym. Sci. A Polym. Chem.* **2007**, *45*, 5649–5661, doi:10.1002/pola.22313.
75. Rafiee, Z.; Keshavarz, V. Synthesis and characterization of polyurethane/microcrystalline cellulose bionanocomposites. *Progress in Organic Coatings* **2015**, *86*, 190–193, doi:10.1016/j.porgcoat.2015.05.013.
76. Uhlig, K. *Polyurethan-Taschenbuch*: *Mit 33 Tabellen;* Hanser: München, Wien, 1998, ISBN 3446189130.
77. Szycher, M. *Szycher's handbook of polyurethanes*, 2nd ed.; CRC Press: Boca Raton, FL, 2013, ISBN 9781439863138.
78. Levchik, S.V.; Weil, E.D. Thermal decomposition, combustion and fire-retardancy of polyurethanes—a review of the recent literature. *Polym. Int.* **2004**, *53*, 1585–1610, doi:10.1002/pi.1314.
79. Weil, E.D.; Levchik, S.V. Commercial Flame Retardancy of Polyurethanes. *Journal of Fire Sciences* **2004**, *22*, 183–210, doi:10.1177/0734904104040259.
80. Chattopadhyay, D.K.; Webster, D.C. Thermal stability and flame retardancy of polyurethanes. *Progress in Polymer Science* **2009**, *34*, 1068–1133, doi:10.1016/j.progpolymsci.2009.06.002.
81. Das, A.; Mahanwar, P. A brief discussion on advances in polyurethane applications. *Advanced Industrial and Engineering Polymer Research* **2020**, *3*, 93–101, doi:10.1016/j.aiepr.2020.07.002.
82. Mohamed, M.H.; Wilson, L.D.; Headley, J.V.; Peru, K.M. Investigation of the sorption properties of β-cyclodextrin-based polyurethanes with phenolic dyes and naphthenates. *Journal of Colloid and Interface Science* **2011**, *356*, 217–226, doi:10.1016/j.jcis.2010.11.002.
83. Mao, H.; Wang, C.; Wang, Y. Synthesis of polymeric dyes based on waterborne polyurethane for improved color stability. *New J. Chem.* **2015**, *39*, 3543–3550, doi:10.1039/C4NJ02222J.
84. Sommer, S.A.; Byrom, J.R.; Fischer, H.D.; Bodkhe, R.B.; Stafslien, S.J.; Daniels, J.; Yehle, C.; Webster, D.C. Effects of pigmentation on siloxane–polyurethane coatings and their performance as fouling-release marine coatings. *J Coat Technol Res* **2011**, *8*, 661–670, doi:10.1007/s11998-011-9340-3.
85. Howarth, G.A. Polyurethanes, polyurethane dispersions and polyureas: Past, present and future. *Surface Coatings International Part B: Coatings Transactions* **2003**, *86*, 111–118, doi:10.1007/BF02699621.
86. Pretsch, T.; Müller, W.W. Shape memory poly(ester urethane) with improved hydrolytic stability. *Polymer Degradation and Stability* **2010**, *95*, 880–888, doi:10.1016/j.polymdegradstab.2009.12.020.
87. Chandra, R.; Thapliyal, B.P.; Soni, R.K. Stabilization of polyurethane films against thermal and photo-oxidative degradation. *Polymer Degradation and Stability* **1993**, *39*, 93–101, doi:10.1016/0141-3910(93)90129-7.
88. Jacobasch, H.-J.; Grundke, K.; St. Schneider; Simon, F. The influence of additives on the adhesion behaviour of thermoplastic materials used in the automotive industry. *Progress in Organic Coatings* **1995**, *26*, 131–143, doi:10.1016/0300-9440(96)81582-7.
89. Aranguren, M.I.; Rácz, I.; Marcovich, N.E. Microfoams based on castor oil polyurethanes and vegetable fibers. *J. Appl. Polym. Sci.* **2007**, *105*, 2791–2800, doi:10.1002/app.26526.
90. Khalifa, M.; Anandhan, S.; Wuzella, G.; Lammer, H.; Mahendran, A.R. Thermoplastic polyurethane composites reinforced with renewable and sustainable fillers – a review. *Polymer-Plastics Technology and Materials* **2020**, *59*, 1751–1769, doi:10.1080/25740881.2020.1768544.
91. Vaithylingam, R.; Ansari, M.N.M.; Shanks, R.A. Recent Advances in Polyurethane-Based Nanocomposites: A Review. *Polymer-Plastics Technology and Engineering* **2017**, *56*, 1528–1541, doi:10.1080/03602559.2017.1280683.
92. Leary, M. Chapter 8 - Material extrusion. In *Design for additive manufacturing*: *Tools and optimization / Martin Leary*; Leary, M., Ed.; Elsevier: Amsterdam, 2019; pp 223–268, ISBN 978-0-12-816721-2.

93. Rosato, D.V.; Rosato, D.V.; Rosato, M.V. 5 - EXTRUSION. In *Plastic product material and process selection handbook*; Rosato, D.V., Rosato, D.V., Rosato, M.V., Eds.; Elsevier: Oxford, 2004; pp 227–281, ISBN 978-1-85617-431-2.
94. Vlachopoulos, J.; Strutt, D. Polymer processing. *Materials Science and Technology* **2003**, *19*, 1161–1169, doi:10.1179/026708303225004738.
95. Chalissery, D.; Pretsch, T.; Staub, S.; Andrä, H. Additive Manufacturing of Information Carriers Based on Shape Memory Polyester Urethane. *Polymers* **2019**, *11*, doi:10.3390/polym11061005.
96. Shaqour, B.; Abuabiah, M.; Abdel-Fattah, S.; Juaidi, A.; Abdallah, R.; Abuzaina, W.; Qarout, M.; Verleije, B.; Cos, P. Gaining a better understanding of the extrusion process in fused filament fabrication 3D printing: a review. *Int J Adv Manuf Technol* **2021**, *114*, 1279–1291, doi:10.1007/s00170-021-06918-6.
97. Schrenk, W.J.; Alfrey, T. Chapter 15 - Coextruded Multilayer Polymer Films and Sheets. In *Polymer blends*; Alfrey, T., Ed.; Academic Press: New York [etc.], 1978; pp 129–165, ISBN 978-0-12-546802-2.
98. Hernandez-Izquierdo, V.M.; Krochta, J.M. Thermoplastic processing of proteins for film formation--a review. *J. Food Sci.* **2008**, *73*, R30-9, doi:10.1111/j.1750-3841.2007.00636.x.
99. Wang, L.; Shogren, R.L.; Carriere, C. Preparation and properties of thermoplastic starch-polyester laminate sheets by coextrusion. *Polym. Eng. Sci.* **2000**, *40*, 499–506, doi:10.1002/pen.11182.
100. Zema, L.; Loreti, G.; Melocchi, A.; Maroni, A.; Gazzaniga, A. Injection Molding and its application to drug delivery. *J. Control. Release* **2012**, *159*, 324–331, doi:10.1016/j.jconrel.2012.01.001.
101. Amellal, K.; Tzoganakis, C.; Penlidis, A.; Rempel, G.L. Injection molding of medical plastics: A review. *Adv. Polym. Technol.* **1994**, *13*, 315–322, doi:10.1002/adv.1994.060130407.
102. Johannaber, F. *Injection Molding Machines*: *A User's Guide*, 4. Auflage; Hanser, Carl: München, 2016, ISBN 9783446450110.
103. Ngo, T.D.; Kashani, A.; Imbalzano, G.; Nguyen, K.T.Q.; Hui, D. Additive manufacturing (3D printing): A review of materials, methods, applications and challenges. *Composites Part B: Engineering* **2018**, *143*, 172–196, doi:10.1016/j.compositesb.2018.02.012.
104. Ligon, S.C.; Liska, R.; Stampfl, J.; Gurr, M.; Mülhaupt, R. Polymers for 3D Printing and Customized Additive Manufacturing. *Chem. Rev.* **2017**, *117*, 10212–10290, doi:10.1021/acs.chemrev.7b00074.
105. N. Turner, B.; Strong, R.; A. Gold, S. A review of melt extrusion additive manufacturing processes: I. Process design and modeling. *RPJ* **2014**, *20*, 192–204, doi:10.1108/RPJ-01-2013-0012.
106. Killi, S.W. *Additive manufacturing*: *Design, methods, and processes / edited by Steinar Killi;* Pan Stanford Publishing: Singapore, 2017, ISBN 9781315196589.
107. Awari, G.K.; Thorat, C.S.; Ambade, V.; Kothari, D.P. *Additive manufacturing and 3D printing technology*: *Principles and applications / G.K. Awari, C.S. Thorat, Vishwjeet Ambade, D.P. Kothari*, 1st; CRC Press: Boca Raton, 2021, ISBN 9781000338706.
108. https://www.facebook.com/All3DP. History of 3D Printing: When Was 3D Printing Invented? Available online: https://all3dp.com/2/history-of-3d-printing-when-was-3d-printing-invented/ (accessed on 23 January 2022).
109. *Advanced Manufacturing Systems and Innovative Product Design;* Deepak, B.B.V.L.; Parhi, D.R.K.; Biswal, B.B., Eds.; Springer Singapore: Singapore, 2021, ISBN 978-981-15-9852-4.
110. Gebhardt, A.; Hötter, J.-S. *Additive Manufacturing*: *3D printing for prototyping and manufacturing;* Carl Hanser Verlag GmbH & Co. KG: München, 2016, ISBN 9781569905838.
111. Di Nicolantonio, M.; Rossi, E.; Alexander, T. *Advances in additive manufacturing, modeling systems and 3D prototyping*: *Proceedings of the AHFE 2019 International Conference on Additive Manufacturing, Modeling Systems and 3D Prototyping, July 24-28, 2019, Washington D.C., USA / Massimo Di Nicolantonio, Emilio Rossi, Thomas Alexander, editors;* Springer: Cham, Switzerland, 2020, ISBN 9783030202163.
112. Kulkarni, P.; Kumar, A.; Chate, G.; Dandannavar, P. Elements of additive manufacturing technology adoption in small- and medium-sized companies. *INMR* **2021**, *18*, 400–416, doi:10.1108/INMR-02-2020-0015.
113. Martinsuo, M.; Luomaranta, T. Adopting additive manufacturing in SMEs: exploring the challenges and solutions. *JMTM* **2018**, *29*, 937–957, doi:10.1108/JMTM-02-2018-0030.
114. Wang, L.; Gramlich, W.M.; Gardner, D.J. Improving the impact strength of Poly(lactic acid) (PLA) in fused layer modeling (FLM). *Polymer* **2017**, *114*, 242–248, doi:10.1016/j.polymer.2017.03.011.
115. Liu, X.; Chi, B.; Jiao, Z.; Tan, J.; Liu, F.; Yang, W. A large-scale double-stage-screw 3D printer for fused deposition of plastic pellets. *J. Appl. Polym. Sci.* **2017**, *134*, 45147, doi:10.1002/app.45147.
116. Ning, F.; Cong, W.; Qiu, J.; Wei, J.; Wang, S. Additive manufacturing of carbon fiber reinforced thermoplastic composites using fused deposition modeling. *Composites Part B: Engineering* **2015**, *80*, 369–378, doi:10.1016/j.compositesb.2015.06.013.

117. Kuznetsov, V.E.; Solonin, A.N.; Urzhumtsev, O.D.; Schilling, R.; Tavitov, A.G. Strength of PLA Components Fabricated with Fused Deposition Technology Using a Desktop 3D Printer as a Function of Geometrical Parameters of the Process. *Polymers* **2018**, *10*, doi:10.3390/polym10030313.
118. Krishnanand; Taufik, M. Fused Filament Fabrication (FFF) Based 3D Printer and Its Design: A Review. In *Advanced Manufacturing Systems and Innovative Product Design*; Deepak, B.B.V.L., Parhi, D.R.K., Biswal, B.B., Eds.; Springer Singapore: Singapore, 2021; pp 497–505, ISBN 978-981-15-9852-4.
119. Lendlein, A.; Kelch, S. Shape-Memory Polymers. *Angew. Chem. Int. Ed.* **2002**, *41*, 2034, doi:10.1002/1521-3773(20020617)41:12<2034:AID-ANIE2034>3.0.CO;2-M.
120. Liu, C.; Qin, H.; Mather, P.T. Review of progress in shape-memory polymers. *J. Mater. Chem.* **2007**, *17*, 1543, doi:10.1039/b615954k.
121. Leng, J.; Lan, X.; Liu, Y.; Du, S. Shape-memory polymers and their composites: Stimulus methods and applications. *Progress in Materials Science* **2011**, *56*, 1077–1135, doi:10.1016/j.pmatsci.2011.03.001.
122. Hu, J.; Zhu, Y.; Huang, H.; Lu, J. Recent advances in shape–memory polymers: Structure, mechanism, functionality, modeling and applications. *Progress in Polymer Science* **2012**, *37*, 1720–1763, doi:10.1016/j.progpolymsci.2012.06.001.
123. Pretsch, T. Review on the Functional Determinants and Durability of Shape Memory Polymers. *Polymers* **2010**, *2*, 120–158, doi:10.3390/polym2030120.
124. Jiang, H.Y.; Kelch, S.; Lendlein, A. Polymers Move in Response to Light. *Adv. Mater.* **2006**, *18*, 1471–1475, doi:10.1002/adma.200502266.
125. Zhang, D.; Liu, Y.; Leng, J. Infrared laser-activated shape memory polymer. In *Sensors and Smart Structures Technologies for Civil, Mechanical, and Aerospace Systems 2008.* The 15th International Symposium on: Smart Structures and Materials & Nondestructive Evaluation and Health Monitoring, San Diego, California, Sunday 9 March 2008; Tomizuka, M., Ed.; SPIE, 2008; p 693213.
126. Leng, J.; Wu, X.; Liu, Y. Infrared light-active shape memory polymer filled with nanocarbon particles. *J. Appl. Polym. Sci.* **2009**, *114*, 2455–2460, doi:10.1002/app.30724.
127. Leng, J.; Zhang, D.; Liu, Y.; Yu, K.; Lan, X. Study on the activation of styrene-based shape memory polymer by medium-infrared laser light. *Appl. Phys. Lett.* **2010**, *96*, 111905, doi:10.1063/1.3353970.
128. Maitland, D.J.; Metzger, M.F.; Schumann, D.; Lee, A.; Wilson, T.S. Photothermal properties of shape memory polymer micro-actuators for treating stroke. *Lasers Surg. Med.* **2002**, *30*, 1–11, doi:10.1002/lsm.10007.
129. Liu, T.; Zhou, T.; Yao, Y.; Zhang, F.; Liu, L.; Liu, Y.; Leng, J. Stimulus methods of multi-functional shape memory polymer nanocomposites: A review. *Composites Part A: Applied Science and Manufacturing* **2017**, *100*, 20–30, doi:10.1016/j.compositesa.2017.04.022.
130. Buckley, Patrick Regan, 1981-. Actuation of shape memory polymer using magnetic fields for applications in medical devices; Massachusetts Institute of Technology.
131. Ze, Q.; Kuang, X.; Wu, S.; Wong, J.; Montgomery, S.M.; Zhang, R.; Kovitz, J.M.; Yang, F.; Qi, H.J.; Zhao, R. Magnetic Shape Memory Polymers with Integrated Multifunctional Shape Manipulation. *Adv. Mater.* **2020**, *32*, e1906657, doi:10.1002/adma.201906657.
132. Wenz, F.; Schönfeld, D.; Fischer, S.C.L.; Pretsch, T.; Eberl, C. Controlling Malleability of Metamaterials through Programmable Memory. *Advanced Engineering Materials* **2022**, 2201022, doi:10.1002/adem.202201022.
133. Mather, P.T.; Luo, X.; Rousseau, I.A. Shape Memory Polymer Research. *Annu. Rev. Mater. Res.* **2009**, *39*, 445–471, doi:10.1146/annurev-matsci-082908-145419.
134. Madbouly, S.A.; Lendlein, A. Shape-Memory Polymer Composites. In *Shape-memory polymers*; Lendlein, A., Behl, M., Eds.; Springer: Heidelberg, 2010; pp 41–95, ISBN 978-3-642-12359-7.
135. Kim, Y.-J.; Matsunaga, Y.T. Thermo-responsive polymers and their application as smart biomaterials. *J. Mater. Chem. B* **2017**, *5*, 4307–4321, doi:10.1039/c7tb00157f.
136. Kausar, A. Review on Technological Significance of Photoactive, Electroactive, pH-sensitive, Water-active, and Thermoresponsive Polyurethane Materials. *Polymer-Plastics Technology and Engineering* **2017**, *56*, 606–616, doi:10.1080/03602559.2016.1233279.
137. L. Sun; W.M. Huang; Z. Ding; Y. Zhao; C.C. Wang; H. Purnawali; C. Tang. Stimulus-responsive shape memory materials: A review. *Materials & Design* **2012**, *33*, 577–640, doi:10.1016/j.matdes.2011.04.065.
138. Dietsch, B.; Tong, T. A review-: Features and benefits of shape memory polymers (smps). *Journal of advanced materials* **2007**, *39*, 3–12.
139. Hoffman, A.S. Stimuli-responsive polymers: biomedical applications and challenges for clinical translation. *Advanced Drug Delivery Reviews* **2013**, *65*, 10–16, doi:10.1016/j.addr.2012.11.004.

140. Yin, X.; Hoffman, A.S.; Stayton, P.S. Poly(N-isopropylacrylamide-co-propylacrylic acid) copolymers that respond sharply to temperature and pH. *Biomacromolecules* **2006**, *7*, 1381–1385, doi:10.1021/bm0507812.
141. Ratna, D.; Karger-Kocsis, J. Recent advances in shape memory polymers and composites: a review. *J Mater Sci* **2008**, *43*, 254–269, doi:10.1007/s10853-007-2176-7.
142. Behl, M.; Razzaq, M.Y.; Lendlein, A. Multifunctional shape-memory polymers. *Adv. Mater.* **2010**, *22*, 3388–3410, doi:10.1002/adma.200904447.
143. Rousseau, I.A. Challenges of shape memory polymers: A review of the progress toward overcoming SMP's limitations. *Polym Eng Sci* **2008**, *48*, 2075–2089, doi:10.1002/pen.21213.
144. Du, H.; Zhang, J. Solvent induced shape recovery of shape memory polymer based on chemically cross-linked poly(vinyl alcohol). *Soft Matter* **2010**, *6*, 3370, doi:10.1039/b922220k.
145. Liu, C.; Chun, S.B.; Mather, P.T.; Zheng, L.; Haley, E.H.; Coughlin, E.B. Chemically Cross-Linked Polycyclooctene: Synthesis, Characterization, and Shape Memory Behavior. *Macromolecules* **2002**, *35*, 9868–9874, doi:10.1021/ma021141j.
146. Behl, M.; Lendlein, A. Actively moving polymers. *Soft Matter* **2006**, *3*, 58–67, doi:10.1039/b610611k.
147. Nagata, M.; Yamamoto, Y. Synthesis and characterization of photocrosslinked poly(ε-caprolactone)s showing shape-memory properties. *J. Polym. Sci. A Polym. Chem.* **2009**, *47*, 2422–2433, doi:10.1002/pola.23333.
148. Frost, B.A.; Carlton, H.; Martinez, R.; Lovett, E.; Huitink, D.; Foster, E.J. Controlled shape memory effects of magnetic polymer nanocomposites by induction heating. *Green Materials* **2021**, *9*, 167–181, doi:10.1680/jgrma.20.00079.
149. Xie, T. Tunable polymer multi-shape memory effect. *Nature* **2010**, *464*, 267–270, doi:10.1038/nature08863.
150. Mohr, R.; Kratz, K.; Weigel, T.; Lucka-Gabor, M.; Moneke, M.; Lendlein, A. Initiation of shape-memory effect by inductive heating of magnetic nanoparticles in thermoplastic polymers. *PNAS* **2006**, *103*, 3540–3545, doi:10.1073/pnas.0600079103.
151. Gu, J.; Zhao, S.; Duan, H.; Wan, M.; Sun, H. Electro-thermo-mechanical modeling of shape memory polymers filled with nano-carbon powder. *Journal of Intelligent Material Systems and Structures* **2021**, 1045389X2110643, doi:10.1177/1045389X211064336.
152. Siwakoti, M.; Mailen, R. Self-folding origami of prestrained shape memory polymer by resistive Joule-heating. In *Behavior and Mechanics of Multifunctional Materials IX.* Behavior and Mechanics of Multifunctional Materials XIV, Online Only, United States, 4/27/2020 - 5/8/2020; Harne, R.L., Ed.; SPIE, 2020 - 2020; p 29, ISBN 9781510635319.
153. Elsisy, M.; Poska, E.; Abdulhafez, M.; Bedewy, M. Current-Dependent Dynamics of Bidirectional Self-Folding for Multi-Layer Polymers Using Local Resistive Heating. *Journal of Engineering Materials and Technology* **2021**, *143*, doi:10.1115/1.4049588.
154. Kim, B.K.; Lee, S.Y.; Xu, M. Polyurethanes having shape memory effects. *Polymer* **1996**, *37*, 5781–5793, doi:10.1016/S0032-3861(96)00442-9.
155. Li, F.; Zhang, X.; Hou, J.; Xu, M.; Luo, X.; Ma, D.; Kim, B.K. Studies on thermally stimulated shape memory effect of segmented polyurethanes. *J. Appl. Polym. Sci.* **1997**, *64*, 1511–1516, doi:10.1002/(SICI)1097-4628(19970523)64:8<1511:AID-APP8>3.0.CO;2-K.
156. Lee, B.S.; Chun, B.C.; Chung, Y.-C.; Sul, K.I.; Cho, J.W. Structure and Thermomechanical Properties of Polyurethane Block Copolymers with Shape Memory Effect. *Macromolecules* **2001**, *34*, 6431–6437, doi:10.1021/ma001842l.
157. Ji, F.L.; Hu, J.L.; Li, T.C.; Wong, Y.W. Morphology and shape memory effect of segmented polyurethanes. Part I: With crystalline reversible phase. *Polymer* **2007**, *48*, 5133–5145, doi:10.1016/j.polymer.2007.06.032.
158. Pereira, I.M.; Oréfice, R.L. The morphology and phase mixing studies on poly(ester–urethane) during shape memory cycle. *J Mater Sci* **2010**, *45*, 511–522, doi:10.1007/s10853-009-3969-7.
159. Huang, W.M.; Yang, B.; Zhao, Y.; Ding, Z. Thermo-moisture responsive polyurethane shape-memory polymer and composites: a review. *J. Mater. Chem.* **2010**, *20*, 3367, doi:10.1039/b922943d.
160. Wang, W.; Jin, Y.; Ping, P.; Chen, X.; Jing, X.; Su, Z. Structure Evolution in Segmented Poly(ester urethane) in Shape-Memory Process. *Macromolecules* **2010**, *43*, 2942–2947, doi:10.1021/ma902781e.
161. Müller, W.W.; Pretsch, T. Hydrolytic aging of crystallizable shape memory poly(ester urethane): Effects on the thermo-mechanical properties and visco-elastic modeling. *European Polymer Journal* **2010**, *46*, 1745–1758, doi:10.1016/j.eurpolymj.2010.05.004.

162. Petchsuk, A.; Klinsukhon, W.; Sirikittikul, D.; Prahsarn, C. Parameters affecting transition temperatures of poly(lactic acid-co-polydiols) copolymer-based polyester urethanes and their shape memory behavior. *Polym. Adv. Technol.* **2012**, *23*, 1166–1173, doi:10.1002/pat.2017.
163. Liu, W.; Zhang, R.; Huang, M.; Dong, X.; Xu, W.; Wang, Y.; Hu, G.-H.; Zhu, J. Synthesis and shape memory property of segmented poly(ester urethane) with poly(butylene 1,4-cyclohexanedicarboxylate) as the soft segment. *RSC Adv.* **2016**, *6*, 95527–95534, doi:10.1039/C6RA16325D.
164. Ren, H.; Mei, Z.; Chen, S.; Zhuo, H.; Chen, S.; Yang, H.; Zuo, J.; Ge, Z. A new strategy for designing multifunctional shape memory polymers with amine-containing polyurethanes. *J Mater Sci* **2016**, *51*, 9131–9144, doi:10.1007/s10853-016-0166-3.
165. Mirtschin, N.; Pretsch, T. Programming of One- and Two-Step Stress Recovery in a Poly(ester urethane). *Polymers* **2017**, *9*, doi:10.3390/polym9030098.
166. Raasch, J.; Ivey, M.; Aldrich, D.; Nobes, D.S.; Ayranci, C. Characterization of polyurethane shape memory polymer processed by material extrusion additive manufacturing. *Additive Manufacturing* **2015**, *8*, 132–141, doi:10.1016/j.addma.2015.09.004.
167. Villacres, J.; Nobes, D.; Ayranci, C. Additive manufacturing of shape memory polymers: effects of print orientation and infill percentage on mechanical properties. *RPJ* **2018**, *24*, 744–751, doi:10.1108/RPJ-03-2017-0043.
168. Villacres, J.; Nobes, D.; Ayranci, C. Additive manufacturing of shape memory polymers: effects of print orientation and infill percentage on shape memory recovery properties. *RPJ* **2020**, *26*, 1593–1602, doi:10.1108/RPJ-09-2019-0239.
169. Hendrikson, W.J.; Rouwkema, J.; Clementi, F.; van Blitterswijk, C.A.; Farè, S.; Moroni, L. Towards 4D printed scaffolds for tissue engineering: exploiting 3D shape memory polymers to deliver time-controlled stimulus on cultured cells. *Biofabrication* **2017**, *9*, 31001, doi:10.1088/1758-5090/aa8114.
170. Yang, Y.; Chen, Y.; Wei, Y.; Li, Y. 3D printing of shape memory polymer for functional part fabrication. *Int J Adv Manuf Technol* **2016**, *84*, 2079–2095, doi:10.1007/s00170-015-7843-2.
171. Athimoolam, M.; Moorthy, T.V. Polymer Nanocomposite Materials and Shape Memory Applications-A Review. *Procedia Engineering* **2012**, *38*, 3399–3408, doi:10.1016/j.proeng.2012.06.393.
172. DIN EN ISO 527-2 - 1996-07 - Beuth.de. Available online: https://www.beuth.de/en/standard/din-en-iso-527-2/2808009 (accessed on 19 January 2022).
173. Monzón, M.D.; Paz, R.; Pei, E.; Ortega, F.; Suárez, L.A.; Ortega, Z.; Alemán, M.E.; Plucinski, T.; Clow, N. 4D printing: processability and measurement of recovery force in shape memory polymers. *Int J Adv Manuf Technol* **2017**, *89*, 1827–1836, doi:10.1007/s00170-016-9233-9.
174. Koualiarella, A.; Arvanitidis, A.; Argyros, A.; Kousiatza, C.; Karakalas, A.; Lagoudas, D.; Michailidis, N. Tuning of shape memory polymer properties by controlling 3D printing strategy. *CIRP Annals* **2020**, *69*, 213–216, doi:10.1016/j.cirp.2020.04.070.
175. Chung, T.; Romo-Uribe, A.; Mather, P.T. Two-Way Reversible Shape Memory in a Semicrystalline Network. *Macromolecules* **2008**, *41*, 184–192, doi:10.1021/ma071517z.
176. Chen, S.; Hu, J.; Zhuo, H. Properties and mechanism of two-way shape memory polyurethane composites. *Composites Science and Technology* **2010**, *70*, 1437–1443, doi:10.1016/j.compscitech.2010.01.017.
177. Behl, M.; Zotzmann, J.; Lendlein, A. One-way and reversible dual-shape effect of polymer networks based on polypentadecalactone segments. *Int. J. Artif. Organs* **2011**, *34*, 231–237, doi:10.5301/ijao.2011.6424.
178. Li, J.; Rodgers, W.R.; Xie, T. Semi-crystalline two-way shape memory elastomer. *Polymer* **2011**, *52*, 5320–5325, doi:10.1016/j.polymer.2011.09.030.
179. Bothe, M.; Pretsch, T. Two-Way Shape Changes of a Shape-Memory Poly(ester urethane). *Macromol. Chem. Phys.* **2012**, *213*, 2378–2385, doi:10.1002/macp.201200096.
180. Zare, M.; Prabhakaran, M.P.; Parvin, N.; Ramakrishna, S. Thermally-induced two-way shape memory polymers: Mechanisms, structures, and applications. *Chemical Engineering Journal* **2019**, *374*, 706–720, doi:10.1016/j.cej.2019.05.167.
181. Wu, Y.; Hu, J.; Han, J.; Zhu, Y.; Huang, H.; Li, J.; Tang, B. Two-way shape memory polymer with "switch–spring" composition by interpenetrating polymer network. *J. Mater. Chem. A* **2014**, *2*, 18816–18822, doi:10.1039/C4TA03640A.
182. Behl, M.; Kratz, K.; Noechel, U.; Sauter, T.; Lendlein, A. Temperature-memory polymer actuators. *PNAS* **2013**, *110*, 12555–12559, doi:10.1073/pnas.1301895110.
183. Behl, M.; Kratz, K.; Zotzmann, J.; Nöchel, U.; Lendlein, A. Reversible bidirectional shape-memory polymers. *Adv. Mater. Weinheim.* **2013**, *25*, 4466–4469, doi:10.1002/adma.201300880.

184. Tibbits, S. Skylar Tibbits: The emergence of “4D printing”. Available online: https://www.ted.com/talks/skylar_tibbits_the_emergence_of_4d_printing (accessed on 20 January 2022).
185. Tibbits, S. 4D Printing: Multi-Material Shape Change. *Archit Design* **2014**, *84*, 116–121, doi:10.1002/ad.1710.
186. van Manen, T.; Janbaz, S.; Zadpoor, A.A. Programming 2D/3D shape-shifting with hobbyist 3D printers. *Mater. Horiz.* **2017**, *4*, 1064–1069, doi:10.1039/c7mh00269f.
187. Hu, G.F.; Damanpack, A.R.; Bodaghi, M.; Liao, W.H. Increasing dimension of structures by 4D printing shape memory polymers via fused deposition modeling. *Smart Mater. Struct.* **2017**, *26*, 125023, doi:10.1088/1361-665X/aa95ec.
188. Bodaghi, M.; Damanpack, A.R.; Liao, W.H. Adaptive metamaterials by functionally graded 4D printing. *Materials & Design* **2017**, *135*, 26–36, doi:10.1016/j.matdes.2017.08.069.
189. Bodaghi, M.; Damanpack, A.R.; Liao, W.H. Triple shape memory polymers by 4D printing. *Smart Mater. Struct.* **2018**, *27*, 65010, doi:10.1088/1361-665X/aabc2a.
190. Noroozi, R.; Bodaghi, M.; Jafari, H.; Zolfagharian, A.; Fotouhi, M. Shape-Adaptive Metastructures with Variable Bandgap Regions by 4D Printing. *Polymers* **2020**, *12*, doi:10.3390/polym12030519.
191. Bodaghi, M.; Noroozi, R.; Zolfagharian, A.; Fotouhi, M.; Norouzi, S. 4D Printing Self-Morphing Structures. *Materials (Basel)* **2019**, *12*, doi:10.3390/ma12081353.
192. Nezhad, I.S.; Golzar, M.; Behravesh, A.; Zare, S. *Comprehensive Study on Shape Shifting Behaviors of Thermally Activated Hinges in FDM-based 4D Printing*, 2021.
193. Zhang, Q.; Yan, D.; Zhang, K.; Hu, G. Pattern transformation of heat-shrinkable polymer by three-dimensional (3D) printing technique. *Sci Rep* **2015**, *5*, 8936, doi:10.1038/srep08936.
194. Rajkumar, A.R.; Shanmugam, K. Additive manufacturing-enabled shape transformations via FFF 4D printing. *J. Mater. Res.* **2018**, *33*, 4362–4376, doi:10.1557/jmr.2018.397.
195. Gladman, A.S.; Matsumoto, E.A.; Nuzzo, R.G.; Mahadevan, L.; Lewis, J.A. Biomimetic 4D printing. *Nat. Mater.* **2016**, *15*, 413–418, doi:10.1038/nmat4544.
196. Zhao, Q.; Qi, H.J.; Xie, T. Recent progress in shape memory polymer: New behavior, enabling materials, and mechanistic understanding. *Progress in Polymer Science* **2015**, *49-50*, 79–120, doi:10.1016/j.progpolymsci.2015.04.001.
197. 2021. Nezhad, I.S.; Golzar, M.; Behravesh, A.; Zare, S. *Comprehensive Study on Shape Shifting Behaviors of Thermally Activated Hinges in FDM-based 4D Printing*. Available online: https://www.researchsquare.com/article/rs-791407/v1.pdf?c=1631891144000.
198. Ke, D.; Chen, Z.; Momo, Z.Y.; Jiani, W.; Xuan, C.; Xiaojie, Y.; Xueliang, X. Recent advances of two-way shape memory polymers and four-dimensional printing under stress-free conditions. *Smart Mater. Struct.* **2020**, *29*, 23001, doi:10.1088/1361-665X/ab5e6d.
199. Mao, Y.; Ding, Z.; Yuan, C.; Ai, S.; Isakov, M.; Wu, J.; Wang, T.; Dunn, M.L.; Qi, H.J. 3D Printed Reversible Shape Changing Components with Stimuli Responsive Materials. *Sci Rep* **2016**, *6*, 24761, doi:10.1038/srep24761.
200. Yuan, C.; Roach, D.J.; Dunn, C.K.; Mu, Q.; Kuang, X.; Yakacki, C.M.; Wang, T.J.; Yu, K.; Qi, H.J. 3D printed reversible shape changing soft actuators assisted by liquid crystal elastomers. *Soft Matter* **2017**, *13*, 5558–5568, doi:10.1039/c7sm00759k.
201. Shafranek, R.T.; Millik, S.C.; Smith, P.T.; Lee, C.-U.; Boydston, A.J.; Nelson, A. Stimuli-responsive materials in additive manufacturing. *Progress in Polymer Science* **2019**, *93*, 36–67, doi:10.1016/j.progpolymsci.2019.03.002.
202. Momeni, F.; Ni, J. Nature-inspired smart solar concentrators by 4D printing. *Renewable Energy* **2018**, *122*, 35–44, doi:10.1016/j.renene.2018.01.062.
203. Rastogi, P.; Kandasubramanian, B. Breakthrough in the printing tactics for stimuli-responsive materials: 4D printing. *Chemical Engineering Journal* **2019**, *366*, 264–304, doi:10.1016/j.cej.2019.02.085.
204. Baker, A.B.; Bates, S.R.G.; Llewellyn-Jones, T.M.; Valori, L.P.B.; Dicker, M.P.M.; Trask, R.S. 4D printing with robust thermoplastic polyurethane hydrogel-elastomer trilayers. *Materials & Design* **2019**, *163*, 107544, doi:10.1016/j.matdes.2018.107544.
205. Zhang, H.; Guo, X.; Wu, J.; Fang, D.; Zhang, Y. Soft mechanical metamaterials with unusual swelling behavior and tunable stress-strain curves. *Sci. Adv.* **2018**, *4*, eaar8535, doi:10.1126/sciadv.aar8535.
206. Zhu, P.; Yang, W.; Wang, R.; Gao, S.; Li, B.; Li, Q. 4D Printing of Complex Structures with a Fast Response Time to Magnetic Stimulus. *ACS Appl. Mater. Interfaces* **2018**, *10*, 36435–36442, doi:10.1021/acsami.8b12853.

207. Kokkinis, D.; Schaffner, M.; Studart, A.R. Multimaterial magnetically assisted 3D printing of composite materials. *Nat. Commun.* **2015**, *6*, 8643, doi:10.1038/ncomms9643.
208. Kim, Y.; Yuk, H.; Zhao, R.; Chester, S.A.; Zhao, X. Printing ferromagnetic domains for untethered fast-transforming soft materials. *Nature* **2018**, *558*, 274–279, doi:10.1038/s41586-018-0185-0.
209. Xu, T.; Zhang, J.; Salehizadeh, M.; Onaizah, O.; Diller, E. Millimeter-scale flexible robots with programmable three-dimensional magnetization and motions. *Sci. Robot.* **2019**, *4*, doi:10.1126/scirobotics.aav4494.

Chapter 2: Motivation

Chapter 2: Motivation

Shape memory polymers (SMPs) are smart materials that can promptly recover their original shapes from their temporary shapes in stress-free conditions upon exposure to external stimuli. The SMP takes the temporary shape through a thermomechanical treatment called programming [1,2]. Among various stimuli-responsive SMPs, thermoplastic polyurethanes (TPU) with shape memory properties have shown superiority due to their phase segregation and modifiable material properties, like thermal and mechanical behavior. Today, thermally switchable polymers are the most common and studied SMPs [3–5]. A significant advantage is that direct or indirect heating can trigger the shape memory effect (SME). This flexibility makes such materials easy to use and self-sufficient to a certain degree. On the other hand, additive manufacturing (AM), alias three-dimensional (3D) printing, has been developed as a processing technique for thermoplastic polymers, which allows the building of 3D objects from polymers by adding material in a layer-by-layer approach [6–10]. Among various other AM techniques, fused filament fabrication (FFF) is widely used [11–14].

Among various SMP materials, TPUs are the most used and researched technology platform, likewise the FFF technique in AM. Nevertheless, until the beginning of this doctoral study in 2017, only four scientific publications were presented, where TPU with shape memory properties was processed via FFF [15–18]. Furthermore, the presented contributions could only additively manufacture TPUs using custom-made or modified AM machines. The doctoral work focuses on utilizing the FFF technique to process TPU-based SMP to uplift and bring the best of two worlds. The primary goal of the work is to bring the best of the two technologies to explore and achieve different SMEs, where the additively manufactured TPU objects are thermomechanically treated after processing to exhibit one-way (1W) SME and two-way (2W) SME. While on the other hand, the four-dimensional (4D) printing technique is utilized to achieve "*in-situ*" programming of TPU with shape memory properties, where the 3D printed models can exhibit thermoresponsive properties directly following AM for triggering one-time 1W-SME and 2W-4D printed SME.

The initial scientific hurdle of the work was to enable the processing of TPU with shape memory properties by employing a commercially available standard FFF printer, as this can reduce the processing complexity, attain standardization, and ease the manufacturing of 3D models using standard slicer software. In the last decade, quick response (QR) code carriers were developed using TPU-based SMP as functional base material, which has the potential application as anti-counterfeiting technology [19] or for supervising cold chains [20]. Nevertheless, the previously presented manufacturing processes are complex, time-intensive, and tedious, including SMP plaque manufacturing via injection molding, "guest diffusion" for a surface-specific coloration, and laser engraving of computer-generated two-dimensional codes onto the polymer surface [19]. An alternative method involves coating the SMP, code engraving onto the top layer, and laser cutting/ punching [21,22]. These complex manufacturing processes of information carriers motivated me to research and evaluate the

FFF technique for easing information carriers' production. As well as to study the influence on the print quality along *XY*- and *Z*- planes and, thereby, the build time for the production of information carriers using different nozzles. As the functionality and durability of 3D printed models are the primary functions of the SMP information carriers, the SMEs and programming techniques were essential to evaluate. After evaluating the influence of print quality from employing different nozzle sizes, the printability of Arial fonts and filigree structures was explored. To utilize the full potential of TPU with shape memory properties fabricated via FFF for developing novel applications that can be addressed with FFF.

Once the 1W-SME of 3D printed TPU-SMP was realized, it was clear that the main disadvantage of such systems is the need for programming, which is a time-, energy- and cost-intensive process. Here, the 4D-printing technique that Skylar Tibbits first presented in 2013 can overcome the drawbacks mentioned above; the technique showed that the 3D printed objects could transform their shape directly after removal from the print platform on exposure to a distinct stimulus. Later, researchers learned how to attain "*in-situ"* programming or 4D-printing using FFF [23]. Even though a few similar kinds of research were carried out to harness 4D-printing effects, the 4D effect diminished with increasing layers, and the printed objects could not attain uniform shrinking. In other words, on increasing the object's height ($z<5$ mm) [24–26], the 4D effect weakened drastically, which could be caused by the selection of suboptimal printing parameters. Additionally, there were very few applications developed utilizing the 4D-printing technique. Here, it was essential to determine whether preferred orientations can also be introduced into printed objects in higher layers, which significantly pushes the limits of what is technically feasible. Furthermore, to explore and understand the potential applications of 4D printed parts for active assembly, active disassembly, and others.

On the other hand, scientists have learned how to transfer semicrystalline polymers into two metastable states in the last few years, where SMPs can be switched back and forth by varying the temperature [27–34]. However, several materials were developed and studied for 2W-SME in previous contributions; 3D printing has not been used to manufacture SMPs that can later actuate.

In parallel, programmable materials are currently the subject of intensive research [34–41]. The programmable material utilizes external structure, molecular structure, and material functionality advantageously for achieving specific shape changes or property changes to perform specific tasks. An essential advantage of programmable materials is that they are not dependent on a constant power supply, making them highly resistant to failure and characterized as self-sufficient material behavior, which makes them fulfill both sensor and actuator functionality [34–37,39–44].

From previous contributions, it was clear that scientists could implement 2W-SMEs for physically cross-linked TPU-SMP [39,45,46]. Nevertheless, actuation achieved for such polymers under constant strain or stress-free conditions was lower than for their chemically cross-linked counterparts [32,47–51]. One of the reasons could be selecting an inappropriate temperature range for actuation, as there were no proper temperature screening

characterization methods. Therefore, a new characterization technique was essential for identifying the ideal actuation scenarios. Furthermore, the previous contributions showed that the 2W-SME could grab or lift smaller objects, like screws and nuts [52]. However, the scalability of the effect was unknown, and it was not identified how to magnify the 2W-SME and the combination of 2W-SME programmed polymer with metamaterials for the development of programmable materials using TPU-based SMP. Another question was whether an SMP could exhibit bidirectional actuation when programmed by bending on utilizing programmable material structured TPU-SMP.

The previous investigations on 2W-SMEs revealed that the programming method required for the SMP to achieve the desired actuation is tedious, complex, and non-economical. Alternatively, it was apparent from previous works of literature that even though researchers could attain 2W-SMEs directly after 3D printing without needing a further programming step, there were many drawbacks to the presented solutions. Some drawbacks are that the 2W-SME was achieved only with composite materials, such as two- or multilayered material systems [46] or embedded materials [53–56], where one material provides the elastic property and the other for changing or fixing temporary shape. Moreover, such systems' complicated recycling ability and detachability at their end-of-life or end-of-use scenarios make them significantly less unattractive for a sustainable ecosystem. There are also no proposed solutions or technological approaches for a single material system to exhibit 2W-SME directly after its manufacturing.

References

1. Pretsch, T. Review on the Functional Determinants and Durability of Shape Memory Polymers. *Polymers* **2010**, *2*, 120–158, doi:10.3390/polym2030120.
2. Wang, K.; Strandman, S.; Zhu, X.X. A mini review: Shape memory polymers for biomedical applications. *Front. Chem. Sci. Eng.* **2017**, *11*, 143–153, doi:10.1007/s11705-017-1632-4.
3. Kim, Y.-J.; Matsunaga, Y.T. Thermo-responsive polymers and their application as smart biomaterials. *J. Mater. Chem. B* **2017**, *5*, 4307–4321, doi:10.1039/c7tb00157f.
4. Hoffman, A.S. Stimuli-responsive polymers: biomedical applications and challenges for clinical translation. *Advanced Drug Delivery Reviews* **2013**, *65*, 10–16, doi:10.1016/j.addr.2012.11.004.
5. Yin, X.; Hoffman, A.S.; Stayton, P.S. Poly(N-isopropylacrylamide-co-propylacrylic acid) copolymers that respond sharply to temperature and pH. *Biomacromolecules* **2006**, *7*, 1381–1385, doi:10.1021/bm0507812.
6. Ngo, T.D.; Kashani, A.; Imbalzano, G.; Nguyen, K.T.Q.; Hui, D. Additive manufacturing (3D printing): A review of materials, methods, applications and challenges. *Composites Part B: Engineering* **2018**, *143*, 172–196, doi:10.1016/j.compositesb.2018.02.012.
7. Ligon, S.C.; Liska, R.; Stampfl, J.; Gurr, M.; Mülhaupt, R. Polymers for 3D Printing and Customized Additive Manufacturing. *Chem. Rev.* **2017**, *117*, 10212–10290, doi:10.1021/acs.chemrev.7b00074.
8. N. Turner, B.; Strong, R.; A. Gold, S. A review of melt extrusion additive manufacturing processes: I. Process design and modeling. *RPJ* **2014**, *20*, 192–204, doi:10.1108/RPJ-01-2013-0012.
9. Killi, S.W. *Additive manufacturing*: *Design, methods, and processes / edited by Steinar Killi;* Pan Stanford Publishing: Singapore, 2017, ISBN 9781315196589.
10. Awari, G.K.; Thorat, C.S.; Ambade, V.; Kothari, D.P. *Additive manufacturing and 3D printing technology*: *Principles and applications / G.K. Awari, C.S. Thorat, Vishwjeet Ambade, D.P. Kothari*, 1st; CRC Press: Boca Raton, 2021, ISBN 9781000338706.
11. Wang, L.; Gramlich, W.M.; Gardner, D.J. Improving the impact strength of Poly(lactic acid) (PLA) in fused layer modeling (FLM). *Polymer* **2017**, *114*, 242–248, doi:10.1016/j.polymer.2017.03.011.

12. Liu, X.; Chi, B.; Jiao, Z.; Tan, J.; Liu, F.; Yang, W. A large-scale double-stage-screw 3D printer for fused deposition of plastic pellets. *J. Appl. Polym. Sci.* **2017**, *134*, 45147, doi:10.1002/app.45147.
13. Ning, F.; Cong, W.; Qiu, J.; Wei, J.; Wang, S. Additive manufacturing of carbon fiber reinforced thermoplastic composites using fused deposition modeling. *Composites Part B: Engineering* **2015**, *80*, 369–378, doi:10.1016/j.compositesb.2015.06.013.
14. Kuznetsov, V.E.; Solonin, A.N.; Urzhumtsev, O.D.; Schilling, R.; Tavitov, A.G. Strength of PLA Components Fabricated with Fused Deposition Technology Using a Desktop 3D Printer as a Function of Geometrical Parameters of the Process. *Polymers* **2018**, *10*, doi:10.3390/polym10030313.
15. Raasch, J.; Ivey, M.; Aldrich, D.; Nobes, D.S.; Ayranci, C. Characterization of polyurethane shape memory polymer processed by material extrusion additive manufacturing. *Additive Manufacturing* **2015**, *8*, 132–141, doi:10.1016/j.addma.2015.09.004.
16. Yang, Y.; Chen, Y.; Wei, Y.; Li, Y. 3D printing of shape memory polymer for functional part fabrication. *Int J Adv Manuf Technol* **2016**, *84*, 2079–2095, doi:10.1007/s00170-015-7843-2.
17. Hendrikson, W.J.; Rouwkema, J.; Clementi, F.; van Blitterswijk, C.A.; Farè, S.; Moroni, L. Towards 4D printed scaffolds for tissue engineering: exploiting 3D shape memory polymers to deliver time-controlled stimulus on cultured cells. *Biofabrication* **2017**, *9*, 31001, doi:10.1088/1758-5090/aa8114.
18. Monzón, M.D.; Paz, R.; Pei, E.; Ortega, F.; Suárez, L.A.; Ortega, Z.; Alemán, M.E.; Plucinski, T.; Clow, N. 4D printing: processability and measurement of recovery force in shape memory polymers. *Int J Adv Manuf Technol* **2017**, *89*, 1827–1836, doi:10.1007/s00170-016-9233-9.
19. Pretsch, T.; Ecker, M.; Schildhauer, M.; Maskos, M. Switchable information carriers based on shape memory polymer. *J. Mater. Chem.* **2012**, *22*, 7757, doi:10.1039/c2jm16204k.
20. Fritzsche, N.; Pretsch, T. Programming of Temperature-Memory Onsets in a Semicrystalline Polyurethane Elastomer. *Macromolecules* **2014**, *47*, 5952–5959, doi:10.1021/ma501171p.
21. Ecker, M.; Pretsch, T. Novel design approaches for multifunctional information carriers. *RSC Adv* **2014**, *4*, 46680–46688, doi:10.1039/C4RA08977D.
22. Mirtschin, N.; Pretsch, T. Designing temperature-memory effects in semicrystalline polyurethane. *RSC Adv.* **2015**, *5*, 46307–46315, doi:10.1039/C5RA05492C.
23. Zhang, Q.; Yan, D.; Zhang, K.; Hu, G. Pattern transformation of heat-shrinkable polymer by three-dimensional (3D) printing technique. *Sci Rep* **2015**, *5*, 8936, doi:10.1038/srep08936.
24. van Manen, T.; Janbaz, S.; Zadpoor, A.A. Programming 2D/3D shape-shifting with hobbyist 3D printers. *Mater. Horiz.* **2017**, *4*, 1064–1069, doi:10.1039/c7mh00269f.
25. Rajkumar, A.R.; Shanmugam, K. Additive manufacturing-enabled shape transformations via FFF 4D printing. *J. Mater. Res.* **2018**, *33*, 4362–4376, doi:10.1557/jmr.2018.397.
26. Hu, G.F.; Damanpack, A.R.; Bodaghi, M.; Liao, W.H. Increasing dimension of structures by 4D printing shape memory polymers via fused deposition modeling. *Smart Mater. Struct.* **2017**, *26*, 125023, doi:10.1088/1361-665X/aa95ec.
27. Xia, Y.; He, Y.; Zhang, F.; Liu, Y.; Leng, J. A Review of Shape Memory Polymers and Composites: Mechanisms, Materials, and Applications. *Adv. Mater.* **2021**, *33*, e2000713, doi:10.1002/adma.202000713.
28. Scalet, G. Two-Way and Multiple-Way Shape Memory Polymers for Soft Robotics: An Overview. *Actuators* **2020**, *9*, 10, doi:10.3390/act9010010.
29. Zhao, Q.; Qi, H.J.; Xie, T. Recent progress in shape memory polymer: New behavior, enabling materials, and mechanistic understanding. *Progress in Polymer Science* **2015**, *49-50*, 79–120, doi:10.1016/j.progpolymsci.2015.04.001.
30. Bothe, M.; Pretsch, T. Two-Way Shape Changes of a Shape-Memory Poly(ester urethane). *Macromol. Chem. Phys.* **2012**, *213*, 2378–2385, doi:10.1002/macp.201200096.
31. Bothe, M.; Mya, K.Y.; Jie Lin, E.M.; Yeo, C.C.; Lu, X.; He, C.; Pretsch, T. Triple-shape properties of star-shaped POSS-polycaprolactone polyurethane networks. *Soft Matter* **2012**, *8*, 965–972, doi:10.1039/C1SM06474F.
32. Behl, M.; Kratz, K.; Zotzmann, J.; Nöchel, U.; Lendlein, A. Reversible bidirectional shape-memory polymers. *Adv. Mater. Weinheim.* **2013**, *25*, 4466–4469, doi:10.1002/adma.201300880.
33. Behl, M.; Kratz, K.; Noechel, U.; Sauter, T.; Lendlein, A. Temperature-memory polymer actuators. *PNAS* **2013**, *110*, 12555–12559, doi:10.1073/pnas.1301895110.
34. Walter, M.; Friess, F.; Krus, M.; Zolanvari, S.M.H.; Grün, G.; Kröber, H.; Pretsch, T. Shape Memory Polymer Foam with Programmable Apertures. *Polymers* **2020**, *12*, doi:10.3390/polym12091914.
35. Fischer, S.C.L.; Hillen, L.; Eberl, C. Mechanical Metamaterials on the Way from Laboratory Scale to Industrial Applications: Challenges for Characterization and Scalability. *Materials (Basel)* **2020**, *13*, doi:10.3390/ma13163605.

36. Jin, L.; Forte, A.E.; Deng, B.; Rafsanjani, A.; Bertoldi, K. Kirigami-Inspired Inflatables with Programmable Shapes. *Adv. Mater. Weinheim.* **2020**, *32*, e2001863, doi:10.1002/adma.202001863.
37. Berwind, M.F.; Kamas, A.; Eberl, C. A Hierarchical Programmable Mechanical Metamaterial Unit Cell Showing Metastable Shape Memory. *Adv. Eng. Mater.* **2018**, *20*, 1800771, doi:10.1002/adem.201800771.
38. Restrepo, D.; Mankame, N.D.; Zavattieri, P.D. Programmable materials based on periodic cellular solids. Part I: Experiments. *International Journal of Solids and Structures* **2016**, *100-101*, 485–504, doi:10.1016/j.ijsolstr.2016.09.021.
39. Schönfeld, D.; Chalissery, D.; Wenz, F.; Specht, M.; Eberl, C.; Pretsch, T. Actuating Shape Memory Polymer for Thermoresponsive Soft Robotic Gripper and Programmable Materials. *Molecules* **2021**, *26*, doi:10.3390/molecules26030522.
40. Specht, M.; Berwind, M.; Eberl, C. Adaptive Wettability of a Programmable Metasurface. *Adv. Eng. Mater.* **2021**, *23*, 2001037, doi:10.1002/adem.202001037.
41. Zhang, X.; Pint, C.L.; Lee, M.H.; Schubert, B.E.; Jamshidi, A.; Takei, K.; Ko, H.; Gillies, A.; Bardhan, R.; Urban, J.J.; et al. Optically- and thermally-responsive programmable materials based on carbon nanotube-hydrogel polymer composites. *Nano Lett.* **2011**, *11*, 3239–3244, doi:10.1021/nl201503e.
42. Restrepo, D.; Mankame, N.D.; Zavattieri, P.D. Programmable materials based on periodic cellular solids. Part I: Experiments. *International Journal of Solids and Structures* **2016**, *100-101*, 485–504, doi:10.1016/j.ijsolstr.2016.09.021.
43. Takeuchi, N.; Nakajima, S.; Yoshida, K.; Kawano, R.; Hori, Y.; Onoe, H. Microfiber-Shaped Programmable Materials with Stimuli-Responsive Hydrogel. *Soft Robot.* **2022**, *9*, 89–97, doi:10.1089/soro.2020.0038.
44. Wenz, F.; Schönfeld, D.; Fischer, S.C.L.; Pretsch, T.; Eberl, C. Controlling Malleability of Metamaterials through Programmable Memory. *Advanced Engineering Materials* **2022**, 2201022, doi:10.1002/adem.202201022.
45. Bothe, M.; Emmerling, F.; Pretsch, T. Poly(ester urethane) with Varying Polyester Chain Length: Polymorphism and Shape-Memory Behavior. *Macromolecular Chemistry and Physics* **2013**, *214*, 2683–2693, doi:10.1002/macp.201300464.
46. Ke, D.; Chen, Z.; Momo, Z.Y.; Jiani, W.; Xuan, C.; Xiaojie, Y.; Xueliang, X. Recent advances of two-way shape memory polymers and four-dimensional printing under stress-free conditions. *Smart Mater. Struct.* **2020**, *29*, 23001, doi:10.1088/1361-665X/ab5e6d.
47. Pilate, F.; Stoclet, G.; Mincheva, R.; Dubois, P.; Raquez, J.-M. Poly(ε-caprolactone) and Poly(ω-pentadecalactone)-Based Networks with Two-Way Shape-Memory Effect through [2+2] Cycloaddition Reactions. *Macromol. Chem. Phys.* **2018**, *219*, 1700345, doi:10.1002/macp.201700345.
48. Zhou, J.; Turner, S.A.; Brosnan, S.M.; Li, Q.; Carrillo, J.-M.Y.; Nykypanchuk, D.; Gang, O.; Ashby, V.S.; Dobrynin, A.V.; Sheiko, S.S. Shapeshifting: Reversible Shape Memory in Semicrystalline Elastomers. *Macromolecules* **2014**, *47*, 1768–1776, doi:10.1021/ma4023185.
49. Basit, A.; L'Hostis, G.; Durand, B. Multi-shape memory effect in shape memory polymer composites. *Materials Letters* **2012**, *74*, 220–222, doi:10.1016/j.matlet.2012.01.113.
50. Basit, A.; L'Hostis, G.; Pac, M.J.; Durand, B. Thermally Activated Composite with Two-Way and Multi-Shape Memory Effects. *Materials (Basel)* **2013**, *6*, 4031–4045, doi:10.3390/ma6094031.
51. Wu, Y.; Hu, J.; Han, J.; Zhu, Y.; Huang, H.; Li, J.; Tang, B. Two-way shape memory polymer with "switch–spring" composition by interpenetrating polymer network. *J. Mater. Chem. A* **2014**, *2*, 18816–18822, doi:10.1039/C4TA03640A.
52. Ge, Q.; Sakhaei, A.H.; Lee, H.; Dunn, C.K.; Fang, N.X.; Dunn, M.L. Multimaterial 4D Printing with Tailorable Shape Memory Polymers. *Sci Rep* **2016**, *6*, 1–11, doi:10.1038/srep31110.
53. Zhu, P.; Yang, W.; Wang, R.; Gao, S.; Li, B.; Li, Q. 4D Printing of Complex Structures with a Fast Response Time to Magnetic Stimulus. *ACS Appl. Mater. Interfaces* **2018**, *10*, 36435–36442, doi:10.1021/acsami.8b12853.
54. Kokkinis, D.; Schaffner, M.; Studart, A.R. Multimaterial magnetically assisted 3D printing of composite materials. *Nat. Commun.* **2015**, *6*, 8643, doi:10.1038/ncomms9643.
55. Kim, Y.; Yuk, H.; Zhao, R.; Chester, S.A.; Zhao, X. Printing ferromagnetic domains for untethered fast-transforming soft materials. *Nature* **2018**, *558*, 274–279, doi:10.1038/s41586-018-0185-0.
56. Xu, T.; Zhang, J.; Salehizadeh, M.; Onaizah, O.; Diller, E. Millimeter-scale flexible robots with programmable three-dimensional magnetization and motions. *Sci. Robot.* **2019**, *4*, doi:10.1126/scirobotics.aav4494.

Chapter 3:
One-Way Shape Memory Effect of Objects Programmed After Fused Filament Fabrication

Chapter 3.1: Additive Manufacturing of Information Carriers Based on Shape Memory Polyester Urethane

Chapter 3.1: Additive Manufacturing of Information Carriers Based on Shape Memory Polyester Urethane

The original article Chalissery, D.; Pretsch, T.; Staub, S.; Andrä, H. Additive Manufacturing of Information Carriers Based on Shape Memory Polyester Urethane. Polymers 2019, 11, 1005 and graphical abstract are published in MDPI polymers and available at https://doi.org/10.3390/polym11061005.

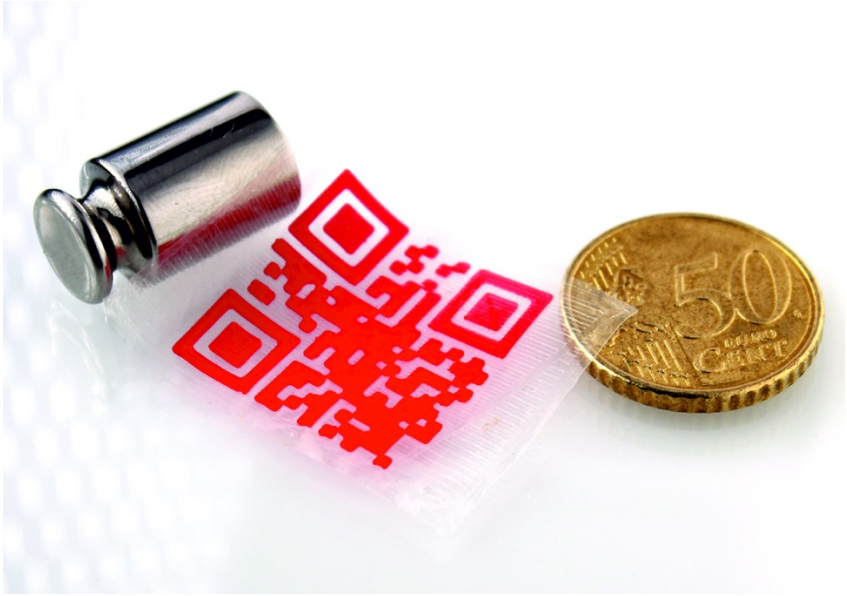

Figure 3.1.0. The graphical abstract of the article "Additive Manufacturing of Information Carriers Based on Shape Memory Polyester Urethane" is published in MDPI Polymers 2019, 11, 1005.

Contribution

My contribution: The concept idea of additive manufacturing of information carriers, utilization of different nozzle sizes, the idea of the whole manuscript, design development, conducting experiments, formal analysis, investigation, methodology, validation, visualization, preparation of images (including graphical abstract) and writing—original draft. **Not included in my contribution**: Congruence analysis.

Pretsch, T.: Conceptualization of the manuscript, funding acquisition, project administration, supervision, writing—review and editing

Staub, S.: Congruence analysis: formal analysis, investigation, methodology, visualization, and writing—original draft.

Andrä, H.: Congruence analysis: funding acquisition, project administration, conceptualization and formal analysis

Chapter 3.1: Additive Manufacturing of Information Carriers Based on Shape Memory Polyester Urethane

Dilip Chalissery [1], Thorsten Pretsch [1,*], Sarah Staub [2] and Heiko Andrä [2]

[1] Fraunhofer Institute for Applied Polymer Research IAP, Geiselbergstr. 69, 14476 Potsdam, Germany; dilip.chalissery@iap.fraunhofer.de
[2] Fraunhofer Institute for Industrial Mathematics ITWM, Fraunhofer-Platz 1, 67663 Kaiserslautern, Germany; sarah.staub@itwm.fraunhofer.de (S.S.); heiko.andrae@itwm.fraunhofer.de (H.A.)
* Correspondence: thorsten.pretsch@iap.fraunhofer.de; Tel.: +49-(0)-331/568-1414

Received: 5 April 2019; Accepted: 4 June 2019; Published: 5 June 2019

3.1.0. Abstract: Shape memory polymers (SMPs) are stimuli-responsive materials, which are able to retain an imposed, temporary shape and recover the initial, permanent shape through an external stimulus like heat. In this work, a novel manufacturing method is introduced for thermoresponsive quick response (QR) code carriers, which originally were developed as anticounterfeiting technology. Motivated by the fact that earlier manufacturing processes were sometimes too time-consuming for production, filaments of a polyester urethane (PEU) with and without dye were extruded and processed into QR code carriers using fused filament fabrication (FFF). Once programmed, the distinct shape memory properties enabled a heating-initiated switching from non-decodable to machine-readable QR codes. The results demonstrate that FFF constitutes a promising additive manufacturing technology to create complex, filigree structures with adjustable horizontal and vertical print resolution and, thus, an excellent basis to realize further technically demanding application concepts for shape memory polymers.

Keywords: additive manufacturing; 3D printing; shape memory polymer; fused filament fabrication; QR code carrier; thermoplastic polyurethane; filigree structures

3.1.1. Introduction

Additive manufacturing (AM) alias three-dimensional (3D) printing is increasingly gaining importance, especially because of the rapid availability and the infinite design variety of print objects. Within the commercially established AM technologies, fused filament fabrication (FFF), which is a hot-melt extrusion-based 3D printing process, is widely used [1–3]. It requires a virtual 3D model and appropriate slicing software to convert the model into thin layers and gain the essential printing instructions. After melting in the extruder nozzle, the polymer strand is deposited layer-by-layer on the building platform of a 3D printer by moving the nozzle along a pre-calculated path. Once deposited, the polymer hardens immediately in the desired arrangement of polymer strands, which set the final shape of an object. Since FFF is

an extrusion-based technique, it easily gives access to new thermoplastic materials provided they can be processed with filaments that meet the requirements of a 3D printer. To date, many thermoplastic materials have been investigated via FFF, at which special attention was devoted to polylactic acid (PLA), acrylonitrile-butadiene-styrene copolymers (ABS), polycarbonates, and polyamides [3]. Other indispensable polymer-based AM methods include stereolithography (SLA), multi-jet fusion (MJF), selective laser sintering (SLS), and big area additive manufacturing (BAAM).

Basically, the prospect of developing new applications for 3D printing improves as new functional materials are developed [4,5]. In general, many shape memory polymers (SMPs) are thermoresponsive thermoplastics. They are able to retain an imposed, temporary shape after programming and to recover the initial, permanent shape upon exposure to an external stimulus like heat [6–11]. Today, thermoplastic polyurethanes belong to the most intensively studied shape memory polymers [12–25]. Intriguingly, there are only a few publications in which FFF has been employed as a printing method for thermoresponsive polyurethane-based SMPs, the majority of them concentrating on polyether urethanes. Obviously good printing results could be achieved by Hendrikson et al. [26]. who demonstrated that scaffolds can be produced via FFF from the polyether urethane DiAPLEX® MM 3520 from SMP Technologies Inc. The scaffolds were characterized by a fiber spacing of 982 ± 11 µm, a fiber diameter of 171 ± 5 µm, and a layer height of 154 ± 2 µm. In another work, Raasch et al. reported on the extrusion of the thermoplastic polyether urethane DiAPLEX® MM 4520 from the same company and used the obtained filaments to manufacture specimens out of them; the 3D objects were later examined by three-point bend tests to study the influence of annealing upon shape memory behavior [27]. In a work by Yang et al., the same material was extruded and FFF used to print parts with shape memory properties [28]. Villacres et al. fabricated tensile bars of DiAPLEX® MM 4520 and proved how to influence the mechanical properties by varying geometrical parameters like print orientation and infill percentage [29]. The apparently only work on extrusion-based AM of polyester urethane so far has been reported by Monzón et al. [30], who employed a custom-made 3D printer to produce parts of Desmopan® DP 2795A SMP from Covestro Deutschland AG. The setting of the individual layer height was selected to be 400 µm; the stress recovery behavior of programmed parts was studied and there was a potential seen to be used as mechanical actuators.

Until today, plenty of applications have been suggested for SMPs [31–40]. One of these applications is switchable information carriers [41–43]. According to the underlying concept of SMP Tagnologies™, e.g., a quick response (QR) code, which can be considered as an example for a complex two-dimensional structure, is contained in the surface of an SMP. After fabrication, the code can be converted from machine-readable to unreadable by programming. Upon thermally triggering the shape memory effect, the QR code returns into the machine-readable state. The special material behavior of information release on demand can be helpful to verify and identify counterfeit products [41] or to supervise cold chains [44]. In the past, the preparation of information carriers turned out to be labor-intensive, since several manufacturing steps had to be passed through. In fact, once an SMP was processed

via, e.g., injection molding, “guest diffusion” had to be applied to achieve a surface-specific coloration and laser treatment to generate a two-dimensional code in the polymer surface, before the information carrier could be obtained in its final shape by going through a cutting process [41]. Alternatively, an SMP can be coated and a code engraved into the resulting top layer, followed, e.g., by laser cutting [45,46]. Since the procedures are partly very complex, the primary goal of this work includes the introduction of an easier approach to fabricate QR code carriers. To keep it as simple as possible, the same polyester urethane (PEU), which was employed as base material in earlier generations of information carriers, was used. On the way to the production of QR code carriers, the individual steps of filament manufacturing and processing via FFF were examined, before appropriate programming paths were explored and the functionality of the QR code carriers was evaluated. Finally, the results of 3D printing were considered against the background of other technologies used in additive manufacturing.

3.1.2. Experimental Section

Material: The polyester urethane (PEU) Desmopan® DP 2795A SMP from Covestro Deutschland AG (Leverkusen, Germany) was chosen as model compound and used as received in the form of a granulate. The hard segment of the PEU is composed of 4,4’-methylenediphenly diisocyanate and a 1,4-butanediol chain extender. The soft segment is based on poly(1,4-butylene adipate) (PBA). Further information regarding the thermal and mechanical properties of the PEU is given in previous publications [25,46,47].

Extrusion: The PEU granulate was dried at 110 °C in a Binder vacuum drying chamber VDL 53 from Binder GmbH (Tuttlingen, Germany) in order to remove water and avoid bubble formation when extruding filaments at a later stage. The thermal pre-treatment was finalized after 150 min. Subsequently, the pellets were fed into an extrusion line to produce filaments (**Figure 3.1.1**).

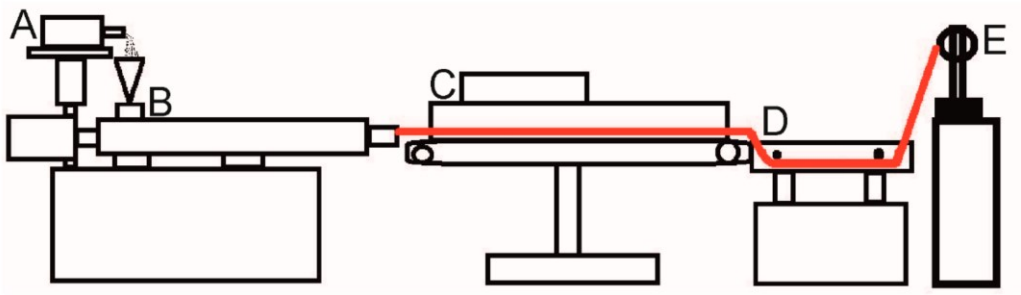

Figure 3.1.1. Technical drawing of an extrusion line as used for the production of PEU filaments: Material feeding system (**A**), twin screw extruder (**B**), conveyor belt (**C**), water bath (**D**), and filament winding machine (**E**). The extrudate is drawn in red.

The individual units of the extrusion line were put together in such a way that it included a volumetric material feeding system Color-exact 1000 from Plastic Recycling Machinery (Zhangjiagang City, China), a Leistritz twin screw extruder MICRO 18 GL from Leistritz AG

(Nürnberg, Germany), characterized by seven heating zones and a screw length of 600 mm, a conveyor belt, a water bath and a filament winder from Brabender GmbH and Co. KG (Duisburg, Germany). The temperature of the individual heating zones of the extruder was 180, 185, 190, 195, 200, 190, and 190 °C. The screw speed of the extruder was set to 77 rpm. Initially, the PEU granulate was processed without additives. In another experiment 0.5 wt. % of Irgazin® Red DPP BO from Kremer Pigmente GmbH and Co. KG (Aichstetten, Germany) were added to obtain a red filament. To evaluate the quality of the filaments, the evolution of filament diameter was manually detected at regular intervals using a Vernier caliper from Fowler High Precision (Auburndale, FL, USA).

Virtual Design: The bar code generator goQR.me [48] was used to create a QR code (Reed-Solomon error correction, error correction level H) with the encoded information "Fraunhofer IAP" (**Figure 3.1.2**) [49].

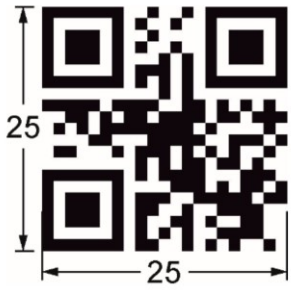

Figure 3.1.2. Technical drawing of a QR code, which was used as structural motif for the production of information carriers. All data are provided in mm.

The code was saved in the .jpeg image format and used as starting point to build a virtual information carrier by means of the vector-oriented drawing program AutoCAD from Autodesk, Inc. (San Rafael, CA, USA) (**Figure 3.1.3**) [50].

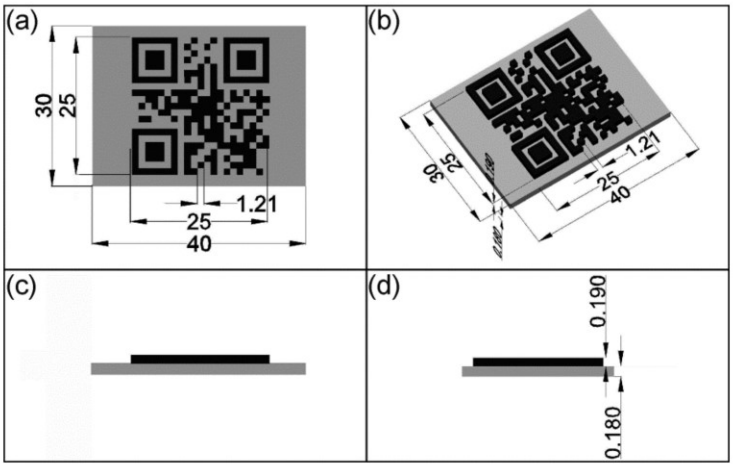

Figure 3.1.3. Technical drawing of a virtual QR code carrier including a substrate layer (gray color) and a structural QR code elevation (black color): Top view (**a**), isometric view (**b**), front view (**c**), and left view (**d**). All data are provided in mm.

The edge length of the QR code was set to 25 mm (**Figures 3.1.2 and 3.1.3a**). For the substrate layer a dimensioning of 30 mm × 40 mm was selected. As can be seen in **Figure 3.1.3b–d**, the QR code carrier was built up by two structural units including a substrate layer with a height of 180 µm and a structural QR code elevation with a height of 190 µm. The design of the QR code carrier as provided by **Figure 3.1.3** was used for most of the experiments, which are described in this contribution. The only exception was an approach in which the target height of the substrate was reduced to 15 µm. For convenience, a terminology for the different types of QR code carriers and the associated print settings is introduced in Fused Filament fabrication Section. After finalizing the design, the 3D models were imported into the slicer program Cura 3.3.1 from Ultimaker B. V. (Watermolen, The Netherlands) [51]. As a result, numerically controlled codes, also denoted as G-codes, were generated, containing the instructions for the 3D printer in the form of printing paths, information with reference to the amount of extruded material and the spatially resolved printing parameters. Finally, the codes were transferred to the 3D printer.

Fused Filament Fabrication (3D Printing): Fused filament fabrication was used to produce QR code carriers with differing technical specifications. The experiments were carried out with the commercially available 3D printer Ultimaker 3 from Ultimaker B. V. (Geldermalsen, The Netherlands). The manufacturer provides an XYZ resolution for Ultimaker 3 of 12.5, 12.5, and 2.5 µm [52], defining the smallest movement that the 3D printer can make with regard to the XY plane and in the Z direction. To calibrate the print bed, the Ultimaker build plate manual leveling calibration method was carried out before the beginning of each experiment. Therefore, a calibration card characterized by a thickness of about 170 µm was used. The process included a rough leveling of the build plate followed by a fine leveling. The fine leveling was achieved with the calibration card, at which the knurled nut was adjusted at the rear center, front left, and front right of the build plate until slight friction occurred, when sliding the card between built plate and print head.

Basically, the same design of QR code carriers was used as introduced in Section 3.1.2.3. The two print heads of the FFF-printer were either equipped with two nozzles having different diameters of 100 and 400 µm, respectively, or the same diameter of 400 µm. For simplicity, the following terminology is introduced, pointing out the most relevant variations when producing QR code carriers:

Type 1: The substrate was printed with non-dyed PEU using a 400 µm nozzle and a target layer thickness of 180 µm. The elevation was built from red PEU with a 100 µm nozzle.

Type 2: In analogy to the type 1 QR code carrier, the substrate was printed with non-dyed PEU using a 400 µm nozzle. Again, a target layer thickness of 180 µm was selected for the substrate, but the elevation was built with red PEU employing a 400 µm nozzle.

Type 3: Similar as in the previous cases, the substrate was printed with non-dyed PEU using a 400 µm nozzle, but this time a reduced target layer thickness of 15 µm was selected. The elevation was built with red PEU using a 400 µm nozzle.

The most relevant settings for the 3D printing processes are listed in **Table 3.1.1**.

Table 3.1.1. Printing instructions for Ultimaker 3 to produce the three different prototypes of QR code carriers based on PEU.

Specifications	Substrate (Non-Dyed PEU)		Elevation (Red PEU)	
Type of QR code carrier	1, 2	3	1	2, 3
Diameter of the nozzle (µm)	400	400	100	400
Temperature of the nozzle (°C)	225	225	190	190
Speed of print head (mm × s^{-1})	50	50	4	7
Build rate (ml × h^{-1})	34.2	34.2	5.4	22.8
Build platform temperature (°C)	23	23	23	23
Number of layers	1	1	3	1
Layer height (µm)	180	15	63	190

Characterization of Thermal Properties: Dynamic mechanical analysis (DMA) was used to investigate the thermomechanical properties of the PEU. The experiments were carried out on two samples including a cylindrical granulate grain, having a diameter of 1.8 mm and a length of 4.86 mm, and a sample of a 3D printed substrate of a type 2 QR code carrier having the size of 5.15 mm × 3.8 mm × 0.19 mm. The measurements were conducted with a Q800 DMA from TA Instruments (New Castle, DE, USA) at a frequency of 10 Hz. At first, the sample was heated to 100 °C, before it was cooled to −100 °C to finalize the first heating-cooling cycle. Adjacently, the measurement cycle was repeated once more. For all experiments, heating and cooling rates of 3 °C·min^{-1} were selected and the holding time at the highest and lowest temperature was set to 10 min. The storage modulus (E'), loss factor (tan δ) and the glass transition temperature (T_g) were determined for the second heating.

The phase transition behavior of the PEU was also studied by differential scanning calorimetry (DSC) using a Q100 DSC from TA Instruments (New Castle, DE, USA). The measurements were performed on a granulate grain, a piece of the filament and a sample of the 3D printed substrate of a type 2 QR code carrier. In any case, the sample weight was approximately 5 mg. In the experiments a sample was first cooled to −90 °C, before it was heated to 100 °C and cooled back to −90 °C, which finalized the measurement. Cooling and heating were carried out with a rate of 10 °C x min^{-1}. The temperature holding time was 10 min at −90 and 100 °C, respectively.

Characterization of Print Quality: Topography measurements were performed on QR code carriers using a FocusCam LV150 confocal microscope from Confovis GmbH (Jena, Germany), which was equipped with an objective lens of 5×/0.15 N.A. Any time, the sample was illuminated with a ring light. The data recorded by the focus variation microscope was evaluated with the software MountainsMap® imaging topography 7.4 from Digital Surf (Besançon, France) [53]. The development of the surface profile with regard to a scanned cuboid including its surrounding was exemplarily determined for type 1 and type 2 QR code carriers. For a detailed analysis, a line was inserted along the mid-perpendicular through the

cuboid. The cuboid was characterized with a step measurement to determine its height and width.

Further microscopic investigations were carried out with the microscope Axio Scope.A1 from Carl Zeiss Microscopy GmbH (Jena, Germany) using the imaging software Zen 2.3 lite also from Carl Zeiss Microscopy GmbH [54]. The experiments were conducted to evaluate the resolution of the QR code in the XY-plane and to estimate the layer thickness of QR code carriers and thus the Z-parameter. In the latter case, a cut was made with a scalpel along the mid-perpendicular through the abovementioned cuboid.

The printing results were also mathematically investigated. For this purpose, QR code carriers were scanned in a first step as gray value images with a resolution of 600 dpi and then loaded into the software tool ImageJ developed by Wayne Rasband (Bethesda, MD, USA) [55]. With assistance of this tool the images were cropped to the dimension of the original QR code and scaled to the corresponding resolution. The brightness and contrast were adjusted such that the influence of reflections and possible shadows was minimized. Then, the gray value images were binarized by the automatic binarization function in ImageJ. In a next step, the binarized images of the printing results were inverted. Thus, those areas where there was only the substrate of the QR code carrier were marked in black while the printed elevation parts were marked white. Adjacently, the inverse images of the printing results as well as the original QR code were imported into the software tool Paraview from Kitware, Inc. (Saratoga County, NY, USA) [56] and exported into the vtk format. The software Paraview allows mathematical operations on the values of images. The binary values of the printing results and the QR code were added up in each pixel. Due to the applied inversion for the printing results, three different gray values V were obtained in the summation (**Equation 3.1.1)**:

$$V = \begin{cases} 0, erraneously\ not\ filled\ (blue) \\ 255, congruent\ (green) \\ 510, irregularly\ filled\ (red) \end{cases} \qquad (\mathbf{3.1.1})$$

Based on these values, the print quality of the different prototypes was evaluated as a percentage p by means of **Equation 3.1.2:**

$$p = \frac{\text{\# pixels of certain gray value}}{\text{\# pixels}} \qquad (\mathbf{3.1.2})$$

Programming and Characterization of Shape Memory Properties: The programming of QR code carriers was carried out with an MTS Criterion universal testing machine from MTS Systems Corporation (Eden Prairie, MN, USA). The device was operated with a temperature chamber, which was controlled by a Eurotherm temperature controller unit. Two heating elements were located at the back of the chamber. Liquid nitrogen from a Dewar vessel was fed into the chamber under a pressure of 1.3 bar as an essential prerequisite for cooling. At the beginning of programming, a QR code carrier was clamped with a length of 25 mm, corresponding to the edge length of the QR code, in the pneumatic grips of the universal testing machine, the chamber was heated to 60 °C and a maximum force F_{max} of either 5 or

25 N was applied using a loading rate of 300 mm x min^{-1}. The maximum distance between the outer sides of the QR code was immediately determined by means of a Vernier caliper from Fowler High Precision. The QR code carrier was then cooled to –15 °C, whereby the clamping distance was kept constant. After 10 min, the sample was unloaded and the chamber was heated to 23 °C.

A ZTNG-100B heating plate from Dr. Neumann Peltier-Technik GmbH (Neuried, Germany) was used to investigate the thermoresponsiveness of the programmed QR code carriers. Therefore, the temperature was gradually raised from 23 to 60 °C and images of the sample were taken in regular time intervals during shape recovery. After finalizing the experiment, the congruence of the QR code pattern with regard to the permanent and the recovered shape was determined and used to evaluate shape recoverability. In this connection, a similar approach was followed as described in Programming and characterization of shape memory properties. Section, but this time gray value images were generated for the QR code carrier in its permanent and recovered shape. The gray value image of the permanent shape was regarded as the standard with which the recovered shape was compared. Therefore, the binarized gray value image of the recovered shape was inverted and added to the image containing the information of the permanent shape. The resulting gray values V were evaluated such that in the case of consistent pixels the areas were considered to be congruent while, for nonexistent pixels, the areas were regarded as incongruent (**Equation 3.1.3**):

$$V = \begin{cases} 255, congruent\ (green) \\ else, incongruent\ (red) \end{cases} \qquad (\mathbf{3.1.3})$$

By analogy with the above procedure, the percentage was determined again according to **Equation 3.1.2**, but this time it was the measure of shape recoverability.

A multiple cycle experiment was carried out with the MTS Criterion universal testing machine, which was equipped with a temperature chamber. For loading, a type 2 QR code carrier was clamped with a length of 25 mm, corresponding to the edge length of the QR code, in the pneumatic grips of the universal testing machine, heated to 60 °C, deformed with a rate of 300 mm x min^{-1} to a maximum clamping distance of 55 mm, before unloading was carried out at the same temperature with a rate of 150 mm x min^{-1}. In total, 20 cycles of loading and unloading were conducted. In the 21st cycle, the sample was loaded and the imposed shape was fixed by cooling to −15 °C. After unloading, the temperature was raised to 23 °C and the machine readability of the QR code was checked. The programmed QR code carrier was adjacently heated to 60 °C where, again, the readability of the QR code was investigated. To characterize the boundary between substrate and elevation, another programming was accomplished. In this 22nd cycle, a cut was made with a scalpel along the mid-perpendicular through the abovementioned cuboid and investigated by means of light microscopy. The sample was finally heated to 60 °C and a microscopic investigation was carried out with the microscope Axio Scope.A1, which was equipped with an objective lens of 20× and 40× magnification. Following other programming scenarios, a QR code carrier was folded in the

middle or rolled up at 60 °C, before it was cooled under load to −15 °C. Afterwards, the thermoresponsiveness was again followed on the heating plate when triggering the shape memory effect. Independent of the programming technique applied, the machine readability of QR codes was checked with a Samsung Galaxy S8 smartphone from Samsung Electronics (Seoul, South Korea), which was equipped with the software "Optical Reader" version 4.4.07 also from Samsung Electronics Co., Ltd [57].

3.1.3. Results and Discussion

The melt extrusion of the physically cross-linked PEU block copolymer led to the production of a whitish filament whose color can be traced back to the presence of crystals from poly(1,4-butylene adipate) (PBA); the proof will be given below in a DSC measurement. In another experiment, 0.5 wt. % of Irgazin® Red DPP BO was added in the course of PEU extrusion so that a red filament could also be obtained. It is noteworthy that the two filaments had a homogenous diameter of 2.85 ± 0.07 mm, regardless of whether the dye was added or not (**Figure 3.1.4**).

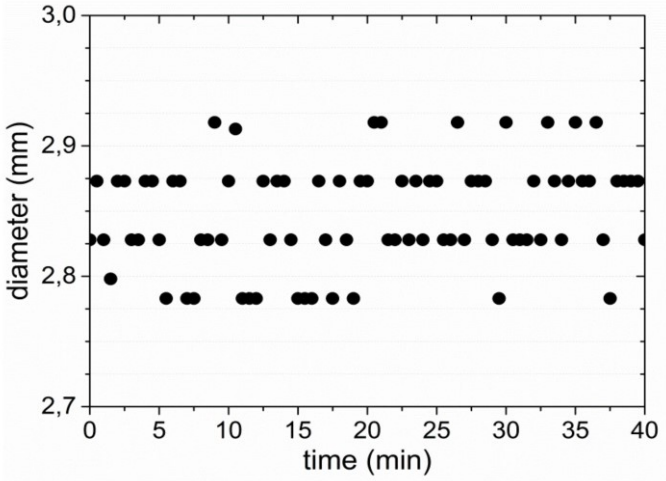

Figure 3.1.4. Evolution of filament diameter over time when extruding PEU. The development in measured values is also representative for an experiment in which Irgazin® Red DPP BO was added during extrusion of PEU.

Before starting with the 3D printing experiments, the design of the QR code carriers was developed (**Figure 3.1.3**). The objects were sliced to obtain the essential printing instructions. In a next step, a dual extrusion FFF process was established, in which the already obtained filaments were reprocessed to build up QR code carriers, characterized by a whitish substrate and a red QR code elevation. The most relevant settings for the 3D printing processes are provided in **Table 3.1.1.**

For the production of a type 1 QR code carrier, a single-layer substrate with a target height of 180 µm was printed, using the white filament and a nozzle with a diameter of 400 µm. In contrast, the QR code elevation having a virtual height of 190 µm was then built up in three layers by melting the red filament in the 100 µm nozzle and placing the resulting strands on

the substrate. The printing results are portrayed in **Figure 3.1.5** together with their microscopic characterization.

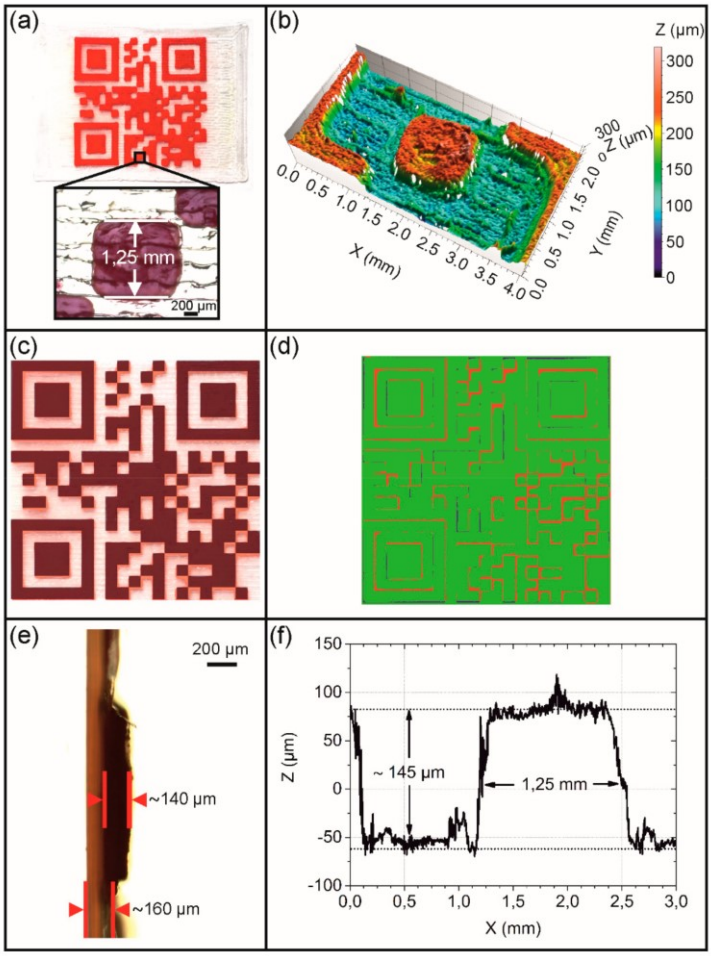

Figure 3.1.5. Type 1 QR code carrier as investigated by light and confocal microscopy including an evaluation of print quality: Top view and inset exhibiting a randomly selected cuboid (**a**), surface topography of the cuboid and its surrounding (**b**), superposition with a virtual QR code having a transparency of 60% (**c**), result of a mathematic calculation to determine the congruence of the virtual QR code with the physical print object: consistent print areas (green color), irregularly filled areas (red color) and unfilled print areas (blue color) (**d**), side view of a cut through the cuboid and the substrate (**e**), and the evolution of layer thickness Z with regard to the cuboid and its surrounding (**f**).

The obtained type 1 QR code carrier exhibited a good spatial resolution with respect to the XY level as exemplified by the presence of finely resolved rectangles (**Figure 3.1.5a**). In order to better assess the print quality with regard to the smallest structural unit of the QR code pattern, a cuboid of the finished part with a virtual edge length of 1.21 mm was microscopically examined (**Figure 3.1.5a,b**). Here, an edge length of approximately 1.25 mm could be determined. This value exceeded the one of our CAD model by 40 µm corresponding to 3.2% of the object dimension (**Figure 3.1.3a**). Basically, a deviation from the technical specification was anticipated due to slight fluctuations in filament diameter (**Figure 3.1.4**) and minor differences in the print bed height resulting from the calibration [58]. However, in the XY plane the print quality of the overall QR code pattern was pretty good as supported by the

result of a superposition experiment, in which the virtual QR code was put with a transparency of 60% over the printing pattern (**Figure 3.1.5c**). In addition, a congruence measurement was carried out, subtracting the overhanging regions of the QR code elevation from the black regions of the virtual code. The result gave that 90.7% of the code areas were congruent, 8.1% were irregularly filled with red PEU and 1.2% were erroneously not filled (**Figure 3.1.5d**). Next, the resolution in the Z-direction was closely investigated for the same cuboid and its nearest surrounding. The substrate of the QR code carrier had a thickness of about 160 µm (**Figure 3.1.5e**). The averaged profile height of the elevation was determined to be approximately 145 µm, corresponding to a mean layer height of about 48 µm (**Figure 3.1.5f**). The layer thickness was slightly below the target value, presumably due to deficits in calibration accuracy. The production of the QR code elevation took 17 min, culminating for the whole QR code carrier in a production time of 25 min. For a faster production, the 100 µm nozzle was replaced by a 400 µm nozzle and the technical parameters were adjusted accordingly (see **Table 3.1.1**). As a result, a type 2 QR code carrier was obtained and examined microscopically (**Figure 3.1.6**).

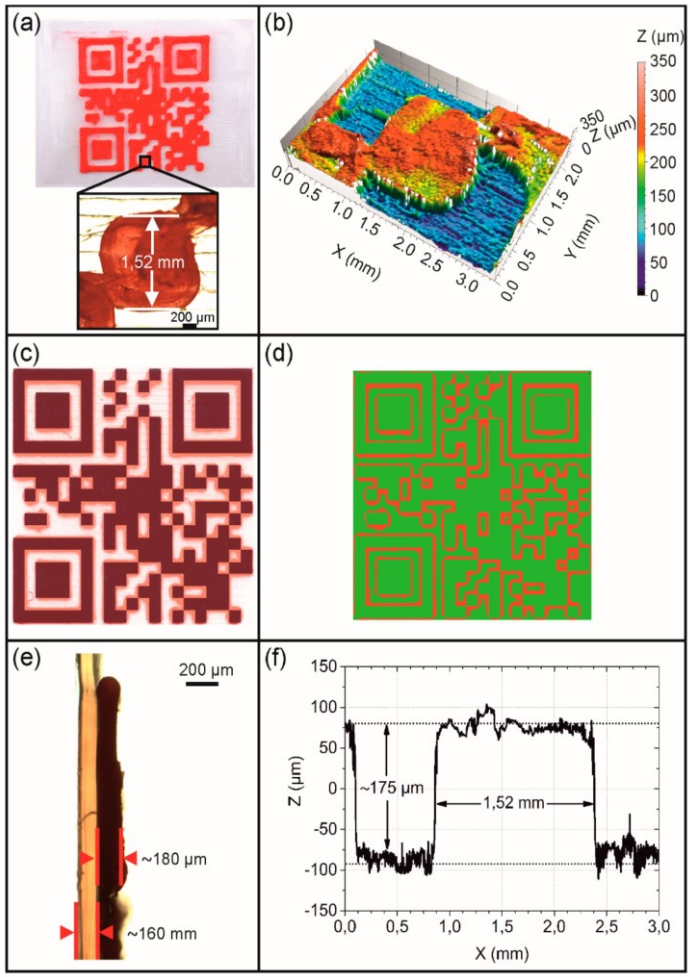

Figure 3.1.6. Type 2 QR code carrier as investigated by light and confocal microscopy including an evaluation of print quality: Top view and inset exhibiting a randomly selected cuboid (**a**), surface topography of the cuboid and its surrounding (**b**), superposition with a virtual QR code having a transparency of 60% (**c**), result of a mathematic calculation to determine the congruence of the virtual

QR code with the physical print object: consistent print areas (green color) and irregularly filled areas (red color) (**d**), side view of a cut through the cuboid and the substrate (**e**), and the evolution of layer thickness Z with regard to the cuboid and its surrounding (**f**).

This time, the presence of more imperfect rectangles could be witnessed in the QR code pattern (**Figure 3.1.6a,b**). Once more, the cuboid was studied, which was located at the same position of the QR code as in the preceding case (**Figure 3.1.5a**), in order to get a first impression about the precision in the XY printing plane. Here, a drastically increased edge length was determined as documented by a value of about 1.52 mm (**Figure 3.1.6a**), exceeding the virtual dimensions of this element by 26% (**Figure 3.1.3a**). The fact that the horizontal print resolution substantially deteriorated in the whole QR code area was confirmed by another superimposition experiment. As visible to the naked eye, the printed regions generously overlapped the black areas of the virtual QR code pattern (**Figure 3.1.6c**). Against this background, another mathematic calculation was carried out. It turned out that 77.4% of the code areas were congruent, whereas 22.6% of those code areas, in which no printing was desired, were covered with red PEU (**Figure 3.1.6d**). However, compared to the type 1 QR code carrier, the same substrate thickness could be verified as expected, but better control over the vertical print resolution could be achieved as indicated by an average profile height of 175 µm (**Figure 3.1.6e,f**). Furthermore, the production time of the QR code elevation could be drastically reduced to 3 min and 30 s so that the printing of the entire QR code carrier was finalized after 11 min and 30 s.

Despite the abovementioned dimensional inaccuracies in the 3D printed objects, the QR codes enabled an error-free decoding with a standard smartphone, independent of which technical equipment and parameter settings were used for printing. This clearly shows that the surface contrast was sufficiently high as ensured by the processing of the differently colored filaments.

To investigate the influence of reprocessing via extrusion and FFF on the viscoelastic properties of the PEU, dynamic mechanical analyses were conducted. Therefore, the raw material in the form of a granulate grain was studied and compared with the thermomechanical behavior of a sample, which was taken from the 3D printed substrate of a type 2 QR code carrier. The associated temperature-dependent evolution in storage modulus E’ and in tan δ is provided by **Figure 3.1.7**.

In both cases, E’ exhibits a two-step decrease in the DMA measurement as characteristic for physically cross-linked PEU [22,59–61]. The investigation of the granulate grain reveals a strong drop in E’, starting at −51 °C and indicating the presence of a glass transition. The tan δ peak is located at about −18 °C. Upon further heating, a weaker decline in E’ takes place, which can be associated with the melting of PBA crystals as earlier verified for the same material [44]. The 3D printed sample shows a similarly pronounced drop in *E*’, starting again at approximately −50 °C, and a tan δ peak at −20 °C, which is in accordance with the thermal behavior of the granulate grain. In contrast, the decline in storage modulus associated with PBA melting is slightly extended toward higher temperatures. This could be related to an orientation effect as supported by reprocessing via FFF, favoring the formation of PBA crystals

with higher temperature stability. In other words, the conditions under which parts of the PBA phase of PEU crystallized were expected to be more favorable for the 3D printed sample. To take another look at this, DSC measurements were carried out (**Figure 3.1.8**).

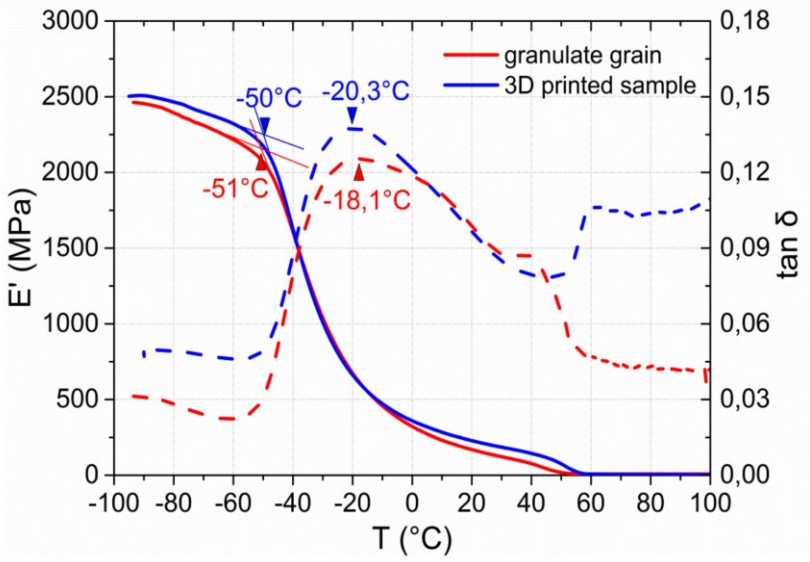

Figure 3.1.7. Thermal and mechanical properties of PEU as determined by DMA: Evolution of storage modulus *E'* (solid line) and tan δ (dashed line) at the second heating of a granulate grain (red color) and the sample of the substrate of a type 2 QR code carrier as manufactured via FFF (blue color).

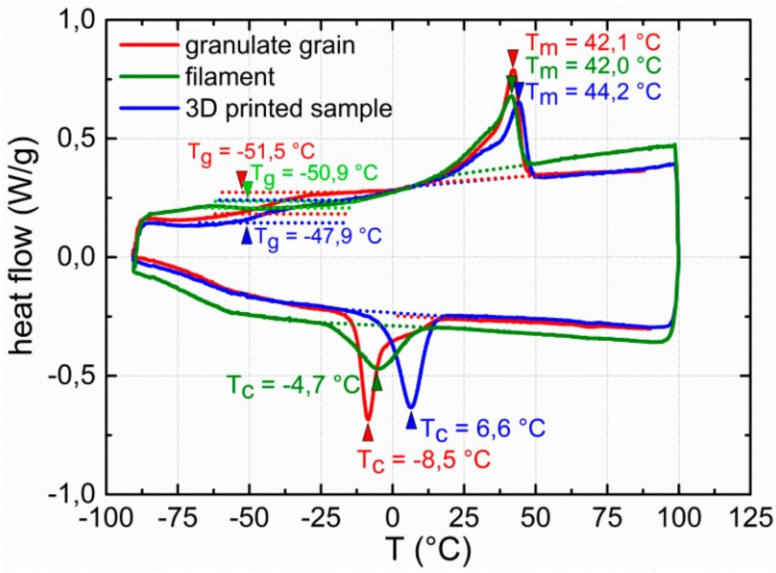

Figure 3.1.8. DSC thermograms of PEU: Thermal behavior of a granulate grain (red color), a piece of filament (green color) and a sample from the substrate of a type 2 QR code carrier as obtained via FFF (blue color). The thermograms are exhibited for the second heating and cooling. The individual enthalpies of melting are 25.9 J x g^{-1} (granulate grain), 21.1 J x g^{-1} (filament) and 25.1 J x g^{-1} (3D printed sample), the enthalpies of crystallization are −25.7 J x g^{-1} (granulate grain), −21.0 J x g^{-1} (filament), and −25.0 J x g^{-1} (3D printed sample).

The DSC cooling trace of the 3D printed sample shows an exothermic signal at about 7 °C associated with the recrystallization of the PBA phase [25]. Compared with the thermal

behavior of the granulate grain, the peak crystallization temperature increased by about 15 °C. This observation can be taken as further hint that strand deposition in course of 3D printing favored a better alignment of polymer chains, thus facilitating the recrystallization of PBA. In a third DSC measurement, the filament of PEU was investigated. Here, another exothermic signal associated with PBA crystallization appeared on cooling, justifying the whitish color of the filament. In this case, the peak crystallization temperature was closer to the one of the granulate grain. In turn, the DSC heating traces of the three samples show the presence of two phase transitions. The first one is located at around −50 °C and, thus, close to the point at which E' started to drop in the DMA measurement. It is related to the glass transition temperature of the PBA phase, while the endothermic signal in between 20 and 50 °C with a maximum at around 40 °C can be assigned to the melting of PBA crystallites [25]. Here, the same trend as in the DMA measurement could be verified, but the melting peak temperature of PBA only increased by 2 °C for the 3D printed sample compared with the granulate grain. Beyond that, the melting behavior of the crystalline PBA phase appeared to be similar for the filament and the granulate grain. Most importantly, when considering both the DMA and DSC data, no further evidence was found that two-step processing, including extrusion and FFF, had a significant impact on the thermal properties of the PEU.

In a next step, the shape memory properties of a type 2 QR code carrier were investigated (**Figure 3.1.9**).

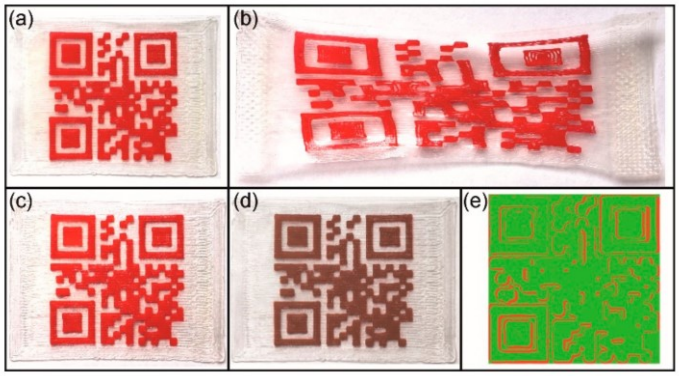

Figure 3.1.9. Type 2 QR code carrier: Permanent shape after 3D printing (**a**), temporary shape as obtained after programming (F_{max} = 5 N) (**b**), and recovered shape after heating to 60 °C (**c**). To visualize shape recoverability, the image of the permanent shape was converted to black-and-white and superimposed with a transparency of 60% on the image of the recovered shape (**d**). The result of a mathematical calculation comparing the permanent shape with the recovered shape: congruent areas (green color) and incongruent areas (red color) (**e**).

Therefore, the additively manufactured QR code carrier (**Figure 3.1.9a**) was heated to 60 °C, at which the melting of the PBA phase was completed. Subsequently, a tensile force F_{max} of 5 N was applied, whereupon a maximum distance length of 55 mm between the outer sides of the QR code was detected. The elongated QR code carrier was fixed by cooling below the crystallization temperature of the PBA phase and unloaded (**Figure 3.1.9b**). Due to changes in the design of the QR code carrier and in particular because of the much smaller

structural thickness of only 160 µm, a significantly lower deformation force was required to achieve a similar QR code distortion in the programmed shape compared to an earlier generation of QR code carriers, which was characterized by a thickness of 2 mm and required a tensile force F_{max} of 48 N [41]. Intriguingly, the bonding was strong enough to withstand a removal of the QR code elevation from the substrate in the course of deformation. The programmed shape of the QR code carrier, which was stable at 23 °C, was characterized by the largest distance length between the outer sides of the QR code of 54 mm, speaking for the excellent shape fixity of the polymer. Due to its drastic distortion the code was no longer machine-readable. Upon triggering the shape memory effect, the QR code pattern almost completely returned to the original shape (**Figure 3.1.9c**), which was accompanied with the restoration of machine readability. For a more detailed study, another image analysis was carried out. Herein, the superimposed QR codes of the original shape and the recovered shape turned out to be almost identical (**Figure 3.1.9d**). The distinct shape recoverability was evidenced by another mathematic calculation, unveiling that 87.8% of the code areas of the permanent shape and the recovered shape were congruent (**Figure 3.1.9e**). Overall, the pronounced shape memory properties, which were detected in the first experimental series, raised the question if type 2 QR code carriers are able to resist even stronger deformations. To find out the answer, a similar programming experiment as described above was performed, but this time F_{max} was raised to 25 N (**Figure 3.1.10**).

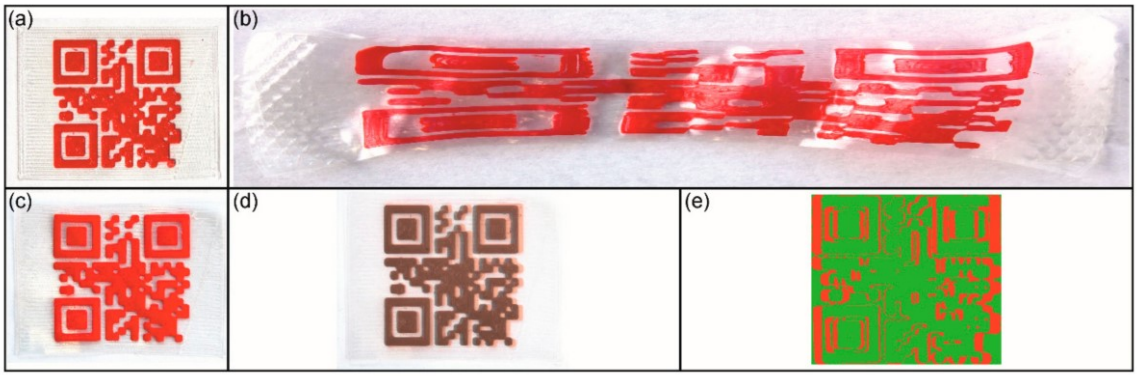

Figure 3.1.10. Type 2 QR code carrier: Permanent shape after 3D printing (**a**), the temporary shape as obtained after programming (F_{max} = 25 N) (**b**), and the recovered shape after heating to 60 °C (**c**). To visualize shape recoverability, the image of the permanent shape was converted to black-and-white and superimposed with a transparency of 60% on the image of the recovered shape (**d**). The result of a mathematical calculation comparing the permanent shape with the recovered shape: congruent areas (green color) and incongruent areas (red color) (**e**).

As a matter of fact, the QR code carrier produced by FFF (**Figure 3.1.10a**) was elongated so that the outer sides of the QR code had a maximum distance of about 155 mm. After cooling below the crystallization temperature of the PBA phase and unloading, the temperature was raised to 23 °C. Here the new, even more strongly deformed shape proved to be stable (**Figure 3.1.10b**). The distance between the outer sides of the elongated QR code measured 153 mm in tensile direction which, again, revealed the excellent shape fixity of the polymer.

It is remarkable that even in this case the QR code became machine-readable again after triggering the shape memory effect (**Figure 3.1.10c**), which demonstrates that the concept of information release on demand was still working. Apparently, the decoding algorithm of the smartphone was able to compensate the residual distortion. The discrepancy between the QR code pattern of the permanent shape and the recovered shape can be clearly seen in the corresponding superimposed images (**Figure 3.1.10d**). As quantified in one further mathematical calculation, 72.7% of the code areas were congruent (**Figure 3.1.10e**). Compared to the previous case, a weakening of shape recoverability was expected due to the stronger deformation applied. It can be assumed that this phenomenon of growing residuals with increasing elongation can be traced back to the flow of amorphous segments in the polymer [62].

To determine the degree of deformation, at which the QR code was no longer machine-readable, another type 2 QR code carrier was deformed at 60 °C with a rate of 0.5 mm x min^{-1} while the machine readability of the QR code was regularly checked. It turned out that the QR code became unreadable as soon as a distance length of 30 mm between the outer sides of the QR code was exceeded.

In an attempt to study the reliability of shape memory properties, a type 2 QR carrier was exposed to a multiple cycle experiment (**Figure 3.1.11**).

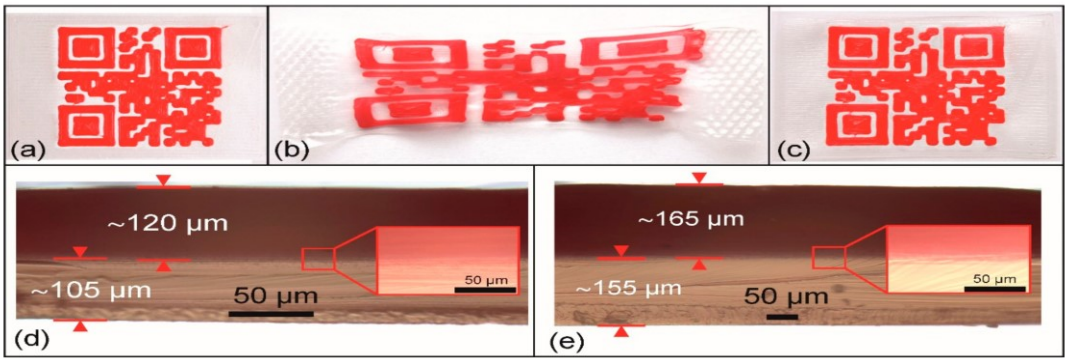

Figure 3.1.11. Type 2 QR code carrier: Permanent shape after 3D printing (**a**), initial clamping distance = 25 mm), temporary shape as obtained after 20 loading-unloading cycles (maximum clamping distance = 55 mm) at 60 °C, followed by programming (**b**), and the recovered shape after heating to 60 °C in the 21st cycle (**c**). Microscopic investigation of a cut through the cuboid and the substrate as examined in the 22nd cycle for the programmed shape (**d**) and the recovered shape (**e**); the insets show an enlarged view of the boundary between the substrate (below) and the elevation (above).

The additively manufactured QR code carrier (**Figure 3.1.11a**) was loaded to a clamping distance of 55 mm and unloaded twenty times, before a loading at 60 °C and unloading at −15 °C was accomplished. In this 21st cycle, the QR code was non-decodable at 23 °C and characterized by a maximum distance length of 55 mm between its outer sides (**Figure 3.1.11b**). Triggering the shape memory effect by reheating to 60 °C resulted in shape recovery as accompanied with the restoration of the machine-readable code, characterized by a maximum edge length of 26.8 mm (**Figure 3.1.11c**). This unequivocally demonstrates the reliability of the concept of switchable information carriers. In the ensuing 22nd cycle, the

thermomechanical treatment of the previous cycle was repeated, but neither micro cracks nor delamination could be microscopically detected at the boundary between the substrate and the elevation both for the programmed shape (**Figure 3.1.11d**) and for the recovered shape (**Figure 3.1.11e**). This finding indicates good layer coalescence. As expected, the triggering of the shape memory effect led to an increase in layer thickness. In fact, a recovery from 105 to 155 µm for the substrate and from 120 to 165 µm for the elevation could be verified.

Next, the deformation scenarios for the programming of QR code carriers were expanded toward rolling and bending, before the respective thermoresponsivity was studied (**Figure 3.1.12**).

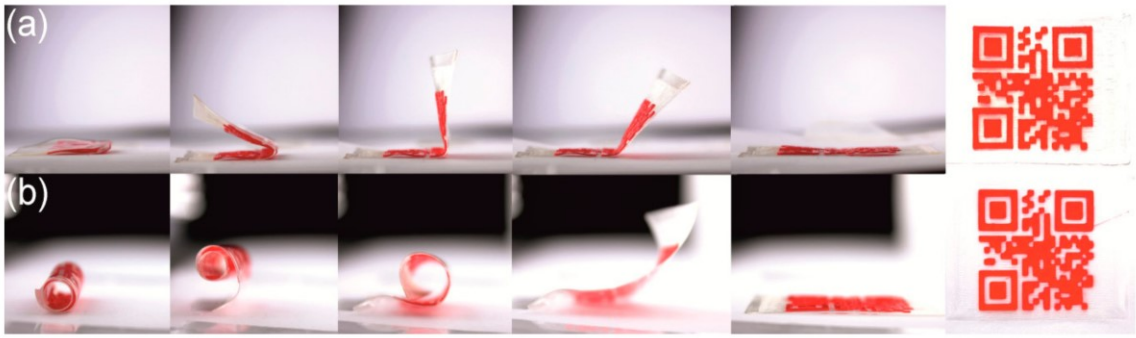

Figure 3.1.12. Thermoresponsiveness of type 2 QR code carriers, which were deformed in a folding approach (**a**) and a rolling approach (**b**): Programmed shapes (left), sequential shape recovery when placed on a 60 °C hot heating plate (images 2–4) and recovered shapes (images 5–6).

Therefore, two of our type 2 QR code carriers were heated to 60 °C, at which the PBA phase of the PEU was completely amorphous. The first sample was folded in the middle (**Figure 3.1.12a),** the other was rolled up (**Figure 3.1.12b**). The fixation of the resulting temporary shapes was then achieved on cooling below the crystallization temperature of the PBA phase. After unloading, the QR code carriers were placed on a heating plate, which had a temperature of 60 °C. In both cases it took about 10 s to finalize shape recovery, which again was accompanied with the restauration of the machine-readable QR codes, thus demonstrating that the concept is not restricted to deformation scenarios like elongation or compression [41,63].

Following another design approach, the dimensions of the QR code carrier were altered by drastically reducing the target substrate thickness from 180 to 15 µm. As a result, a type 3 QR code carrier was obtained (**Figure 3.1.13**).

The production time of the type 3 QR code carrier was about 11 min 30 s, corresponding to the processing time of the type 2 QR code carriers. To illustrate the low thickness, a 50 euro cent coin having a thickness of 2 mm was placed next to it (**Figure 3.1.13a**). As determined in a microscopic measurement, the thickness of the PEU substrate varied from about 7 to 10 µm (**Figure 3.1.13b**).

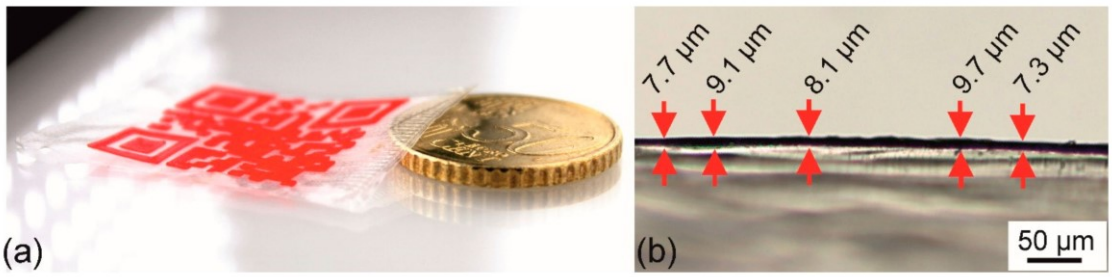

Figure 3.1.13. Type 3 QR code carrier: Illustration of size and thickness in comparison with a 50 euro cent coin, which is characterized by a height of 2 mm (**a**) and image of a light microscopic investigation to estimate the thickness of the QR code carrier (**b**).

It is also worth mentioning that the weight of all QR code carriers described herein was significantly lower compared to earlier generations of prototypes, which were obtained by other processing techniques [41,45,46]. In direct comparison with each other, the introduced type 1 and type 2 QR code carriers were approximately weighing 340 mg while the weight of the type 3 QR code carrier was 100 mg and, thus, significantly lower, qualifying it for applications, in which the costs for transport must be kept under control.

For the purpose of comprehensive consideration, the printing results described herein were compared with those of other printing materials, which were processed by FFF, and additionally with the results of other 3D printing techniques. For convenience, the same approach was followed as by Quinlan et al. [64], who compared polymer-based processes like fused filament fabrication (FFF), stereolithography (SLA), big area additive manufacturing (BAAM), multi-jet fusion (MJF) and selective laser sintering (SLS) with particular emphasis on build rate and layer thickness, the latter of which can be considered as a measure of Z-direction accuracy. The corresponding results are supplied in **Figure 3.1.14**.

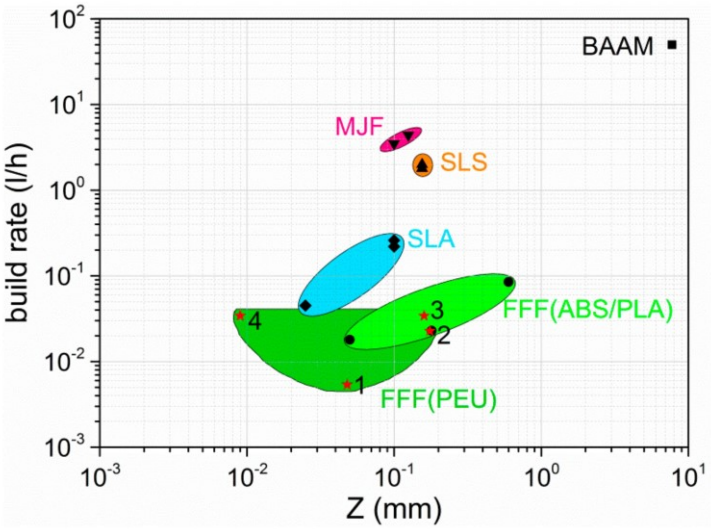

Figure 3.1.14. Build rate versus layer thickness for common additive manufacturing processes. The initial data was extracted from Quinlan et al [64]. The red stars represent data points for the QR code elevation as part of the type 1 QR code carrier (1) and the type 2 QR code carrier (2), while the remaining data points refer to the substrate of the type 1 and type 2 QR code carrier (3) and the type 3 QR code carrier (4).

It can be clearly seen that SLA, BAAM, MJF, and SLS provide higher build rates compared with FFF. In turn, FFF makes it particularly possible to control the layer thickness, namely, the Z-parameter, over quite a wide range as apparent for printing materials like ABS and PLA. However, the data points introduced for the presented QR code carriers do also cover a broad area, which in parts overlaps with the already existing data for FFF. Due to the printing result of the thin layer as evident for the substrate of the type 3 QR code carrier, a data point emerges, defining the lowest value for Z. Interestingly, this reasonably good print resolution could neither be achieved by other groups, working on shape memory polyurethanes using extrusion-based AM techniques [26–30,65,66] nor by other researchers who utilized those 3D printing techniques, which were described by Quinlan et al. [64]. Admittedly, two-photon lithography (2PL) is another AM technology, which was not included in our considerations, but allows obtaining 3D objects, which are characterized by even smaller layer thicknesses of 0.2 to 0.3 µm [67]. Although being particularly advantageous in resolution, the good print results of 2PL are at the expense of the build rate. Therefore, a compromise is needed, which seems to be achievable by FFF, well-balancing the build rate with print resolution and, thus, qualifying it as promising technology to obtain shape memory polymers in entirely new shapes.

3.1.4. Conclusions

Fused filament fabrication is a suitable technique to produce bicolored additively manufactured QR code carriers in a dual extrusion process as demonstrated for a polyester urethane, which was used as model compound. The print resolution both in the XY-plane with regard to the QR code pattern and in Z-direction with reference to the layer height could be controlled by the experimental setup and the print instructions. This way, filigree, well-resolved structures could be obtained. The objects were able to resist strong deformations and characterized by distinct shape memory properties. Even in a multiple cycle experiment no major damage could be witnessed for the print objects. The use of congruence measurements has proven to be a valuable tool to determine the printing accuracy and shape recoverability. Although a higher resolution of the QR code pattern was achieved when using a setup with a 100 µm nozzle, with extending the production time, FFF seems to be a practical method in this scenario as well, which may give access to other technically demanding objects. The main advantages of the new manufacturing process for QR code carriers are that polymer extrusion can be easily controlled, a significantly lower amount of base material is needed, facilitating the fabrication of very thin layers with a thickness below 10 µm, and the use of solvents can be avoided. The latter is of ecological importance. All these aspects emphasize that the novel production process for QR code carriers is not only attractive for research purposes, but also from an economic point of view, not least because the material could be qualified for processing with a commercially available 3D printer. Therefore, FFF could turn out as an enabling technology to realize applications for SMPs in fields like counterfeit-proof marking of goods at risk of plagiarism and supervision of cold chains. Future

challenges consist in shortening the production time without compromising on resolution and using the dimension of time to autonomously manipulate 3D printed objects, which is also known as 4D-printing, thus eliminating the need for programming.

Author Contributions: Conceptualization: T.P. and H.A.; formal analysis: D.C., S.S., and H.A.; funding acquisition: T.P. and H.A.; investigation: D.C. and S.S.; methodology: D.C. and S.S.; project administration: T.P. and H.A.; supervision: T.P.; validation: D.C.; visualization: D.C. and S.S.; writing—original draft: D.C., T.P., and S.S.; writing—review and editing: T.P.

Funding: This research was funded by Fraunhofer High Performance Center for Functional Integration in Materials, grant number 630039, and by Fraunhofer Excellence Cluster "Programmable Materials", grant number 630527.

Acknowledgments: This work was supported as Fraunhofer High Performance Center for Functional Integration in Materials (project 630039). T.P., S.S., and H.A. also acknowledge support by the Fraunhofer Excellence Cluster "Programmable Materials" under project 630527. T.P. wishes to thank the European Regional Development Fund for financing a large part of the laboratory equipment (project 85007031). The authors thank Chris Eberl (Fraunhofer IWM) for fruitful discussions on two-photon lithography. Tobias Rümmler is kindly acknowledged for carrying out the DMA measurements and Katrin Hohmann for light microscopic investigations.

Conflicts of Interest: The authors declare no conflict of interest.

3.1.5. References

1. Wendel, B.; Rietzel, D.; Kühnlein, F.; Feulner, R.; Hülder, G.; Schmachtenberg, E. Additive Processing of Polymers. *Macromol. Mater. Eng.* **2008**, *293*, 799–809, doi:10.1002/mame.200800121.
2. Mohamed, O.A.; Masood, S.H.; Bhowmik, J.L. Optimization of fused deposition modeling process parameters: a review of current research and future prospects. *Adv. Manuf.* **2015**, *3*, 42–53, doi:10.1007/s40436-014-0097-7.
3. Ligon, S.C.; Liska, R.; Stampfl, J.; Gurr, M.; Mülhaupt, R. Polymers for 3D Printing and Customized Additive Manufacturing. *Chem. Rev.* **2017**, *117*, 10212–10290, doi:10.1021/acs.chemrev.7b00074.
4. Lee, A.Y.; An, J.; Chua, C.K. Two-Way 4D Printing: A Review on the Reversibility of 3D-Printed Shape Memory Materials. *Engineering* **2017**, *3*, 663–674, doi:10.1016/J.ENG.2017.05.014.
5. Boydston, A.J.; Cao, B.; Nelson, A.; Ono, R.J.; Saha, A.; Schwartz, J.J.; Thrasher, C.J. Additive manufacturing with stimuli-responsive materials. *J. Mater. Chem. A* **2018**, *6*, 20621–20645, doi:10.1039/C8TA07716A.
6. Lendlein, A.; Kelch, S. Shape-Memory Polymers. *Angew. Chem. Int. Ed.* **2002**, *41*, 2034–2057, doi:10.1002/1521-3773(20020617)41:12<2034:AID-ANIE2034>3.0.CO;2-M.
7. Dietsch, B.; Tong, T. A Review - Features and Benefits of Shape Memory Polymers (SMPs). *J. Adv. Mater.* **2007**, *39*, 3–12.
8. Liu, C.; Qin, H.; Mather, P.T. Review of progress in shape-memory polymers. *J. Mater. Chem.* **2007**, *17*, 1543–1558, doi:10.1039/b615954k.
9. Ratna, D.; Karger-Kocsis, J. Recent advances in shape memory polymers and composites: a review. *J Mater Sci* **2008**, *43*, 254–269, doi:10.1007/s10853-007-2176-7.

10. Pretsch, T. Review on the Functional Determinants and Durability of Shape Memory Polymers. *Polymers* **2010**, *2*, 120–158, doi:10.3390/polym2030120.
11. Sun, L.; Huang, W.M.; Ding, Z.; Zhao, Y.; Wang, C.C.; Purnawali, H.; Tang, C. Stimulus-responsive shape memory materials: A review. *Mater. Des.* **2012**, *33*, 577–640, doi:10.1016/j.matdes.2011.04.065.
12. Kim, B.K.; Lee, S.Y.; Xu, M. Polyurethanes having shape memory effects. *Polymer* **1996**, *37*, 5781–5793, doi:10.1016/S0032-3861(96)00442-9.
13. Li, F.; Zhang, X.; Hou, J.; Xu, M.; Luo, X.; Ma, D.; Kim, B.K. Studies on thermally stimulated shape memory effect of segmented polyurethanes. *J. Appl. Polym. Sci.* **1997**, *64*, 1511–1516, doi:10.1002/(SICI)1097-4628(19970523)64:8<1511:AID-APP8>3.0.CO;2-K.
14. Lee, B.S.; Chun, B.C.; Chung, Y.-C.; Sul, K.I.; Cho, J.W. Structure and Thermomechanical Properties of Polyurethane Block Copolymers with Shape Memory Effect. *Macromolecules* **2001**, *34*, 6431–6437, doi:10.1021/ma001842l.
15. Ji, F.L.; Hu, J.L.; Li, T.C.; Wong, Y.W. Morphology and shape memory effect of segmented polyurethanes. Part I: With crystalline reversible phase. *Polymer* **2007**, *48*, 5133–5145, doi:10.1016/j.polymer.2007.06.032.
16. Pereira, I.M.; Oréfice, R.L. The morphology and phase mixing studies on poly(ester–urethane) during shape memory cycle. *J Mater Sci* **2010**, *45*, 511–522, doi:10.1007/s10853-009-3969-7.
17. Huang, W.M.; Yang, B.; Zhao, Y.; Ding, Z. Thermo-moisture responsive polyurethane shape-memory polymer and composites: a review. *J. Mater. Chem.* **2010**, *20*, 3367–3381, doi:10.1039/b922943d.
18. Wang, W.; Jin, Y.; Ping, P.; Chen, X.; Jing, X.; Su, Z. Structure Evolution in Segmented Poly(ester urethane) in Shape-Memory Process. *Macromolecules* **2010**, *43*, 2942–2947, doi:10.1021/ma902781e.
19. Pretsch, T.; Müller, W.W. Shape memory poly(ester urethane) with improved hydrolytic stability. *Polym. Degrad. Stab.* **2010**, *95*, 880–888, doi:10.1016/j.polymdegradstab.2009.12.020.
20. Müller, W.W.; Pretsch, T. Hydrolytic aging of crystallizable shape memory poly(ester urethane): Effects on the thermo-mechanical properties and visco-elastic modeling. *Eur. Polym. J.* **2010**, *46*, 1745–1758, doi:10.1016/j.eurpolymj.2010.05.004.
21. Petchsuk, A.; Klinsukhon, W.; Sirikittikul, D.; Prahsarn, C. Parameters affecting transition temperatures of poly(lactic acid-co-polydiols) copolymer-based polyester urethanes and their shape memory behavior. *Polym. Adv. Technol.* **2012**, *23*, 1166–1173, doi:10.1002/pat.2017.
22. Bothe, M.; Emmerling, F.; Pretsch, T. Poly(ester urethane) with Varying Polyester Chain Length: Polymorphism and Shape-Memory Behavior. *Macromol. Chem. Phys.* **2013**, *214*, 2683–2693, doi:10.1002/macp.201300464.
23. Liu, W.; Zhang, R.; Huang, M.; Dong, X.; Xu, W.; Wang, Y.; Hu, G.-H.; Zhu, J. Synthesis and shape memory property of segmented poly(ester urethane) with poly(butylene 1,4-cyclohexanedicarboxylate) as the soft segment. *RSC Adv.* **2016**, *6*, 95527–95534, doi:10.1039/C6RA16325D.
24. Ren, H.; Mei, Z.; Chen, S.; Zhuo, H.; Chen, S.; Yang, H.; Zuo, J.; Ge, Z. A new strategy for designing multifunctional shape memory polymers with amine-containing polyurethanes. *J Mater Sci* **2016**, *51*, 9131–9144, doi:10.1007/s10853-016-0166-3.
25. Mirtschin, N.; Pretsch, T. Programming of One- and Two-Step Stress Recovery in a Poly(ester urethane). *Polymers* **2017**, *9*, 98 (12pp), doi:10.3390/polym9030098.
26. Hendrikson, W.J.; Rouwkema, J.; Clementi, F.; van Blitterswijk, C.A.; Farè, S.; Moroni, L. Towards 4D printed scaffolds for tissue engineering: exploiting 3D shape memory polymers to deliver time-controlled stimulus on cultured cells. *Biofabrication* **2017**, *9*, 31001, doi:10.1088/1758-5090/aa8114.
27. Raasch, J.; Ivey, M.; Aldrich, D.; Nobes, D.S.; Ayranci, C. Characterization of polyurethane shape memory polymer processed by material extrusion additive manufacturing. *Additive Manufacturing* **2015**, *8*, 132–141, doi:10.1016/j.addma.2015.09.004.
28. Yang, Y.; Chen, Y.; Wei, Y.; Li, Y. 3D printing of shape memory polymer for functional part fabrication. *Int J Adv Manuf Technol* **2016**, *84*, 2079–2095, doi:10.1007/s00170-015-7843-2.
29. Villacres, J.; Nobes, D.; Ayranci, C. Additive manufacturing of shape memory polymers: effects of print orientation and infill percentage on mechanical properties. *Rapid Prototyping Journal* **2018**, *24*, 744–751, doi:10.1108/RPJ-03-2017-0043.
30. Monzón, M.D.; Paz, R.; Pei, E.; Ortega, F.; Suárez, L.A.; Ortega, Z.; Alemán, M.E.; Plucinski, T.; Clow, N. 4D printing: processability and measurement of recovery force in shape memory polymers. *Int J Adv Manuf Technol* **2017**, *89*, 1827–1836, doi:10.1007/s00170-016-9233-9.
31. Jung, Y.C.; Cho, J.W. Application of shape memory polyurethane in orthodontic. *J. Mater. Sci: Mater. Med.* **2010**, *21*, 2881–2886, doi:10.1007/s10856-008-3538-7.

32. Nardo, L.D.; Bertoldi, S.; Tanzi, M.C.; Haugen, H.J.; Farè, S. Shape memory polymer cellular solid design for medical applications. *Smart Mater. Struct.* **2011**, *20*, 035004 (12pp), doi:10.1088/0964-1726/20/3/035004.
33. Hu, J.; Meng, H.; Li, G.; Ibekwe, S.I. A review of stimuli-responsive polymers for smart textile applications. *Smart Mater. Struct.* **2012**, *21*, 053001 (23pp), doi:10.1088/0964-1726/21/5/053001.
34. Ahmad, M.; Luo, J.; Miraftab, M. Feasibility study of polyurethane shape-memory polymer actuators for pressure bandage application. *Sci. Technol. Adv. Mater.* **2012**, *13*, 015006 (7pp), doi:10.1088/1468-6996/13/1/015006.
35. Liu, Y.; Du, H.; Liu, L.; Leng, J. Shape memory polymers and their composites in aerospace applications: a review. *Smart Mater. Struct.* **2014**, *23*, 023001 (22pp), doi:10.1088/0964-1726/23/2/023001.
36. Pilate, F.; Toncheva, A.; Dubois, P.; Raquez, J.-M. Shape-memory polymers for multiple applications in the materials world. *Eur. Polym. J.* **2016**, *80*, 268–294, doi:10.1016/j.eurpolymj.2016.05.004.
37. Zhao, Q.; Qi, H.J.; Xie, T. Recent progress in shape memory polymer: New behavior, enabling materials, and mechanistic understanding. *J. Prog. Polym. Sci.* **2015**, *49-50*, 79–120, doi:10.1016/j.progpolymsci.2015.04.001.
38. Wang, K.; Strandman, S.; Zhu, X.X. A mini review: Shape memory polymers for biomedical applications. *Front. Chem. Sci. Eng.* **2017**, *11*, 143–153, doi:10.1007/s11705-017-1632-4.
39. Patil, D.; Song, G. A review of shape memory material's applications in the offshore oil and gas industry. *Smart Mater. Struct.* **2017**, *26*, 093002 (17pp), doi:10.1088/1361-665X/aa7706.
40. Hosseini, S.M.; Rihani, R.; Batchelor, B.; Stiller, A.M.; Pancrazio, J.J.; Voit, W.E.; Ecker, M. Softening Shape Memory Polymer Substrates for Bioelectronic Devices With Improved Hydrolytic Stability. *Front. Mater.* **2018**, *5*, 12pp, doi:10.3389/fmats.2018.00066.
41. Pretsch, T.; Ecker, M.; Schildhauer, M.; Maskos, M. Switchable information carriers based on shape memory polymer. *J. Mater. Chem.* **2012**, *22*, 7757, doi:10.1039/c2jm16204k.
42. Ecker, M.; Pretsch, T. Durability of switchable QR code carriers under hydrolytic and photolytic conditions. *Smart Mater. Struct.* **2013**, *22*, 094005 (10pp), doi:10.1088/0964-1726/22/9/094005.
43. Li, W.; Liu, Y.; Leng, J. Programmable and Shape-Memorizing Information Carriers. *ACS Appl. Mater. Interfaces* **2017**, *9*, 44792–44798, doi:10.1021/acsami.7b13284.
44. Fritzsche, N.; Pretsch, T. Programming of Temperature-Memory Onsets in a Semicrystalline Polyurethane Elastomer. *Macromolecules* **2014**, *47*, 5952–5959, doi:10.1021/ma501171p.
45. Ecker, M.; Pretsch, T. Multifunctional poly(ester urethane) laminates with encoded information. *RSC Adv* **2014**, *4*, 286–292, doi:10.1039/C3RA45651J.
46. Ecker, M.; Pretsch, T. Novel design approaches for multifunctional information carriers. *RSC Adv* **2014**, *4*, 46680–46688, doi:10.1039/C4RA08977D.
47. Mirtschin, N.; Pretsch, T. Designing temperature-memory effects in semicrystalline polyurethane. *RSC Adv.* **2015**, *5*, 46307–46315, doi:10.1039/C5RA05492C.
48. QR Code Generator – create QR codes for free (Logo, T-Shirt, vCard, EPS). http://goqr.me/ (accessed on 19 March 2019).
49. ISO/IEC 18004:2006. https://www.iso.org/standard/43655.html (accessed on 19 March 2019).
50. AutoCAD For Mac & Windows | CAD Software | Autodesk. https://www.autodesk.eu/products/autocad/overview (accessed on 19 March 2019).
51. Ultimaker Cura: Advanced 3D printing software, made accessible | Ultimaker. https://ultimaker.com/en/products/ultimaker-cura-software (accessed on 19 March 2019).
52. Ultimaker 3 specifications | Ultimaker. https://ultimaker.com/en/products/ultimaker-3/specifications (accessed on 19 March 2019).
53. Scanning Probe Microscopy. https://www.digitalsurf.com/software-solutions/scanning-probe-microscopy/ (accessed on 19 March 2019).
54. Free Microscope Software ZEN lite from ZEISS Microscopy. https://www.zeiss.com/microscopy/int/products/microscope-software/zen-lite.html (accessed on 19 March 2019).
55. ImageJ. https://imagej.nih.gov/ij/ (accessed on 29 March 2019).
56. ParaView. https://www.paraview.org/ (accessed on 29 March 2019).
57. SamMobile. Optical Reader 4.4.07. https://www.sammobile.com/apk/optical-reader/optical-reader-4-4-07/ (accessed on 19 March 2019).
58. Fuenmayor, E.; Forde, M.; Healy, A.V.; Devine, D.M.; Lyons, J.G.; McConville, C.; Major, I. Material Considerations for Fused-Filament Fabrication of Solid Dosage Forms. *Pharmaceutics* **2018**, *10*, 27pp, doi:10.3390/pharmaceutics10020044.

59. Chen, S.; Hu, J.; Liu, Y.; Liem, H.; Zhu, Y.; Meng, Q. Effect of molecular weight on shape memory behavior in polyurethane films. *Polym. Int.* **2007**, *56*, 1128–1134, doi:10.1002/pi.2248.
60. Chen, S.; Hu, J.; Liu, Y.; Liem, H.; Zhu, Y.; Liu, Y. Effect of SSL and HSC on morphology and properties of PHA based SMPU synthesized by bulk polymerization method. *J. Polym. Sci. B Polym. Phys.* **2007**, *45*, 444–454, doi:10.1002/polb.21046.
61. Petrović, Z.S.; Milić, J.; Zhang, F.; Ilavsky, J. Fast-Responding Bio-Based Shape Memory Thermoplastic Polyurethanes. *Polymer* **2017**, *121*, 26–37, doi:10.1016/j.polymer.2017.05.072.
62. Takahashi, T.; Hayashi, N.; Hayashi, S. Structure and properties of shape-memory polyurethane block copolymers. *J. Appl. Polym. Sci.* **1996**, *60*, 1061–1069, doi:10.1002/(SICI)1097-4628(19960516)60:7<1061:AID-APP18>3.0.CO;2-3.
63. Ecker, M.; Pretsch, T. Freely configurable Functionalization Tool for switchable Information Carriers. In *Materials challenges and testing for manufacturing, mobility, biomedical applications and climate*; Udomkichdecha, W., Böllinghaus, T., Manonukul, A., Lexow, J., Eds.; Springer: New York, 2014; pp 25–35, ISBN 978-3-319-11339-5.
64. Quinlan, H.E.; Hasan, T.; Jaddou, J.; Hart, A.J. Industrial and Consumer Uses of Additive Manufacturing: A Discussion of Capabilities, Trajectories, and Challenges. *J. Indu. Ecol.* **2017**, *21*, S15-S20, doi:10.1111/jiec.12609.
65. Garces, I.T.; Aslanzadeh, S.; Boluk, Y.; Ayranci, C. Effect of Moisture on Shape Memory Polyurethane Polymers for Extrusion-Based Additive Manufacturing. *Materials (Basel)* **2019**, *12, doi:*10.3390/ma12020244.
66. Kashyap, D.; Kishore Kumar, P.; Kanagaraj, S. 4D printed porous radiopaque shape memory polyurethane for endovascular embolization. *Additive Manufacturing* **2018**, *24*, 687–695, doi:10.1016/j.addma.2018.04.009.
67. Berwind, M.F.; Kamas, A.; Eberl, C. A Hierarchical Programmable Mechanical Metamaterial Unit Cell Showing Metastable Shape Memory. *Adv. Eng. Mater.* **2018**, *20*, 1800771 (6pp), doi:10.1002/adem.201800771.

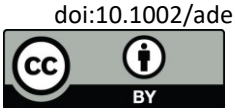

© 2019 by the authors. Licensee MDPI, Basel, Switzerland. This article is an open access article distributed under the terms and conditions of the Creative Commons Attribution (CC BY) license (http://creativecommons.org/licenses/by/4.0/).

Chapter 3.2:
Influence of Print Orientation on Shape Memory- and Mechanical- Properties After Fused Filament Fabrication

Chapter 3.2: Influence of Print Orientation on Shape Memory- and Mechanical- Properties After Fused Filament Fabrication

3.2.1. Introduction

Shape memory polymers (SMPs) are smart materials that can retain a temporary shape attained through a thermomechanical treatment, also known as programming [1–6]. In the case of thermoresponsive SMPs, the exposure to an external stimulus, like heat, recovers the initial, permanent shape [7–9]. The permanent shape of the SMP is determined by conventional processing techniques, like injection molding, extrusion, and additive manufacturing (AM) [10–16]. In the last few decades, thermoplastic polyurethanes belonged to the most researched SMPs [17–30].

Fused filament fabrication (FFF) is widely used amidst various AM methods due to its cost-effectiveness and short manufacturing times [31–33]. Recently, researchers were able to process SMPs using FFF [6,34–40]. For instance, our group utilized the dual-material printing technique to manufacture high-contrast information carriers with quick response (QR) machine-readable codes employing non-dyed and dyed thermoplastic polyester urethane (PEU) [6]. Our group also showed that a small cuboidal elevation part of the QR code carrier was found to have exceeded the CAD model by just 40 µm on utilizing a 100 µm nozzle, thereby demonstrating a higher print resolution. In contrast, Villacres et al. used the amorphous polyurethane DiAPLEX® MM 4520 as base material to study the influence of geometrical parameters like print orientation and infill percentage upon the mechanical properties of tensile bars obtained from FFF [38]. The contribution showed that the higher the infill percentage, the higher the elastic modulus. On the other hand, the ultimate tensile strength was highest when the print orientation was parallel to the direction of tensile stretching. Similarly, the group studied the bending-related shape memory behavior of samples with different print orientations [41]. The results demonstrated that the shape recovery force of the samples was highest when the loading direction was in the direction of the printing pattern.

Here the investigation focuses on how far the mechanical and shape recovery behavior of FFF printed samples made from semicrystalline PEUs can be controlled by print orientation when applying a tensile deformation during programming. The selection of the commercially available semicrystalline PEU Desmopan® DP 2795A SMP was primarily due to its excellent shape memory properties. Moreover, the ability to be processed via extrusion and FFF (**Chapter 3.1**) [6]. After processing, the obtained filaments were used for FFF to fabricate tensile bars of either horizontal or vertical strand orientation. Once characterized, the results were compared with standard tensile bars punched out from injection molded plaques.

3.2.2. Results and Discussion

The Desmopan® DP 2795A SMP is a poly(1,4-butylene adipate) (PBA)-based polyester urethane (PEU) that showed good printing results upon processing via FFF in our previous work (**Chapter 3.1**) [6,30]. The PBA phase exhibits a melting transition (T_m) peak at ≈ 42 °C in the DSC thermogram, with the onset and offset of the melting temperature at about 33 °C and 55 °C, respectively [6]. As the melting transition is above room temperature, the PEU can be applied advantageously in systems like automotive transmissions, in-door safety appliances, and others. As the quality of filament is a crucial requirement for achieving seamless print results, the primary requirement is to have a homogenous filament with the appropriate diameter and low error tolerance. For this reason, extrusion processing is first carried out to produce virgin PEU filaments, which are later characterized by a diameter of 2.85 ± 0.05 mm. Subsequently, the tensile bars were designed and sliced using the printing parameters from our previous literature (**Chapter 3.1**) [6] (**Table 3.2.2**) and modified by RepetierHost software [42]. The GCODE was modified to manipulate the strand deposition printing pattern to obtain either horizontally or vertically oriented tensile bars. The altered GCODE of the tensile bars was simulated for visualization, and the errors were rectified. Afterward, the files were used for FFF. The resulting three-dimensional (3D) printed parts and their quality control was investigated using confocal microscopy, as depicted in **Figure 3.2.1**.

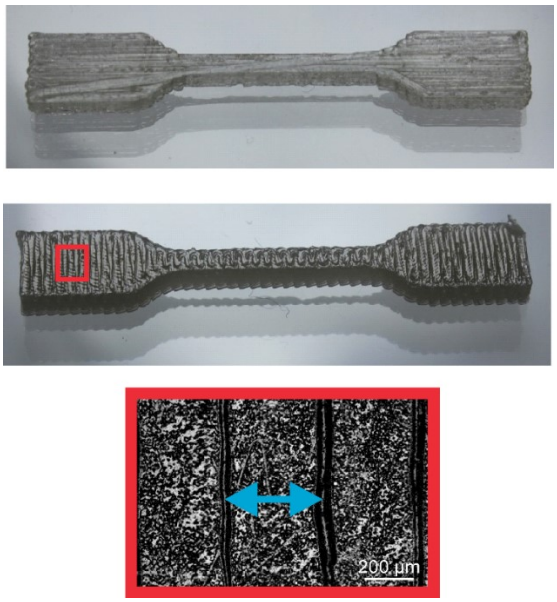

Figure 3.2.1. Tensile bars of PEU are printed in horizontal- (topmost) and vertical- (middle) orientation. The inset (bottom) shows the enlarged image of a vertically oriented tensile bar (middle) as investigated with a confocal microscope (red box).

From **Figure 3.2.1,** it is noticeable to mention that the printed parts showed very high dimensional accuracy compared to their virtual design. In order to evaluate the quality of the strand deposition, the surface of the tensile bar (red box) was closely examined using a confocal microscope (**Figure 3.2.1** bottom image). A closer look at the tensile bar showed that

each deposited strand has a width of about 400 µm. The width of the strand directly coincides with the diameter of the nozzle opening, and it can also be seen that the strands were free from air bubbles. Furthermore, no surface damage or distortion was observed. This indicates that the selected printing parameters were ideally suited.

Once the excellent quality of the 3D-printed parts was proven, a mechanical characterization was carried out on the tensile bars, printed in the horizontal or vertical orientation, and compared to the behavior of injection-molded specimens (**Figure 3.2.2**).

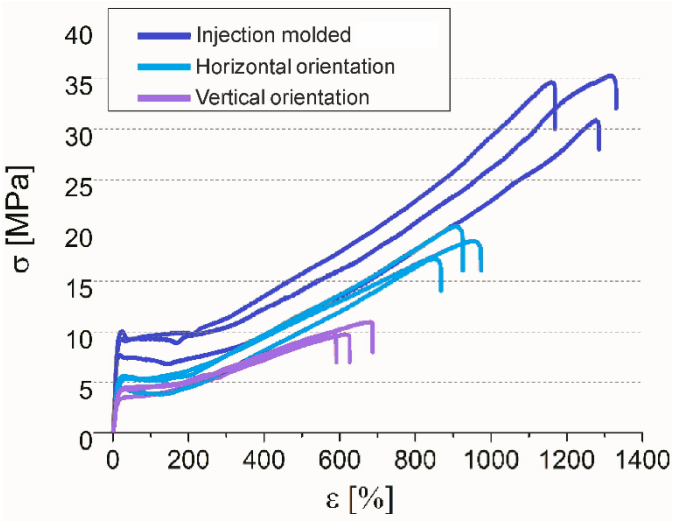

Figure 3.2.2. Mechanical characterization of PEU showing the evolution of engineering stress-strain for specimens, which were punched out from an injection molded plaque (dark blue), and of three tensile bars, each additively manufactured in horizontal (blue) and vertical preferential orientation (violet). The tensile experiments were carried out at 23 °C with an initial strain rate of 1%·min^{-1} until 5% of strain was reached and continued with 2000%·min^{-1} until rupture occurred.

From the engineering stress-strain diagram, the averaged Young's modulus of the tensile bars was determined. Among the three specimens, the injection-molded plaque-punched tensile bars showed the highest Young's modulus of 56.3 ± 18.2 MPa, followed by the vertical tensile bars with 26.5 ± 2.0 MPa, and the horizontal tensile bars with 19.6 ± 14.4 MPa. In the case of the yield point, the strain value was observed to be 21.5 ± 2.5%, 27.1 ± 4.2%, and 29.4 ± 0.9%, with corresponding stresses at 9.0 ± 1.2 MPa, 5.2 ± 0.6 MPa, and 4.1 ± 0.5 MPa, for injection molded plaque punched, horizontally and vertically printed tensile bars, respectively (**Figure 3.2.2**). In any case, further increase of the load resulted in necking and strain softening first, followed by strain hardening as accompanied by an increase in stress, culminating in sample rupture at strains of 1262.4 ± 83.4%, 922.6 ± 52.9%, and 635.0 ± 48.9% for injection-molded specimens, horizontal and vertical tensile bars, respectively. The material behavior can be explained by the coexistence of two types of PBA segments, at which, depending on temperature, one part was highly flexible and amorphous. At the same time, the other was more rigid and crystalline [27]. A progressive conversion from amorphous to crystalline segments occurred during deformation. The assumption was supported by a whitish coloring of the tensile bars and is associated with the crystallization of hitherto amorphous PBA. The

mechanical properties of the 3D printed samples were inferior compared to the injection-molded ones, which was expected due to the layer-by-layer manufacturing method [43–45]. The FFF-processed semicrystalline PEU behaved similarly to other horizontal and vertically oriented tensile bars, where higher mechanical properties were observed for horizontal orientation than the vertically oriented tensile bars [44]. Some of FFF processed materials in vertical and horizontal orientations are acrylonitrile butadiene styrene (ABS) [46,47], ABS-carbon nanotubes composite [48], polycarbonate-ABS blends [45], polypropylene [43,49,50], and polyethylene glycol diamines [51].

Having the good mechanical properties of the PEU in mind, a method for programming and triggering of one-way (1W) shape memory effect (SME) was developed in line with the thermal properties of the PEU (**see chapter 3.1**) [6]. For this purpose, cyclic thermomechanical measurements (CTMs) were conducted (**Figure 3.2.3**). The shape memory properties were analyzed using **Equations 3.2.1**, **3.2.2**, and **3.2.3**, summarized in **Table 3.2.1**.

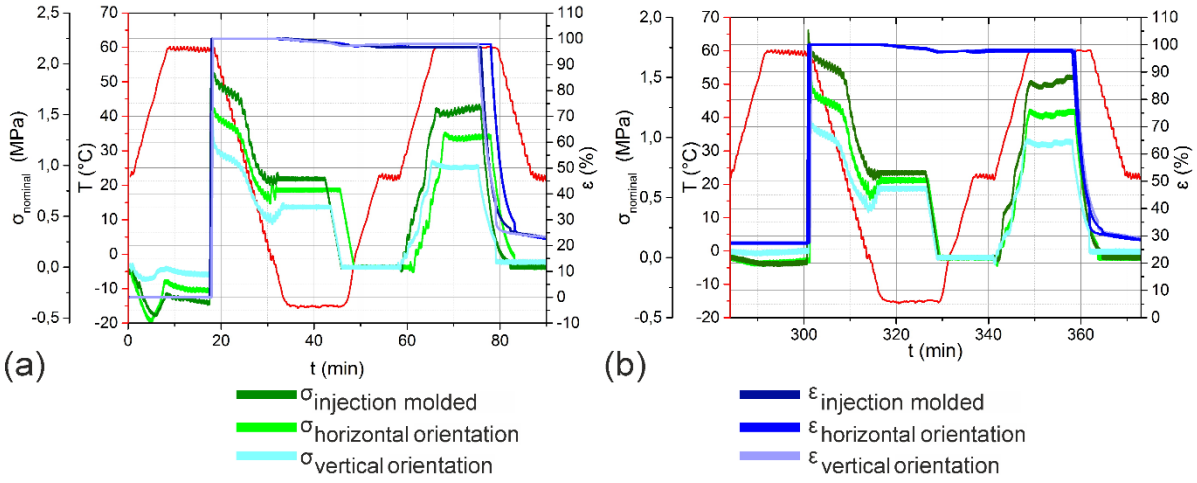

Figure 3.2.3. Cyclic thermomechanical measurements of tensile bars were obtained by punching from an injection molded plaque (dark green and dark blue), FFF in a horizontal direction (light green and blue), and FFF in a vertical direction (cyan and violet). Evolution of stress (σ), strain (ε), and temperature (T in °C, red line) against time for the first (b) and fourth measurement cycle (b).

From **Figure 3.2.3** and **Table 3.2.1**, it can be deduced that the shape memory properties of injection molded or differently additively manufactured tensile bars are very similar. In detail, the strain fixity ratio was most pronounced for the 3D printed samples, with about 98% for horizontal and vertical samples. In contrast, the injection-molded sample had a respective value of about 97%. The strain recovery ratio increased from ≈96% to ≈99% from the first to the fourth cycle for all the investigated samples. In contrast, the total strain recovery ratio decreased from 75% to 71% from the first to the fourth cycle. The main difference among the samples was the recovery stresses when triggering the SME; namely, 1.5 MPa for an injection molded tensile bar, 1.25 MPa for an additively manufactured horizontal tensile bar, and 1 MPa for an additively manufactured vertical tensile bar. From this, it is understood that the mechanical properties and the recovery stresses followed the same trend. The evolution in recovery stress of the FFF samples is in line with the one verified by Villacres et al. [41]. The

recovery stress and tensile strength are highest when the direction of strand orientation is parallel to the direction of the load acting [44]. From this, it is clear that it can alter the properties by introducing preferred orientations. By changing the design, it is now necessary to make the best possible use of the orientation effects to open up new applications.

Table 3.2.1. Overview of the shape memory properties quantified in cyclic thermomechanical measurements for different tensile bars.

Sample	Shape memory properties	Cycle			
		1	2	3	4
		[%]			
Injection molded	Strain fixity ratio	96.9	97.0	97.4	97.6
	Strain recovery ratio	95.9	98.1	98.6	98.9
	Total strain recovery ratio	74.2	72.8	71.8	71.5
Horizontally printed	Strain fixity ratio	97.9	98.2	98.0	98.2
	Strain recovery ratio	94.0	97.8	98.8	98.9
	Total strain recovery ratio	74.0	72.4	71.5	71.2
Vertically printed	Strain fixity ratio	98.0	98.2	98.1	98.1
	Strain recovery ratio	96.1	98.5	98.6	98.9
	Total strain recovery ratio	75.1	72.5	71.5	71.3

3.2.3. Conclusions

Chapter 3.2 shows that the FFF is a powerful AM technique to gain control over mechanical properties and, more importantly, shape recovery stress without using another shape memory polymer. The study also unravels that the recovery stress and tensile strength are highest when the direction of strand orientation is parallel to the direction of loading in the course of programming and weakest in the perpendicular direction. From this work, it was also understood that the orientation effects brought via FFF for altering shape recovery stresses and mechanical properties for semicrystalline SMPs, where likewise the amorphous SMPs. This ability to manipulate the mechanical properties and shape recovery stresses may be helpful for product developers and researchers to locally optimize or customize parts or products according to the respective application or requirement.

3.2.4. Experimental Section

Materials: The polyester urethane (PEU) Desmopan® DP 2795A SMP from Covestro Deutschland AG (Leverkusen, Germany) was chosen as the model compound and used as received in the form of granules. Further information regarding the PEU's material, thermal and mechanical properties is given in previous publications [30,52,53].

Extrusion: The PEU granulate was dried at 110 °C in a Binder vacuum drying chamber VDL 53 from Binder GmbH (Tuttlingen, Germany) to remove water and avoid bubble formation

when extruding filaments at a later stage. The thermal pre-treatment was finalized after 150 min. Subsequently, the pellets were fed into an extrusion line to produce filaments-

The individual units of the extrusion line were put together. They were volumetric material feeding system Color-exact 1000 from Plastic Recycling Machinery (Zhangjiagang City, China), a Leistritz twin screw extruder MICRO 18 GL from Leistritz AG (Nürnberg, Germany), characterized by seven heating zones, and a screw length of 600 mm, a conveyor belt, a water bath and a filament winder from Brabender GmbH and Co. KG (Duisburg, Germany). The temperatures of the individual heating zones of the extruder were 180, 185, 190, 195, 200, 190, and 190 °C. The screw speed of the extruder was set to 77 rpm. The PEU granulates were processed without additives. The filament diameter evolution was manually detected at regular intervals using a Vernier caliper from Fowler High Precision (Auburndale, FL, USA) to evaluate the filaments' quality.

Virtual Design: The virtual designs of the type 5B tensile bars [54], which were used for the evaluation of the mechanical and shape memory properties, were designed by using AutoCAD from Autodesk, Inc. (San Rafael, CA, USA).

Fused Filament Fabrication (3D Printing): Fused filament fabrication was used to produce the 3D printed models. The experiments were carried out using the commercially available 3D printer Ultimaker 3 from Ultimaker B. V. (Geldermalsen, The Netherlands). The manufacturer provides an XYZ resolution for Ultimaker 3 of 12.5, 12.5, and 2.5 µm, defining the slightest movement the 3D printer can make concerning the XY plane and in the Z direction. The Ultimaker build plate manual leveling calibration method was carried out before the beginning of each experiment to calibrate the print bed. Therefore, a calibration card with a thickness of about 170 µm was used. The process included a rough leveling of the build plate followed by a fine leveling. The calibration card achieved fine leveling, at which the knurled nut was adjusted at the rear center, front left, and front right of the build plate until slight friction occurred when sliding the card between the built plate and print head.

The most relevant settings for the 3D printing processes are listed in **Table 3.2.2**.

Table 3.2.2. Printing instructions for Ultimaker 3 to produce the different prototypes of 3D printed objects.

Specifications	Values
Diameter of the nozzle (µm)	400
Temperature of the nozzle (°C)	225
Speed of print head (mm × s^{-1})	50
Build platform temperature (°C)	60
Layer height (µm)	150

Characterization of Mechanical Properties: The mechanical behavior of the PEU was investigated in tensile tests using the universal testing machine Criterion Model 43 from MTS Systems Corporation (Eden Prairie, MN, USA). The device was equipped with a 500 N load

cell. As obtained from FFF, the measurements were carried out on dog-bone-shaped tensile bars of type 5B [54]. While stretching, the velocity of 1% x min^{-1} was kept constant until a total strain of 5% was achieved to enable a more precise determination of Young's modulus before the specimen was further elongated with a velocity of 100% x min^{-1} until failure occurred. Every tensile test was carried out three times at ambient temperature.

Shape Memory Effect (SME): The programming of the tensile bars was carried out with an MTS Criterion universal testing machine from MTS Systems Corporation (Eden Prairie, MN, USA). The device was operated with a temperature chamber controlled by a Eurotherm temperature controller unit. Two heating elements were located at the back of the chamber. Liquid nitrogen from a Dewar vessel was fed into the chamber under a pressure of 1.3 bar as an essential prerequisite for cooling. At the beginning of programming, the tensile bars were clamped with a clamp length of 10 mm. The chamber was then heated to 60 °C, and a tensile strain (ε_m) of 100% was applied for tensile bars using a loading rate of 100 mm x min^{-1}. The tensile bars were cooled to –15 °C, while the clamp distance remained constant. After 10 min, the sample was unloaded, and the chamber was heated to 23 °C. While maintaining the new strain constant (ε_u), the tensile bars were heated to 60 °C to trigger the SME and held for 10 min before unloading the generated recovery stress. Once cooled back to 23°C and held for 5 min, the CTM measurement was completed by measuring the recovered specimen strain (ε_p). The CTM was repeated for four more cycles. A heating and cooling rate of 5 °C x min^{-1} was used for the whole experiment.

The shape memory properties were determined with the following formulas:

$$\text{Strain fixity ratio}, R_f(\text{N}) = \frac{\varepsilon_u(N)}{\varepsilon_m} \times\ 100\% \qquad Equation\ 3.2.1$$

$$\text{Strain recovery ratio}, R_r(\text{N}) = \frac{\varepsilon_m - \varepsilon_p(N)}{\varepsilon_m - \varepsilon_p(N-1)} \times 100\% \qquad Equation\ 3.2.2$$

$$\text{Total strain recovery ratio}, R_{r,tot}(\text{N}) = \frac{\varepsilon_m - \varepsilon_p(N)}{\varepsilon_m} \times 100\% \qquad Equation\ 3.2.3$$

Where, ε_u = the fixed strain after programming

ε_p = the residual strain after shape recovery

N = the number of cycles

Characterization of Print Quality: Topography measurements were performed on tensile bars using a FocusCam LV150 confocal microscope from Confovis GmbH (Jena, Germany), equipped with an objective lens of 5×/0.15 N.A. Any time, the sample was illuminated with a ring light. The data recorded by the focus variation microscope was evaluated with the software MountainsMap® imaging topography 7.4 from Digital Surf (Besançon, France) [55].

3.2.5. Reference

1. Liu, C.; Qin, H.; Mather, P.T. Review of progress in shape-memory polymers. *J. Mater. Chem.* **2007**, *17*, 1543, doi:10.1039/b615954k.

2. Dietsch, B.; Tong, T. A review-: Features and benefits of shape memory polymers (smps). *Journal of advanced materials* **2007**, *39*, 3–12.
3. Ratna, D.; Karger-Kocsis, J. Recent advances in shape memory polymers and composites: a review. *J Mater Sci* **2008**, *43*, 254–269, doi:10.1007/s10853-007-2176-7.
4. Pretsch, T. Review on the Functional Determinants and Durability of Shape Memory Polymers. *Polymers* **2010**, *2*, 120–158, doi:10.3390/polym2030120.
5. L. Sun; W.M. Huang; Z. Ding; Y. Zhao; C.C. Wang; H. Purnawali; C. Tang. Stimulus-responsive shape memory materials: A review. *Materials & Design* **2012**, *33*, 577–640, doi:10.1016/j.matdes.2011.04.065.
6. Chalissery, D.; Pretsch, T.; Staub, S.; Andrä, H. Additive Manufacturing of Information Carriers Based on Shape Memory Polyester Urethane. *Polymers* **2019**, *11*, doi:10.3390/polym11061005.
7. Kim, Y.-J.; Matsunaga, Y.T. Thermo-responsive polymers and their application as smart biomaterials. *J. Mater. Chem. B* **2017**, *5*, 4307–4321, doi:10.1039/c7tb00157f.
8. Hoffman, A.S. Stimuli-responsive polymers: biomedical applications and challenges for clinical translation. *Advanced Drug Delivery Reviews* **2013**, *65*, 10–16, doi:10.1016/j.addr.2012.11.004.
9. Yin, X.; Hoffman, A.S.; Stayton, P.S. Poly(N-isopropylacrylamide-co-propylacrylic acid) copolymers that respond sharply to temperature and pH. *Biomacromolecules* **2006**, *7*, 1381–1385, doi:10.1021/bm0507812.
10. Ge, Q.; Sakhaei, A.H.; Lee, H.; Dunn, C.K.; Fang, N.X.; Dunn, M.L. Multimaterial 4D Printing with Tailorable Shape Memory Polymers. *Sci Rep* **2016**, *6*, 1–11, doi:10.1038/srep31110.
11. Ge, Q.; Qi, H.J.; Dunn, M.L. Active materials by four-dimension printing. *Appl. Phys. Lett.* **2013**, *103*, 131901, doi:10.1063/1.4819837.
12. Momeni, F.; M.Mehdi Hassani.N, S.; Liu, X.; Ni, J. A review of 4D printing. *Materials & Design* **2017**, *122*, 42–79, doi:10.1016/j.matdes.2017.02.068.
13. Razzaq, M.Y.; Anhalt, M.; Frormann, L.; Weidenfeller, B. Thermal, electrical and magnetic studies of magnetite filled polyurethane shape memory polymers. *Materials Science and Engineering: A* **2007**, *444*, 227–235, doi:10.1016/j.msea.2006.08.083.
14. Jing, X.; Mi, H.-Y.; Huang, H.-X.; Turng, L.-S. Shape memory thermoplastic polyurethane (TPU)/poly(ε-caprolactone) (PCL) blends as self-knotting sutures. *J. Mech. Behav. Biomed. Mater.* **2016**, *64*, 94–103, doi:10.1016/j.jmbbm.2016.07.023.
15. Tan, L.J.; Zhu, W.; Zhou, K. Recent Progress on Polymer Materials for Additive Manufacturing. *Adv. Funct. Mater.* **2020**, *30*, 2003062, doi:10.1002/adfm.202003062.
16. Senatov, F.S.; Niaza, K.V.; Zadorozhnyy, M.Y.; Maksimkin, A.V.; Kaloshkin, S.D.; Estrin, Y.Z. Mechanical properties and shape memory effect of 3D-printed PLA-based porous scaffolds. *J. Mech. Behav. Biomed. Mater.* **2016**, *57*, 139–148, doi:10.1016/j.jmbbm.2015.11.036.
17. Kim, B.K.; Lee, S.Y.; Xu, M. Polyurethanes having shape memory effects. *Polymer* **1996**, *37*, 5781–5793, doi:10.1016/S0032-3861(96)00442-9.
18. Li, F.; Zhang, X.; Hou, J.; Xu, M.; Luo, X.; Ma, D.; Kim, B.K. Studies on thermally stimulated shape memory effect of segmented polyurethanes. *J. Appl. Polym. Sci.* **1997**, *64*, 1511–1516, doi:10.1002/(SICI)1097-4628(19970523)64:8<1511:AID-APP8>3.0.CO;2-K.
19. Lee, B.S.; Chun, B.C.; Chung, Y.-C.; Sul, K.I.; Cho, J.W. Structure and Thermomechanical Properties of Polyurethane Block Copolymers with Shape Memory Effect. *Macromolecules* **2001**, *34*, 6431–6437, doi:10.1021/ma001842l.
20. Ji, F.L.; Hu, J.L.; Li, T.C.; Wong, Y.W. Morphology and shape memory effect of segmented polyurethanes. Part I: With crystalline reversible phase. *Polymer* **2007**, *48*, 5133–5145, doi:10.1016/j.polymer.2007.06.032.
21. Pereira, I.M.; Oréfice, R.L. The morphology and phase mixing studies on poly(ester–urethane) during shape memory cycle. *J Mater Sci* **2010**, *45*, 511–522, doi:10.1007/s10853-009-3969-7.
22. Huang, W.M.; Yang, B.; Zhao, Y.; Ding, Z. Thermo-moisture responsive polyurethane shape-memory polymer and composites: a review. *J. Mater. Chem.* **2010**, *20*, 3367, doi:10.1039/b922943d.
23. Wang, W.; Jin, Y.; Ping, P.; Chen, X.; Jing, X.; Su, Z. Structure Evolution in Segmented Poly(ester urethane) in Shape-Memory Process. *Macromolecules* **2010**, *43*, 2942–2947, doi:10.1021/ma902781e.
24. Pretsch, T.; Müller, W.W. Shape memory poly(ester urethane) with improved hydrolytic stability. *Polymer Degradation and Stability* **2010**, *95*, 880–888, doi:10.1016/j.polymdegradstab.2009.12.020.
25. Müller, W.W.; Pretsch, T. Hydrolytic aging of crystallizable shape memory poly(ester urethane): Effects on the thermo-mechanical properties and visco-elastic modeling. *European Polymer Journal* **2010**, *46*, 1745–1758, doi:10.1016/j.eurpolymj.2010.05.004.

26. Petchsuk, A.; Klinsukhon, W.; Sirikittikul, D.; Prahsarn, C. Parameters affecting transition temperatures of poly(lactic acid-co-polydiols) copolymer-based polyester urethanes and their shape memory behavior. *Polym. Adv. Technol.* **2012**, *23*, 1166–1173, doi:10.1002/pat.2017.
27. Bothe, M.; Emmerling, F.; Pretsch, T. Poly(ester urethane) with Varying Polyester Chain Length: Polymorphism and Shape-Memory Behavior. *Macromolecular Chemistry and Physics* **2013**, *214*, 2683–2693, doi:10.1002/macp.201300464.
28. Liu, W.; Zhang, R.; Huang, M.; Dong, X.; Xu, W.; Wang, Y.; Hu, G.-H.; Zhu, J. Synthesis and shape memory property of segmented poly(ester urethane) with poly(butylene 1,4-cyclohexanedicarboxylate) as the soft segment. *RSC Adv.* **2016**, *6*, 95527–95534, doi:10.1039/C6RA16325D.
29. Ren, H.; Mei, Z.; Chen, S.; Zhuo, H.; Chen, S.; Yang, H.; Zuo, J.; Ge, Z. A new strategy for designing multifunctional shape memory polymers with amine-containing polyurethanes. *J Mater Sci* **2016**, *51*, 9131–9144, doi:10.1007/s10853-016-0166-3.
30. Mirtschin, N.; Pretsch, T. Programming of One- and Two-Step Stress Recovery in a Poly(ester urethane). *Polymers* **2017**, *9*, doi:10.3390/polym9030098.
31. Wendel, B.; Rietzel, D.; Kühnlein, F.; Feulner, R.; Hülder, G.; Schmachtenberg, E. Additive Processing of Polymers. *Macro Materials & Eng* **2008**, *293*, 799–809, doi:10.1002/mame.200800121.
32. Mohamed, O.A.; Masood, S.H.; Bhowmik, J.L. Optimization of fused deposition modeling process parameters: a review of current research and future prospects. *Adv. Manuf.* **2015**, *3*, 42–53, doi:10.1007/s40436-014-0097-7.
33. Ligon, S.C.; Liska, R.; Stampfl, J.; Gurr, M.; Mülhaupt, R. Polymers for 3D Printing and Customized Additive Manufacturing. *Chem. Rev.* **2017**, *117*, 10212–10290, doi:10.1021/acs.chemrev.7b00074.
34. Schönfeld, D.; Chalissery, D.; Wenz, F.; Specht, M.; Eberl, C.; Pretsch, T. Actuating Shape Memory Polymer for Thermoresponsive Soft Robotic Gripper and Programmable Materials. *Molecules* **2021**, *26*, doi:10.3390/molecules26030522.
35. Chalissery, D.; Schönfeld, D.; Walter, M.; Shklyar, I.; Andrae, H.; Schwörer, C.; Amann, T.; Weisheit, L.; Pretsch, T. Highly Shrinkable Objects as Obtained from 4D Printing. *Macro Materials & Eng* **2022**, *307*, 2100619, doi:10.1002/mame.202100619.
36. Raasch, J.; Ivey, M.; Aldrich, D.; Nobes, D.S.; Ayranci, C. Characterization of polyurethane shape memory polymer processed by material extrusion additive manufacturing. *Additive Manufacturing* **2015**, *8*, 132–141, doi:10.1016/j.addma.2015.09.004.
37. Yang, Y.; Chen, Y.; Wei, Y.; Li, Y. 3D printing of shape memory polymer for functional part fabrication. *Int J Adv Manuf Technol* **2016**, *84*, 2079–2095, doi:10.1007/s00170-015-7843-2.
38. Villacres, J.; Nobes, D.; Ayranci, C. Additive manufacturing of shape memory polymers: effects of print orientation and infill percentage on mechanical properties. *RPJ* **2018**, *24*, 744–751, doi:10.1108/RPJ-03-2017-0043.
39. Monzón, M.D.; Paz, R.; Pei, E.; Ortega, F.; Suárez, L.A.; Ortega, Z.; Alemán, M.E.; Plucinski, T.; Clow, N. 4D printing: processability and measurement of recovery force in shape memory polymers. *Int J Adv Manuf Technol* **2017**, *89*, 1827–1836, doi:10.1007/s00170-016-9233-9.
40. Hendrikson, W.J.; Rouwkema, J.; Clementi, F.; van Blitterswijk, C.A.; Farè, S.; Moroni, L. Towards 4D printed scaffolds for tissue engineering: exploiting 3D shape memory polymers to deliver time-controlled stimulus on cultured cells. *Biofabrication* **2017**, *9*, 31001, doi:10.1088/1758-5090/aa8114.
41. Villacres, J.; Nobes, D.; Ayranci, C. Additive manufacturing of shape memory polymers: effects of print orientation and infill percentage on shape memory recovery properties. *RPJ* **2020**, *26*, 1593–1602, doi:10.1108/RPJ-09-2019-0239.
42. https://www.facebook.com/repetier3d/. - Repetier Software. Available online: https://www.repetier.com/ (accessed on 20 January 2022).
43. Saroia, J.; Wang, Y.; Wei, Q.; Lei, M.; Li, X.; Guo, Y.; Zhang, K. A review on 3D printed matrix polymer composites: its potential and future challenges. *Int J Adv Manuf Technol* **2020**, *106*, 1695–1721, doi:10.1007/s00170-019-04534-z.
44. Syrlybayev, D.; Zharylkassyn, B.; Seisekulova, A.; Akhmetov, M.; Perveen, A.; Talamona, D. Optimisation of Strength Properties of FDM Printed Parts-A Critical Review. *Polymers* **2021**, *13*, doi:10.3390/polym13101587.
45. Zhou, Y.-G.; Zou, J.-R.; Wu, H.-H.; Xu, B.-P. Balance between bonding and deposition during fused deposition modeling of polycarbonate and acrylonitrile-butadiene-styrene composites. *Polym. Compos.* **2020**, *41*, 60–72, doi:10.1002/pc.25345.
46. Ahn, S.-H.; Montero, M.; Odell, D.; Roundy, S.; Wright, P.K. Anisotropic material properties of fused deposition modeling ABS. *RPJ* **2002**, *8*, 248–257, doi:10.1108/13552540210441166.

47. Durgun, I.; Ertan, R. Experimental investigation of FDM process for improvement of mechanical properties and production cost. *RPJ* **2014**, *20*, 228–235, doi:10.1108/RPJ-10-2012-0091.
48. Dul, S.; Fambri, L.; Pegoretti, A. Filaments Production and Fused Deposition Modelling of ABS/Carbon Nanotubes Composites. *Nanomaterials (Basel)* **2018**, *8*, doi:10.3390/nano8010049.
49. Zhou, Y.-G.; Su, B.; Turng, L.-S. Deposition-induced effects of isotactic polypropylene and polycarbonate composites during fused deposition modeling. *RPJ* **2017**, *23*, 869–880, doi:10.1108/RPJ-12-2015-0189.
50. Carneiro, O.S.; Silva, A.F.; Gomes, R. Fused deposition modeling with polypropylene. *Materials & Design* **2015**, *83*, 768–776, doi:10.1016/j.matdes.2015.06.053.
51. Jin, M.; Stihl, M.; Giesa, R.; Neuber, C.; Schmidt, H.-W. (AB) n Segmented Copolyetherimides for 4D Printing. *Macro Materials & Eng* **2021**, *306*, 2000473, doi:10.1002/mame.202000473.
52. Mirtschin, N.; Pretsch, T. Designing temperature-memory effects in semicrystalline polyurethane. *RSC Adv.* **2015**, *5*, 46307–46315, doi:10.1039/C5RA05492C.
53. Ecker, M.; Pretsch, T. Novel design approaches for multifunctional information carriers. *RSC Adv* **2014**, *4*, 46680–46688, doi:10.1039/C4RA08977D.
54. DIN EN ISO 527-2 - 1996-07 - Beuth.de. Available online: https://www.beuth.de/en/standard/din-en-iso-527-2/2808009 (accessed on 19 January 2022).
55. Scanning Probe Microscopy. Available online: https://www.digitalsurf.com/software-solutions/scanningprobe-microscopy/ (accessed on 19 March 2019).

Chapter 3.3: Fused Filament Fabrication of Filigree Objects With Shape Memory Properties

Chapter 3.3: Fused Filament Fabrication of Filigree Objects With Shape Memory Properties

3.3.1. Introduction

Shape memory polymers (SMPs) are smart materials that stabilize a temporary shape through a thermomechanical treatment, also called programming [1–6]. The programmed shape remains stable until the one-way (1W) shape memory effect (SME) is triggered, after which the polymer almost completely returns to the permanent shape [1]. The shape memory effect is generally triggered by heat [1,4,7–12]. Thermoplastic polyurethane (TPU) with shape memory properties has shown its superiority among other SMPs due to their modifiable thermal properties and phase segregation.

Additive manufacturing (AM), alias three-dimensional (3D) printing, is a rapid prototyping technique. That is gaining increasing importance in prototyping, material testing, and small-scale production due to its design freedom, cost-effectiveness, and short manufacturing time. Among the other established AM technologies, fused filament fabrication (FFF) is a widely used AM process and is a melt extrusion-based 3D printing process [13–15]. Later, scientists learned how to process SMPs via FFF [6,16–22]. In the case of filigree printing using TPU-SMP with FFF printers, our group employed a commercially available polyester urethane (PEU) Desmopan® DP 2795A SMP along with a 400 µm and 100 µm nozzle on a standard FFF printer to produce high resolution machine-readable quick response (QR) code carriers [6]. On employing the 100 µm nozzle for printing QR code elevations, the code's small cuboidal cell was found to have high dimensional accuracy and exceeded the CAD model by just 40 µm. Comparing the print quality results of extrusion-based AM techniques to process TPU with shape memory properties, our group discloses superior print results to other working groups [19–21,23–27]. The achievement is primarily from using a smaller nozzle opening and highly refined printing parameters like lower printing speed, enabling excellent print quality. The ability to precisely control the printing parameters in *XY*- and *Z*- planes proved that the FFF could achieve excellent printing resolution in printing TPU- SMP, even compared to other AM techniques [6]. This has directly opened up the possibility of fabricating filigree structures of TPU with shape memory properties utilizing FFF. Nonetheless, exploring the lowest printing limits for manufacturing filigree structures using FFF is of scientific interest to enable the manufacturing of miniature objects.

The work utilizes a commercially available PEU Desmopan® DP 2795A SMP in the form of filament processed in **Chapter 3.1** [6] and **Chapter 3.2** to address the points mentioned above. The PEU filaments were later processed using a commercially available FFF 3D printer to produce filigree structures. The Arial fonts of "A" in sizes 3, 4, and 10 were first printed to analyze the printability of smaller structures. Later, the filigree-printed letters were used to develop smart keyboard keys and shape memory gears, which can activate or deactivate transmission systems on demand.

3.3.2. Results and Discussion

The commercially available poly(1,4-butylene adipate) (PBA)-based polyester urethane (PEU), Desmopan® DP 2795A SMP from Covestro Deutschland AG (Leverkusen, Germany), was chosen as the functional base material. The PEU's primary selection criteria were its good processability via FFF and its excellent shape memory properties. The virgin and red PEU filaments processed into filaments in **Chapter 3.1** [6] and **Chapter 3.2** were again selected for this work. Further, a black-colored PEU filament was extruded using graphite powder as an additive to dye the filament during extrusion.

The soft segmental PBA phase of the PEU exhibits a melting transition (T_m) onset and offset at about 33 °C and 55 °C, with a peak at ≈ 42 °C, as observed in a DSC measurement [6]. For 3D printing filigree structures to understand and study the printing of the least possible printing structures using FFF, the letters in Arial font size 3, 4, and 10 on top of a thin substrate were designed using AutoCAD software. Our QR code carrier contribution documented that a 100 µm nozzle, a printing speed of 4 mm x s^{-1}, and a nozzle temperature of 190 °C can process PEU to achieve high printing resolution [6]. This motivated me to take the same dual extrusion setup along with the respective printing parameters for this study.

In order to achieve contrast structures of Arial fonts to distinguish the structures clearly, the virgin PEU and red PEU were selected for FFF. Here, the elevations of Arial fonts were processed using red PEU filament atop a virgin PEU substrate. The font dimension and FFF printing results are presented in **Figure 3.3.1**.

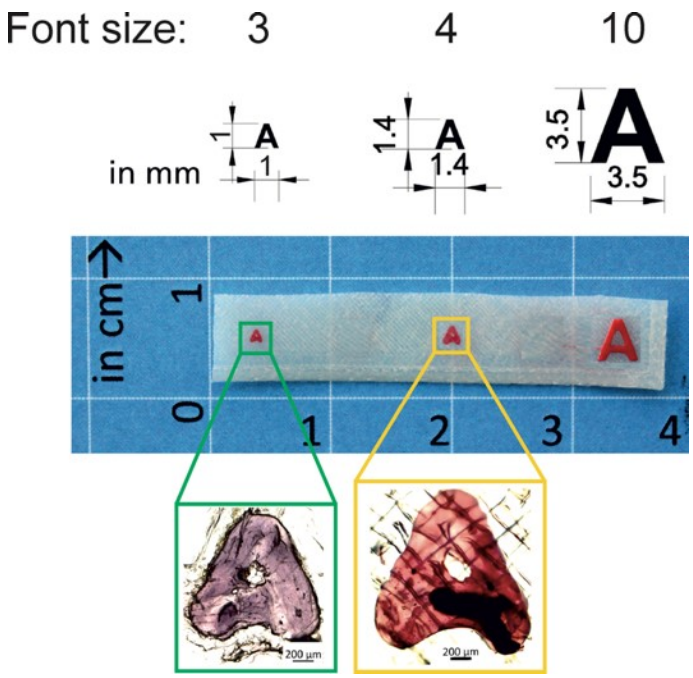

Figure 3.3.1. Additive manufacturing of Arial fonts using FFF. The elevations were made from a red PEU printed atop a virgin PEU substrate. Arial fonts differ in size (topmost row), the respective printing results (middle row), and the inset exhibiting the light microscopic images of smaller fonts. (all the dimensions are in mm)

From Figure 3.3.1., the excellent printing quality and the legibility of the Arial fonts can be observed by the naked eye. The font size 3 was the least possible size to be printed (middle row of Figure 3.3.1). The excellent print quality was confirmed by light microscopic images (bottom row images of Figure 3.3.1). It can be observed that the lower fonts tend to have edges with rounded corners. The roundness is supposed to be due to a round nozzle opening and the nozzle movements to build the letter "A." Once 3D scanned using a confocal microscope, the characterization revealed a good surface quality of the Arial fonts (Figure 3.3.2a and b). Additionally, the imaging processing tool found that the elevation had a height of about 65 µm (Figure 3.3.2a and b), which coincides with the given layer height parameter during 3D printing. Here, the dimensions of the letter "A" along the *X* and *Y*- printing plane were characterized to be about 1.1 mm (**Figure 3.3.2a and b**), which almost coincides with the virtual dimensions of the Arial font size 3 (**Figure 3.3.1, top row**).

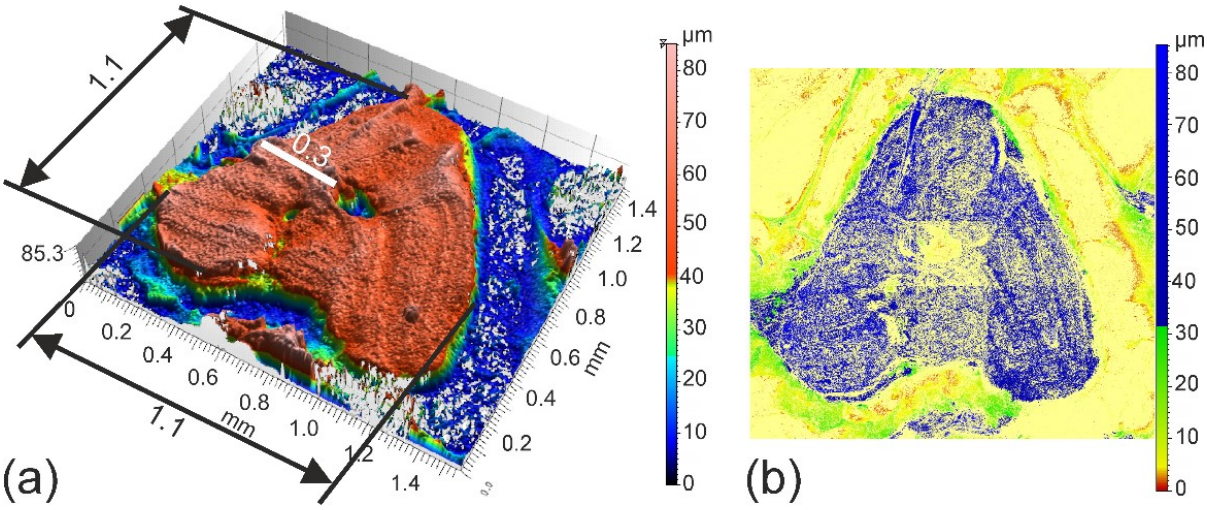

Figure 3.3.2. Confocal microscopic images of FFF manufactured Arial "A" in font size three are represented in (a) isometric view and (b) top view. (all the dimensions are in mm)

As the materials used for producing the 3D objects (**Figure 3.3.1**, middle row) were the same red PEU and virgin PEU as in our previous literature [6], likewise the QR code carriers, the 3D models could also be programmed.

The filigree printing was further used to develop smart keyboard keys with Arial letters "A" or "B" in font size 10. After CAD modeling (**Figure 3.3.3 a**), red-colored Desmopan® 9370AU and grey-colored polylactic acid (PLA) substrates were printed, and atop the letters "A" and "B" were printed using black PEU (**Figure 3.3.3 b** and **c**, respectively). The programmability and the SME of the filigree structures were later investigated. The results are presented in **Figures 3.3.3 b1**, **c1, and c2**.

From **Figure 3.3.3. b and c,** the good printing quality of the filigree letters can be deduced even when printing at increased elevations. On heating to 60 °C, applying a compression load and cooling to –15 °C permitted the letters "A" and "B" to fix the programmed shape (second image in **Figure 3.3.3. b1** and **c1&2**). The structure's height was observed to reduce and flatten onto the top surface of the substrate due to the thermomechanical treatment. The

structures were visually in a non-readable state, which can be noticed clearly in the second image of **Figure 3.3.3. c2**. This shape remains stable until the SME is triggered. The initial shape was almost completely recovered by raising the temperature to 60 °C (rightmost image in **Figure 3.3.3. b1, c1,** and **c2**). The developed SMP letters may be used in security labels, text-based cold chain indicators, information carriers, or entry tickets.

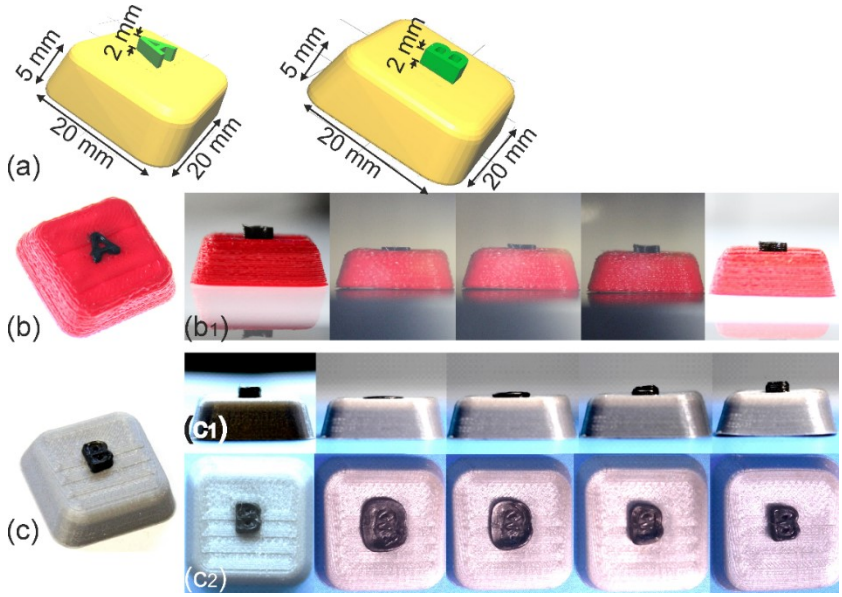

Figure 3.3.3. Additively manufactured computer keys exhibiting the letters Arial "A" and "B," made from black PEU, in font size ten and the corresponding CAD designs (**a**), letter "A" printed atop a substrate of red Desmopan® 9370AU (**b**), letter "B" printed atop a substrate of grey PLA (**c**). From left to right, the permanent shape, programmed shape, shape recovery, and recovered shape of the letter "A" in front view (**b1**) and "B" (**c1**(front view) and **c2** (top view)) are depicted (all the dimensions are in mm).

Next, the filigree printing of PEUs was extended to develop shape memory gears. Mechanical transmission systems may generate heat during operation. Once overheated, this can negatively affect and damage the machine's electronic or other parts and lead to high repair costs. Such damages can be prevented using PEU as intermediate gear to cut off the force transmission and stop overheating. A PEU may help to perform preventive maintenance and save repair costs. Once the overheating problem has been solved, interchanging the PEU gear or reprogramming it can prepare the system for further operation.

For this, novel gears from PEU were designed and developed to demonstrate their technical suitability. First, the programming possibilities of the gear were explored (**Figure 3.3.4**).

The urge for new gear designs emerged since conventional designs are solidly built and cannot provide enough space for the tooth of the gear to change its shape. For this, a standard gear design was modified by introducing hollow oval-shaped structures above the root of each tooth to facilitate the programmability of individual tooths (leftmost image of **Figure 3.3.4**). For thermomechanical treatment of PEU, the gear was first heated to 60 °C, and the tooth was stretched and blocked/ fixed using a template before cooling to –15 °C [6] (**Figure 3.2.5 a and b**). After holding the programmed shape isothermally at –15°C for 15 min, the template was removed, and the PEU gear was brought to room temperature (23 °C), resulting

in successful programming, as evidenced by a 3 mm extension in length for every single tooth (middle image of **Figure 3.2.4**). The programmed shape of the gear qualifies it as a novel force transfer system. Once the temperature exceeded the T_m of the PEU (42 °C) [6], here at 60 °C, the almost permanent shape was recovered (rightmost image of **Figure 3.2.4**).

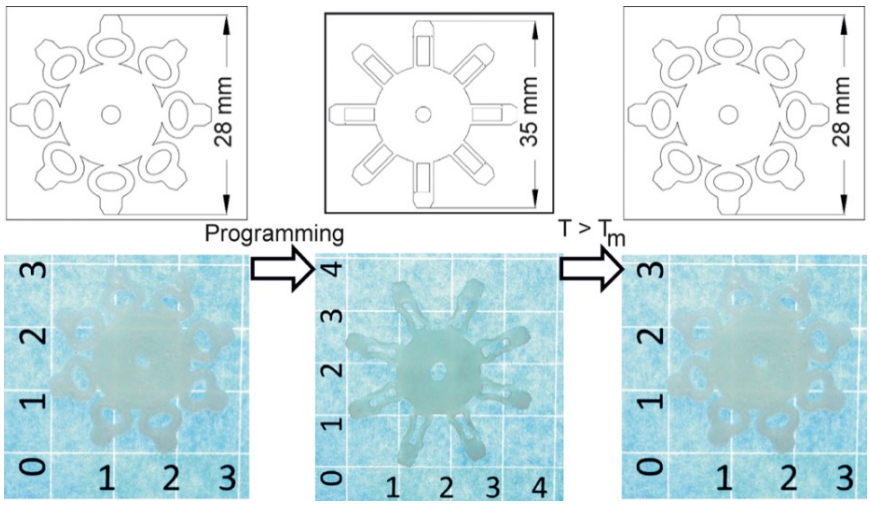

Figure 3.3.4. Schematic drawings of the permanent, temporary, and recovered shape of a gear (top row) and the associated additively manufactured objects made from PEU (bottom row) (all the dimensions are in mm).

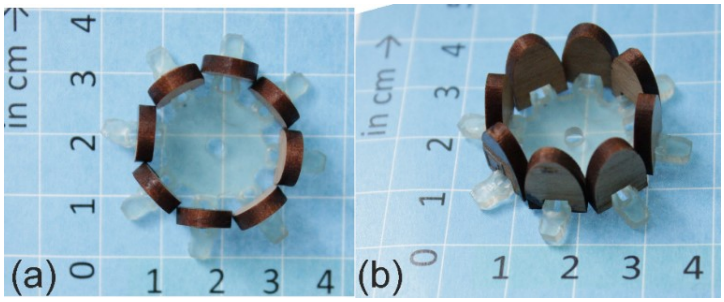

Figure 3.3.5. Programming of an additively manufactured gear from PEU after heating to 60°C for 10 min, stretching the tooth, and fixing with the help of a template tool (brownish color) in the perspectives of top view (a) and isometric view (b).

The programmed gear was employed as an intermediate between an input and an output gear to demonstrate the practicability of PEU shape memory gears (**Figure 3.3.6**).

The PEU gear was developed and designed this way so that its temporary shape makes contact with the input and output gear (green highlighted in the top image of **Figure 3.3.6**). This ensured a continuous force transfer from the input to the output gear with minimal transmission loss. The temporary shape remained stable until the temperature exceeded the PBA soft segment offset melting transition temperature (~60 °C) [6]. Resulting in recovering the permanent shape of the gear (red highlighted gear in the bottom image of **Figure 3.3.6**), thereby the contact of the PEU gear with the input and output gear was interrupted due to the SME.

Another gear design was developed in a different approach to enable a force transfer above T_m (**Figure 3.3.7**).

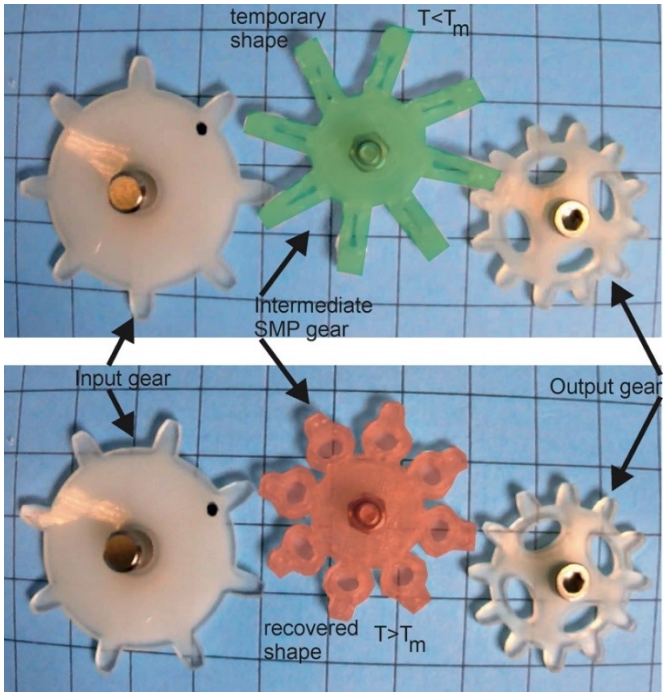

Figure 3.3.6. Force transfer system with a shape memory gear in its center position. The temporary shape is highlighted in green color (top image), and the recovered shape is highlighted in red color (bottom image).

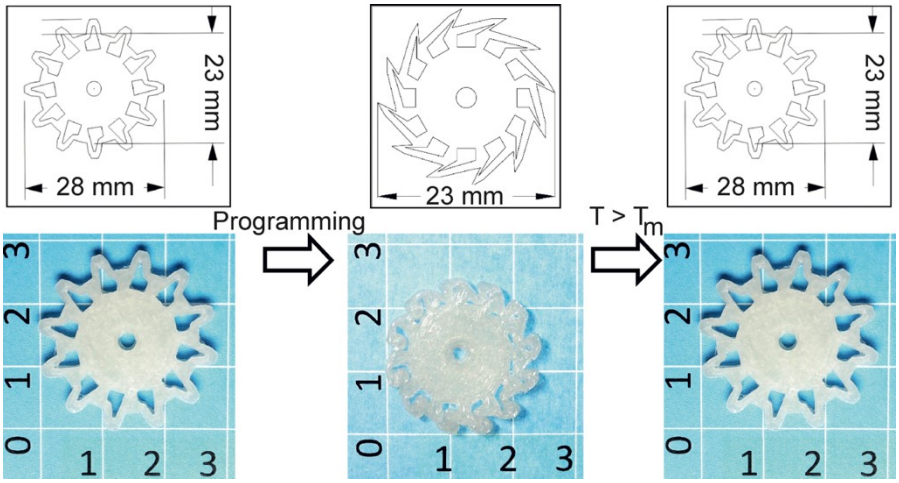

Figure 3.3.7. Schematic drawing (top row) and the respective additively manufactured gears (bottom row). From left to right, the permanent, programmed, and recovered shapes are exhibited (all the dimensions are in mm).

The new gear design was conceived by introducing hollow-shaped structures below the gear's root circle (leftmost image of **Figure 3.3.7**). Heating the SMP to 60 °C, compressing the teeth towards the hollow region, and cooling the compressed shape to –15 °C completed the programming [6] (middle image of **Figure 3.3.7**). A smaller outer diameter than the permanent shape characterized the resulting temporary shape. The discrepancy was about 5 mm. Upon heating the gear above 60 °C (above T_m of the PBA soft segment of the PEU) [6], the permanent shape was almost recovered (rightmost image of **Figure 3.3.7**). The

practicability of the gear to activate the system once heated is evaluated next. The resulting shape changes are shown in **Figure 3.3.8**.

After assembling the programmed gear between the input and output gears, the system can undergo an operation (green highlighted in the top image of **Figure 3.3.8**). Since the teeth of the temporary shape remained inside the hollow structures, the force transmission from the input gear was not in contact with the PEU and then to the output gear. When triggering the SME, the permanent shape of the gear was recovered, thereby resulting in the teeth' extension—allowing the PEU gear to engage with the input and output gear to enable the power transmission (red highlighted gear in the bottom image of **Figure 3.3.8**).

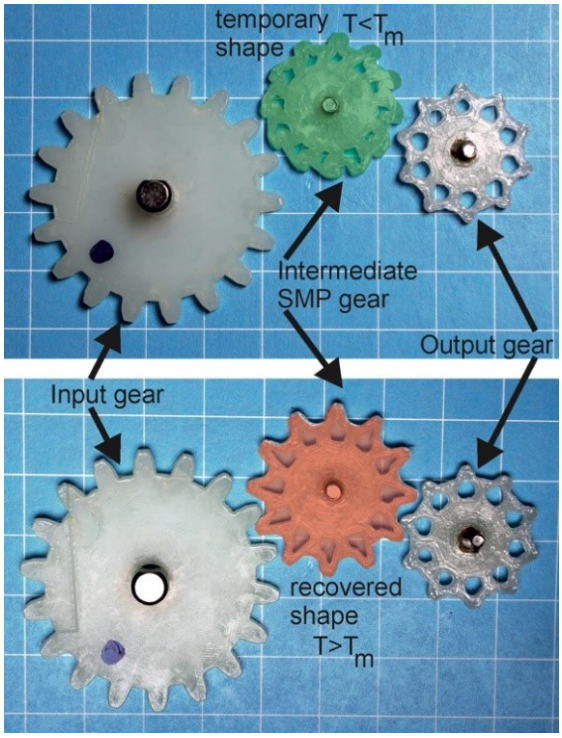

Figure 3.3.8. Force transfer system with a shape memory gear in its center position. The temporary shape is highlighted in green color (top image), and the recovered shape is highlighted in red color (bottom image)

3.3.3. Conclusions

Chapter 3.3 explores miniature structures obtained from 3D printing using FFF along with an SMP and a 100 µm nozzle. The work shows the possibility of 3D printing filigree structures such as Arial fonts of the letter “A” in sizes 3, 4, and 10. Since the printing material was the same PEU used in our previous QR code carriers contribution in **Chapter 3.1** [6], it is possible to program it into a different shape and recover the original shape by heating above the soft segment's melting transition temperature. This work further utilizes filigree printing to develop smart keyboard keys, where PEU was used to print the letters “A” or “B” in font size ten atop a non-thermoresponsive substrate. The shape memory keyboard keys have a potential application for switching between two scripts, like braille and standard (QWERTY)

keyboards. Here, for the better applicability of smart keyboard keys, the 1W-SME of letters has to be later extended to a two-way SME to transfer them into two metastable states so that the tedious 1W-SME reprogramming process can be eliminated. The introduction of heating and cooling elements for the SMP letters can further help to trigger the 2W-SME on command. Printing letters from SMP can also be used to develop text-based information carriers, cold-chain indicators, or even security labels for fighting against product piracy.

Furthermore, novel mechanical force transmission systems were introduced, where the design of toothed gears facilitates thermoresponsiveness attained through thermomechanical treatment. The developed gear permitted the shape recovery to be used advantageously for starting or stopping a force transfer system. Here, the structural design of the object was crucial to realizing the desired functionality. One of the potential applications of the developed SMP-toothed gear is a preventive system to break or start a process to avoid overheating or ensure the preferred temperature is reached. The work thereby shows that FFF is a powerful AM technique to achieve good print quality and functional objects with a shape memory effect to address specific applications.

3.3.4. Experimental Section

Materials: The virgin PEU Desmopan® DP 2795A SMP from Covestro Deutschland AG (Leverkusen, Germany) is used as the functional base material for this study. The red PEU was attained using 0.5 wt. % of Irgazin® Red DPP BO additive and virgin PEU filaments processed in the previous literature is again in the study [6]. Further information regarding the PEU's thermal, mechanical, thermomechanical, and shape memory properties is given in previous publications [6,28–30]. The graphite powder was bought from Kremer Pigmente GmbH, and Co (Aichstetten, Germany) and was used as received. The red ether-based thermoplastic polyurethane elastomer Desmopan® 9370AU was supplied by Covestro Deutschland AG (Leverkusen, Germany). The grey PLA filaments were bought from Prusa Research A.S. (Prague, Czech Republic).

Extrusion: The PEU granulates are dried at 110 ◦C in a Binder vacuum drying chamber VDL 53 from Binder GmbH (Tuttlingen, Germany) to remove water and avoid bubble formation when extruding filaments. The drying was finalized after 150 min. Subsequently, the pellets were fed into an extrusion line to produce filaments.

The individual units of the extrusion line were put together in such a way that it included a volumetric material feeding system Color-exact 1000 from Plastic Recycling Machinery (Zhangjiagang City, China), a Leistritz twin screw extruder MICRO 18 GL from Leistritz AG (Nürnberg, Germany), characterized by seven heating zones and a screw length of 600 mm, a conveyor belt, a water bath and a filament winder from Brabender GmbH and Co. KG (Duisburg, Germany). In any case, the temperature of the individual heating zones of the extruder was 180, 185, 190, 195, 200, 190, and 190 ◦C. The screw speed of the extruder was set to 77 rpm. The PEU granulate was processed with additives of 0.35 wt.% of graphite powder to obtain a black-colored PEU filament. Whereas the Desmopan® 9370AU was

extruded into filaments without additives. To evaluate the filaments' quality, the filament diameter evolution was manually detected at regular intervals using a Vernier caliper from Fowler High Precision (Auburndale, FL, USA).

Virtual Design: The virtual designs of the models were designed using AutoCAD from Autodesk, Inc. (San Rafael, CA, USA). These include Arial fonts of the letter “A” in sizes 3, 4, and 10 with a substrate to test the printing of the least possible filigree structures, letterings “A” and “B” with a substrate in font size 10 to demonstrate the shape memory effects of filigree printing structures, and the gears to activate and deactivate a transmission system. The CAD models were exported as .STL files.

Fused Filament Fabrication (3D Printing): Fused filament fabrication was used to produce the 3D printed models. The experiments were carried out using the commercially available 3D printer Ultimaker 3 from Ultimaker B. V. (Geldermalsen, The Netherlands). The manufacturer provides an XYZ resolution for Ultimaker 3 of 12.5, 12.5, and 2.5 µm, defining the slightest movement that the 3D printer can make concerning the XY plane and in the Z direction. The Ultimaker build plate manual leveling calibration method was carried out before the beginning of each experiment to calibrate the print bed. Therefore, a calibration card with a thickness of about 170 µm was used. The process included a rough leveling of the build plate followed by a fine leveling. Fine leveling was achieved with the calibration card, at which the knurled nut was adjusted at the rear center, front left, and front right of the build plate until slight friction occurred when sliding the card between the build plate and print head.

The two print heads of the FFF-printer were either equipped with two nozzles having different diameters of 100 and 400 µm or the same diameter of 400 µm. For simplicity, the following terminology is introduced, pointing out the most relevant variations when manufacturing 3D printed objects:

- Type 1: The 3D model of the gears was printed using a 400 µm nozzle and a target layer thickness of 180 µm.
- Type 2: The substrate of the letters was printed with non-dyed PEU using a 400 µm nozzle and a target layer thickness of 180 µm. The elevation was built from red PEU with a 100 µm nozzle. Using these settings, the Arial font of the letter “A” in sizes 3, 4, and 10 were printed, where the red PEU makes the elevation with a target layer thickness of 63 µm and virgin PEU as the substrate. In the case of the lettering “A” and “B” along with a substrate, the substrates were printed using red Desmopan® 9370AU or grey PLA. While the elevation of the letter “A” and “B” with black PEU.

The most relevant settings for the 3D printing process are listed in **Table 3.3.1**.

Shape Memory Effect (SME): The programming of the letterings “A” and “B” on the substrates were carried out with an MTS Criterion universal testing machine from MTS Systems Corporation (Eden Prairie, MN, USA). The device was operated with a temperature chamber controlled by a Eurotherm temperature controller unit. Two heating elements were located at the back of the chamber. Liquid nitrogen from a Dewar vessel was fed into the chamber under a pressure of 1.3 bar as an essential prerequisite for cooling.

Table 3.3.1. Printing instructions for Ultimaker 3 to produce the different demonstrators.

Specifications	Substrate/ Model (Non-Dyed PEU)	Elevation (Red or black PEU)	Desmopan® 9370AU / PLA
3D Model - Type	1	2	2
Diameter of the nozzle (µm)	400	100	400
Temperature of the nozzle (°C)	225	190	200
Speed of print head (mm × s^{-1})	50	4	50
Build platform temperature (°C)	23	23	60
Layer height (µm)	180	63	150

At the beginning of the programming, the demonstrators were placed between compression clamps. After heating to 60 °C and a holding time of 10 min, a compression force was applied till the upper clamp touched the substrate of the model. After cooling to –15 °C and holding the temperature isothermally for 10 min, the load was removed. The temperature was brought back to 23 °C and held for 5 min. After that, the 1W-SME was triggered by heating again to 60 °C with an additional isothermal holding time of 10 min. During 1W-SME, the letters could recover freely/without an external load or by so-called free-strain conditions. Later, the temperature was brought back to 23 °C and held for 5 min, completing the first shape memory cycle to repeat the procedure. A loading rate of 100 mm x min^{-1}, while a heating and cooling rate of 5 °C x min^{-1} were used for the whole experiment.

In the case of the PEU gears, the demonstrators were first heated to 60 °C and held isothermally for 10 min in a UF110 heating chamber from Memmert GmbH + Co. KG (Schwabach, Germany). Afterward, the gears were deformed according to the use-case/application described above and cooled to –15 °C using a freezer. After 10 min, the load was removed, and the models were brought back to 23°C (room temperature). Then, the programmed gear was mounted as an intermediate gear between the input and output gear. The programmed gear was heated to 60 °C using a heating gun from Conrad Electronic (Hirschau, Germany) to demonstrate the SME.

Characterization of Print Quality: Topography measurements were performed on the filigree printed Arial letter “A” with font size three, using a FocusCam LV150 confocal microscope from Confovis GmbH (Jena, Germany), which was equipped with an objective lens of 5×/0.15 N.A. The sample was illuminated with a ring light. The data recorded by the focus variation microscope was evaluated with the software MountainsMap® imaging topography 7.4 from Digital Surf (Besançon, France) [31]. The development of the surface profile surrounding was exemplarily determined.

Further microscopic investigations were carried out with the microscope Axio Scope.A1 from Carl Zeiss Microscopy GmbH (Jena, Germany) using the imaging software Zen 2.3 lite also from Carl Zeiss Microscopy GmbH [32]. The experiments were conducted to evaluate the resolution of the Arial fonts three and four in the XY-plane.

3.3.5. Reference

1. Liu, C.; Qin, H.; Mather, P.T. Review of progress in shape-memory polymers. *J. Mater. Chem.* **2007**, *17*, 1543, doi:10.1039/b615954k.
2. Dietsch, B.; Tong, T. A review-: Features and benefits of shape memory polymers (smps). *Journal of advanced materials* **2007**, *39*, 3–12.
3. Ratna, D.; Karger-Kocsis, J. Recent advances in shape memory polymers and composites: a review. *J Mater Sci* **2008**, *43*, 254–269, doi:10.1007/s10853-007-2176-7.
4. Pretsch, T. Review on the Functional Determinants and Durability of Shape Memory Polymers. *Polymers* **2010**, *2*, 120–158, doi:10.3390/polym2030120.
5. L. Sun; W.M. Huang; Z. Ding; Y. Zhao; C.C. Wang; H. Purnawali; C. Tang. Stimulus-responsive shape memory materials: A review. *Materials & Design* **2012**, *33*, 577–640, doi:10.1016/j.matdes.2011.04.065.
6. Chalissery, D.; Pretsch, T.; Staub, S.; Andrä, H. Additive Manufacturing of Information Carriers Based on Shape Memory Polyester Urethane. *Polymers* **2019**, *11*, doi:10.3390/polym11061005.
7. Huang, W.M.; Ding, Z.; Wang, C.C.; Wei, J.; Zhao, Y.; Purnawali, H. Shape memory materials. *Materials Today* **2010**, *13*, 54–61, doi:10.1016/S1369-7021(10)70128-0.
8. Small, W.; Singhal, P.; Wilson, T.S.; Maitland, D.J. Biomedical applications of thermally activated shape memory polymers. *J. Mater. Chem.* **2010**, *20*, 3356–3366, doi:10.1039/B923717H.
9. Peponi, L.; Navarro-Baena, I.; Kenny, J.M. 7 - Shape memory polymers: properties, synthesis and applications. In *Smart polymers and their applications*; Aguilar, M.R., San Román, J., Eds.; Woodhead Publishing: Cambridge, 2014; pp 204–236, ISBN 978-0-85709-695-1.
10. Pilate, F.; Toncheva, A.; Dubois, P.; Raquez, J.-M. Shape-memory polymers for multiple applications in the materials world. *European Polymer Journal* **2016**, *80*, 268–294, doi:10.1016/j.eurpolymj.2016.05.004.
11. Karger-Kocsis, J.; Kéki, S. Review of Progress in Shape Memory Epoxies and Their Composites. *Polymers* **2017**, *10*, doi:10.3390/polym10010034.
12. Sun, L.; Wang, T.X.; Chen, H.M.; Salvekar, A.V.; Naveen, B.S.; Xu, Q.; Weng, Y.; Guo, X.; Chen, Y.; Huang, W.M. A Brief Review of the Shape Memory Phenomena in Polymers and Their Typical Sensor Applications. *Polymers* **2019**, *11*, doi:10.3390/polym11061049.
13. Wendel, B.; Rietzel, D.; Kühnlein, F.; Feulner, R.; Hülder, G.; Schmachtenberg, E. Additive Processing of Polymers. *Macro Materials & Eng* **2008**, *293*, 799–809, doi:10.1002/mame.200800121.
14. Mohamed, O.A.; Masood, S.H.; Bhowmik, J.L. Optimization of fused deposition modeling process parameters: a review of current research and future prospects. *Adv. Manuf.* **2015**, *3*, 42–53, doi:10.1007/s40436-014-0097-7.
15. Ligon, S.C.; Liska, R.; Stampfl, J.; Gurr, M.; Mülhaupt, R. Polymers for 3D Printing and Customized Additive Manufacturing. *Chem. Rev.* **2017**, *117*, 10212–10290, doi:10.1021/acs.chemrev.7b00074.
16. Schönfeld, D.; Chalissery, D.; Wenz, F.; Specht, M.; Eberl, C.; Pretsch, T. Actuating Shape Memory Polymer for Thermoresponsive Soft Robotic Gripper and Programmable Materials. *Molecules* **2021**, *26*, doi:10.3390/molecules26030522.
17. Chalissery, D.; Schönfeld, D.; Walter, M.; Shklyar, I.; Andrae, H.; Schwörer, C.; Amann, T.; Weisheit, L.; Pretsch, T. Highly Shrinkable Objects as Obtained from 4D Printing. *Macro Materials & Eng* **2022**, *307*, 2100619, doi:10.1002/mame.202100619.
18. Raasch, J.; Ivey, M.; Aldrich, D.; Nobes, D.S.; Ayranci, C. Characterization of polyurethane shape memory polymer processed by material extrusion additive manufacturing. *Additive Manufacturing* **2015**, *8*, 132–141, doi:10.1016/j.addma.2015.09.004.
19. Yang, Y.; Chen, Y.; Wei, Y.; Li, Y. 3D printing of shape memory polymer for functional part fabrication. *Int J Adv Manuf Technol* **2016**, *84*, 2079–2095, doi:10.1007/s00170-015-7843-2.
20. Villacres, J.; Nobes, D.; Ayranci, C. Additive manufacturing of shape memory polymers: effects of print orientation and infill percentage on mechanical properties. *RPJ* **2018**, *24*, 744–751, doi:10.1108/RPJ-03-2017-0043.
21. Monzón, M.D.; Paz, R.; Pei, E.; Ortega, F.; Suárez, L.A.; Ortega, Z.; Alemán, M.E.; Plucinski, T.; Clow, N. 4D printing: processability and measurement of recovery force in shape memory polymers. *Int J Adv Manuf Technol* **2017**, *89*, 1827–1836, doi:10.1007/s00170-016-9233-9.
22. Hendrikson, W.J.; Rouwkema, J.; Clementi, F.; van Blitterswijk, C.A.; Farè, S.; Moroni, L. Towards 4D printed scaffolds for tissue engineering: exploiting 3D shape memory polymers to deliver time-controlled stimulus on cultured cells. *Biofabrication* **2017**, *9*, 31001, doi:10.1088/1758-5090/aa8114.

23. Raasch, J.; Ivey, M.; Aldrich, D.; Nobes, D.S.; Ayranci, C. Characterization of polyurethane shape memory polymer processed by material extrusion additive manufacturing. *Additive Manufacturing* **2015**, *8*, 132–141, doi:10.1016/j.addma.2015.09.004.
24. Jung, Y.C.; Cho, J.W. Application of shape memory polyurethane in orthodontic. *J Mater Sci: Mater Med* **2010**, *21*, 2881–2886, doi:10.1007/s10856-008-3538-7.
25. Kashyap, D.; Kishore Kumar, P.; Kanagaraj, S. 4D printed porous radiopaque shape memory polyurethane for endovascular embolization. *Additive Manufacturing* **2018**, *24*, 687–695, doi:10.1016/j.addma.2018.04.009.
26. Berwind, M.F.; Kamas, A.; Eberl, C. A Hierarchical Programmable Mechanical Metamaterial Unit Cell Showing Metastable Shape Memory. *Adv. Eng. Mater.* **2018**, *20*, 1800771, doi:10.1002/adem.201800771.
27. Hendrikson, W.J.; Rouwkema, J.; Clementi, F.; van Blitterswijk, C.A.; Farè, S.; Moroni, L. Towards 4D printed scaffolds for tissue engineering: exploiting 3D shape memory polymers to deliver time-controlled stimulus on cultured cells. *Biofabrication* **2017**, *9*, 31001, doi:10.1088/1758-5090/aa8114.
28. Mirtschin, N.; Pretsch, T. Designing temperature-memory effects in semicrystalline polyurethane. *RSC Adv.* **2015**, *5*, 46307–46315, doi:10.1039/C5RA05492C.
29. Ecker, M.; Pretsch, T. Novel design approaches for multifunctional information carriers. *RSC Adv* **2014**, *4*, 46680–46688, doi:10.1039/C4RA08977D.
30. Mirtschin, N.; Pretsch, T. Programming of One- and Two-Step Stress Recovery in a Poly(ester urethane). *Polymers* **2017**, *9*, doi:10.3390/polym9030098.
31. Digital Surf - Oberflächen-Imaging- & Messtechnik-Software. Available online: https://www.digitalsurf.com/de/ (accessed on 7 June 2022).
32. undefined. Available online: undefined (accessed on 7 June 2022).

Chapter 4:
Four-Dimensional (4D) Printing Via Fused Filament Fabrication

Chapter 4.1: Highly Shrinkable Objects as Obtained from 4D-printing

Chapter 4.1: Highly Shrinkable Objects as Obtained from 4D-printing

The original article Chalissery, D., Schönfeld, D., Walter, M., Shklyar, I., Andrae, H., Schwörer, C., Amann, T., Weisheit, L. and Pretsch, T. (2022), Highly Shrinkable Objects as Obtained from 4D-printing. Macromol. Mater. Eng. 2100619 and graphical abstract are published in Wiley Macromolecular Materials and Engineering and available at https://doi.org/10.1002/mame.202100619.

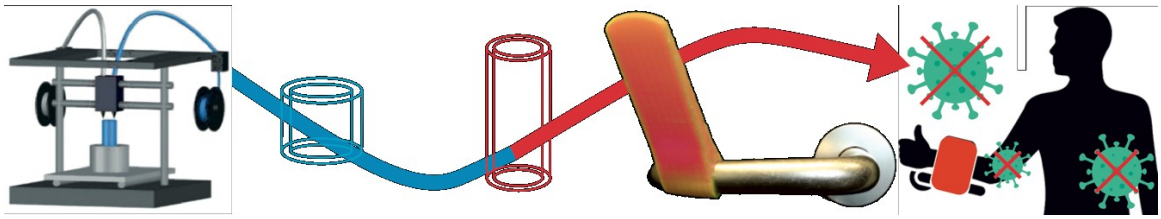

Figure 4.1.0.0. The table of content image of the article "Highly Shrinkable Objects as Obtained from 4D-printing" is published in Wiley Macromolecular Materials and Engineering 2100619.

Contribution

My contribution: The concept idea of 4D-printing and hands-free door opener. Visualization, preparation of images (including table of content image and cover image, excluding **Figure 4.1.1** and **Figure S4.1.1**.), design development and design iteration (every individual design of hands-free door opener), filament extrusion and re-extrusion, mechanical recycling, 4D-printing, characterization using tensile test, DSC and DMA, and writing—original draft. Project lead of the article.
Not included in my contribution: Synthesis, titration and FT-IR, simulation of door handle design and tribological analysis

Schönfeld, D.: Synthesized the polyether urethane (PEU) for the work, carried out FT-IR, thermal analysis (DSC) and material analysis of PEU (directly after synthesis). Conducted mechanical recycling, extrusion and re-extrusion. Writing—original draft (synthesis), preparation and visualization of **Figure 4.1.1** and **Figure S4.1.1**.

Walter, M.: Developed the PEU, conducted first validation, and investigation of PEU.

Shklyar, I.: Conducted simulation of different door handle designs, and prepared images of simulation. Writing—original draft (simulation), preparation and visualization of **Figure 4.1.9** and **Figure 4.1.12**.

Andrä, H.: Funding acquisition, conceptualization and formal analysis of the of simulation analysis.

Schwörer, C.: Formal analysis, validation, investigation, and methodology of the tribological tests.

Amann, T.: Funding acquisition of tribological tests, preparation and visualization of **Figure 4.1.11** and **Figure S4.1.14**.

Weisheit, L.: Funding acquisition and conceptualization of end-of-life concept.

Pretsch, T.: Conceptualization of the manuscript, funding acquisition, project administration, supervision, writing—review and editing

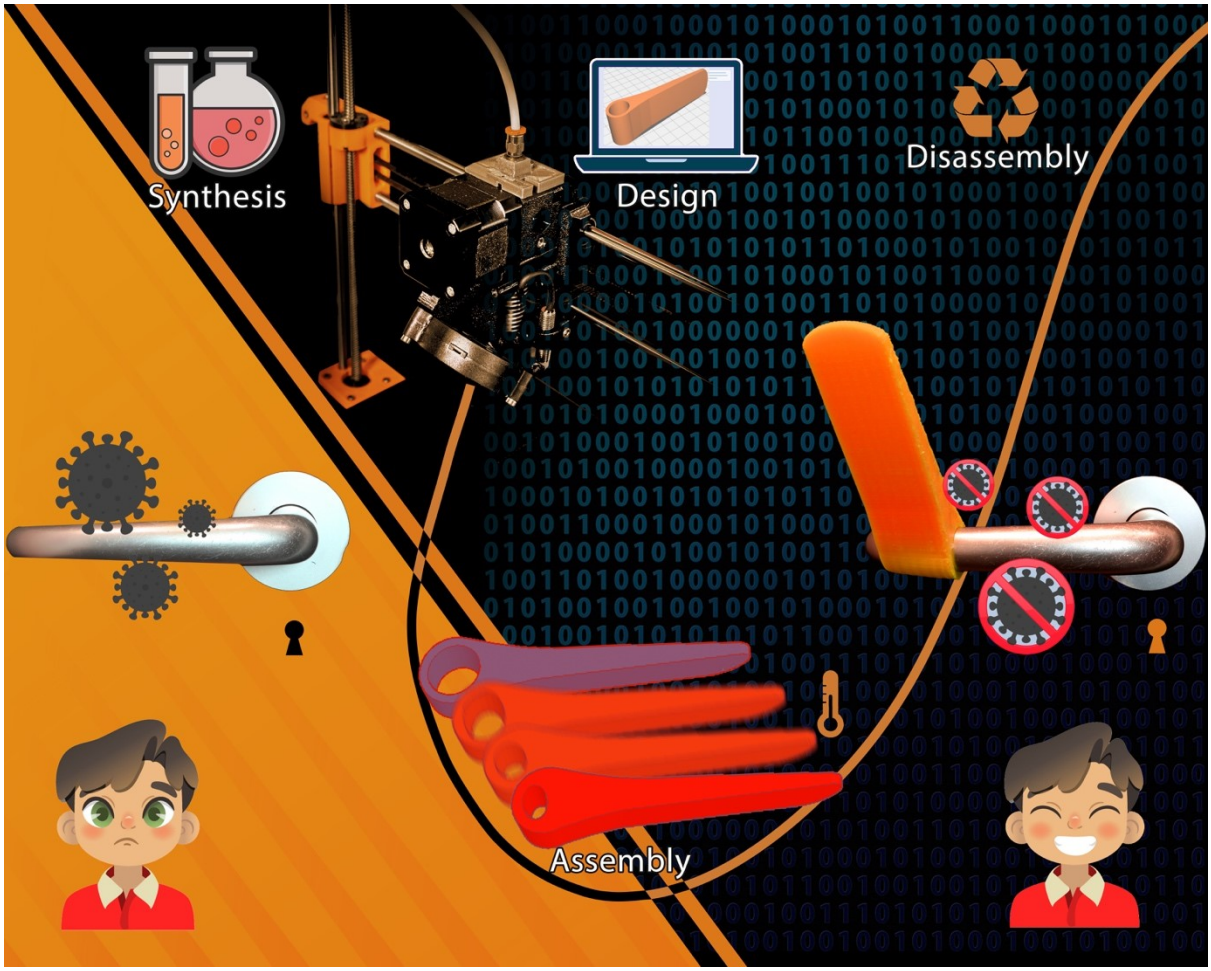

Figure 4.1.0.1. Suggested cover image of "Highly Shrinkable Objects as Obtained from 4D-printing" (not published).

Chapter 4.1. Highly Shrinkable Objects as Obtained from 4D-printing

Dilip Chalissery[1], Dennis Schönfeld[1], Mario Walter[1], Inga Shklyar[2], Heiko Andrae[2], Christoph Schwörer[3], Tobias Amann[3], Linda Weisheit[4], and Thorsten Pretsch[1]*

1 Fraunhofer Institute for Applied Polymer Research IAP, Geiselbergstraße 69, Potsdam 14476, Germany E-mail: dilip.chalissery@iap.fraunhofer.de; thorsten.pretsch@iap.fraunhofer.de
2 Fraunhofer Institute for Industrial Mathematics ITWM, Fraunhofer-Platz 1, 67663 Kaiserslautern, Germany;
3 Fraunhofer Institute for Mechanics of Materials IWM, Wöhlerstraße 11, Freiburg 79108, Germany
4 Fraunhofer Institute for Machine Tools and Forming Technology IWU, Nöthnitzer Straße 44, Dresden 01187, Germany
* Correspondence: thorsten.pretsch@iap.fraunhofer.de; Tel.: +49-(0)-331/568-1414

4.1.0. Abstract: 4D-printing of shape memory polymers enables the production of thermoresponsive objects. In this contribution, a facile printing strategy is followed for an in-house synthesized thermoplastic poly(ether urethane). Processing by means of fused filament fabrication, in which the difference between nozzle temperature and material-specific glass transition temperature of the polymer is kept as low as possible, allows to obtain highly shrinkable objects whose shape and thermoresponsiveness can be precisely controlled. The effectiveness of the method also applies to the printing material polylactic acid. One possible application lies in highly shrinkable objects for assembly purposes. As proof-of-concept, lightweight hands-free door openers for healthcare applications are functionally simulated and developed. Once printed, such devices shrink when heated to fit on door handles, allowing an easy assembly. At the end-of-use, a heating-initiated disassembling and mechanical recycling are proposed. In perspective, a reuse of the materials in 4D-printing can contribute to the emergence of a circular economy for such highly functional materials.

4.1.1. Introduction

Shape memory polymers (SMPs) can retain a temporary shape after a thermomechanical treatment, also denoted as “programming.” When exposed to heat, the one-way shape memory effect is triggered and the polymer almost completely returns to its permanent shape.[1–5] The advantageous shape-memory behavior of polymers has already been utilized, among others, in connection with the development of biomedical devices,[6–13] the counterfeit-proof marking of goods susceptible to plagiarism,[14–19] and for active

assembly[20– 23] and disassembly,[22,24–28] which both requires a rethinking of classical design processes.

Additive manufacturing (AM) alias 3D printing has gained considerable attention and enthusiasm as an innovative manufacturing technology.[29] Amidst different known 3D printing methods, fused filament fabrication (FFF) is a widely used technique.[30] A few studies have been reporting on FFF with SMPs, in particular with thermoplastic polyurethanes (TPUs).[19,31–35] Most importantly, in the past few years, it has become known how to implement internal stresses during AM, which is the so-called "4D-printing,"[36,37] addressing time evolving structural functions as unattainable by conventional 3D printing.[38–40] The main advantage of such function integration is that the finished objects can be removed directly from the printer without the need for an additional thermomechanical treatment. Thus, it is an important step to reduce the effort required in production of thermoresponsive objects.

Today, there are only a few contributions on the 4D-printing of TPUs,[41] as researchers have primarily concentrated on other materials like polylactic acid (PLA). For instance, a more drastic 4D shrinkage behavior was verified for PLA, when printing with a lower nozzle temperature,[42] building up structures of lower layer height,[42] and/or using higher printing speeds.[43,44] All these approaches have in common that polymer relaxation on the print platform can efficiently be inhibited. With regard to shape memory TPU, Bodaghi et al.[36] unveiled that a decrease in nozzle temperature and an increase in printing speed enhance the 4D bending effect of a straight printed beam. Similarly, Hu et al.[45] studied the bending behavior caused by the 4D-printing of a polyurethane-based SMP. Once again, a stronger shrinkage was associated with a higher printing speed. Although it is evident in the literature that thermoresponsiveness of PLA and TPU can be controlled by 4D-printing when selecting appropriate printing parameters, the number of TPU materials which can be used for this purpose still appears to be limited.[36,37,45] Another weakness is that the geometrical complexity and the extent of the 4D effects are restricted.

Here we propose the synthesis of a poly(ether urethane) (PEU) with promising thermal, mechanical, and shape memory properties and suitable for processing via extrusion and FFF to obtain objects with thermally inducible strong shrinkage. Based on the findings from previous works, we demonstrate that reduced energy consumption during printing is a key to witness the presumably most efficient storage and release of strain so far. Furthermore, we give evidence how to transfer our findings to the printing material PLA and suggest opening up applications in the field of assembly. This includes "hands-free door openers," which can ensure that in the current corona pandemic door handles no longer need to be touched by hand. To keep raw material consumption as low as possible, a lightweight construction was developed using finite element analysis. In this regard, both the outer shape and core structure were optimized for the occurrence of compressive loads. The fabrication of hands-free door openers unveiled that shrinking on demand can advantageously be used for assembly, while the temperature-sensitive mechanical stiffness of the polymer later enables a disassembling as required at the end-of-use. To address the reusability, hands-free door openers made from PEU were mechanically recycled and the material was re-extruded,

before being subjected to one further 4D reprinting. In this way, we pursued a holistic approach—from the molecule to the demonstrator, its assembly to disassembly, recycling and functional reuse.

4.1.2. Results and Discussion

PEUs are attractive polymeric materials due to their pronounced shape memory properties, thermoplastic nature, which is a prerequisite for processing via FFF, and the possibility of precisely setting a glass transition at temperatures relevant to a desired application.[46–48] For instance, PEUs with a glass transition temperature T_g higher than room temperature can be obtained by polymer synthesis when soft segments of lower molecular weight are used or when the weight content of aromatic hard segments is increased.[46,47] Against this background, we selected a polypropylene glycol (PPG) with a low molecular weight of about 430 g x mol^{-1}.Theunderlyingsynthesis approach followed the prepolymer method.[49] First, PPG was brought to reaction with 4,4'diphenylmethane diisocyanate (MDI) to build up an isocyanate end capped prepolymer, before the chain extender 1,4-butanediol (BD) was added, which resulted in the formation of a PEU (**Figure 4.1.1**).

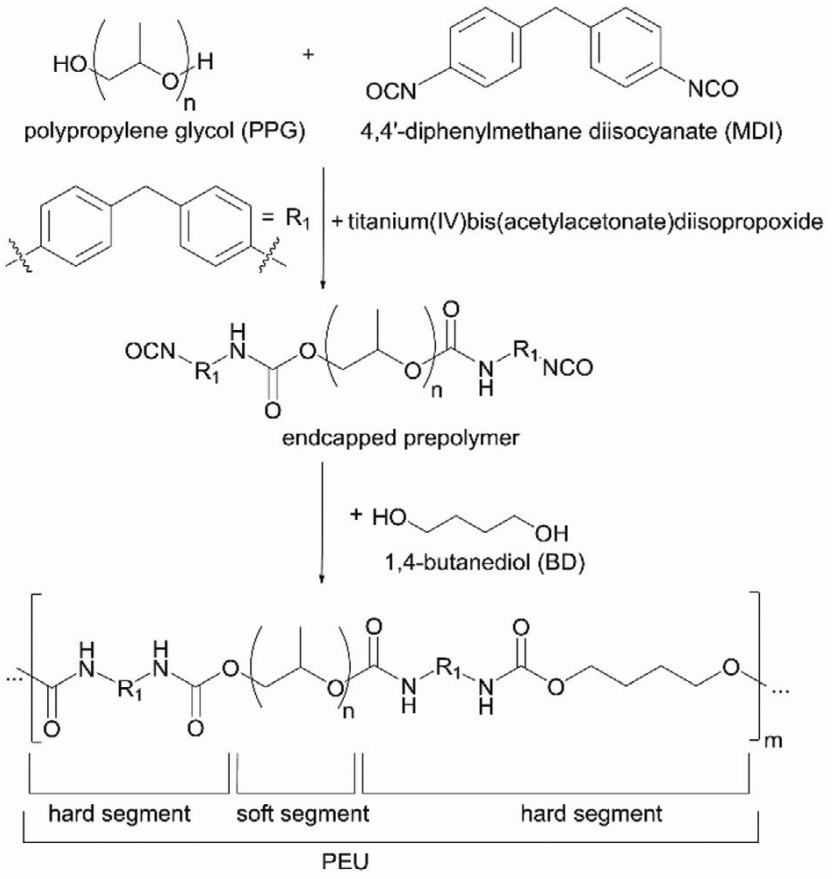

Figure 4.1.1. Synthesis of polypropylene glycol (PPG)-based poly(ether urethane) (PEU) via polyaddition reaction using the prepolymer method.

From a structural point of view, the so-called soft segment was composed of the synthesis building block PPG while the hard segment was obtained from the reaction of MDI and BD. In order to obtain a PEU characterized by a good mechanical strength under room temperature conditions, the hard segment content was selected to be 60 wt.%.

The completeness of the polyaddition reaction was verified by Fourier-transform infrared spectroscopy (FTIR) spectroscopy (**Figure S4.1.1**, Supporting Information). In this connection, the characteristic, PEU-related vibrational modes were detected. The reaction was mostly complete since only a very weak signal at 2270 cm^{-1} associated with the presence of freely available isocyanate appeared in the spectrum. Afterward, the PEU was melt extruded into a filament as essential for additive manufacturing via FFF. For this purpose, the same extrusion line was used as recently reported.[19,49] The obtained filament had a smooth surface and a diameter of 2.85 ± 0.10 mm. The narrow tolerance range ensured that an important processing criterion was fulfilled.[19] Afterward, tensile bars and cuboidal specimens were additively manufactured and their mechanical properties characterized (**Figure 4.1.2**).

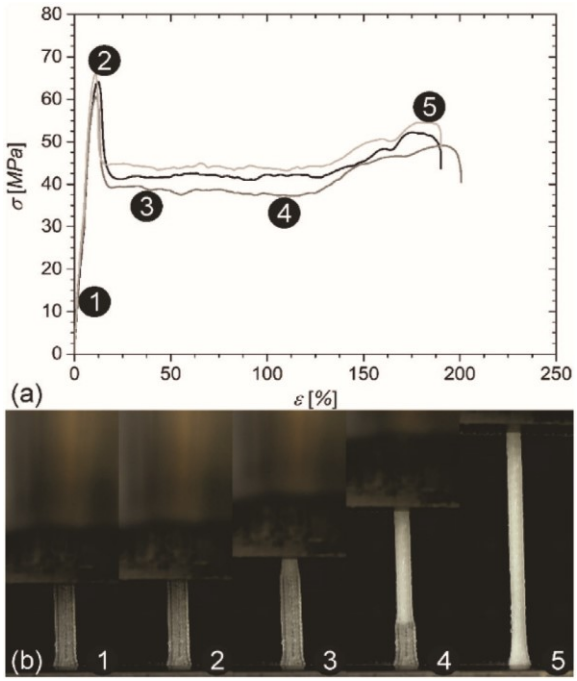

Figure 4.1.2. Engineering stress–strain diagram for PPG-based PEU as determined in tensile tests: a) engineering stress–strain curves and b) the associated deformation behavior. The experiments were carried out at 23 °C with an initial clamping distance of 10 mm.

From the stress–strain relationship, an averaged Young's modulus of 1101.1 ± 80.7 MPa was determined. Compared to other literature on PEU elastomers,[50] the high Young's modulus was expected due to the relatively high hard segment content and the fact that the material was in its glassy state at 23 °C as will be demonstrated below. In all measurements a yield-point was detected at a strain value of 11% ± 1%, corresponding to a stress of 63.6 ± 2.7 MPa (**Figure 4.1.2a**). Further increasing the load resulted in necking (**Figure 4.1.2b**, images 3– 5) as known from other polyurethane-based networks[49,51–53] and strain softening,

followed by weak strain hardening as accompanied by an increase in stress, culminating in specimen rupture at strains of 195% ± 6%. The deformation-related material behavior can be explained with the presence of flexible amorphous PPG segments, which in parts may have been transformed during stretching into stiffer crystalline segments. In another tensile test, the Poisson's ratio of the material was determined to be 0.36, which is a typical value for tough and rigid thermoplastic materials.[54] Furthermore, the density of the PEU was specified to be 1170 kg m^{-3}; the value is in accordance with the one of other PEUs.[55]

Differential scanning calorimetry (DSC) and dynamic mechanical analysis (DMA) were used to investigate the thermal behavior of the PEU and to determine the temperature dependence of the mechanical properties (**Figure 4.1.3**).

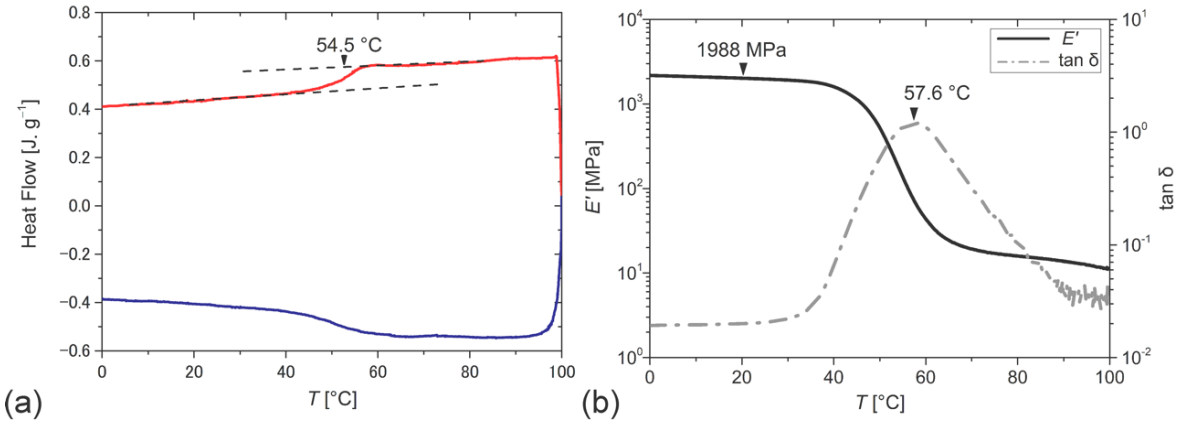

Figure 4.1.3. Thermal and thermomechanical properties of PPG-based PEU as investigated by a) DSC (second heating and cooling at temperature rates of 10 °C x min^{-1}) and b) DMA (temperature dependence of storage modulus *E'*, solid line, and loss factor tan δ, dashed dotted line, at a heating rate of 3 °C x min^{-1}).

In the respective DSC thermogram a thermal transition between 40 and 60 °C could be detected. The temperature associated with the inflection point was about 55 °C (**Figure 4.1.3a**) and assigned to the glass transition temperature of the PEU. The results were confirmed in the DMA measurement (**Figure 4.1.3b**). Here, the stiffness as exemplified by the evolution of the storage modulus *E'* exhibited a one-step decrease corresponding to a drop by more than two orders of magnitude between 40 and 70 °C when passing through the glass transition (**Figure 4.1.3b**, solid line). Thus, a drastic softening occurred. The tan δ peak, which is often used to determine T_g in urethane-based polymers[18] was located at about 58 °C (**Figure 4.1.3b**, dashed dotted line). In comparison with the DSC results, T_g is commonly a few degrees higher in the DMA due to differences in testing procedures and chain dynamics under the respective conditions.[56]

After finalizing the characterization of the PEU, three FFF approaches were followed. First, a 3D printing scenario was considered in which common print settings were used to obtain almost non-thermoresponsive objects from PEU.[32] This was realized by choosing a comparatively high nozzle temperature T_N and by heating the print bed at the same time. Furthermore, a 4D-printing scenario was selected that aimed at the implementation of

stresses by enabling faster cooling of the PEU on the print bed by lowering T_N and turning off the heating element of the build platform. As a final case, 4D-printing of PLA was considered and the same principle as for PEU was applied. The exact print settings are listed in **Table 4.1.1**, along with the print results and evaluation of thermoresponsiveness, as visualized in **Figure 4.1.4**.

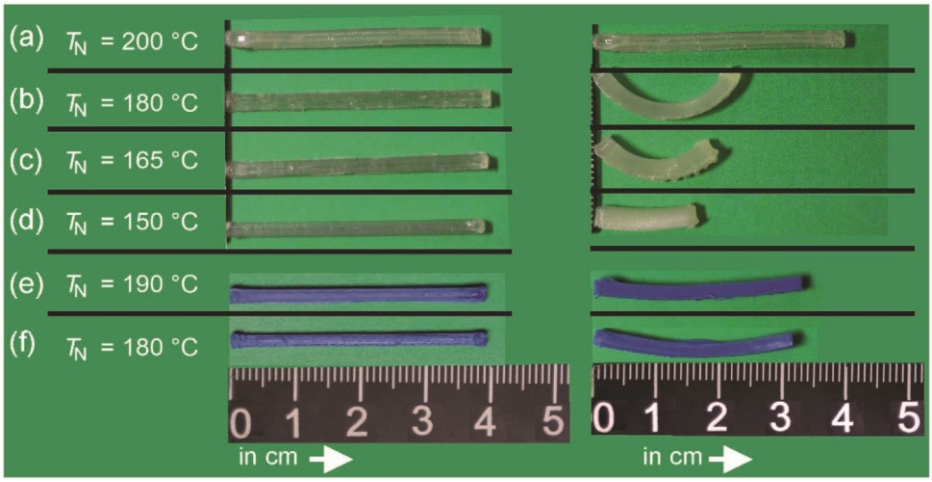

Figure 4.1.4. Printing results and 4D effects after a) classical 3D printing with PEU, b–d) 4D-printing with PEU, and e,f 4D-printing with PLA. The underlying printing conditions are specified in **Table 4.1.1.** The states of the samples are exhibited after printing (left, nozzle temperature T_N) and after heating to 75 °C right).

Table 4.1.1. Selection of printing materials, printing scenarios and parameters (print platform temperature T_p, nozzle temperature T_N, and printing speed S_p = 50 mm x s^{-1}) used for FFF and results of the characterization of the samples before and after triggering the 4D effects regarding the amount of maximum thermally shrinkable strain $\epsilon_{pre} - \epsilon$, arc measure ϑ, and radius of curvature r.

Printing materials/ printing scenarios	Printing parameters		Characterization of 4D effects		
	T_p (°C)	T_N (°C)	$\varepsilon_{pre} - \varepsilon$ (%)	ϑ (°)	r (mm)
PEU, 3D printing	65	200	2.2	≈ 0	∞
PEU, 4D-printing	23	180	41.7	129.8	7.3
PEU, 4D-printing	23	165	50.9	105.3	6.5
PEU, 4D-printing	23	150	58.7	≈ 0	∞
PLA, 4D-printing	23	190	17.8	18.7	140.9
PLA, 4D-printing	23	180	21.0	30.6	81.8

It is noticeable that all additively manufactured samples had a length of about 40 mm (**Figure 4.1.4a–f**). Even when selecting a lower T_N of 150 °C, the adhesion between the individual layers was strong enough in the PEU. When heated to 75 °C, the PEU samples behaved differently: After 3D printing of PEU (**Table 4.1.1**), almost no thermoresponsiveness was detected; the 4D effect was very weak (**Figure 4.1.4a**). Apparently, stress relaxation during printing was supported by the elevated build platform temperature. In contrast, a more rapid cooling of polymer strands after leaving the nozzle and thus a quicker vitrification

could be achieved by 4D-printing (**Table 4.1.1**). As a matter of fact, stress relaxation was only permitted to a minor extent and distinct 4D effects could be witnessed (**Figure 4.1.4b–d**). Intriguingly, almost linear shrinkage occurred when the lowest T_N was used for printing and the PEU was heated to 75 °C (**Figure 4.1.4d**). We assume that the stress stored in every layer was almost the same, which helped the printed part to shrink uniformly without bending. As a result, triggering of the 4D effect gave a very short sample with a length of 16.6 mm (**Figure 4.1.4d**); in relation to the original size of the object, a shrinkage of 59% was detected (**Table 4.1.1**).

When systematically raising T_N, a clear trend toward decreasing shrinkage behavior was verified (**Figure 4.1.4b,c**). Apparently, a partial triggering of the 4D effect occurred when printing the first layers, as hotter layers were laid on top of them. Furthermore, the samples were curved as evidenced by values for arc measure $\theta > 85°$, while the corresponding radius of curvature r increased (**Table 4.1.1**). This allowed a very high degree of control over the shrinkage behavior and shows the possibility to control not only the degree of shrinkage but also the shape transformation. Thus, the PEU followed the same physical laws as known from thermoplastics such as other poly(ether urethanes),[36,45] PLA,[42,43,44,57,58] acrylonitrile butadiene styrene (ABS),[44] and high impact polystyrene (HIPS).[44]

The results of 4D-printing with PLA (**Table 4.1.1**) are exhibited in **Figure 4.1.4e,f**. In this case, the shrinkage of PLA was smaller than the 4D effect of PEU (**Figure 4.1.4b–d**). Anyway, further printing tests were carried out with different 3D printers. In each case, the 4D effects could be reproduced regardless of the 3D printer and material used and were therefore printer independent.

For a more detailed insight into the evolution of strain upon heating, DMA measurements were carried out on 3D and 4D-printed samples (**Figure 4.1.5**).

Heating to 75 °C and thus above the glass transition temperature of the PEU resulted in strain decreases of ≈−3.9% when applying 3D printing (**Figure 4.1.5a**) and of −64.1% after 4D-printing (**Figure 4.1.5b**). Upon 4D-printing with PLA a strain decreases of −18.7% was detected (**Figure 4.1.5c**). The reason for the even higher release of strain compared with the measurement above (**Figure 4.1.4d**) was that the material was allowed to relax 15 min longer at 75 °C. Returning to PEU, it can be clearly seen in **Figure 4.1.5b** that the polymer started shrinking upon heating to about 40 °C, which almost corresponds to the onset temperature of the glass transition determined in the DSC measurement (**Figure 4.1.3a**). It can also be deduced that the state of the PEU as achieved after heating is stable at ambient temperature, which also applies to PLA (**Figure 4.1.5c**).

To elucidate the effect of 4D-printing on the thermomechanical properties, the respective PEU sample was investigated by DMA (**Figure S4.1.2**, Supporting Information). In comparison with

3D printed PEU (**Figure 4.1.3b**), the 4D-printed sample had an increased storage modulus at lower temperatures together with a slightly higher value for the tan δ signal. Latter is assumed to be due to the more rapid cooling of the material under its T_g in a higher oriented state, which obviously contributed to an accelerated vitrification of the PEU.

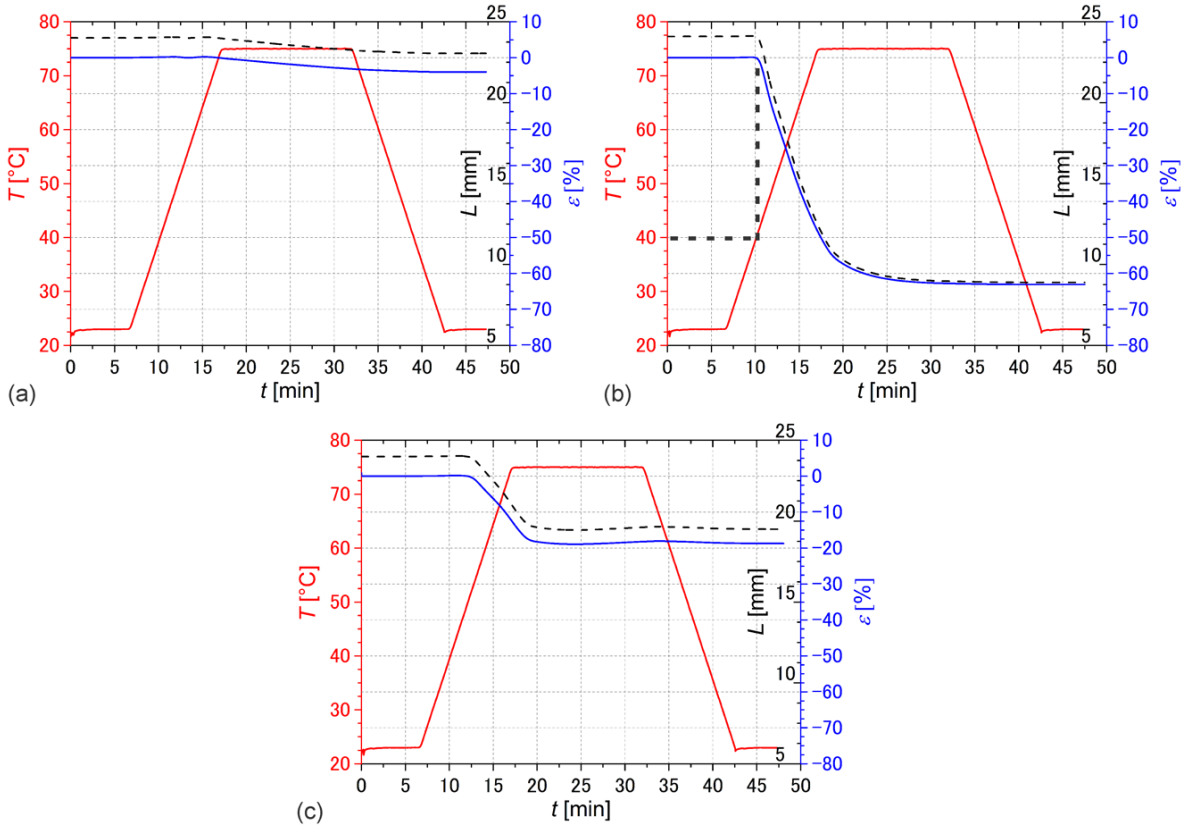

Figure 4.1.5. DMA, illustrating the evolution of strain ϵ (blue, solid line) and length L (black, dashed line) on variation of temperature T (red, solid line). The samples investigated were a) 3D printed PEU, b) 4D-printed PEU (T_N = 150 °C), and c) 4D-printed PLA (T_N = 180 °C).

Next, the temperature distribution during 3D and 4D-printing of PEU was followed by in-situ thermal imaging (**Figure 4.1.6**); a more detailed evaluation is included in **Table S4.1.1** in the Supporting Information.

As expected, when selecting a T_N of 200 °C and a build platform temperature of 65 °C, the latter temperature was approximately maintained by the PEU after strand deposition so that the material was almost not able to cool below its T_g (**Figure 4.1.6a** and **Table S4.1.1**, Supporting Information). The choice of a lower T_N of 150 °C combined with a build platform temperature of 23 °C in turn allowed the individual strands of PEU to cool rapidly to ambient temperature on the print bed (**Figure 4.1.6b** and **Table S4.1.1**, Supporting Information), thus reducing polymer stress relaxation to a minimum and later enabling a pronounced 4D effect. As most crucial for our approach, the PEU only took about 10 ms to cool below its T_g. Another aspect is that the topmost layer's temperature increased from the first layer to about the sixth layer and then remained almost constant (**Table S4.1.1**, Supporting Information), which later supported a uniform shrinkage behavior of the 4D-printed sample.

In a progressive approach, we discovered that the chosen 4D-printing method is not limited to the production of smaller samples. In fact, three objects made from PEU with heights strongly exceeding 5 mm could be fabricated (**Figure 4.1.7**).

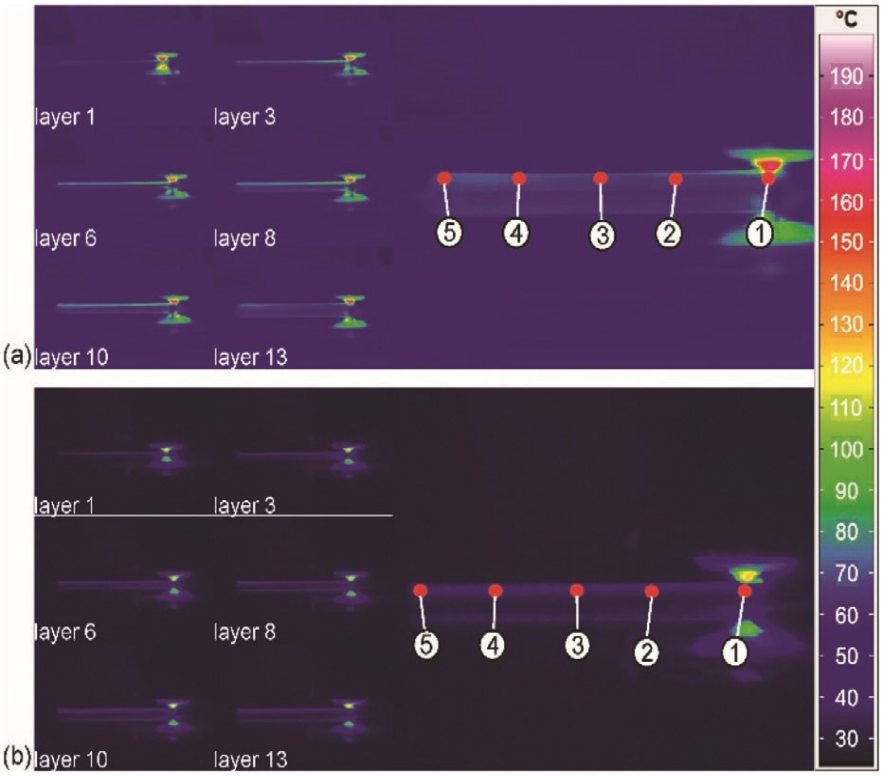

Figure 4.1.6. In situ thermal imaging to supervise PEU during a, top) 3D printing and below) 4D-printing. On the left side, randomly selected top layers are exhibited while the strand is being deposited. The enlarged images on the right side show the temperature distribution in layer number 13 at five randomly selected positions. A printing speed of 50 mm x s^{-1} and a T_N of a) either 200 °C or b) 150 °C were used.

Upon heating to 75 °C for 15 min, the length of the samples decreased in the *x*-, *y*-printing plane while the height *z* increased substantially (**Figure 4.1.7**). In detail, the thin solid cuboid sample shrank by about −53% along the *x*-axis and expanded by about +33% and +85% along the *y*- and *z*-axis, respectively (**Figure 4.1.7a**). The hollow cuboid sample also showed a similar dimensional change on heating with about −47%, −47%, and +85% along the *x*-, *y*-, and *z*-axis (**Figure 4.1.7b**). The third print object, namely the hollow cylinder (**Figure 4.1.7c**), was also able to uniformly shrink in the printing plane by about −55% and expanded along the *z*-axis by about +79%. This demonstrates that another massive expansion could be achieved, although a different sample geometry was used. As a result, the inner diameter decreased from 13.5 to 3.9 mm. In other words, drastic almost uniform shrinkage behavior could be verified in every single case.

In **Table 4.1.2** our results are compared with previous works on 4D-printing using PLA, HIPS, ABS, and TPU. The PEU examined here exhibits by far the greatest 4D effect. Although a systematic is not necessarily obvious, which is in particular because of the different printing parameters and discrepancies in the height of the objects, we assume that more pronounced 4D effects can essentially be attributed to the fact that the temperature difference between the nozzle and the material-specific glass transition temperature ($T_N - T_g$) is as low as possible. This seems particularly logical in view that the polymer must be cooled as quickly as possible below its T_g after leaving the nozzle in order to fix the orientation of polymer chains without

strong stress relaxation. In the current work, the temperature delta $T_N - T_g$ is with 90 °C for PEU by far the lowest compared to the other scientific contributions on TPU. In the case of PLA, it is also obvious that the magnitude of the 4D effect is the strongest for higher objects that could be proven so far, even drastically exceeding the value for $\epsilon_{pre} - \epsilon$ as published by Rajkumar et al.[44]

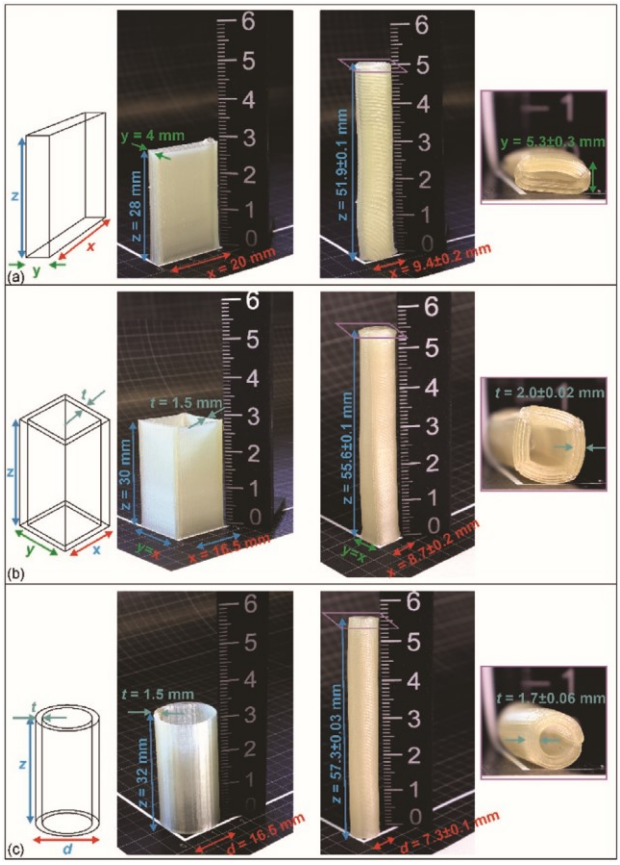

Figure 4.1.7. Samples of 4D-printed PEU (**Table 4.1.1**, T_N = 160 °C) consisting of a a) solid cuboid, b) hollow cuboid, and c) hollow cylinder. The objects were built up by 187, 200, and 213 layers, respectively. From left to right in every image series, a vector diagram, the states after 4D-printing and after heating to 75 °C for 15 min are shown together with the inset focusing on the cross-section. The parameters of the samples were specified in terms of their *x*, *y*, and *z* coordinates same as the wall thickness *t* and outer diameter *d*.

As we now had the right materials and high degree of control over their thermoresponsiveness, the potential application as hands-free door opener moved into our focus. Therefore, an initial rough design was developed for an elliptical profiled door handle (**Figure 4.1.8**).

To keep the complexity as small as possible, the entire system was designed from one material. In a next step, the structure was analyzed, and a numerical shape optimization was carried out. Finally, the ribbing in the core was optimized. The objective functions in the structural optimization steps are the compliance minimization and the reduction of stresses under the constraint of easy printability. The same pressure load on the top surface of the handle was assumed in the finite element simulation for all variants in the successive

optimization procedure. Different intermediate designs were made for PEU and PLA (**Figure 4.1.9**).

Table 4.1.2. Overview on thermal properties, processing temperatures, and the amount of the maximum thermally shrinkable strain $\epsilon_{pre} - \epsilon$ for 4D-printed objects built up from thermoplastic polymers via FFF.

Material	Literature	T_N [°C]	T_g [°C]	$\Delta(T_N - T_g)$ [°C]	T_p [°C]	S_p [mm · s^{-1}]	$\varepsilon_{pre} - \varepsilon$ [%]
PLA	Zhang et al.[186]	230	60-65	170	90	10-150	22.7 (z = 0.6 mm)
	van Manen et al.[178]	210	60-65	150	60	60	38 (z = 0.05 mm)
	Rajkumar et al.[185]	220	60	160	60	30-120	14 (z = 2 mm)
							10 (z = 5 mm)
	current work	190/180	60	130	23	70	21.0 (z = 2 mm)
HIPS	Rajkumar et al.[185]	260	100	160	100	30-120	27 (z = 2 mm)
							20 (z = 5 mm)
ABS	Rajkumar et al.[185]	240	110	130	110	30-120	20 (z = 2 mm)
							14 (z = 5 mm)
TPU	Bodaghi et al.[180]	210/230	60	150/170	24	30-40	37.3 (z = 1 mm)
	Hu et al.[179]	233	60	173	24	20-50	26.7 (z = 1 mm)
	current work	180-150	60	120-90	23	50	63.1 (z = 2 mm)
							–53 (x), +33 (y), and +85 (z) (z = 28 mm, solid cuboid)
							–47 (x), –47 (y), and +85 (z) (z = 30 mm, hollow cuboid)
							–55 (x and y), and +79 (z) (z = 32 mm, hollow cylinder)

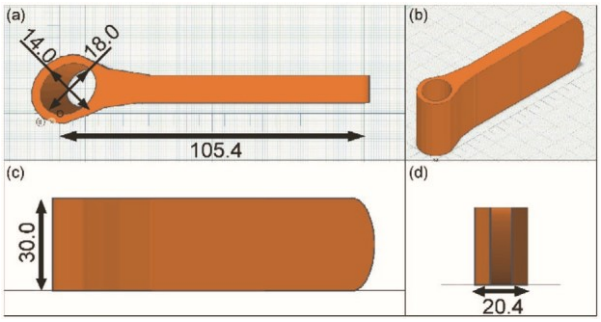

Figure 4.1.8. Technical drawing of a 4D-printable hands-free door opener in the perspectives a) top view, b) isometric view, c) front view, and d) right view. All data are provided in mm.

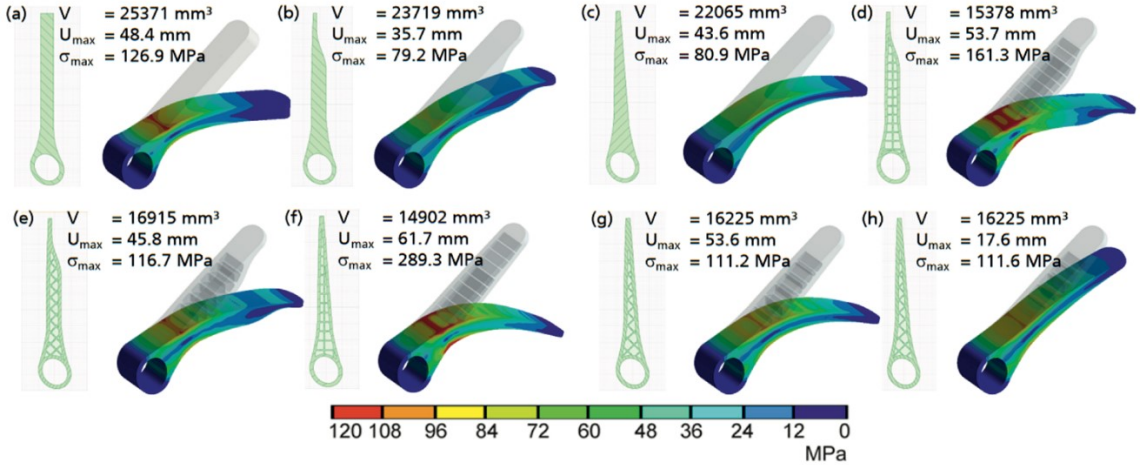

Figure 4.1.9. Simulation of hands-free door openers using ANSYS software. Simulation results for PEU: a) Design 1, b) design 2, and c) design 3 with an infill of 100%. Design 2 with d) 90° grid infill (design 2.1) and e) 45° grid infill (design 2.2), design 3 with f) 90° grid infill (design 4.1), g) 45° grid infill (design 3.2), and for PLA h) 45° grid infill (design 3.2) (volume V, max. deformation U_{max}, and max. von Mises equivalent stress σ_{max}).

The rough design of the hands-free door opener (**Figure 4.1.8**) was used as starting point for our simulation (**Figure 4.1.9a**). To optimize the mechanical behavior, two further designs were developed based on an infill of 100% (**Figure 4.1.9b,c**). To keep the consumption of printing material as low as possible, further modifications were made by introducing support structures as included in **Figure 4.1.9d–g**. In the respective simulations, a load of 0.5 MPa was distributed over the topmost surface of the hands-free door openers, which measured about 2070 mm^2 in surface area, corresponding to a resulting force of 1035 N. The associated deformation behavior as well as the maximum von Mises equivalent stress largely depended on the respective design. In this context, the design shown in **Figure 4.1.9g** proved to be particularly advantageous. Here, the comparatively lowest maximum stress was detected in the material, which means that the virtual design, when also considering potential material savings, was best able to uniformly distribute the applied load as evidenced by a maximum stress of 111.2 MPa. Due to the material-efficient production and optimum stress-loading capability, the corresponding standard triangle language (STL) file was chosen for the 4D-printing of demonstrators using the optimized printing parameters for PEU (**Table 4.1.1**,

T_N = 160 °C). Taking into account the respective deformation behavior of PLA (**Figure 4.1.9h**), the same design was selected for 4D-printing with PLA (**Table 4.1.1**).

In the next step, the practicability of our demonstrator was investigated starting with PEU as print material (**Figure 4.1.10**).

Therefore, the hands-free door opener was pushed onto a door handle (**Figure 4.1.10a,b**) and the polymer was localized heated to 100 °C (**Figure 4.1.10c–e**; more detailed information is supplied in **Figure S4.1.3**, Supporting Information). Due to the triggering of the 4D effect, the door opener connected with the door handle. Once cooled to 23 °C, an opening of the door with a forearm or an elbow became possible without the hand coming into contact with the door handle (**Figure 4.1.10f,g**), thus supporting the underlying hygiene concept.

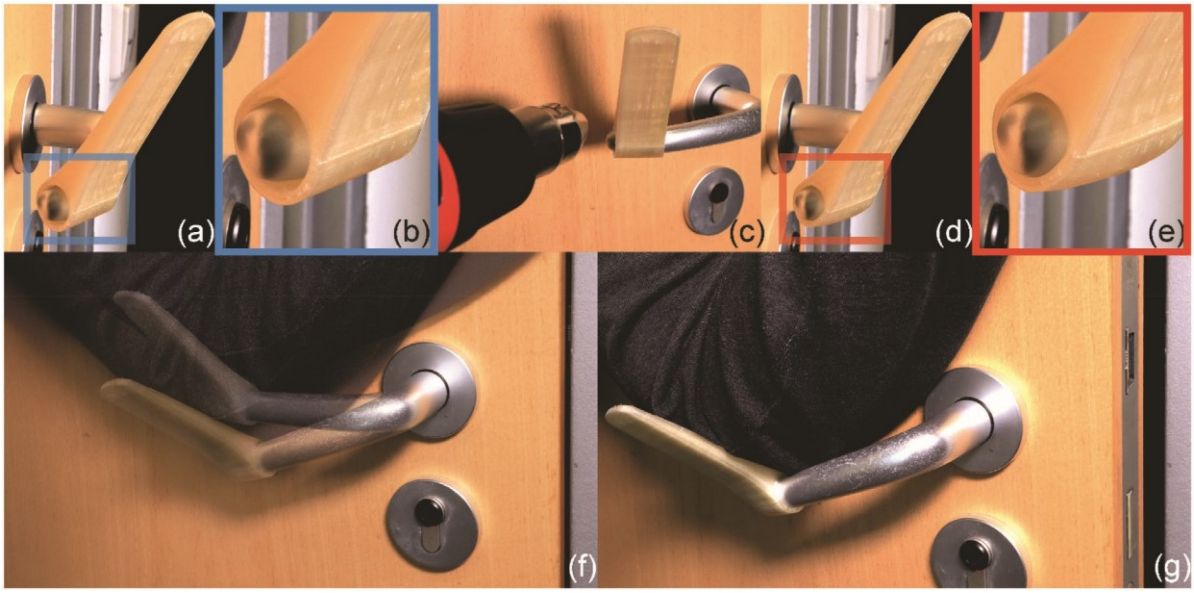

Figure 4.1.10. Assembly and usage of a 4D-printed hands-free door opener made from PEU. An elliptical profiled door handle served as a counterpart. a) Step one: Placement on the door handle, b) enlarged image of (a), blue box, c) step two: triggering of the 4D effect with a heating gun, d) fixation as achieved by shrinking the hands-free door opener, e) enlarged image of (d), red box, f) step three: two overlapping images of the system in use and g) opening of the door.

To illustrate the good application perspective in the current corona situation, the print material was exchanged by commercially widely available PLA and further demonstrators were fabricated (**Figure S4.1.4**, Supporting Information). Compared to the demonstrator made of PEU, the 4D shrinkage behavior was not as pronounced here when a shrinkage temperature of 100 °C was selected, which caused the fastener to slip off the door handle. This was traced back to the weaker 4D effect of PLA (**Figure 4.1.4**), but could be avoided when increasing the localized temperature up to 140 °C, whereby a considerably improved shape fit between the attachment and the door handle could be achieved. Due to the high shrinkage temperature selected, we assume that in parts a physical melting of PLA could have occurred.

Tribological tests were conducted to measure the breakaway torque of the door openers after their attachment to a rotating oval shaft. In **Figure 4.1.11** can be seen that the attachments made from PLA showed higher breakaway torque values of about 1.5 N m

compared to those manufactured from PEU (≈0.75 N m). Beyond that, after the initial relative movement between the polymer and the shaft, a higher torque had to be applied when selecting PLA as base material to move the opener further against the shaft. This can be explained with the in parts physical melting and solidifying of PLA since a significantly higher temperature was used to trigger the 4D effect. Anyway, the behavior of both PLA and PEU emphasizes the good suitability of the hands-free door openers investigated.

In a next step, a disassembling of 4D-printed hands-free door openers made from PEU and PLA was carried out (**Figure S4.1.5**, Supporting Information). Upon heating, the materials became soft, where upon the attachment could be easily removed. In other words, it was the material stiffness, which could be thermoreversibly changed according to a program that has been defined by the molecular structure, which opened an advantage for the outlined application at its end-of-use. The thermoplastic nature of the two polymers allowed for a mechanical recycling as exemplarily done for PEU. Therefore, the disassembled door handles were collected, granulated, and re-extruded (**Figure S4.1.6**, Supporting Information). After the first cycle consisting of mechanical recycling and reprocessing of PEU, the glass transition temperature remained almost identical while the mechanical properties were hardly affected (compare **Figure 4.1.3b** and **Figure S4.1.7**, Supporting Information). By contrast, T_g and the Young's modulus of PEU tended to decrease at lower temperatures after conducting a fifth recycling step (**Figure S7**, Supporting Information), which may be associated with the degradation effects. For this reason, varying thermomechanical properties should be taken into account when reusing PEU in 4D-printing processes. Alternatively, the usage of stabilizers may contribute to a further enhancement of technological maturity. However, 4D re-printability was proven for one-time recycled PEU as evidenced by a maximum thermally shrinkable strain $\epsilon_{pre} - \epsilon$ of 57%.

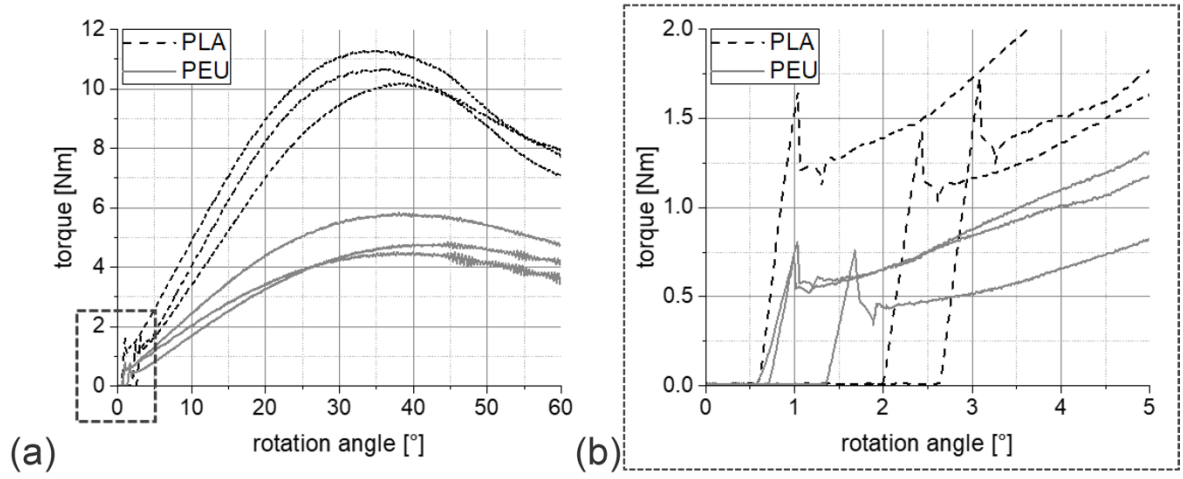

Figure 4.1.11. Measurement of the torque via the rotation angle for 4D-printed PEU- and PLA-based hands-free door openers, which in course of assembling were heated to 90 °C (PEU) and 140 °C (PLA), respectively. a) Torque over the complete rotation angles of 90°. b) Enlarged section of the torque within the first 5°.

4.1.3. Conclusions

In this contribution, we introduce a new type of PEU as suitable for additive manufacturing via FFF. If the difference between the nozzle temperature and the material-specific glass transition temperature of the polymer is kept as small as possible in the printing process, objects are obtained whose shape and thermoresponsiveness can be precisely controlled. Most remarkably, the results demonstrate 4D effects of a previously unknown degree. The transfer of the findings from the FFF process to PLA as a printing material indicates that the suggested 4D-printing method can be applied to other thermoplastics, too. Since heating of the printing bed can be avoided, the FFF process consumes less energy compared with the standard settings used in 3D printing. 4D-printing is generally attractive because it does not require any energy-consuming thermomechanical treatment of a shape memory polymer afterward—the thermoresponsive object can be taken directly from the printer. Therefore, a wide range of potential applications based on highly shrinkable objects is foreseeable. In a first step, hands-free door openers for the health sector were developed. The door handle attachments have the potential to support the containment of viruses, like in the current severe acute respiratory syndrome coronavirus-2 (SARS-CoV-2) pandemic, as well as smear infections. A sustainable “product” design is now available. The developed lightweight constructionischaracterizedbyhighmechanicalload-bearingcapability at optimized printing material consumption. In principle, other shapes of door handles can be addressed by minor design adjustments. As a result of shrinking hands-free door openers onto door handles, permanent mounting is possible; no additional fastening elements are required as in other systems.[59–62] In addition, our concept allows an uncomplicated disassembly at the end-of-use due to the thermally switchable mechanical stability, which we consider as programmable mechanical stiffness. As our demonstrators are made in every single case from one thermoplastic material, a mechanical recycling is possible. Exactly this step allows for a reprinting with PEU, whose one-time recycled sample also exhibited a high degree of thermally inducible shrinkage. Although this can be understood as a step toward laying the foundations for a circular economy for highly functional 4D materials, further research efforts are needed to stabilize the functional properties in the long term and thus enable safe reusability. It is the combination of technological approaches like functional design development, 4Dprinting, assembly, disassembly and mechanical recycling that should be considered from the beginning of the development of a demonstrator to the end of its use. This illustrates the great application potential of programmable materials, with which they can fulfill the function of products or their components and thus make valuable contributions in the future.

4.1.4. Experimental Section

Materials: Desmophen 1262 BD was supplied by Covestro Deutschland AG (Leverkusen, Germany). The polymer is a linear PPG exhibiting a molecular weight of about 430 g x mol^{-1}

(acid value ≤ 0.1 mg KOH x g^{-1} and hydroxyl value = 260 ± 10 mg KOH x g^{-1}, Covestro AG, Desmophen 1262 BD, Technical Data Sheet 2016[63]) and was used as soft segment component for PEU synthesis. Titanium(IV)bis(acetylacetonate) diisopropoxide was obtained from Merck (Darmstadt, Germany), 4,4'-methylene diphenyl diisocyanate (MDI) was purchased from Fisher Scientific (Schwerte, Germany), BD, and a sodium aluminosilicate molecular sieve (Zeolite 4Å) were obtained from Alfa Aesar (Kandel, Germany). To absorb water prior synthesis, PPG-diol and BD were stored over molecular sieve for at least one day at 23 °C.

Grey PLA filaments were bought from Prusa Research A.S. (Prague, Czech Republic) while commercially available neon-yellow, blue, and orange PLA filaments were obtained from Filamentworld (Ulm, Germany). In any case, the samples were characterized by a glass transition temperature T_g of about 60 °C.

Synthesis of Thermoplastic Polyurethane: The polypropylene glycol based thermoplastic polyurethane (PPG-PEU) was synthesized using the prepolymer method. The ratio of the reactants was chosen so that the hard segment content was ≈60 wt.%. Therefore, the molar ratio of the reactants PPG, MDI and BD was set to 1: 2.17: 1.16. The reaction was carried out with a slight excess of isocyanate (NCO/OH = 1.005). First, the PPG-diol was heated under nitrogen flow and stirring to 125 °C. Then, two droplets of a catalyst solution consisting of PPG-diol and 5 wt.% of titanium (IV) bis(acetylacetonate) diisopropoxide were added. After a few seconds, MDI was added, and the mixture was further heated to 155 °C and held there under continuous stirring for 5 min. Afterward the obtained prepolymer was brought to reaction with BD, serving as chain extender. In parallel, the stirring speed was raised. As soon as the viscosity increased significantly, the reaction was stopped, and the melt was poured onto a plate covered with a thin foil made of polytetrafluoroethylene. Finally, the obtained PEU was cured in an oven at 80 °C for 120 min.

Extrusion: The synthesized PEU was ground with a cutting mill of the type M 50/80 from Hellweg Maschinenbau (Roetgen, Germany). The obtained flakes were dried at 110 °C for 150 min in a vacuum drying chamber VDL 53 from Binder GmbH (Tuttlingen, Germany). Subsequently, the flakes were fed into an extruder to produce filaments with a diameter of 2.85 mm. The individual units of the extrusion line were put together in such a way that it included the volumetric material feeding system Color-exact 1000 from Plastic Recycling Machinery (Tranekær, Denmark), a Leistritz twin screw extruder MICRO 18 GL from Leistritz AG (Nürnberg, Germany), characterized by seven heating zones and a screw length of 600 mm, a conveyor belt, and a filament winder from Brabender GmbH and Co. KG (Duisburg, Germany). The temperatures of the individual heating zones of the extruder were 200, 200, 202, 203, 190, 180, and 180 °C.

Determination of Density: The density of the PEU was determined for a piece of filament by means of the buoyancy method following the Archimedes principle. Therefore, a KERN YDB-03 attachment was used for the analytical balance KERN AJE from KERN and SOHN GmbH (Balingen, Germany). At 23 °C, ≈0.7 g of the PEU were weighed out both in air as well as in ≈300 mL of demineralized water. The density ρ_{PEU} was calculated according to **Equation 4.1.1**,

considering the determined masses m_{air} and m_{water}, respectively, and the density of demineralized water ρ_{water} at 23 °C.

$$\rho_{PEU} = \frac{m_{air}}{m_{air} - m_{water}} \times \rho_{water} \qquad (4.1.1)$$

Virtual Design, Simulation, and Fused Filament Fabrication: Tinkercad is an online 3D modeling computer-aided design (CAD) program.[64] It was used for the virtual design of the samples described in this work. These include type 5B tensile bars[65] as used for the evaluation of the mechanical properties and cuboids with dimensions of 35 mm × 6 mm × 3 mm for thermal investigations. Solid cuboids measuring either 40 mm × 2 mm × 2 mm or 40 mm × 4 mm × 28 mm were designed to study the 4d shrinkage behavior same as a hollow cuboid having a dimension of 16.5 mm × 16.5 mm × 30 mm with a wall thickness of 1.5 mm and a hollow cylinder with an outer diameter of 16.5 mm and a height of 30 mm at a wall thickness of 1.5 mm. Furthermore, demonstrators for hands-free door openers were designed. The CAD models were exported as STL files.

The initial design of a door handle attachment is exhibited in **Figure 4.1.12** and was imported into the finite element analysis software ANSYS,[66] which was used for design optimization and simulation.

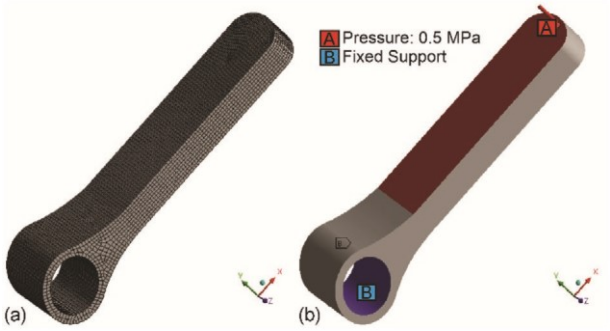

Figure 4.1.12. Mesh and boundary conditions for the stress–strain analysis of a door handle attachment using ANSYS. a) Hexahedral finite element mesh and b) definition of the boundary condition, A = applied load and B = fixed bearing.

In the first step, a mesh was generated for the CAD geometry (STL format) consisting of 26931 hexahedral elements and 123592 nodes (**Figure 4.1.12a**). To evaluate the stress distribution, a pressure load of 0.5 MPa was applied on the top surface (A in **Figure 4.1.12b**) while at the same time it was assumed that the elliptical hollow part of the door opener was attached to a rigid rod (B in **Figure 4.1.12b**). The stress distribution and the material required for the fabrication of the design were analyzed. The design was optimized in two steps. In the first step, the topology optimization tool of ANSYS was applied to optimize the outer shape. Then, in the second optimization step, several designs for the inner rib structure were studied and compared manually.

The following parameters were considered in the finite element analysis of the door handle attachment: the density of the PEU, the Young's modulus, and the Poisson's ratio. In case of PLA, a Young's modulus of 3500 MPa, a density of 1240 kg m^{-3} and a Poisson's ratio of 0.36

were extracted from literature[67,68] to carry out the structural analysis within the design optimization loop.

After finalizing the design of the hands-free door opener and cuboidal samples, the 3D models in STL format were imported into the slicer program Cura 4.8.0.[69] The cuboidal samples were first processed with standard 3D printing parameters. In case of 4D-printing, the T_P and T_N were varied while keeping S_p = 50 mm x s^{-1} constant for both PEU and PLA. Additionally, the layer height of 0.15 mm and a nozzle diameter of 400 µm were kept the same throughout the study. Subsequently, additive manufacturing was carried out to fabricate the abovementioned samples in three different printing scenarios (**Table 4.1.1**). All printed objects were produced via FFF using the commercially available 3D printers Ultimaker S5 and Ultimaker 3 from Ultimaker B.V. (Utrecht, the Netherlands), Roboze One Xtreme from Roboze S.P.A. (Bari, Italy), PYOT OneProfessional from PYOT Labs GmbH (Berlin, Germany), and Original PRUSA I3 MK2 from Prusa Research A.S. (Prague, Czech Republic). At the beginning of every printing process, a thin layer of Magigoo adhesive from Thought3D Ltd.[70] was applied to the building platform to achieve a good adhesion of the printed objects. As a starting point for conducting the experiments, print settings were chosen that were based on those from a previous work.[19]

Characterization of Mechanical Properties: The mechanical behavior of the synthesized PEU was investigated in tensile tests using the universal testing machine Criterion Model 43 from MTS Systems Corporation (Eden Prairie, MN, USA). The device was equipped with a 500 N load cell. The measurements were carried out on dog-bone shaped tensile bars of type 5B[65] as obtained from FFF. While stretching, the velocity of 1% x min^{-1} was kept constant until a total strain of 5% was achieved in order to enable a more precise determination of the Young's modulus and the Poisson's ratio, before the specimen was further elongated with a velocity of 100% x min^{-1} until failure occurred. Every tensile test was carried out three times at ambient temperature.

The Poisson's ratio *v* of the PEU was characterized in tensile tests on type 5B tensile bars.[65] For this purpose, a Canon M50 camera was used to take pictures of the sample every second as the stretching progressed. The images were then imported into GOM Correlate 2020 from GOM GmbH (Braunschweig, Germany). The 2 mm width of the tensile bar was used to calibrate the reference length. After selecting the front face of the tensile bar using the surface component tool, the axial strain ϵ_{axial} and the transverse strain ϵ_{trans} were determined for strains between 2% and 6%. The Poisson's ratio *v* was then calculated according to **Equation 4.1.2**.

$$v = \frac{\varepsilon_{trans}}{\varepsilon_{axial}} \qquad (\mathbf{4.1.2})$$

Characterization of Thermal and Thermomechanical Properties: The phase transitions of the PEU or PLA were characterized by DSC using a Q100 DSC from TA Instruments (New Castle, DE, USA). The experiments were conducted on dried pieces of filament made from PEU and PLA and on the respective recycled samples. In any case, the samples were characterized by a weight of about 5 mg. The samples were first heated from 0 to 100 °C before being cooled back to 0 °C. The whole thermal cycle was repeated to finalize the measurement. Both for

cooling and heating, a rate of 10 °C x min^{-1} was applied. The temperature holding time at the minimum and maximum temperature was 2 min. The glass transition temperature was determined for the second heating as the temperature at half the step height between the tangents of the baseline using the standard analyzing software of the calorimeter.

The thermomechanical properties of PEU and PLA were studied on both 3D and 4D-printed samples of PEU and on 4D-printed samples of PLA. Additionally, mechanically recycled samples of PEU were investigated by DMA. The experiments were carried out with a Q800 DMA from TA Instruments (New Castle, DE, USA) using single cantilever clamps on multifrequency–strain mode. A frequency of 10 Hz, a static force of 0.1 N, and an oscillating amplitude of 10 µm were selected. Additively manufactured cuboidal samples with dimensions of 35 mm × 6 mm × 3 mm were clamped with a length of 17 mm in the specimen holder. At first, every sample was cooled to 0 °C and held there for 5 min, before it was heated to 100 °C with a rate of 3 °C x min^{-1} and held there once again for 5 min.

Characterization of 4D Effects: The additively manufactured samples (**Table 4.1.1**) were placed for either 5 or 15 min at 75 °C in a UF110 heating chamber from Memmert GmbH + Co. KG (Schwabach, Germany). The dimensions of the samples before and after heating were measured with a Vernier caliper from Fowler High Precision GmbH (Massachusetts, USA).

In detail, the strain before heating ϵ_{pre} and the strain ϵ after triggering of the 4D effect were determined. In those cases, in which samples have bent through, the radius of curvature *r*, and arc measure θ were determined. Therefore, the sample before and after heating was photographed using a Canon M50, and the images were imported into CorelDraw 2019[71] and evaluated with a dimensioning tool as illustrated in **Figure 4.1.13**.

A Q800 DMA from TA Instruments (New Castle, DE, USA) was utilized to investigate the heating-initiated shrinking behavior of PEU and PLA. For this purpose, cuboid samples with a dimension of 40 mm × 2 mm × 2 mm according to 3D printing and 4D-printing of PEU (T_N = 150 °C, **Table 4.1.1**) and 4D-printing with PLA (T_N = 180 °C, **Table 4.1.1**) were manufactured and fixed in the film tension clamps of the DMA device. The 4D effect was adjacently studied under stress-free conditions by following changes in strain. For this purpose, every sample was first kept at 23 °C for 5 min, before it was heated to 75 °C and the temperature was held constant for 15 min. Afterward, the samples were cooled back to 23 °C and kept there for 5 min.

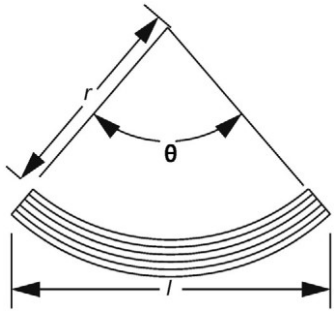

Figure 4.1.13. Schematic representation of a curved 4D-printed object after heating (final length *l*, radius of curvature *r*, and arc measure θ).

In Situ Thermal Imaging of FFF Printing Process: In situ thermal imaging was done with a VarioCAM High Definition from InfraTec GmbH (Dresden, Germany) to study the FFF printing processes (**Table 4.1.1**). In course of additive manufacturing the thermal images were recorded with a frequency of 15 Hz and evaluated with the software IRBIS 4.1[72] from InfraTec GmbH. The temperature of the PEU was measured at five different points on the topmost layer of every sample investigated.

Assembly and Disassembly of Hands-Free Door Openers: The handsfree door opener was either additively manufactured from self-synthesized PEU or from commercially available PLA (Filamentworld-Ulm, Germany and Prusa Research A.S.-Prague, Czech Republic) using the abovementioned 4D-printing scenarios (**Table 4.1.1**, PEU: T_N = 160 °C; PLA: T_N = 190 °C). After inserting the attachment to the end of the door handle on an exemplary selected door, the elliptical part of the attachment was heated to 100 °C in case of PEU and to either 100 or 140 °C in case of PLA using a heating gun from Conrad Electronic (Hirschau, Germany). Upon triggering the 4D effect, the materials became soft and the attachment was manually placed in the right position of the door handle. The attachment was later allowed to cool to 23 °C, which took ≈20 min. To investigate the disassembly process, hands-free door openers were heated to 100 °C in case of PEU and to 140 °C in case of PLA. As the materials became soft, the attachments could be removed from the door handle without residue.

Tribological Characterization: The tribological properties of the handsfree door openers were investigated by means of a two-column testing system (Co. Instron, E10000, torque: max. 100 Nm, normal load: max. 10 kN). With this electrically controlled universal testing machine, the load on the hands-free door opener was simulated as closely as possible to the application by a rotational movement (**Figure 4.1.14**).

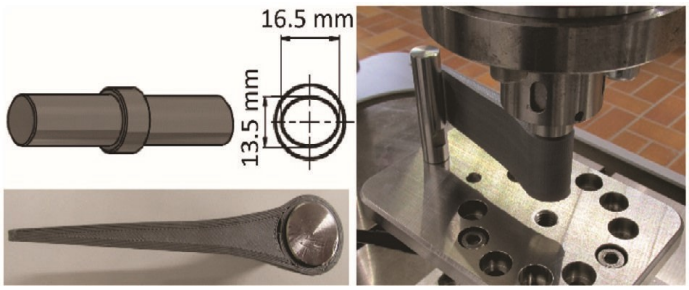

Figure 4.1.14. Mechanical characterization of the hands-free door openers using a two-column testing system.

The hands-free door opener was attached to the rotating oval shaft by heating with an air gun (Co. Steinel, HG2310LCD) whose temperature was set to 140 °C for PLA and 90 °C for PEU. After 5 min, the polymers were cooled back to 23 °C and stored there for 15 min. Adjacently, the experiment started. The test was carried out in a path-controlled manner at a speed of 0.5° x s^{-1}. As a result, the torque was specified via the deflection angle. This allowed to determine the breakaway torque, i.e., the initial slip between the shaft and the polymer, and the further deformation at larger deflection angles.

Mechanical Recycling: Disassembled hands-free door openers made from PEU were collected and shredded separately with a cutting mill type M 50/80 from Hellweg Maschinenbau (Roetgen, Germany) to obtain small granules. The shredded material was subsequently dried, before it was extruded to filament. The PEU was examined by DMA after passing through one and five mechanical recycling and re-extrusion steps, respectively.

The one-time recycled filament was used for 4D reprinting and had a dimension of 40 mm x 2 mm x 2 mm (PEU: T_N = 150 °C, and PLA: T_N = 180 °C, **Table 4.1.1**). The 4D shrinkage behavior was studied.

Supporting Information: Supporting Information is available from the Wiley Online Library or from the author.

Acknowledgements: This work was supported by Fraunhofer Cluster of Excellence "Programmable Materials" under project 630507. T.P. wishes to thank the European Regional Development Fund for financing a large part of the laboratory equipment (project 85007031), Fraunhofer High Performance Center for Functional Integration in Materials for the funding of some of the 3D printers (project 630505) and the future cluster candidate Additive Manufacturing Cluster Berlin-Brandenburg (AMBER), Bundesministerium für Bildung und Forschung, (BMBF project 03ZK102AC) for the conceptual development of end-of-use ideas. Tobias Rümmler is kindly acknowledged for determining the density of the polymer and Nishit Puvati for his contribution in designing some of the images.

Conflict of Interest: The authors declare no conflict of interest.

Author Contributions: The author contribution is as follows: Conceptualization (T.P., L.W.); methodology (D.C., D.S., M.W.); software (D.C., I.S., H.A.); validation (M.W., D.C., D.S., C.S., I.S.); formal analysis (D.C., D.S., C.S., I.S.); investigation (D.C., M.W., D.S.); writing—original draft preparation (D.C., D.S.); writing—review and editing (T.P.); visualization (D.C., D.S., C.S., I.S.); supervision (T.P.); project administration (T.P.); funding acquisition (T.P., T.A., L.W., H.A.). All authors have read and agreed to the published version of the paper.
Data Availability Statement: The data that support the findings of this study are available on request from the corresponding author.

Keywords: 4D-printing, additive manufacturing, device design, healthcare, mechanical properties, shape memory polymers
Received: August 19, 2021; Revised: September 23, 2021; Published online: October 13, 2021

4.1.5. References

1. Dietsch, B., and Tong, T.H., *J Adv Mater*, Vol. 39, 3–12, 2007.
2. Liu, C., Qin, H., and Mather, P.T., *J. Mater. Chem.*, Vol. 17, 1543, 2007.
3. Ratna, D., and Karger-Kocsis, J., *J Mater Sci*, Vol. 43, 254–269, 2008.

4. Pretsch, T., *Polymers*, Vol. 2, 120–158, 2010.
5. Sun, L., Huang, W.M., Ding, Z., Zhao, Y., Wang, C.C., Purnawali, H., and Tang, C., *Materials & Design*, Vol. 33, 577–640, 2012.
6. El Feninat, F., Laroche, G., Fiset, M., and Mantovani, D., *Adv. Eng. Mater.*, Vol. 4, 91–104, 2002.
7. Gall, K., Yakacki, C.M., Liu, Y., Shandas, R., Willett, N., and Anseth, K.S., *Journal of biomedical materials research. Part A*, Vol. 73, 339–348, 2005.
8. Mano, J.F., *Adv. Eng. Mater.*, Vol. 10, 515–527, 2008.
9. Huang, W.M., Yang, B., Zhao, Y., and Ding, Z., *J. Mater. Chem.*, Vol. 20, 3367, 2010.
10. Small, W., Singhal, P., Wilson, T.S., and Maitland, D.J., *J. Mater. Chem.*, Vol. 20, 3356–3366, 2010.
11. Serrano, M.C., and Ameer, G.A., *Macromolecular bioscience*, Vol. 12, 1156–1171, 2012.
12. Wang, K., Strandman, S., and Zhu, X.X., *Front. Chem. Sci. Eng.*, Vol. 11, 143–153, 2017.
13. Sabahi, N., Chen, W., Wang, C.-H., Kruzic, J.J., and Li, X., *JOM*, Vol. 72, 1229–1253, 2020.
14. Pretsch, T., Ecker, M., Schildhauer, M., and Maskos, M., *J. Mater. Chem.*, Vol. 22, 7757, 2012.
15. Ecker, M., and Pretsch, T., *Smart Mater. Struct.*, Vol. 22, 94005, 2013.
16. Ecker, M., and Pretsch, T., *RSC Adv*, Vol. 4, 286–292, 2014.
17. Ecker, M., and Pretsch, T., *RSC Adv*, Vol. 4, 46680–46688, 2014.
18. Fritzsche, N., and Pretsch, T., *Macromolecules*, Vol. 47, 5952–5959, 2014.
19. Chalissery, D., Pretsch, T., Staub, S., and Andrä, H., *Polymers*, Vol. 11, 2019.
20. Carrell, J., Zhang, H.-C., Tate, D., and Li, H., *International Journal of Sustainable Engineering*, Vol. 2, 252–264, 2009.
21. Purnawali, H., Xu, W.W., Zhao, Y., Ding, Z., Wang, C.C., Huang, W.M., and Fan, H., *Smart Mater. Struct.*, Vol. 21, 75006, 2012.
22. Sun, L., Huang, W.M., Lu, H.B., Wang, C.C., and Zhang, J.L., *Assembly Automation*, Vol. 34, 78–93, 2014.
23. Kim, J.-S., Lee, D.-Y., Koh, J.-S., Jung, G.-P., and Cho, K.-J., *Smart Mater. Struct.*, Vol. 23, 15011, 2014.
24. Chiodo, J.D., Billett, E.H., Harrison, D.J., and Harry, P., "Investigations of generic self disassembly using shape memory alloys", in: *Proceedings of the 1998 IEEE International Symposium on Electronics and the Environment, ISEE-1998, May 4-6, 1998, Oak Brook, Illinois,* IEEE Service Center, Piscataway, N.J., pp. 82–87, 1998.
25. Chiodo, J.D., Harrison, D.J., and Billett, E.H., *Proceedings of the Institution of Mechanical Engineers, Part B: Journal of Engineering Manufacture*, Vol. 215, 733–741, 2001.
26. Chiodo, J.D., and Boks, C., *The Journal of Sustainable Product Design*, Vol. 2, 69–82, 2002.
27. Hussein, H., and Harrison, D., *IJPD*, Vol. 6, 431, 2008.
28. Abuzied, H., Senbel, H., Awad, M., and Abbas, A., *Engineering Science and Technology, an International Journal*, Vol. 23, 618–624, 2020.
29. Ligon, S.C., Liska, R., Stampfl, J., Gurr, M., and Mülhaupt, R., *Chemical reviews*, Vol. 117, 10212–10290, 2017.
30. Gonzalez-Gutierrez, J., Cano, S., Schuschnigg, S., Kukla, C., Sapkota, J., and Holzer, C., *Materials (Basel, Switzerland)*, Vol. 11, 2018.
31. Raasch, J., Ivey, M., Aldrich, D., Nobes, D.S., and Ayranci, C., *Additive Manufacturing*, Vol. 8, 132–141, 2015.
32. Yang, Y., Chen, Y., Wei, Y., and Li, Y., *Int J Adv Manuf Technol*, Vol. 84, 2079–2095, 2016.
33. Monzón, M.D., Paz, R., Pei, E., Ortega, F., Suárez, L.A., Ortega, Z., Alemán, M.E., Plucinski, T., and Clow, N., *Int J Adv Manuf Technol*, Vol. 89, 1827–1836, 2017.
34. Hendrikson, W.J., Rouwkema, J., Clementi, F., van Blitterswijk, C.A., Farè, S., and Moroni, L., *Biofabrication*, Vol. 9, 31001, 2017.
35. Villacres, J., Nobes, D., and Ayranci, C., *RPJ*, Vol. 24, 744–751, 2018.
36. Bodaghi, M., Damanpack, A.R., and Liao, W.H., *Materials & Design*, Vol. 135, 26–36, 2017.
37. Bodaghi, M., Damanpack, A.R., and Liao, W.H., *Smart Mater. Struct.*, Vol. 27, 65010, 2018.
38. Momeni, F., M.Mehdi Hassani.N, S., Liu, X., and Ni, J., *Materials & Design*, Vol. 122, 42–79, 2017.
39. Subash, A., and Kandasubramanian, B., *European Polymer Journal*, Vol. 134, 109771, 2020.
40. Ahn, S.-J., Byun, J., Joo, H.-J., Jeong, J.-H., Lee, D.-Y., and Cho, K.-J., *Adv. Mater. Technol.*, Vol. 6, 2100133, 2021.
41. Valvez, S., Reis, P.N.B., Susmel, L., and Berto, F., *Polymers*, Vol. 13, 701, 2021.
42. van Manen, T., Janbaz, S., and Zadpoor, A.A., *Mater. Horiz.*, Vol. 4, 1064–1069, 2017.
43. Zhang, Q., Yan, D., Zhang, K., and Hu, G., *Sci Rep*, Vol. 5, 8936, 2015.
44. Rajkumar, A.R., and Shanmugam, K., *J. Mater. Res.*, Vol. 33, 4362–4376, 2018.
45. Hu, G.F., Damanpack, A.R., Bodaghi, M., and Liao, W.H., *Smart Mater. Struct.*, Vol. 26, 125023, 2017.
46. Lin, J.R., and Chen, L.W., *J. Appl. Polym. Sci.*, Vol. 69, 1563–1574, 1998.

47. Lin, J.R., and Chen, L.W., *J. Appl. Polym. Sci.*, Vol. 69, 1575–1586, 1998.
48. Merline, J.D., Nair, C.P.R., Gouri, C., Bandyopadhyay, G.G., and Ninan, K.N., *J. Appl. Polym. Sci.*, Vol. 107, 4082–4092, 2008.
49. Schönfeld, D., Chalissery, D., Wenz, F., Specht, M., Eberl, C., and Pretsch, T., *Molecules (Basel, Switzerland)*, Vol. 26, 2021.
50. Oprea, S., *J Mater Sci*, Vol. 43, 5274–5281, 2008.
51. Bothe, M., Mya, K.Y., Jie Lin, E.M., Yeo, C.C., Lu, X., He, C., and Pretsch, T., *Soft Matter*, Vol. 8, 965–972, 2012.
52. Huang, W.M., Lu, H.B., Zhao, Y., Ding, Z., Wang, C.C., Zhang, J.L., Sun, L., Fu, J., and Gao, X.Y., *Materials & Design*, Vol. 59, 176–192, 2014.
53. Mirtschin, N., and Pretsch, T., *RSC Adv.*, Vol. 5, 46307–46315, 2015.
54. Johannes Kunz, *KUNSTSTOFF XTRA*, Vol. 6, 27-30, 2011.
55. Kasprzyk, P., and Datta, J., *Polym Eng Sci*, Vol. 58, E199-E206, 2018.
56. Wilson, T.S., Bearinger, J.P., Herberg, J.L., Marion, J.E., Wright, W.J., Evans, C.L., and Maitland, D.J., *J. Appl. Polym. Sci.*, Vol. 106, 540–551, 2007.
57. Bodaghi, M., Noroozi, R., Zolfagharian, A., Fotouhi, M., and Norouzi, S., *Materials (Basel, Switzerland)*, Vol. 12, 2019.
58. Noroozi, R., Bodaghi, M., Jafari, H., Zolfagharian, A., and Fotouhi, M., *Polymers*, Vol. 12, 2020.
59. Chen, K.-L., Wang, S.-J., Chuang, C., Huang, L.-Y., Chiu, F.-Y., Wang, F.-D., Lin, Y.-T., and Chen, W.-M., *The American journal of medicine*, Vol. 133, 1245–1246, 2020.
60. François, P.-M., Bonnet, X., Kosior, J., Adam, J., and Khonsari, R.H., *Journal of Stomatology, Oral and Maxillofacial Surgery*, 2020.
61. Adolf Würth GmbH & Co. KG, Buy Door handle attachment, hands-free elbow TYPE C online | WÜRTH, https://eshop.wuerth.de/Product-categories/Door-handle-attachment-hands-free-elbow-TYPE-C/14011503101608.cyid/1401.cgid/en/US/EUR/.
62. Hands-Free Door Opener to Help Against the Spread of Coronavirus, https://www.materialise.com/en/hands-free-door-opener.
63. Desmophen® 1262 BD, https://solutions.covestro.com/en/products/desmophen/desmophen-1262-bd_05629268-00010114?SelectedCountry=DE.
64. Dashboard | Tinkercad, https://www.tinkercad.com/dashboard.
65. DIN EN ISO 527-2 - 1996-07 - Beuth.de, https://www.beuth.de/en/standard/din-en-iso-527-2/2808009.
66. Ansys Mechanical | Structural FEA Analysis Software, https://www.ansys.com/products/structures/ansys-mechanical.
67. Jamshidian, M., Tehrany, E.A., Imran, M., Jacquot, M., and Desobry, S., *Comprehensive reviews in food science and food safety*, Vol. 9, 552–571, 2010.
68. Torres, J., Cotelo, J., Karl, J., and Gordon, A.P., *JOM*, Vol. 67, 1183–1193, 2015.
69. Ultimaker Cura: Powerful, easy-to-use 3D printing software, https://ultimaker.com/software/ultimaker-cura.
70. https://www.facebook.com/Magigooo, Magigoo Original - Magigoo, https://magigoo.com/products/magigoo/.
71. CorelDRAW Graphics Suite 2021 | Free Trial, https://www.coreldraw.com/en/product/coreldraw/index-price.html?pcuversion&segid=subscription30&topnav=false&sourceid=cdgs2021-xx-ppc_brkws&x-vehicle=ppc_brkws&trial=big&gclid=CjwKCAjw1uiEBhBzEiwAO9B_HTh3mPZJXfUkRCV9kkJKNZYxLM-alc3rbpcRe_8ooW8RMsZxIWC7FBoCch8QAvD_BwE.
72. IRBIS 3 Analysis Software, https://www.infratec.eu/thermography/thermographic-software/irbis3/.

4.1.6. Supporting Information

4.1.6.1. Fourier-transform infrared (FTIR) spectroscopy

In the FT-IR spectrum of the synthesized PEU a very weak signal occurred at about 2270 cm^{-1}, indicating that only few free isocyanate groups were available.[1; 2] This speaks for the almost complete reaction. At the same time, vibration modes are present as characteristic for the formation of a polyether urethane (**Figure S4.1.1**).

A more detailed analysis of the FT-IR spectrum shows overlapping absorbances between 2970 cm^{-1} and 2852 cm^{-1}, which can be assigned to asymmetric and symmetric stretching vibrations of CH_2 alkyl entities together with CH_3 entities of the PPG side chain.[3; 4] The band at 1065 cm^{-1} can be assigned to corresponding *ν*[C–O-C] ether stretching vibrations of the PPG soft segment.[3; 5] The stretching vibrations *ν*[N–H] at 3313 cm^{-1}, *ν*[C=O] in the carbonyl stretching region at 1703 cm^{-1}, as well as an amide peak (*ν*[C=N] + *δ*[N–H]) at 1531 cm^{-1} are indicating a formation of the hard segment, since the signals can be attributed to urethane species.[3; 6; 7] Consequently, the reaction seemed to be successful.

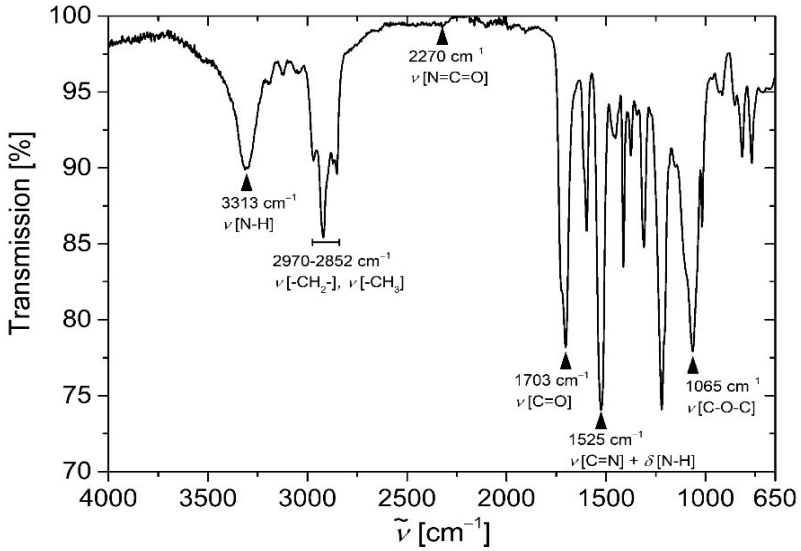

Figure S4.1.1. FT-IR spectrum of polypropylene glycol (PPG)-based polyether urethane (PEU), including the assignment of vibration modes and the specification of their wavenumbers.

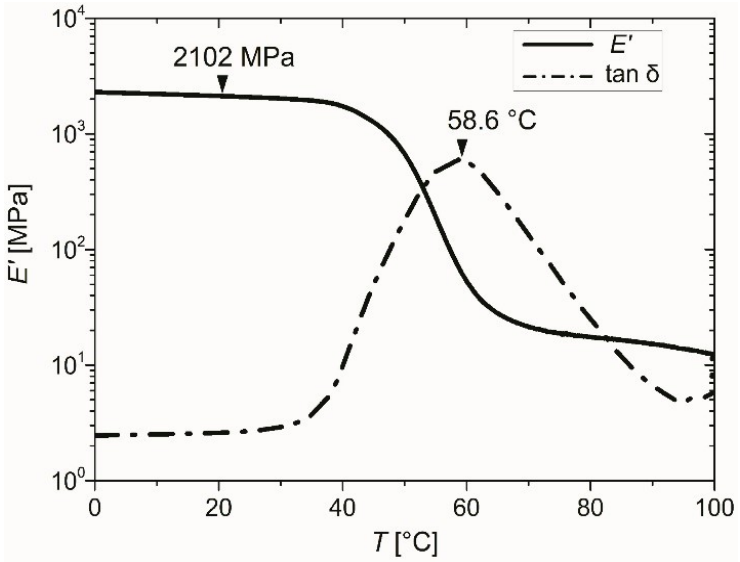

Figure S4.1.2. Thermomechanical properties of PPG-based PEU as determined by DMA for a 4D-printed sample (**Table 4.1.1**, T_N = 150 °C). The evolution of storage modulus *E'* (solid line) and loss factor *tan δ* (dashed dotted line) is considered for a heating rate of 3 °C · min^{-1}.

Table S4.1.1. Temperature variation during 3D printing and 4D-printing of PEU in the first 13 layers at different measuring points as defined in **Figure 4.1.6**. As a starting point for the coloring, a DMA-related

T_g of .54.4 °C was assumed. Temperature values above are marked in red, values below in blue (measurement accuracy: ± 1°C).

Scenario A					
Measurement points	1	2	3	4	5
Layer					
1	104	57	50	50	49
2	107	68	57	54	50
3	130	70	64	63	65
4	143	79	76	73	65
5	145	79	76	73	65
6	149	79	75	74	66
7	153	77	75	74	69
8	156	79	77	74	64
9	165	79	77	75	64
10	151	80	76	75	65
11	149	80	76	73	69
12	151	80	78	73	68
13	152	82	78	76	68
Scenario B					
Measurement points	1	2	3	4	5
Layer					
1	77	44	39	36	35
2	97	46	40	38	35
3	99	47	39	38	36
4	99	47	40	37	37
5	100	48	40	37	37
6	101	49	40	37	37
7	102	51	41	37	38
8	104	51	41	40	38
9	102	49	42	41	40
10	100	51	43	40	40
11	98	51	44	40	39
12	103	49	44	40	38
13	102	51	45	40	39
$T > T_g$ (PEU)		T_g (PEU) =54.5 °C		$T < T_g$ (PEU)	

4.1.6.2. Thermal imaging of FFF printing process

Table S4.1.1. Temperature variation during 3D printing and 4D-printing of PEU in the first 13 layers at different measuring points as defined in **Figure 4.1.6**. As a starting point for the

coloring, a DMA-related T_g of .54.4 °C was assumed. Temperature values above are marked in red, values below in blue (measurement accuracy: ± 1°C).

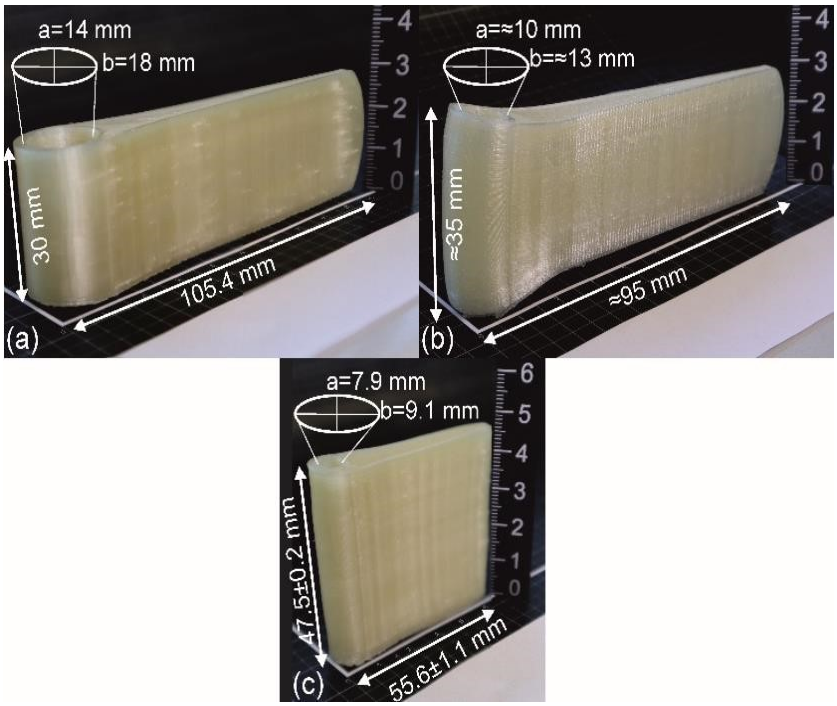

Figure S4.1.3. Thermoresponsiveness of a 4D-printed hands-free door opener made from PEU: (a) As obtained after FFF, (b) as usable in the application after 5 min of localized heating of the elliptical part by means of a heating gun, T = ~100 °C and (c) after heating the whole object for 15 min in a temperature chamber at 75 °C.

The thermoresponsiveness of the hands-free door opener was examined after 4D-printing (**Figure S4.1.4**). In agreement with the material behavior of PEU (**Figure 4.1.10**), an initial localized heating to 100 °C at the position of the ring was conducted for 5 min with a heating gun. As a result, a partial shrinkage along the print direction and an expansion along the z-axis could be achieved. Heating of the whole object in a temperature chamber at 75 °C for 15 min allowed the PEU to almost completely release the 4D effect as exemplified by a shrinkage of about –47% along the print direction and a massive expansion along the z-axis by about 58%. This behavior illustrates that an individualized further shrinking can be conducted after assembly.

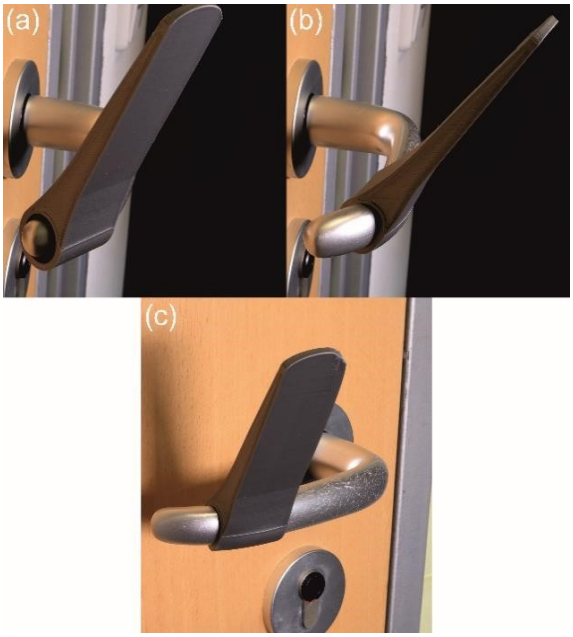

Figure S4.1.4. Assembly and usage of a 4D-printed hands-free door opener made from PLA. (a) The 4D-printed attachment is placed on an elliptical profiled door handle. (b) Fixation as achieved by shrinking the elliptical part of the door opener. (c) System ready to use.

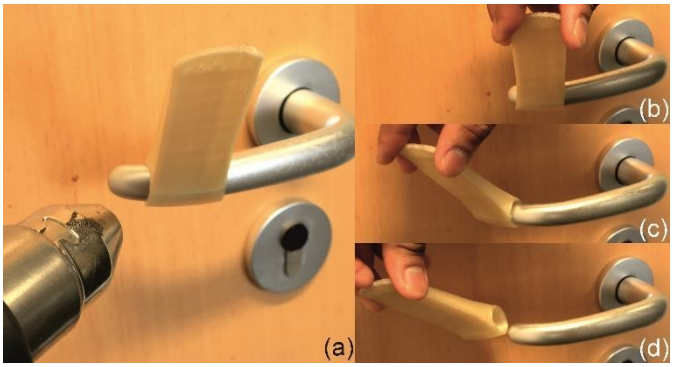

Figure S4.1.5. Disassembling of a 4D-printed PEU hands-free door opener. (a) Heating to 100 °C with a heating gun and (b-d) removing the attachment from the door handle. When using PLA as print material, exactly the same steps were followed.

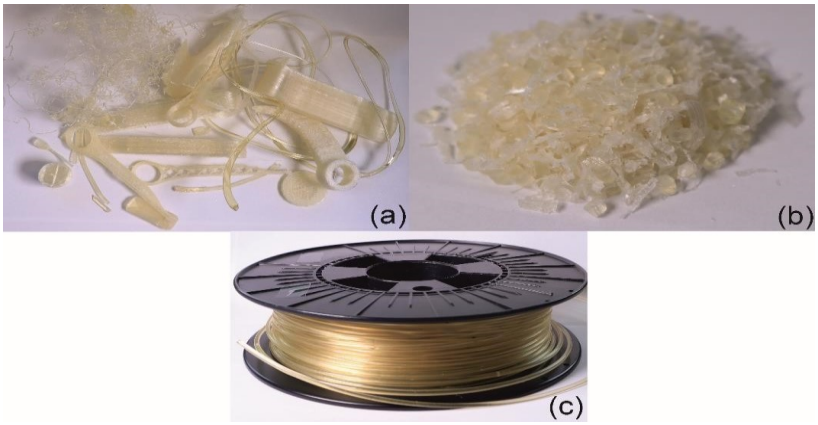

Figure S4.1.6. Recycling of PEU at its end-of-use. The material is (a) collected, (b) granulated and (c) extruded to filament.

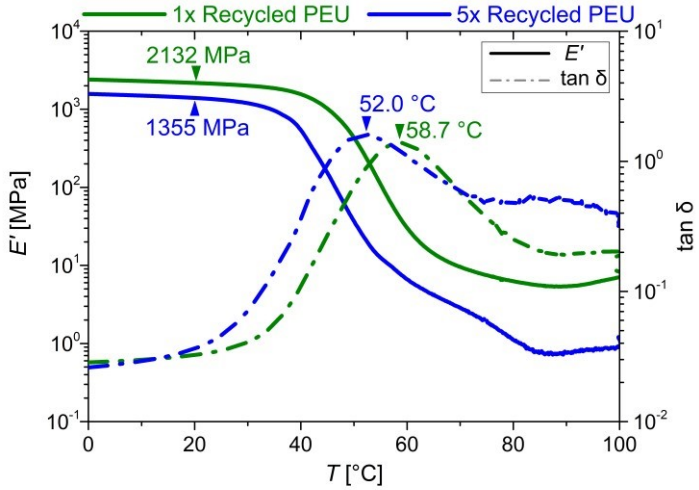

Figure S4.1.7. Influence of mechanical recycling and re-extrusion upon the thermomechanical properties of PPG-based PEU as determined by DMA. The evolution of storage modulus *E'* (solid line) and loss factor *tan δ* (dashed dotted line) is considered after the first recycling (green color) and the fifth recycling (blue color). A heating rate of 3 °C · min^{-1} was selected.

4.1.6.3. References

1. Tereshatov, V.V., Slobodinyuk, A.I., Makarova, M.A., Vnutskikh, Z.A., Pinchuk, A.V., and Senichev, V.Y., *Russ J Appl Chem*, Vol. 89, 943–948, 2016.
2. Klinedinst, D.B., Yilgör, I., Yilgör, E., Zhang, M., and Wilkes, G.L., *Polymer*, Vol. 53, 5358–5366, 2012.
3. Tan, C., Tirri, T., and Wilen, C.-E., *Polymers*, Vol. 9, 2017.
4. Erdem, A., *J. Appl. Polym. Sci.*, Vol. 138, 49997, 2021.
5. Zhang, Y., Qi, Y.-h., and Zhang, Z.-p., *J Polym Res*, Vol. 22, 2015.
6. Pretsch, T., Jakob, I., and Müller, W., *Polymer Degradation and Stability*, Vol. 94, 61–73, 2009.
7. Piril Ertem, S., Yilgor, E., Kosak, C., Wilkes, G.L., Zhang, M., and Yilgor, I., *Polymer*, Vol. 53, 4614–4622, 2012.

Chapter 4.2: Potential Applications of 4D-Printed Objects

Chapter 4.2: Potential Applications of 4D-Printed Objects

4.2.1. Introduction

Four-dimensional (4D) printing is a facile additive manufacturing (AM) technique to obtain, e.g., thermoresponsive objects made from shape memory polymer (SMP) [1–5]. The 4D-printing technique was first introduced by Skylar Tibbits [6], combining a hydrogel as an active material with a static, rigid polymer as a passive material to achieve different degrees of bending or shape transformations [7,8]. Later, scientists transferred the basic principles of 4D-printing to the AM technology "fused filament fabrication" (FFF) [1,2,4,9–14]. In FFF, the choice of specific printing parameters like nozzle temperature, printing pressure, and speed are known to affect the print results, thus gaining control over the orientation of polymer chains in the direction of the nozzle movement or printing pattern [4,10,15]. The basic idea is that an extruded polymer strand, laid on the printing platform or a top polymer layer, is rapidly cooled below the polymer's glass transition temperature so that the individual polymer chains retain highly oriented states. After 4D-printing, the object remains stable until the ambient temperature is raised above the switching temperature of the SMP, most commonly the glass transition temperature [4]. Once heated above the glass transition temperature (T_g), the polymer releases internal stresses by molecular motion, culminating in macroscopical shrinkage along the direction of the nozzle movement [14]. My recent study showed that when selecting a lower nozzle temperature and keeping the difference between the nozzle temperature and glass transition temperature to its minimum, internal stresses can be stored and released upon heating, resulting in a significant thermoresponsiveness, here also denoted as a 4D effect [4]. Until recently, the 4D effect was restricted to objects of smaller height (z < 5 mm), and with increasing layer height, the 4d effect decreases in the z-direction [1,2,4,10,14,16]. This can be explained by the occurrence of pronounced relaxation effects and was one of the main reasons for developing novel applications based on 4D-printing more difficult.

Against this background, our group presented an approach to realize the 4D-printing of objects with a more significant height (z > 30mm) recently (**Chapter 4.1**) [4]. To show that the range of applications is far from exhausted, virtual models of different demonstrators were created using computer-aided design (CAD), and the same polypropylene glycol (PPG)–based polyether urethane as in **Chapter 4.1** was used as 4D-printing material for this study [4]. In a final step, the thermoresponsiveness of 4D-printed objects was evaluated in the context of new applications.

4.2.2. Results and Discussion

The polypropylene glycol (PPG)-based polyether urethane (PEU), which was used in the previous **Chapter 4.1** [4], was again employed in the form of filaments. In order to achieve

the desired 4d effect for demonstrators, the same printing parameters were chosen. The selection was due to the excellent 4D effect exhibited by the material using FFF processing and, most importantly, the proven possibility to build higher objects (z > 5 mm). The glass transition temperature of the PEU is close to 60 °C (**Figure 4.1.3b** in **Chapter 4.1**) [4]. Further, the application potential of the 4D-printing technology was investigated. Firstly, the feasibility of producing active fasteners using 4D-printing was looked into.

Fasteners are widely used in the manufacturing and construction industry and assembly and conjunction lines. They mechanically join or attach several objects. Even though most fasteners are produced according to international standards or norms, the need for a suitable tool to mechanically assemble elements is unavoidable. Here, active assembly techniques are proposed for fasteners using the 4D-printing technique (**Figure 4.2.1**).

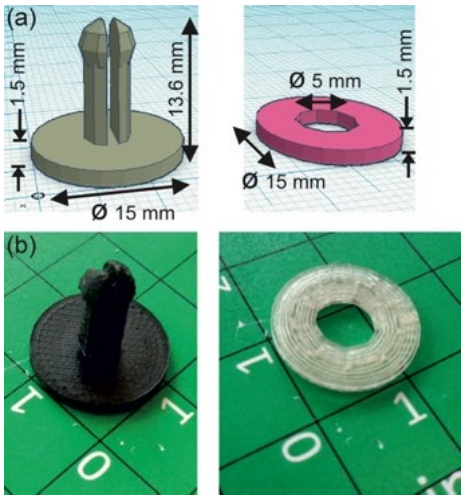

Figure 4.2.1. CAD of a fastener pin and a round disc (a) and its additively manufactured analogues made from PET-G (b, left) and PEU (b, right). The round disc was obtained from 4D-printing.

The fastener pin and its compatible round disk were created using CAD (**Figure 4.2.1 a**). Once modeled, the fastener pin was additively manufactured using black polyethylene terephthalate glycol (PET-G). In contrast, the round disk was 4D-printed using the PEU filament (**Figure 4.2.1 b**). The individual printing parameters are provided in **Table 4.2.1**. Once the 3D printing was complete, active assembly was carried out (**Figure 4.2.2**).

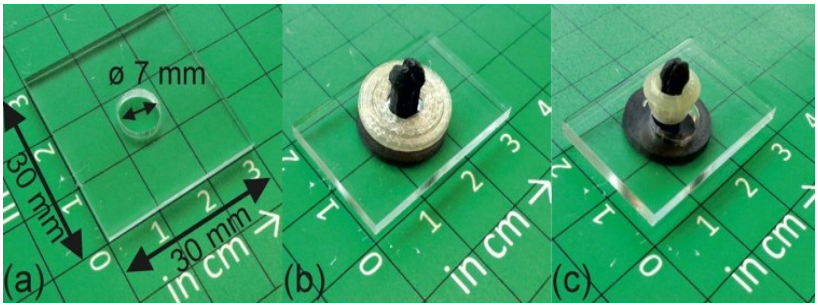

Figure 4.2.2. A one-time active assembly is enabled by heating the 4D-printed round disk made from PPG-based PEU. A poly(methyl methacrylate) sheet with an opening in the middle (a), fastener pin, and round disk were placed together with the sheet (b) and assembled by heating the round disk to 75 °C (c).

The 4D effect is later triggered by heating the round disk to 75 °C, above the PEU's glass transition temperature (T_g). This temperature increase led to the shrinkage of the round disk, thereby connecting the fastener pin, which is inserted through the hole of a poly(methyl methacrylate) sheet. The shrinkage of a round disk from planar to conical shape was achieved from the full annulus or the continuous concentric printing pattern. This is achieved due to the higher shrinkage effect incorporated into the outer circumference than the inner, where the outer circumference attains a longer strand deposition length and a more substantial shrinkage effect than the inner. A similar transformation of round disks from two-dimensional to three-dimensional shapes has been recently reported by Goo et al. [17] and Hu et al. [18]. However, due to the shape change, a tight connection of the three individual parts was achieved, which turned out to be stable under room temperature. In order to remove and dismantle the system, the PEU was reheated to 75 °C. Thereupon softens the PEU, allowing the individual parts to recover.

The accuracy of the fit is an essential criterion for fasteners. For another similar sample, no visual damage or deformation occurred to the shrunk disk when pulling the round disk apart from the poly(methyl methacrylate) (PMMA) sheet with a force of 50 N. However, the fastener pin failed by ripping off its base. A further advantage of using the 4D-printed active assembly is that the only tool required for different-sized objects is a heating gun or a heating chamber. The use of smart fixtures could be beneficial in the interior of space stations or space habitats, or even for furniture, due to its general usability, simplicity, and easy adaptation to other geometric requirements in a wide variety of situations.

Interestingly, the concept can also be applied in another context, namely in closures that can be actively assembled one-time (**Figure 4.2.3**).

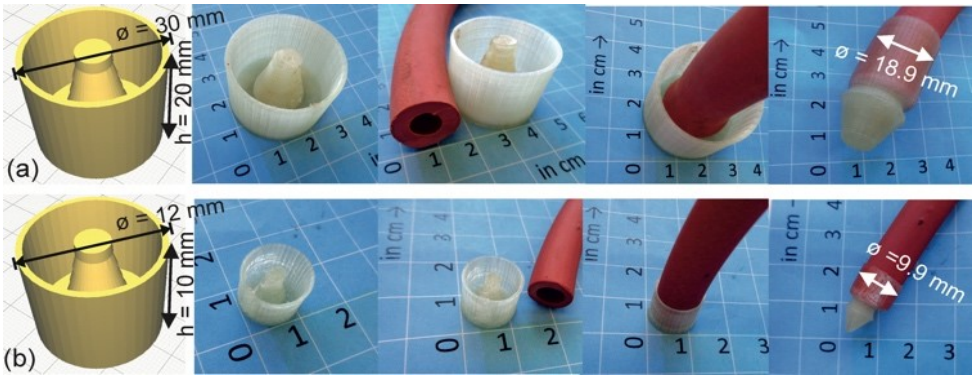

Figure 4.2.3. The concept for one-time active assembly of differently sized closures. CAD of closures with an outer diameter of 30 mm (a, left) and 12 mm (b, left), closures after 4D-printing (2nd image from left) together with red natural rubber tubes (3rd image from left) with outer diameters of rubber tubes of 17 mm (a) and 10 mm (b), and the individual systems before and after heating to 75 °C (image on the right).

The tapered cone pin design of the closure acts as a positioning pin. Due to the tapering, a single design fits various tubes with varying inner diameters (leftmost image of **Figure 4.2.3. a** and **b**). After 4D-printing, the closure presented good visual accuracy compared to the virtual design (first and the second image from the left in **Figure 4.2.3. a** and **b**). After placing

the closure onto the tube opening and heating it to 75 °C for 5 min, the 4D effect was triggered. The closure shrank and snugly fit over the tube (rightmost images of **Figure 4.2.3. a** and **b**). Once again, due to the continuous concentric strand deposition in the circular printing pattern, the closure shrank uniformly along the printing plane (XY-plane). It is worth mentioning that the smaller closure (**Figure 4.2.3. b**) showed almost a similar 4D effect as the more oversized closure (**Figure 4.2.3. a**), even though the smaller closure was a miniaturized filigree version of the bigger one. Interestingly, it could be observed that even after choosing a closure with a bigger outer diameter of 30 mm (leftmost image **Figure 4.2.3. a**), which is twice the outer diameter of the tubing, the closure shrank by about 37%, reaching an outer diameter of 18.9 mm (rightmost image **Figure 4.2.3. a**).

In order to quantify the resistance of the closure system to compressed air, the closed tube was subjected to different air pressures (**Figure 4.2.4.**).

The pressure was gradually increased from 0 to 10 bar (**Figure 4.2.4**). When reaching 8 bar, the closure and tubing were immersed in a water bath. No signs of air bubbles or leakage from the closure could be witnessed; thus, the closure was still tightly connected to the tube. The tube burst and failed on further increase the air pressure to about 10 bar (rightmost image of **Figure 4.2.4 a** and **b**). Immersing the still closed part of the tube again in water showed no signs of air bubbles.

To further investigate the quality of sealing achieved by the 4D effect, the closure with the tubing was connected to a water tap offering a water pressure of approximately 4 bar. The experiment also revealed no visible spilling, leakage, or occurrence of moisture on the surface of the closure. One can see from these that the 4D-printed objects from PPG-PEU can withstand enormous forces after releasing their 4D effect. For this reason, the concept may be helpful in many industries wherever efficient sealing solutions are sought.

Subsequently, the concept was extended to connecting two tubes (**Figure 4.2.5**.).

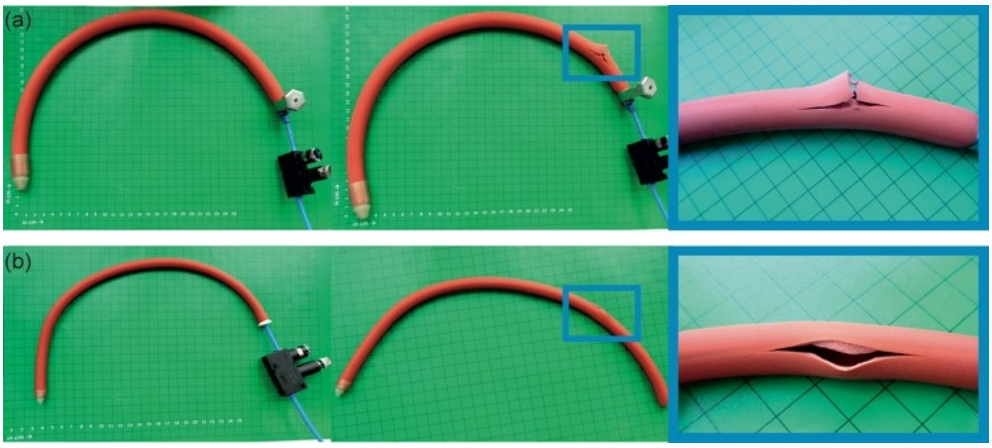

Figure 4.2.4. The pressure resistance of 4D-printed closures is tightly connected to red natural rubber tubes with an outer diameter of 30 mm (a) and 12 mm (b), respectively. After the test, the assembled setup for pneumatic testing states and enlarged images of the blue box in the middle are exhibited from left to right.

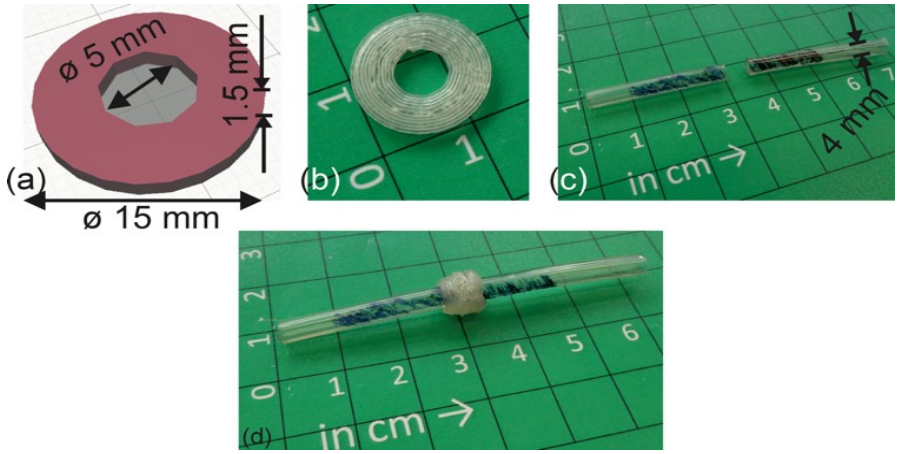

Figure 4.2.5. One-time active assembly: Connecting disk for round tubes or objects. CAD design (a), round disk after 4D-printing (b), two tubes with an outer diameter of 4 mm (c), and system after heating to 75 °C.

The round disk developed for the active assembly of fasteners (right image of **Figure 4.2.1**) was again used for this purpose (**Figure 4.2.5 a and b**). The tubes had an outer diameter of 4 mm (**Figure 4.2.5 c**). The round disk was placed at the contact point of the two tubes and was heated to 75 °C. As a result, the connecting disk shrank and firmly wrapped onto the surface of both tubes. After triggering the 4D effect, the round disk changed its shape into a hollow cylindrical shape, and a uniform shrinking force was exerted on both ends of the tubes, allowing them to connect and hold the tubes together. Connecting the extended hose to a water pipe with a pressure of 4 bar and an air stream with a pressure of 10 bar for at least 5 min showed that no leaks could be detected.

In another approach, a flower was developed using the PEU that closes upon heating. (**Figure 4.2.6**). The 4D-printing of hydrogel-based flowers inspired the 4D-printing of a flower following the FFF concept by Gladman et al. [15] and Shiblee et al. [19].

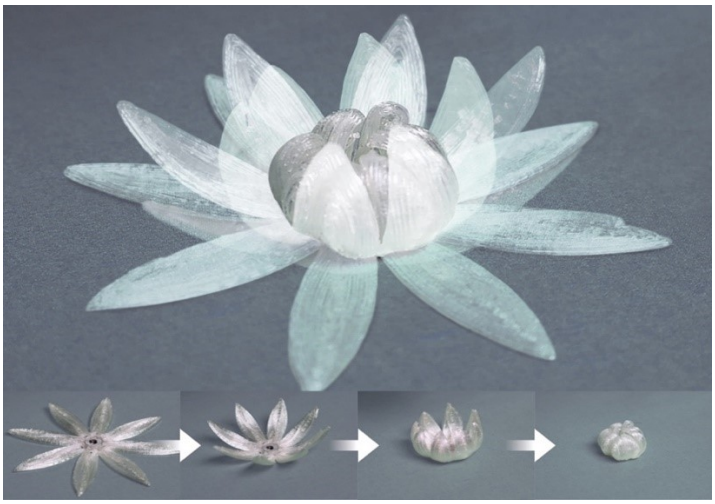

Figure 4.2.6. One-time self-closing flower made of 4D-printed PEU. The four superimposed images (above) exhibit the different stages when heating the flower from 23 °C to 75 °C (below, from left to right).

The flower-shaped structure consisted of a flat thin oval-shaped substrate and a continuous spline printed on top. The printing path of the oval-shaped substrate was selected such that the strand deposition took place in a concentric oval printing pattern along the longer axis of the oval. This printing pattern allowed the structure to shrink along the oval's longer axis and expand on the oval's shorter axis. At the same time, the continuous spline, running over the oval-shaped substrate, was formed by laying down a single continuous strand in a layer-by-layer manner. Thereby, no neighboring deposited strands heated up, which avoided the relaxation of the polymer. Thereby implies that the 4D effect of the spline was comparatively more pronounced than for the oval-shaped substrate. The difference in the 4D shrinkage effect along the longer axis of the petal made each petal bend and shrink simultaneously, resulting in a petal closing movement of a flower. This biomimicry effect caused by 4D-printing could be helpful in applications such as automotive, where individual parts should be assembled.

In the next step, active disassembly as facilitated by 4D-printing was investigated. For this purpose, a two-component system was designed and later manufactured via FFF using the printing parameters in **Table 4.2.1** (**Figure 4.2.7.**). In detail, a thermoresponsive round disk with a protrusion along the outer diameter was 4D-printed from PEU (white part). At the same time, the red-colored block was printed from Desmopan® 9370AU with a grooved hole exhibiting a maximum diameter of 19 mm.

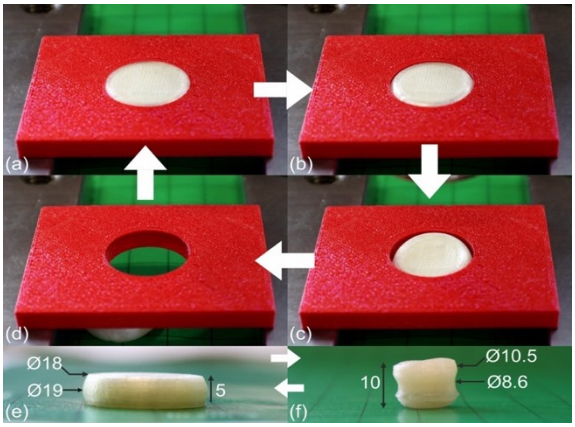

Figure 4.2.7. One-time active disassembly of a two-component system made from 4D-printed PEU (white) and its non-thermoresponsive counterpart made of red-colored Desmopan® 9370AU. The images show the system in its assembled state (a), the states when raising the temperature to 75 °C (b and c), and the disassembled state (d). The thermoresponsive disk is shown separately in its states before (e) and after heating (f) (all the dimensions are in mm).

As the printing pattern of the round disked PEU determines the 4D effect, it was printed with a grid printing pattern consisting of alternating layers of horizontal and vertical strand orientation along with two circled outer shells for achieving shrinkage of the disk and thereby disassembly of the object. The grooved hole of the red block and the protrusion of the round disk (white part) realizes an easy assembly by a snap-fit mechanism. In other words, the 4D-printed PEU part (white part) was inserted into the groove of the red component (**Figure 4.2.7 a**). The assembled system can be used as long as the internal stresses are stored in the PEU.

The assembled system showed good mechanical resilience even after placing a load weighing 500 g on top of the 4D-printed element. The system remained intact until the 4D effect was triggered. Once the temperature was raised to 75 °C, the PEU shrank significantly (**Figure 4.2.7. b and c**), after which the middle part could be removed without effort (**Figure 4.2.7. d**). Due to the PEU's alternating vertical and horizontal printing pattern, the round disk shrank along the printing plane (XY-plane) and expanded from 5 mm to about 10 mm along the direction of layer thickness and height (Z-plane). The states before and after heating the 4D-printed part are shown in **Figures 4.2.7 e and f**. On re-heating the shrunken part (**Figure 4.2.7 f**) to 75 °C, applying a compressive load of 50 N, and cooling to 23 °C, a thermoresponsive shape could be re-obtained similar to the initial shape (**Figure 4.2.7 e**). This implies that it can be used again in another life cycle.

The active disassembly concept enabled by 4D-printing was further extended using snap-fit joining mechanisms. A three-component system was used to demonstrate the working principle (**Figure 4.2.8**). The system's components were produced from two three-dimensional (3D) printed blocks with socket extensions and one 4D-printed block with ball extensions. The component blocks were first 3D-printed using yellow polylactic acid (PLA) filament (**Figure 4.2.8a**) and black PET-G filament (**Figure 4.2.8c**), while the PEU (**Figure 4.2.8b**) was 4D-printed using the printing parameters from **Table 4.2.1**.

Figure 4.2.8. Snap-fit joining mechanism and one-time active disassembly as enabled by 4D-printing. The first component was made from PLA (a), the second component from 4d-printed PEU (b), and the third component from PET-G (c). The assembled state of the system is shown before (d) and after heating to 75 °C (e) to visualize active disassembly.

After additively manufacturing the different blocks, the design of the components allowed to snap-fit the individual members by connecting the ball and socket joint [20–22]. Once assembled, the whole system can be employed, e.g., until it reaches a point where a repair is required, or the end-of-use or end-of-life is reached. The system can then be actively disassembled by heating above the glass transition temperature of the PEU. Once heated to 75 °C, the ball mechanism or 4D-printed PEU shrinks and elongates due to the 4D effect. The main reason for the elongation and shrinkage was the choice of the concentric circular printing pattern of the balls along the printing plane (XY-plane), where the strands in the form

of concentric circles shrink along the print direction and expand in the direction of the layer height. Once the balls shrink and elongate, the ball-socket snap-fit mechanism no longer functions, allowing the system to disassemble actively, thereby enabling the separation of mechanically connected parts. Later, the system can be repaired or recycled.

In **Chapter 3.2**, a mechanical gear was introduced to deactivate or disconnect a transmission system by heating above the soft segmental melting transition temperature of the employed polyurethane. However, the most significant disadvantage of the gear was the complex programming. In order to overcome the tedious thermomechanical step, a CAD design of a 4D-printable gear was developed and printed with the PEU (**Figure 4.2.9**).

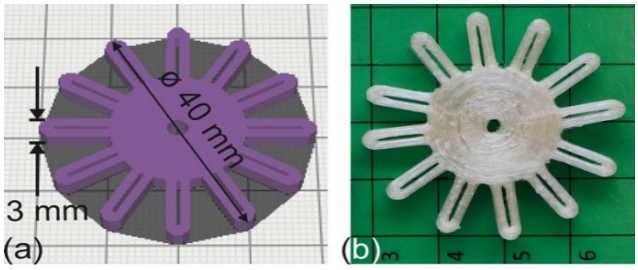

Figure 4.2.9. Thermoresponsive gear as created by CAD (a) and after 4D-printing using the PEU, the base material (b).

After identifying an appropriate design, the model was 4D-printed via FFF. The gear was assembled intermediate between an input and an output gear (**Figure 4.2.10**).

Figure 4.2.10. One-time self-deactivating mechanical system triggered by heat consisting of an output gear made from poly(methyl methacrylate) (left), an intermediate gear made from 4D-printed PEU (middle), and an input gear again made from poly(methyl methacrylate) (right). Overlapping images when triggering the 4D effect (top) and states after assembly and during heating to 75 °C (below, from left to right).

Once the gear was assembled into the system, it responded to heat with a one-time change of shape. In detail, as soon as the temperature rose above T_g of the PEU, the 4D effect of the

PEU was triggered, resulting in shrinkage of the teeth and the body of the gear. The teeth of the gear shrank uniformly along the print direction, as achieved through the straight-lined printing pattern. The strand deposition movement was from the gear's root to the top land and back to the gear root. In **Figure 4.2.10**, slight bending of the PEU gear could be observed during heating. This occurred because the gear was heated with a heat gun, and the heat transfer was not uniformly attained throughout the gear (from top to bottom). This temperature gradient caused the bending. However, the substantial reduction in gear size broke the contact between the input and output gear and thus interrupted the transmission system. A temperature-induced interruption of a process can bring significant advantages, for example, in industrial safety appliances or systems to prevent overheating. At the same time, the risk of damage to a gearbox, transmission system, or neighboring electronics can also be avoided. Once again, replacing the 4D-printed object with a new thermoresponsive gear after reprocessing or reprogramming is a prerequisite to enter one further life cycle to allow the system to continue operating.

To further explore the potential of 4D-printed objects, the technique was used to program shape memory polymer foam. To demonstrate the concept, a cylindrical element of the PEU measuring 20 mm in height and 52 mm in diameter was designed, 4D-printed, and assembled with a sample of an in-house synthesized polyester urethane urea (PEUU) foam (**Figure 4.2.11**).

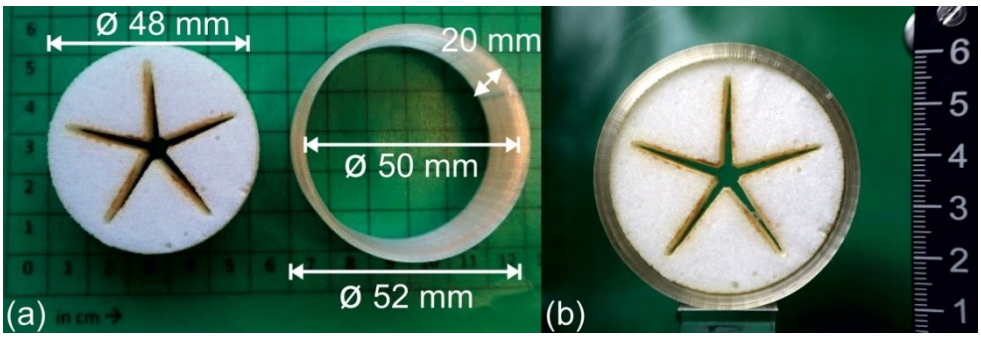

Figure 4.2.11. Polyester urethane urea foam, 4D-printed programming cylinder (a), and both of them in an assembled state (b) (all the dimensions are in mm).

Next, the deformation of the PEUU foam was carried out by triggering the 4D effect of the PEU cylinder (**Figure 4.2.12**).

For developing an effective thermomechanical treatment to program the PEUU foam later, it is necessary to understand the thermal properties of the PEUU foam. The melting transition of the PEUU foam ranges from 20 °C to 65 °C with a maximum of about 57 °C. At the same time, the crystallization transition extends from 45 °C to 0 °C with a peak at 37 °C [23]. On heating the system to 75 °C and holding the temperature for 15 min, the PEUU foam softened, allowing the system to continue operating. The cylindrical element shrank along the continuous concentric circular printing pattern and compressed the foam. Remarkably, the foam could uniformly shrink and close the star-shaped opening (**Figure 4.2.12**). Subsequently, the temperature was brought to –15 °C to crystallize the soft segment of the PEUU foam and

was held isothermally for 15 min to fix the new temporary shape of the PEUU foam. Heating to 23 °C finalized the programming of the foam, and the PEU cylinder was separated from the PEUU foam. One potential application of the programmed foam could be a thermally switchable air permeability system.

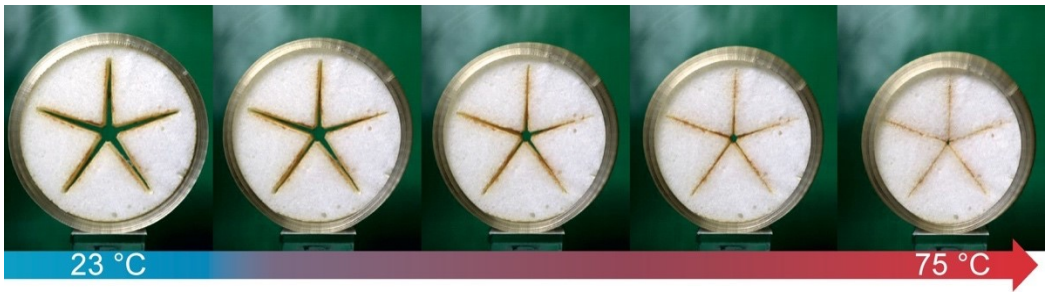

Figure 4.2.12. Thermomechanical treatment of PEUU foam with a star-shaped cutout using a 4D-printed cylinder made of PEU. The temperature was systematically raised from 23 °C to 75 °C (from left to right).

In a final approach, the 4D-printed cylindrical element and the PEUU foam were combined to explore one further application (**Figure 4.2.13**).

After placing the PEUU foam inside the 4D-printed cylinder, the setup was mounted over a rod, holding a weight of 100 g. Upon raising the temperature to 75 °C, the 4D-printed cylinder shrank, thus compressing the PEUU foam and fixing the rod in its center position. It demonstrates that the system can grab or hold objects for, e.g., transporting purposes. Beyond that, it may even stop rotating objects under certain conditions and can be used, e.g., in mechanical machines, biomedical devices, or the aerospace industry.

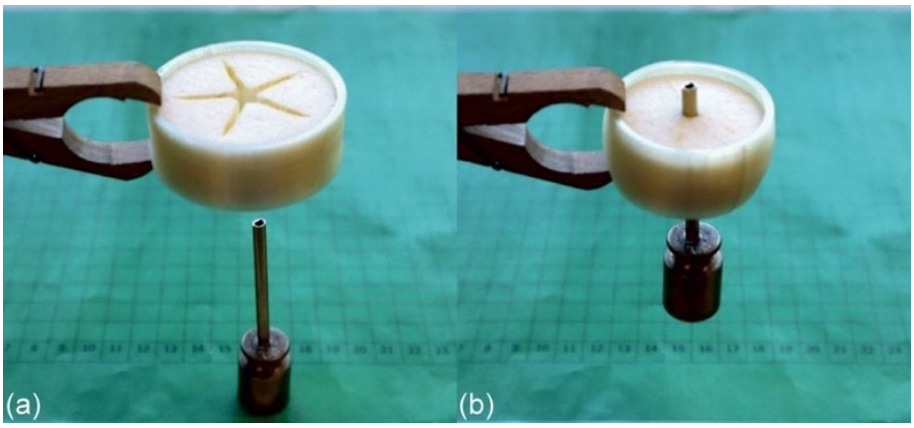

Figure 4.2.13. 4D-printed cylindrical element with PEUU foam before (a) and after triggering the 4D effect to grab and hold an object (b).

4.2.3. Conclusions

Chapter 4.2 presents some application ideas as enabled by 4D-printing with SMPs. These include elements for active assembly and disassembly, concepts for end-of-life components, safety components, and elements that can program other SMPs. The approaches emphasize that 4D-printing eliminates the need for the classical time-consuming thermomechanical

treatments to attain a thermoresponsive state for some SMPs. This is a significant step to save energy, time, and cost. The work also shows that thermoresponsiveness can be efficiently maintained in objects. With the right or appropriate selection of printing patterns, the direction of the 4D effect can be controlled. It is noteworthy that the 4D-printed parts exhibit good mechanical stability and could be assembled or disassembled when triggering the 4D effect. The ability of the PPG-based PEU 4D-printed parts to withstand heavy loads or pressure makes the material, as well as the 4D-printing technique, attractive for industries like aerospace, mechanical, and marine. Most importantly, the development of active disassembly concepts showed that objects could be quickly assembled using mechanical joining mechanisms like snap-fitting. At the same time, the triggering of the 4D effect initiates active disassembly and separates the assembled components. This brings significant advantages in terms of sustainability: The separation of materials by their types enables effective recycling at the end-of-life of a system. In this way, 4D-printing is a promising technology that may assist in developing efficient and sustainable solutions.

4.2.4. Experimental Section

Material: The polypropylene glycol (PPG) based thermoplastic polyurethane (PEU), which was synthesized and developed in the previous literature, is again used in this work in the form of filaments (**Chapter 4.1**) [4]. A filament of black polyethylene terephthalate glycol (PET-G) and yellow polylactic acid (PLA) was purchased from FilamentWorld (Neu-Ulm, Germany). The ether-based thermoplastic polyurethane elastomer Desmopan® 9370AU was supplied by Covestro Deutschland AG (Leverkusen, Germany). A polyester urethane urea (PEUU) foam which was synthesized and developed in previous literature by Walter et al., is used in this work to demonstrate programmable devices [23].

Virtual Design and Fused Filament Fabrication: Tinkercad is an online 3D modeling computer-aided design (CAD) program [24]. It was used for designing and developing the virtual design of the samples described in this work. These include a fastener, closure, connecting disc, two- and three-component system, gear, and programming cylinder. The CAD models were exported as STL files.

After finalizing the designs, the 3D models in STL format were imported into the slicer software Cura 4.8.0. [25]. In the case of 4D-printing, the printing parameters were selected in accordance with previous literature [4]. All printing parameters of PEU, black polyethylene terephthalate glycol (PET-G), yellow polylactic acid, and red Desmopan® 9370AU are summarized in **Table 4.2.1**.

All printed objects were produced via FFF using the commercially available 3D printer, using commercially available 3D printers Ultimaker S5 and Ultimaker 3 from Ultimaker B.V. (Utrecht, the Netherlands). At the beginning of every printing process, a thin layer of Magigoo adhesive from Thought3D Ltd. [26] was applied to the building platform to ensure good adhesion between the build platform and printed objects.

Table 4.2.1. Printing parameters selected for FFF with different materials.

Printing parameter	3D printing			PEU (4D-printing)
	PET-G	Desmopan® 9370AU	PLA	
Diameter of the nozzle (µm)	400	400	400	400
Temperature of the nozzle (°C)	235	225	200	150
Speed of print head (mm × s^{-1})	50	25	40	50
Build platform temperature (°C)	85	60	65	23
Layer height (mm)	0.15	0.15	0.15	0.15

Characterization of 4D Effects: The triggering of the 4D effect was achieved by a heating gun from Conrad Electronic (Hirschau, Germany) or in the heating chamber UF110 from Memmert GmbH + Co. KG (Schwabach, Germany). In any case, the samples were heated to 75 °C within a time of 5 min, else otherwise specified. The dimensions of the samples before and after heating were measured with a Vernier caliper from Fowler High Precision GmbH (Massachusetts, USA).

The mechanical behavior of the shrunk 4D disk fastener was investigated with the universal testing machine Criterion Model 43 from MTS (Eden Prairie, MN, USA). The device was equipped with a 500 N load cell. The measurements were conducted on the poly(methyl methacrylate) sheets fastened with a fastener pin and a 4D-printed round disk. The poly(methyl methacrylate) sheets were fixed on the lower clamp, while the shrunk 4D-printed disk was clamped on the top clamp. Afterward, the parts were pulled apart by stretching with a velocity of 100%·min^{-1} until rupture occurred, while the corresponding load required was measured.

The thermomechanical treatment of the PEUU foam with the 4D-printed programming device was carried out with an MTS Criterion universal testing machine from MTS Systems Corporation (Eden Prairie, MN, USA). The device was operated with a temperature chamber controlled by a Eurotherm temperature controller unit. Two heating elements were located at the back of the chamber. Liquid nitrogen from a Dewar vessel was fed into the chamber under a pressure of 1.3 bar as an essential prerequisite for cooling. The assembled setup was placed on a platform at the beginning of the programming. The chamber was heated to 75 °C and held isothermally for 15 min. The PEU cylinder around the PEUU foam was cooled to – 15 °C. After an isothermal holding time of 15 min, the chamber was heated to 23 °C and held isothermally for another 5 min. A heating and cooling rate of 5 °C x min^{-1} was used for the whole experiment.

4.2.5. References

1. Bodaghi, M.; Damanpack, A.R.; Liao, W.H. Adaptive metamaterials by functionally graded 4D printing. *Materials & Design* **2017**, *135*, 26–36, doi:10.1016/j.matdes.2017.08.069.
2. Hu, G.F.; Damanpack, A.R.; Bodaghi, M.; Liao, W.H. Increasing dimension of structures by 4D printing shape memory polymers via fused deposition modeling. *Smart Mater. Struct.* **2017**, *26*, 125023, doi:10.1088/1361-665X/aa95ec.

3. Valvez, S.; Reis, P.N.B.; Susmel, L.; Berto, F. Fused Filament Fabrication-4D-Printed Shape Memory Polymers: A Review. *Polymers* **2021**, *13*, 701, doi:10.3390/polym13050701.
4. Chalissery, D.; Schönfeld, D.; Walter, M.; Shklyar, I.; Andrae, H.; Schwörer, C.; Amann, T.; Weisheit, L.; Pretsch, T. Highly Shrinkable Objects as Obtained from 4D Printing. *Macro Materials & Eng* **2022**, *307*, 2100619, doi:10.1002/mame.202100619.
5. Demoly, F.; Dunn, M.L.; Wood, K.L.; Qi, H.J.; André, J.-C. The status, barriers, challenges, and future in design for 4D printing. *Materials & Design* **2021**, *212*, 110193, doi:10.1016/j.matdes.2021.110193.
6. Tibbits, S. Skylar Tibbits: The emergence of "4D printing". Available online: https://www.ted.com/talks/skylar_tibbits_the_emergence_of_4d_printing (accessed on 20 January 2022).
7. Tibbits, S. 4D Printing: Multi-Material Shape Change. *Archit Design* **2014**, *84*, 116–121, doi:10.1002/ad.1710.
8. *ACADIA 2014 design agency proceedings*: *Proceedings of the 34th Annual Conference of the Association for Computer Aided Design in Architecture, October 23-25, 2014, Los Angeles, California;* Gerber, D.; Huang, A.; Sanchez, J., Eds.; Riverside Architectural Press: Toronto, Ontario, 2014, ISBN 9781926724478.
9. Zhang, Y.; Qi, Y.-h.; Zhang, Z.-p. The influence of 2,4-toluene diisocyanate content on the intrinsic self-healing performance of polyurethane at room-temperature. *J Polym Res* **2015**, *22*, doi:10.1007/s10965-015-0744-0.
10. van Manen, T.; Janbaz, S.; Zadpoor, A.A. Programming 2D/3D shape-shifting with hobbyist 3D printers. *Mater. Horiz.* **2017**, *4*, 1064–1069, doi:10.1039/c7mh00269f.
11. Bodaghi, M.; Damanpack, A.R.; Liao, W.H. Triple shape memory polymers by 4D printing. *Smart Mater. Struct.* **2018**, *27*, 65010, doi:10.1088/1361-665X/aabc2a.
12. Noroozi, R.; Bodaghi, M.; Jafari, H.; Zolfagharian, A.; Fotouhi, M. Shape-Adaptive Metastructures with Variable Bandgap Regions by 4D Printing. *Polymers* **2020**, *12*, doi:10.3390/polym12030519.
13. Bodaghi, M.; Noroozi, R.; Zolfagharian, A.; Fotouhi, M.; Norouzi, S. 4D Printing Self-Morphing Structures. *Materials (Basel)* **2019**, *12*, doi:10.3390/ma12081353.
14. Nezhad, I.S.; Golzar, M.; Behravesh, A.; Zare, S. *Comprehensive Study on Shape Shifting Behaviors of Thermally Activated Hinges in FDM-based 4D Printing*, 2021.
15. Gladman, A.S.; Matsumoto, E.A.; Nuzzo, R.G.; Mahadevan, L.; Lewis, J.A. Biomimetic 4D printing. *Nat. Mater.* **2016**, *15*, 413–418, doi:10.1038/nmat4544.
16. Rajkumar, A.R.; Shanmugam, K. Additive manufacturing-enabled shape transformations via FFF 4D printing. *J. Mater. Res.* **2018**, *33*, 4362–4376, doi:10.1557/jmr.2018.397.
17. Goo, B.; Kim, J.-B.; Ahn, D.-G.; Park, K. Irreversible and Repeatable Shape Transformation of Additively Manufactured Annular Composite Structures. *Materials (Basel)* **2021**, *14*, doi:10.3390/ma14061383.
18. Hu, G.F.; Damanpack, A.R.; Bodaghi, M.; Liao, W.H. Increasing dimension of structures by 4D printing shape memory polymers via fused deposition modeling. *Smart Mater. Struct.* **2017**, *26*, 125023, doi:10.1088/1361-665X/aa95ec.
19. Shiblee, M.N.I.; Ahmed, K.; Kawakami, M.; Furukawa, H. 4D Printing of Shape-Memory Hydrogels for Soft-Robotic Functions. *Adv. Mater. Technol.* **2019**, *4*, 1900071, doi:10.1002/admt.201900071.
20. Tanner, R.I. Hydrodynamic lubrication of ball and socket joints. *Appl. sci. Res.* **1959**, *8*, 45–51, doi:10.1007/BF00411737.
21. Jastifer, J.R.; Gustafson, P.A.; Labomascus, A.; Snoap, T. Ball and Socket Ankle: Mechanism and Computational Evidence of Concept. *J. Foot Ankle Surg.* **2017**, *56*, 773–775, doi:10.1053/j.jfas.2017.02.019.
22. Vaz, A.; Hirai, S. A simplified model for a biomechanical joint with soft cartilage. In *2004 IEEE International Conference on Systems, Man and Cybernetics (IEEE Cat. No.04CH37583).* 2004 IEEE International Conference on Systems, Man and Cybernetics, The Hague, Netherlands, 10-13 Oct. 2004; IEEE, 2004; pp 756–761, ISBN 0-7803-8567-5.
23. Walter, M.; Friess, F.; Krus, M.; Zolanvari, S.M.H.; Grün, G.; Kröber, H.; Pretsch, T. Shape Memory Polymer Foam with Programmable Apertures. *Polymers* **2020**, *12*, doi:10.3390/polym12091914.
24. Dashboard | Tinkercad. Available online: https://www.tinkercad.com/dashboard (accessed on 19 January 2022).
25. Ultimaker Cura: Powerful, easy-to-use 3D printing software. Available online: https://ultimaker.com/software/ultimaker-cura (accessed on 19 January 2022).
26. https://www.facebook.com/Magigooo. Magigoo Original - Magigoo. Available online: https://magigoo.com/products/magigoo/ (accessed on 11 May 2021).

Chapter 5: *Ex-Situ* Programming of Objects Manufactured via Fused Filament Fabrication to Attain Two-Way Shape Memory Effect

Chapter 5.1: Actuating Shape Memory Polymer for Thermoresponsive Soft Robotic Gripper and Programmable Materials

Chapter 5.1: Actuating Shape Memory Polymer for Thermoresponsive Soft Robotic Gripper and Programmable Materials

The original article Schönfeld, D.; Chalissery, D.; Wenz, F.; Specht, M.; Eberl, C.; Pretsch, T. Actuating Shape Memory Polymer for Thermoresponsive Soft Robotic Gripper and Programmable Materials. Molecules 2021, 26, 522 and graphical abstract are published in MDPI Molecules and are available at https://doi.org/10.3390/molecules26030522.

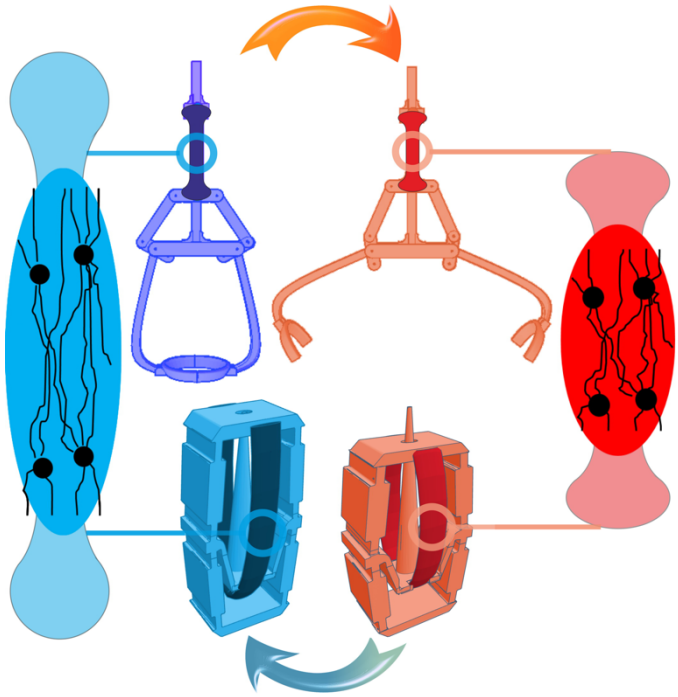

Figure 5.1.0. The graphical abstract of the article "Actuating Shape Memory Polymer for Thermoresponsive Soft Robotic Gripper and Programmable Materials" is published in MDPI Molecules 2021, 26, 522.

Contribution

My contribution: Conceptualization of two-way shape memory effect (2W-SME) screening characterization measurement, the combination of actuating element with linkage mechanism and unit cell (**Figure 5.1.13b and c**). Concept development, design, manufacturing, and actuation of the soft gripper. Design development of actuating elements. 3D printing of both unit cells and actuating elements. 2W actuation analysis of unit cell (**Figure 5.1.14**). Visualization and preparation of images (including videos and graphical abstract, excluding **Figures 5.1.1, 5.1.2, 5.1.3, 5.1.8, 5.1.11c,** and **5.1.12**)

Equal/ shared contribution of Schönfeld, D. and me: Carried out DSC, thermomechanical analysis. (DMA), tensile tests, and filament extrusion. Development of 2W programming

procedure. Contributed equally in methodology, validation, formal analysis, investigation, writing—original draft preparation,
Not included in my contribution: Synthesis, titration and FT-IR, 2W-SME durability experiment, and design development of the unit cells.

Schönfeld, D.: Conceptualization of novel polyester urethane (PEU) for 2W-SME and combination of actuating element with unit cell (**Figure 5.1.11 c**). Conducted the durability experiment of 2W actuating element. 2W actuation analysis of unit cell (**Figure 5.1.12**). Synthesis and development of PEU. Carried out FT-IR. Visualization and preparation of images (**Figures 5.1.1**, **5.1.2**, **5.1.3**, **5.1.8**, **5.1.11c**, and **5.1.12**). Project lead of the article.

Wenz, F.: Design development and writing—original draft preparation of unit cell in **Figure 5.1.11a**.

Specht, M.: Design development and writing—original draft preparation of unit cell in **Figure 5.1.13a**.

Eberl, C.: Project administration, writing—review and editing of unit cell.

Pretsch, T.: Conceptualization of the manuscript, funding acquisition, project administration, supervision, writing—review and editing

Chapter 5.1: Actuating Shape Memory Polymer for Thermoresponsive Soft Robotic Gripper and Programmable Materials

Dennis Schönfeld [1], Dilip Chalissery [1], Franziska Wenz [2,3], Marius Specht [2,3], Chris Eberl[2,3] and Thorsten Pretsch [1,*]

[1] Fraunhofer Institute for Applied Polymer Research IAP, Geiselbergstr. 69, 14476 Potsdam, Germany; dennis.schoenfeld@iap.fraunhofer.de (D.S.); dilip.chalissery@iap.fraunhofer.de (D.C.)

[2] Fraunhofer Institute for Mechanics of Materials IWM, Wöhlerstr. 11, 79108 Freiburg, Germany; franziska.wenz@iwm.fraunhofer.de (F.W.); MariusSpecht@web.de (M.S.); chris.eberl@iwm.fraunhofer.de (C.E.)

[3] Department of Microsystems Engineering IMTEK, University of Freiburg, Georges-Koehler-Allee 078, 79110 Freiburg, Germany

* Correspondence: thorsten.pretsch@iap.fraunhofer.de; Tel.: +49-(0)-331/568-1414.

5.1.0. Abstract: For soft robotics and programmable metamaterials, novel approaches are required enabling the design of highly integrated thermoresponsive actuating systems. In the concept presented here, the necessary functional component was obtained by polymer syntheses. First, poly(1,10-decylene adipate) diol (PDA) with a number average molecular weight M_n of 3290 g·mol^{-1} was synthesized from 1,10-decanediol and adipic acid. Afterward, the PDA was brought to reaction with 4,4'-diphenylmethane diisocyanate and 1,4-butanediol. The resulting polyester urethane (PEU) was processed to the filament, and samples were additively manufactured by fused-filament fabrication. After thermomechanical treatment, the PEU reliably actuated under stress-free conditions by expanding on cooling and shrinking on heating with a maximum thermoreversible strain of 16.1%. Actuation stabilized at 12.2%, as verified in a measurement comprising 100 heating-cooling cycles. By adding an actuator element to a gripper system, a hen's egg could be picked up, safely transported and deposited. Finally, one actuator element each was built into two types of unit cells for programmable materials, thus enabling the design of temperature-dependent behavior. The approaches are expected to open up new opportunities, e.g., in the fields of soft robotics and shape morphing.

Keywords: additive manufacturing; soft robotics; actuation; programmable materials; polyester urethane; shape morphing; unit cell

5.1.1. Introduction

Soft robotics, as well as the still novel metamaterials [1,2] or programmable materials [3], require compliant actuator materials. Shape memory polymers (SMPs) perfectly fulfill this criterion. SMPs are stimuli-responsive materials, which are able to fix a temporary shape after a thermomechanical treatment, also denoted as “programming”. The temporary shape will be stable until the one-way shape memory effect (1W SME) is triggered, whereupon the polymer almost completely returns into the permanent shape [4]. Shape recovery is an entropically driven process. It is based on the phenomenon of entropy elasticity; the theory of rubber elasticity provides the basis [5]. Most commonly, the shape memory effect is triggered by heat [4,6–12]. Alternatively, switching can be realized for materials equipped with appropriate fillers by indirect heating when applying an electric [13,14] or a magnetic field [15,16] or, e.g., by illumination with near-infrared light in the case of SMPs with photoresponsive fillers [17,18].

In the past few years, it has become known how to transfer semicrystalline SMPs into two meta stable states, between which they can be switched back and forth virtually as often as desired by varying the temperature. The driving forces for the so-called two-way shape memory effect (2W-SME) in polymers are phase transitions between crystalline and amorphous phases, supported by entropy elasticity as discovered by Mather’s group for cross-linked poly(cyclooctene) films in the presence of an external load [19]. Later, the programming technology was further developed and transferred to other polymer systems so that actuation in the stress-free state became possible [20–23]. As known from semicrystalline polyester urethane (PEU), actuation can also be very pronounced and complies with the same physical principles [24]. The fact that polymers react to temperature changes in their surroundings makes them interesting candidates for applications in which complex switching and control electronics are to be avoided [25]. For example, in the field of soft robotics, a specific subfield of robotics that deals with the construction of robots from highly compliant materials [26–28], first steps were taken to demonstrate the attractiveness of SMPs [29–32]. Anyway, there are only a few concepts in this respect, and the developments are primarily based on the 1W SME [33–35]. On the other side, an example for the 2W-SME was provided by Behl et al.[20], who employed chemically cross-linked poly(ω-pentadecalactone) and poly(ε-caprolactone)-based polyester urethane to fabricate a gripper, which after programming opened at 50 °C and closed at 0 °C. The system was able to grab and release a small coin upon cooling and heating. In another work, Zhou et al.[36] introduced a gripper from a chemically cross-linked poly(octylene adipate) and demonstrated how programming enables the lifting and depositing of a small screw at temperatures between 10 °C and 36 °C. In both cases, the essential advantage of the two-way shape memory effect becomes clear: autonomous motion. However, both studies focus mainly on the handling of small and simple objects. They have in common that the selection of the lower actuation temperature necessitates active cooling since it is below room temperature. In addition, the complexity of actuation is not really significant.

To address these problems, this contribution reports on the synthesis of a PEU with promising thermal and mechanical properties. Furthermore, we describe a route of how to identify pronounced actuation and used thermomechanical treatment to facilitate reliable actuator functionality. On this basis, a novel system was built in which the actuator transfers its motion to the stiff, mobile components of a gripper, thus opening the door to grab and release bigger and more complex objects.

In order to pursue a new direction, a coupling of actuator elements with the elastic parts of a mechanical unit cell or with a unit cell, which was completely built from one elastomer, was realized. It will be demonstrated that such actuating unit cells can change their states as a function of temperature, thus symbiotically combining actuation with unit cell functionalities. The obtained shape morphing unit cells are considered as the first step toward the production of novel, thermoresponsive metamaterials, which are assembled out of periodically repeated unit cells that determine their physical properties [37]. In essence, it will be demonstrated that the ability of the polymer to transfer its movements makes it possible to produce completely new systems with programmable property profiles.

5.1.2. Results and Discussion

Poly(1,10-decylene adipate) diol (PDA) is a promising building block both in the chemistry of polyester urethanes and polyester urethane ureas [25]. It was synthesized in the present work in a polycondensation reaction from 1,10-decanediol and adipic acid (**Figure 5.1.1**).

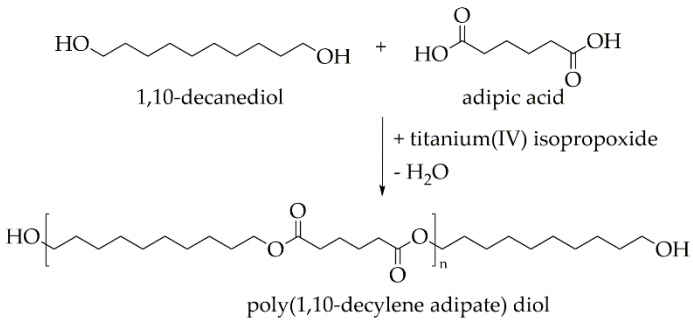

Figure 5.1.1. Synthesis of poly(1,10-decylene adipate) diol via polycondensation reaction.

The number average molecular weight M_n of the PDA was determined to ~3290 g·mol$^{-1,}$ and the calorimetric properties were characterized. The obtained polyester exhibits a melting transition spreading from 55 °C to 77 °C with a peak temperature of 71 °C and a crystallization transition ranging from 62 °C to 43 °C with a peak temperature located at 58 °C (**Figure 5.1.2**). Thus, both phase transition temperatures were well above room temperature. As expected, the assigned phase transitions were in good agreement with those of other aliphatic polyesters [38].

Following the prepolymer method [39–41], the freshly synthesized PDA was brought to reaction with 4,4'-diphenylmethane diisocyanate (4,4'-MDI) in order to build up an

isocyanate-endcapped prepolymer, before the chain extender 1,4-butanediol (BD) was finally added. This resulted in the formation of a polyester urethane (PEU, **Figure 5.1.3**).

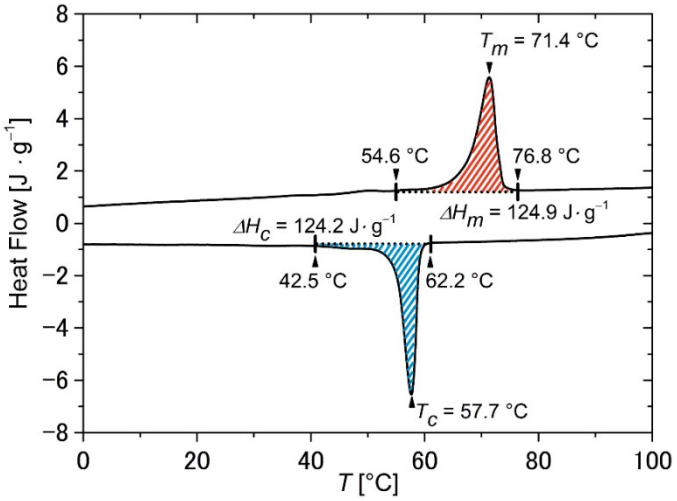

Figure 5.1.2. Differential scanning calorimetry (DSC) thermogram of poly(1,10-decylene adipate) diol showing the second heating and cooling with temperature rates of 10 °C·min^{-1}. The enthalpies of melting ΔH_m (red dashed area) and crystallization ΔH_c (blue dashed area) are included.

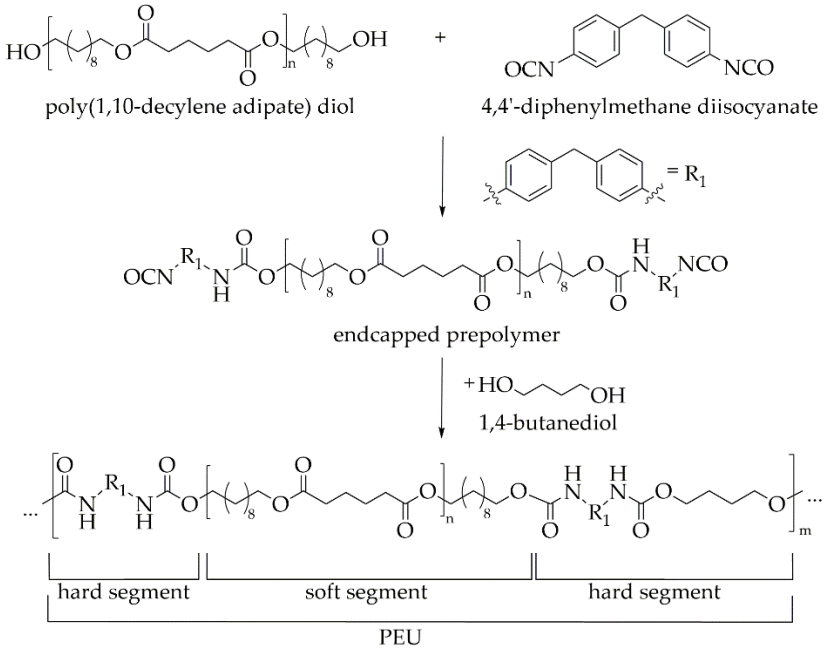

Figure 5.1.3. Synthesis of poly(1,10-decylene adipate) diol (PDA)-based polyester urethane (PEU) via polyaddition reaction using the prepolymer method.

Herein, it is obvious that the so-called soft segment is composed of the synthesis building block PDA while the hard segment was obtained from the reaction of MDI and BD. Fourier-transform infrared (FT-IR) spectroscopy was used to verify the completeness of the polyaddition reaction. Since the characteristic vibrational modes for polyester urethane were visible and, in addition, only a very weak signal associated with freely available isocyanate

appeared in the spectrum, the reaction was mostly complete. A detailed analysis can be found in the supplementary material (**Figure S5.1.16**.).

Once characterized, the PEU was melt-extruded into a filament as essential for further processing via fused filament fabrication (FFF). For this purpose, the same extrusion line was used as reported recently [42]. The obtained filament had a homogenous diameter of 2.85 ± 0.08 mm, so that an important attribute for further processing was fulfilled. Tensile bars of type 5B according to ISO 527-2:1996 [43] were then additively manufactured, and their mechanical behavior was determined in tensile tests at ambient temperature (**Figure 5.1.4**).

From the stress–strain relationship, an averaged Young's modulus of 258.7 ± 10.2 MPa was determined. In all three measurements, a yield-point occurred at a strain value of 17 ± 3%, corresponding to a stress of 7.1 ± 1.4 MPa (**Figure 5.1.4a**). Further increasing the load resulted in necking (**Figure 5.1.4b**, images 2–4) as already verified for similar materials [44–46] and strain softening first, followed by strain hardening as accompanied by an increase in stress, culminating in specimen rupture at strains of 1405 ± 83%. The material behavior can be explained with the coexistence of two types of PDA segments, at which one part was highly flexible and amorphous while the other one was rigid and crystalline. In the course of deformation, a progressive conversion from amorphous to crystalline segments seemed to occur. The assumption was supported by a whitish coloring of the tensile bar as associated with a crystallization process (**Figure 5.1.4b**, image 4).

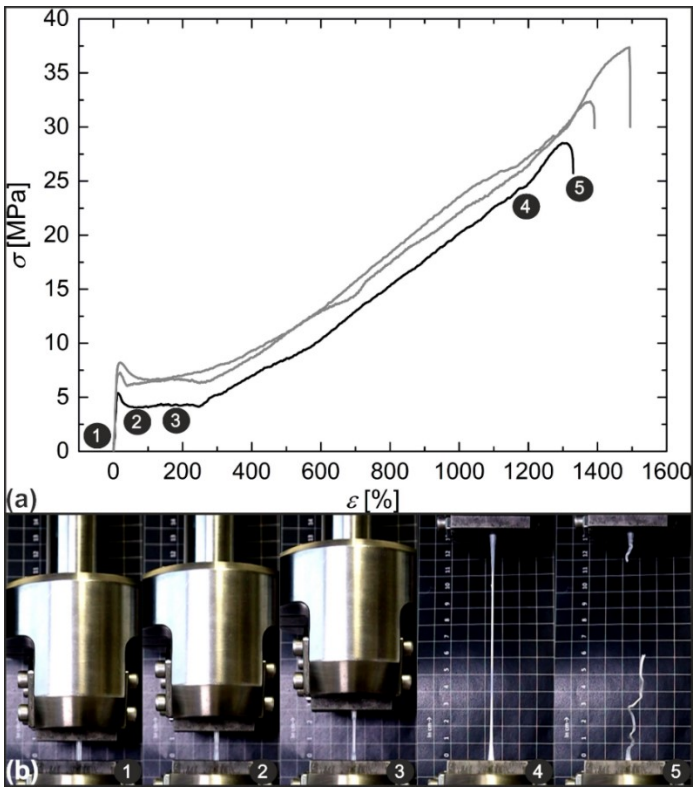

Figure 5.1.4. Mechanical characterization of PDA-based PEU using tensile tests: engineering stress–strain curves (**a**) and the associated deformation behavior (**b**). The experiments were carried out on tensile bars at 23 °C with an initial strain rate of 1%·min^{-1} until 5% of strain were reached and continued with 2000%·min^{-1} until rupture occurred.

Having the good mechanical properties of the PEU in mind, differential scanning calorimetry (DSC) and dynamic mechanical analysis (DMA) were used to study the thermal phase transition behavior (**Figure 5.1.5**). This ensured that later thermomechanical tests were performed at appropriate temperatures. The calorimetric properties of the PEU were characterized by a broad melting transition between 29 °C and 72 °C and a crystallization transition spreading from 52 °C to 24 °C (**Figure 5.1.5a**), which were assigned to the phase transitions of PDA. In comparison with the measurement data provided for pure PDA (**Figure 5.1.2**), an extension of both phase transitions toward lower temperatures could be verified together with lower enthalpies of melting and crystallization. An inhibited crystallization behavior was expected because of the lower content of polyester polyol and phase segregation effects [47]. In the network structure of the PEU, the hard segments were efficiently acting as net points and were thus reducing the crystallinity of the soft segment as verified earlier for similar PEUs [48,49]. Apart from that, the elastic behavior as exemplified by the evolution of the storage modulus *E′* exhibited a two-step decrease in the DMA (**Figure 5.1.5b**). This observation can be traced back to the consecutive devitrification and melting of the PDA phase. Indeed, such behavior is commonly observed for semicrystalline PEUs [50–52]. The presence of the hard segments acting as netpoints ensured that the PEU was still characterized by dimensional stability at temperatures exceeding the melting transition of the PDA phase at approximately 65 °C. In turn, the loss modulus *E′′*, which is a measure for the viscous response of a polymer, exhibited a broad signal with a maximum at about −14 °C, which declined upon heating until a plateau formed at temperatures above 65 °C. The *tan δ* peak was located at 7 °C **(Figure 5.1.5b**). It is defined as the ratio between loss modulus *E′′* and storage modulus *E′* and is often used to determine the glass transition temperature T_g in urethane-based polymers [53,54].

In the next step, a method for programming the 2W-SME was developed in line with the thermal and mechanical properties of the PEU. **Figure 5.1.6** shows the evolution of the stress–strain progression for the thermomechanical treatment of a type 5B tensile bar [43], which was obtained from FFF.

In accordance with the thermal behavior of the PEU, the tensile bar was heated to 75 °C and kept there for 20 min in order to ensure that all PDA crystals were molten before the polymer was elongated. In comparison to the stress–strain behavior verified in **Figure 5.1.4**, no yield point could be detected during elongation (**Figure 5.1.6**), and a significantly lower Young's modulus of 1.4 ± 0.1 MPa was determined. A similar temperature dependence in stress–strain behavior is known from other physically cross-linked polymers like poly(1,4-butylene adipate)-based PEU [46]. However, to assure that the polymer chains were aligned in a highly oriented state, the strain was kept constant at a value of 700%, and the sample was slowly cooled to 23 °C in order to enable the extensive crystallization of the PDA phase before unloading was carried out. Although not verified in another experiment, the programming of the 2W-SME appeared to be successful even at a much shorter crystallization time. This finding can be deduced from the inset of **Figure 5.1.6**, which shows that most of the stress relaxation took place immediately after stretching and that the recorded stress did

not change significantly after a holding time of 100 min. Upon unloading, the polymer stabilized at a strain of 695%, which was close to the maximum strain applied.

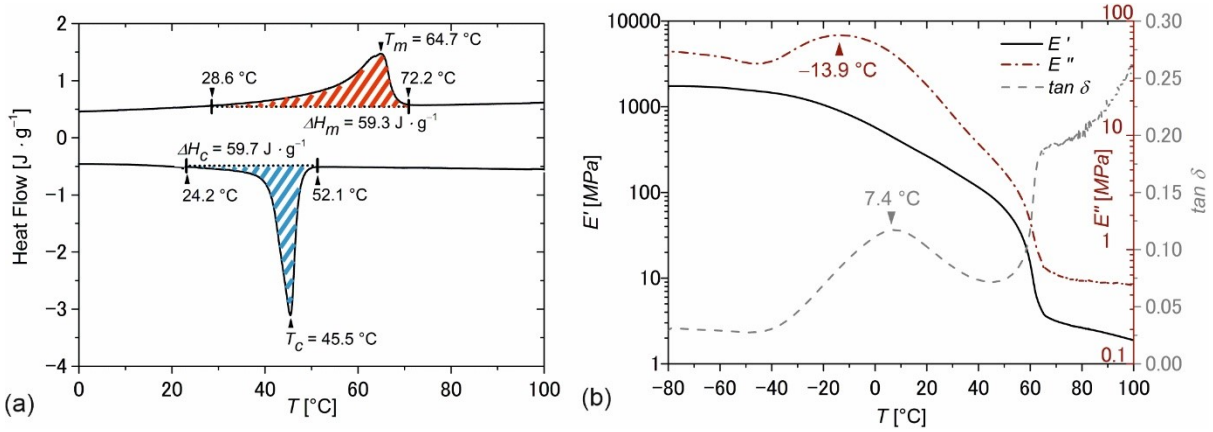

Figure 5.1.5. Thermal and thermomechanical properties of PDA-based PEU as determined by DSC (**a**, second heating and cooling with temperature rates of 10 °C·min^{-1}, the enthalpies of melting ΔH_m, red dashed area, and crystallization ΔH_c, blue dashed area, are included) and DMA (**b**, the temperature dependence of storage modulus *E'*, loss modulus *E''* and loss factor *tan δ* at a heating rate of 3 °C·min^{-1}).

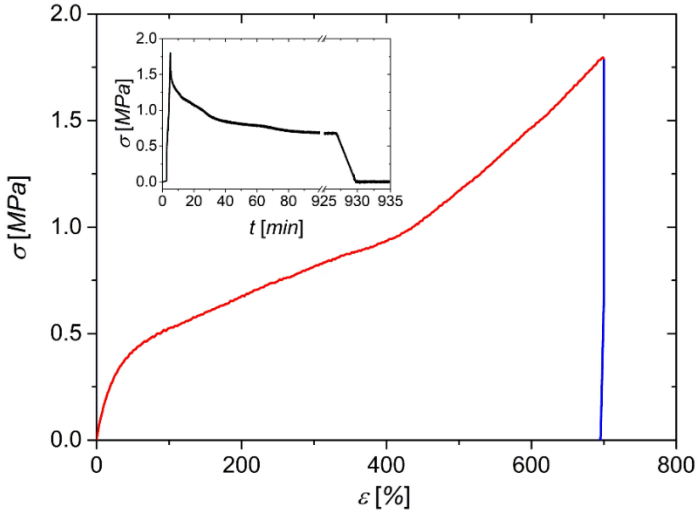

Figure 5.1.6. Stress–strain behavior of PDA-based PEU when programming the 2 W SME. The individual steps consisted of elongation at T_d = 75 °C (red color, strain rate = 300%·min^{-1}) followed by slow cooling and unloading at 23 °C (blue color, unloading rate = 1 N·min^{-1}). The inset shows the evolution of stress over time for a longer period before unloading was carried out.

Afterward, a DMA measurement was carried out on a sample, which was thermomechanically treated as reported before (**Figure 5.1.6**). The aim was to identify an ideal scenario for stress-free actuation by systematically varying the considered temperature range. The results are supplied in **Figure 5.1.7**.

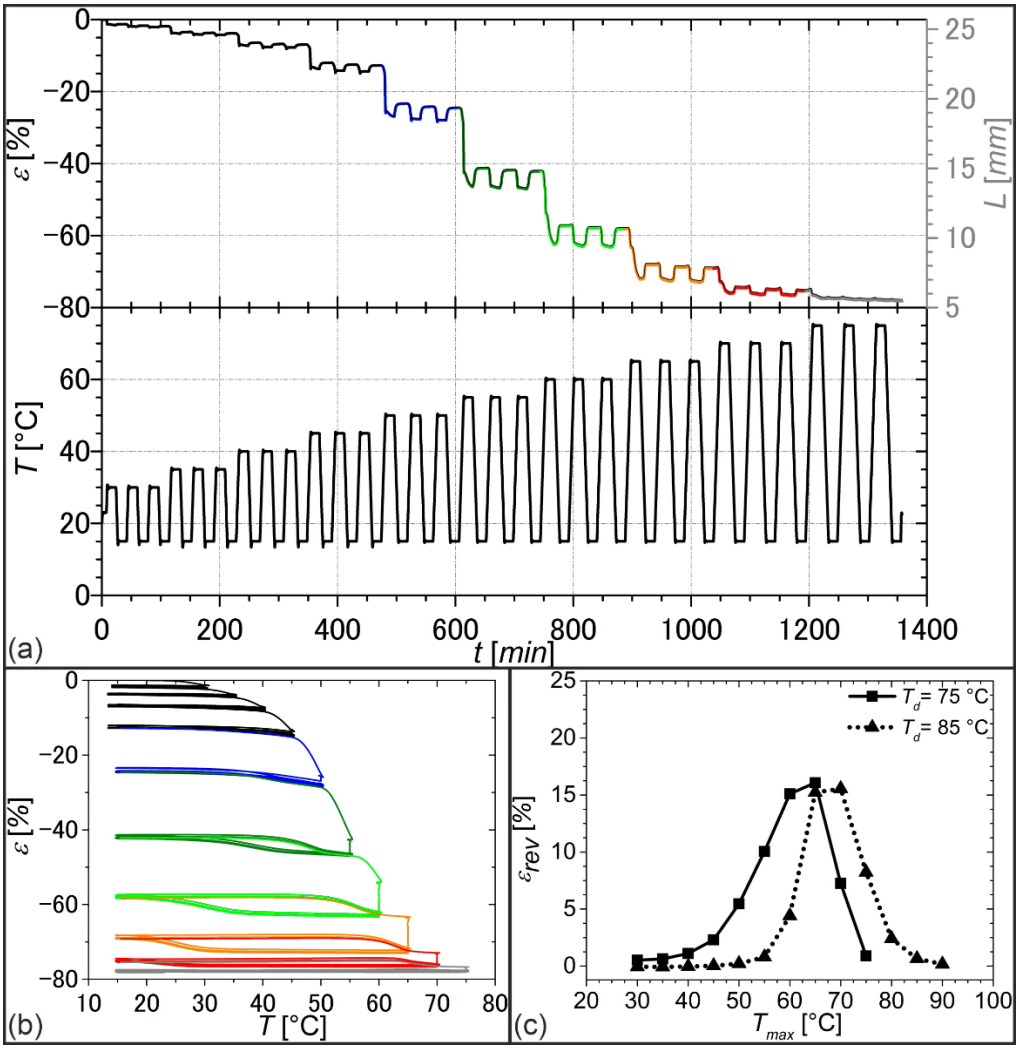

Figure 5.1.7. Influence of the selection of T_{max} on actuation of PDA-based PEU under stress-free conditions: (**a**) evolution of strain ε and sample length L (differently colored according to the temperature intervals investigated) and temperature T with measuring time t for a sample deformed at T_d = 75°; (**b**) strain–temperature relationship to the experiment shown in (**a**) using the same color codes; (**c**) evolution of thermoreversible strain ε_{rev} depending on T_{max} for two deformation temperatures, the values for ε_{rev} are averaged for the second and third cycle.

Thermoreversible strain changes, here also denoted as actuation, could be detected in every single measurement cycle, even when continuously raising the upper temperature T_{max} from 30 °C to 75 °C while keeping the lower temperature at 15 °C (**Figure 5.1.7a,b**). Apart from entropy elasticity, the phenomena of melting-induced contraction (MIC) and crystallization-induced elongation (CIE) were probably the main driving forces for actuation [19]. In fact, only a small quantity of crystallizable segments was present when selecting a lower maximum temperature T_{max} because a larger part of the PDA phase was still in a crystalline state, resulting in weak elongation on cooling and weak contraction on heating, which can particularly be seen in the strain-temperature diagram of **Figure 5.1.7b** (black lines). By contrast, the successive increase in T_{max} led first of all to an increase in the proportion of crystallizable segments because more PDA crystals were molten. In parallel, a hysteresis behavior was observed, and actuation substantially increased. The hysteresis was

first observed when selecting a T_{max} of 55 °C (**Figure 5.1.7b**, dark green color). Further increasing T_{max} to 65 °C culminated in the most pronounced hysteresis (**Figure 5.1.7b**, orange color) with a maximum change in thermoreversible strain ε_{rev} of 16.1%. This becomes particularly clear in the associated $\varepsilon_{rev}/T_{max}$ diagram (**Figure 5.1.7c**, solid line). Interestingly, the value for T_{max} corresponded exactly with the melting peak temperature of the PDA phase in the DSC measurement (**Figure 5.1.5a**). The further increase of T_{max} gave a decrease in actuation since the systematic melting of PDA crystals resulted in strain recovery of the PEU and thus a lower overall strain. In other words, the elongation at the beginning of each cooling step was gradually shifted to smaller values. Obviously, under these conditions, highly oriented crystals serving as netpoints were molten and could therefore no longer support the structural integrity associated with the respective morphological states of the polymer.

Following a different approach, the programming route was modified by raising the deformation temperature T_d to 85 °C, which was even further above the offset melting temperature of the crystalline PDA phase (**Figure 5.1.5a**). This time, a shift in the temperature range, in which actuation took place, could be witnessed (**Figure 5.1.7c**, dotted line). Indeed, the temperature region of actuation was raised together with the temperature, at which the maximum actuation occurred. Especially, in this case, we assume that PDA crystallites of higher temperature stability could be introduced in the course of deformation or directly afterward. These crystals obviously ensured the stability of the actuating polymer at elevated temperatures, namely in actuation states up to a temperature of about 80 °C. The rise in maximum actuation temperature at higher deformation temperature indicates that the temperature window of actuation can be adjusted by varying the deformation temperature and thus the programming conditions.

To investigate the durability of actuation under stress-free conditions, a sample of PEU was programmed (T_d = 75°) as described above and subjected to 100 heating-cooling cycles in the DMA with maximum and minimum temperatures of 64 °C and 15 °C, respectively (**Figure 5.1.8**).

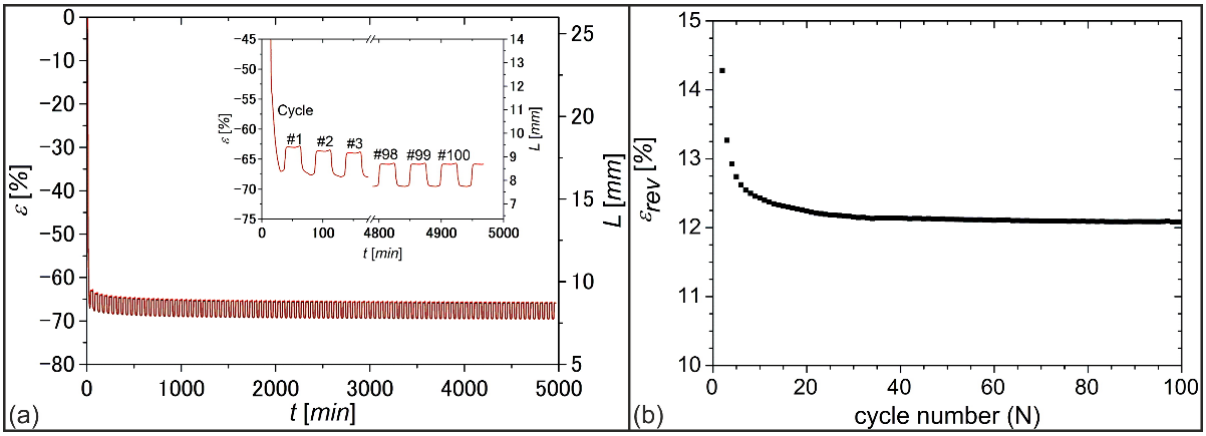

Figure 5.1.8. DMA measurement to determine the durability of actuation for PDA-based PEU: evolution of (**a**) nominal strain ε with time t and (**b**) thermoreversible strain ε_{rev} with cycle number N.

In the beginning, the development of strain over time exhibited a strong drop in strain (**Figure 5.1.8a**), which was attributed to the melting of highly oriented PDA crystals. In particular, in the first five cycles, the actuation showed a drop (**Figure 5.1.8b**), which was presumably caused by rearrangements of polymer chains [55]. A more stable actuation was then observed; after about 25 cycles of heating and cooling, the actuation was nearly the same. Apparently, the PEU formed two temperature-bistable states, which differed in their elongation. In the end, ε_{rev} approached an almost constant value of 12%.

To take advantage of actuation, a suitable design for an actuator element made of PEU was developed, and possibilities for implementation into a gripping technology were explored using the linkage mechanism of Gholaminezhad et al. [56]. The corresponding computer-aided design (CAD) drawing of the gripper is shown in **Figure 5.1.9**. An important aspect of the design was that the base material of the gripper exhibited good mechanical stability, especially in the temperature range of actuation. Therefore polyethylene terephthalate glycol (PET-G) was selected as a rigid base material (**Figure 5.1.9a–g**) [57], while the centerpiece of the gripper, namely the actuator element, was made of thermomechanically pretreated PEU (T_d = 75 °C, **Figure 5.1.9h)**. The design of the gripper was chosen so that one millimeter of actuation was able to trigger a sixteen-fold increase in distance of the two gripper arms (**Figure 5.1.9e**). The diameter of the gripper element (**Figure 5.1.9g**) was set to 35 mm in order to enable that an object with the size of a hen´s egg could be reliably gripped. All parts exhibited in **Figure 5.1.9** were manufactured via FFF. After rapid prototyping, the moving parts were assembled (**Figure 5.1.9i,j**), and care was taken to avoid friction between the individual components.

The main part of the gripper (exhibited in **Figure 5.1.9a**) was constructed to hold the parts of the system either directly or indirectly. Once the actuator element with the PEU being in its low-temperature stable state was installed between the upper actuator holder and the lower actuator- and linkage holder (shown in **Figure 5.1.9b,c**), the actuation capability was studied (**Figure 5.1.10**). In this particular case, the minimum temperature was increased from 15 °C to 23 °C compared to the previous experiments in order to demonstrate a higher degree of practical suitability while the maximum temperature was kept constant at 64 °C.

As expected, the movement of the PEU could be transferred into motion perpendicular to the actuation direction in the form of a thermoreversible opening and closing of the clamps. Taking advantage of this behavior, a hen´s egg could be picked up, transported and deposited without causing any damage (**Figure 5.1.10**, **s5.1.1.movie** in supplementary material).

In detail, raising the temperature to 64 °C resulted in the contraction of the PEU, which pulled the lower actuator- and linkage holder (exhibited in **Figure 5.1.9c**) and the linkage bar (exhibited in **Figure 5.1.9d**) upwards, thereby opening the gripper arms (shown in **Figure 5.1.9e**) with the attached egg holder (shown in **Figure 5.1.9g**). At this time, the gripper system was positioned near to the egg (second image in **Figure 5.1.10**). On cooling to 23 °C, the expansion of the PEU pushed the lower actuator and linkage holder (**Figure 5.1.9c**) and the linkage bar (**Figure 5.1.9d**) downwards, resulting in a closing of the gripper arms and the gripping of the egg. At this moment (middle of **Figure 5.1.10**), the object could be lifted at

ambient temperature and taken to the desired location for further handling. On heating back to 64 °C, the gripper arms opened again, thus enabling the safe unloading of the fragile object (right side of **Figure 5.1.10**). Basically, the gripper system should be capable of repeated gripping and opening in a large number of cycles as indicated by the durability measurement (**Figure 5.1.8**).

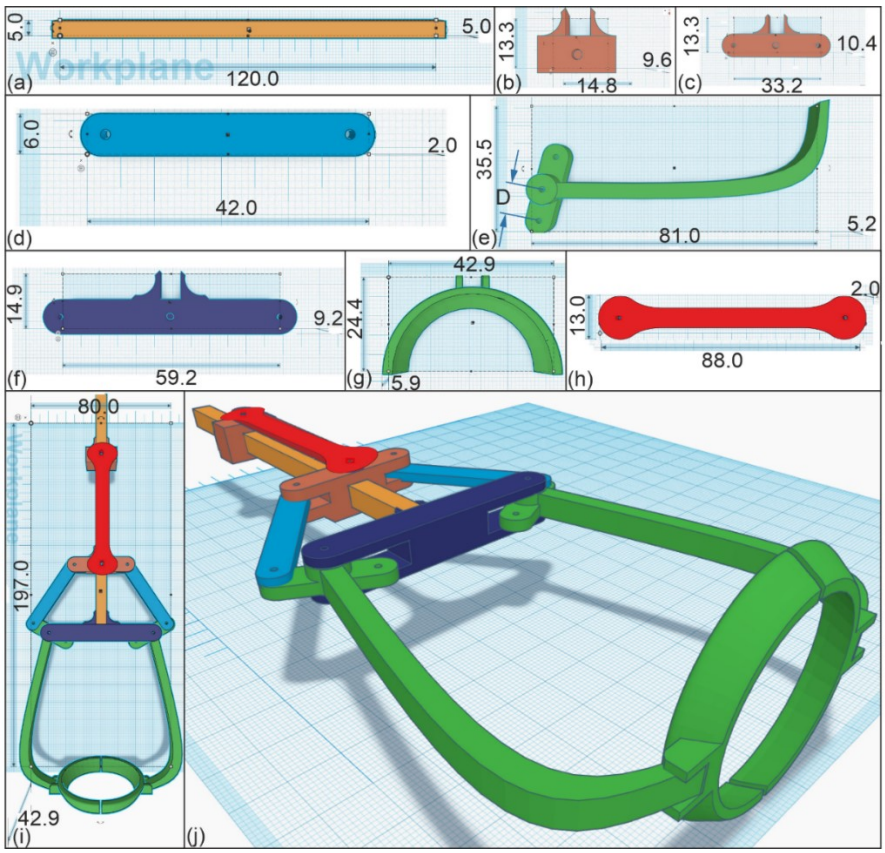

Figure 5.1.9. Technical drawing of a gripper: (**a**) main part; (**b**) upper actuator holder; (**c**) lower actuator- and linkage holder; (**d**) linkage bar; (**e**) gripper arm; (**f**) gripper holding part; (**g**) egg holder; (**h**) actuator element; (**i**) top view of assembled gripper arrangement; and (**j**) isometric view of gripper system. All data are provided in mm.

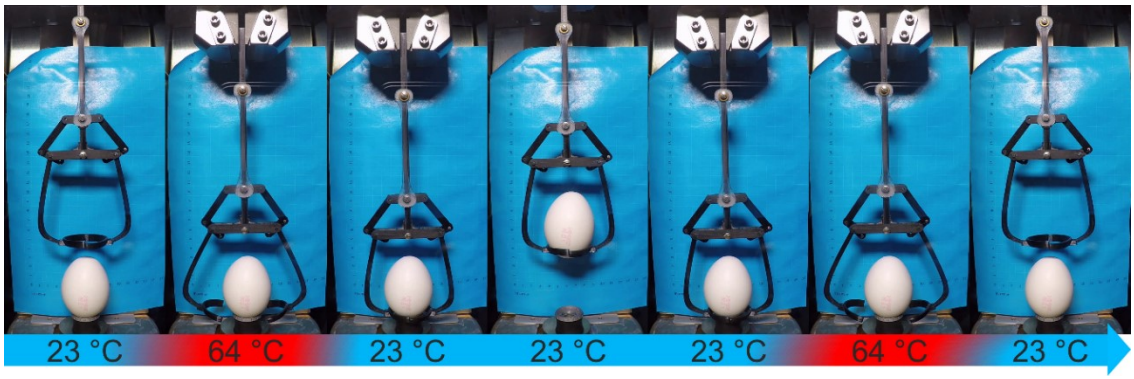

Figure 5.1.10. Gripper with PEU actuator element in operation, enabling the transport of a hen´s egg with a height of 55.5 mm, a width of 39 mm and a weight of 58 g. The lifting and lowering of the whole gripper were done manually.

In a fundamental approach, PEU actuator elements were integrated into distinct unit cells to obtain thermoresponsive programmable materials. Regarding the first concept, an actuator element made of PEU was fixed with glue on the surface of a unit cell to investigate to what extent its motion can be transferred to the cell. The unit cell was designed to allow larger deformation amplitudes between the temperature-dependent states of the PEU (**Figure 5.1.11**).

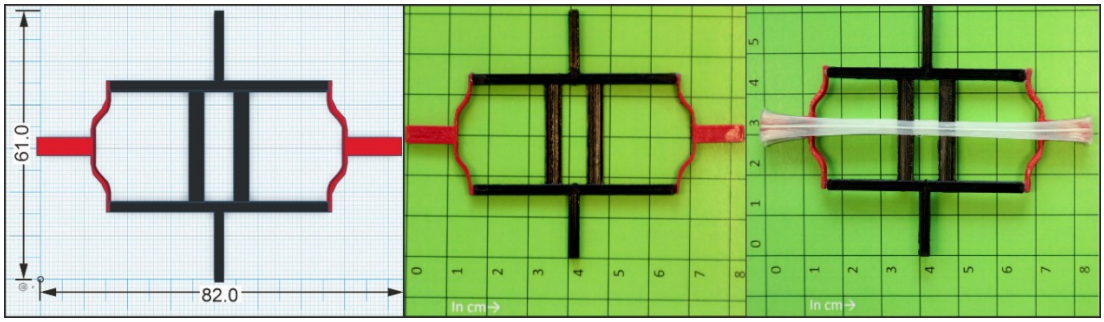

Figure 5.1.11. Unit cell consisting of an elastomeric material (Desmopan® 9370AU, red color) and a stiff material (PET-G, black color): Technical drawing (**left**, all data are provided in mm.), additively manufactured unit cell (in the **middle**) and state after installing the actuator element (whitish color, **right**). Centimeter paper was used as a base in the second and third image.

The cell was built up by the same PET-G as used for most parts of the gripper (black color) and by an elastic base material, here another thermoplastic polyurethane (red color), to which the PEU was attached with adhesive. The cell consisted of two center beams (black color), providing stability for outside buckling beams (red color). The cross beams were connecting all elements. This configuration of buckling beams can be used to provide metastable states, either being popped out or switched through. In this example, the beams were designed. Hence, in combination with the PEU actuator, the switched through the state could be reached at elevated temperature. Basically, such unit cells can be employed to reversibly absorb energy [58] or to implement mechanical memory behavior in materials [3].

Upon heating and cooling between 23 °C and 64 °C, the actuator element was able to transfer its motion to the unit cell, resulting in a change of its structure with regard to the elastomer parts (**Figure 5.1.12**).

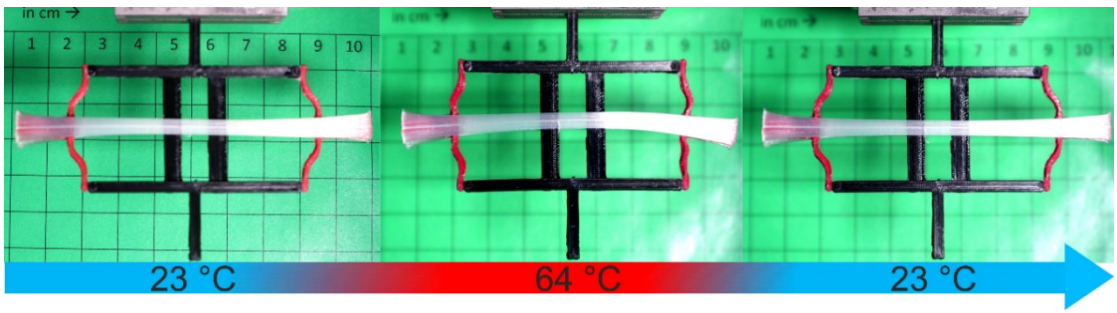

Figure 5.1.12. Thermoresponsiveness of a unit cell with a PEU actuator element. Centimeter paper was used as a base.

The PEU contracted on heating to 64 °C. As a result, the flexible parts of the unit cell were pulled together, which resulted in the formation of a second state whose stability was defined by the length of the actuator element (**Figure 5.1.12**, middle image). Cooling back to 23 °C was accompanied by the expansion of the PEU, leading to the return of the cell into its initial state (**Figure 5.1.12**, right image). This stretch-dominated approach makes clear that the movement of the actuator element could easily be transferred to the elastic parts of a cell, while the stiff parts of the cell remained unaffected. Thus, it could be demonstrated that combining a PEU actuator element with a unit cell allows switching back and forth between mechanical states, which differ in the shape of the elastic material.

As the last example, a macroscopic prototype of a unit cell for programmable wetting was produced. Normally such cells are roughly 100 µm high to work properly [59]. Nevertheless, a macroscopic prototype can be easily tested and scaled-down in a possible next step. The selected unit cell consisted of an outer cage providing potential contact to neighboring cells and mechanical stability for the inner mechanism. The outer cage contained a hole through which the spike can be pushed, leading to a strongly reduced contact area between the unit cell and, e.g., a drop of liquid on top (not shown here). The inner mechanisms allowed again two metastable states, similar to the previous case, with the spike being in or out. Therefore, a three-dimensional unit cell was manufactured from the same elastic base material as used above to autonomously open or close a hole in its surface depending on temperature (**Figure 5.1.13**). To achieve this, thermomechanically treated PEU was bent manually and attached to the unit cell with glue (**Figure 5.1.13**, right).

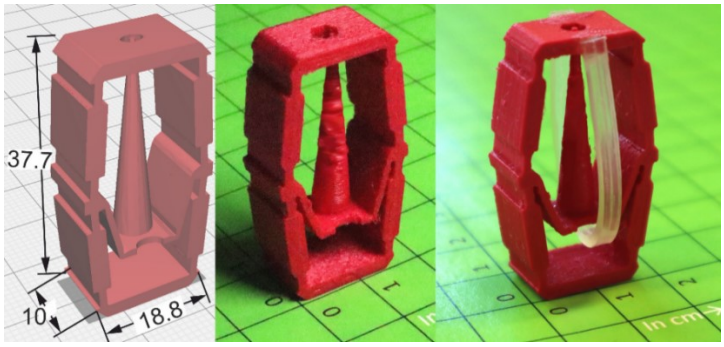

Figure 5.1.13. Unit cell with switchable surface topography. Technical drawing (**left**, all data are provided in mm.), unit cell after additive manufacturing with Desmopan® 9370AU (**middle**) and unit cell as assembled with the PEU actuator element (**right**). Centimeter paper was used as a base in the second and third image.

Figure 5.1.14 shows the actuation of the unit cell upon twofold heating and cooling. First, the increase in temperature from 23 °C to 64 °C led to the contraction of the PEU, thus inducing an external strain on the unit cell and lifting the spike through the opening at the top plane. In parallel, the unit cell itself also changed its structure by broadening. In turn, cooling to 23 °C resulted in the expansion of the PEU actuator element, which led to the relaxation of the unit cell and thereby the retraction of the spike and the thinning of the cell. Following this bend-dominated approach, a proof of principle for the ability of the PEU to

alter the structure of a complex unit cell and thereby the surface of its upper site could be achieved. A time-lapse video of unit cell actuation is provided as supplementary material (**s5.1.2.movie**). The precise opening and closing of the hole in the surface were verified for in total four thermal cycles. However, due to the good durability of actuation (**Figure 5.1.8**), we assume that also, in this case, considerably more cycles can be run through.

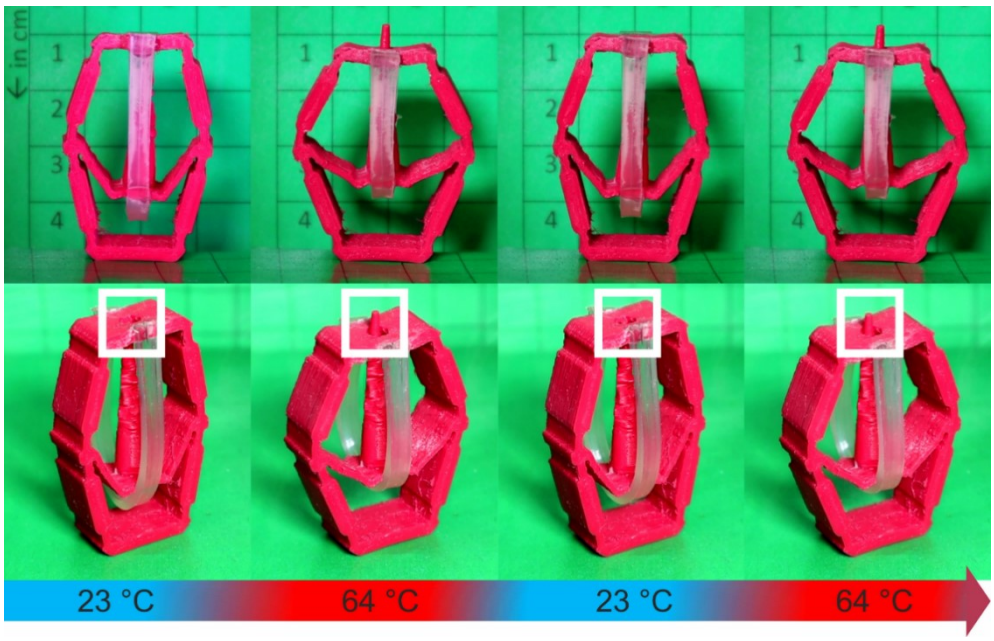

Figure 5.1.14. Thermoresponsiveness of a unit cell with a PEU actuator element. The system was cycled twice between 23 °C and 64 °C (**upper** row: front view, centimeter paper was used as background paper; **lower** row: isometric view, the white box was drawn in to illustrate the shape change in the surface).

5.1.3. Materials and Methods

Materials: 1,10-Decanediol, 4,4'-methylene diphenyl diisocyanate (4,4'-MDI) and titanium(IV) isopropoxide (TTIP) were purchased from Fisher Scientific (Schwerte, Germany). For titration tests, acetic anhydride, methanol and potassium hydroxide solution in methanol with concentrations of 0.5 mol^{-1} and 0.1 mol^{-1} were purchased from Merck (Darmstadt, Germany). *N*-Methyl-2-pyrrolidone (2-NMP), chloroform and 4-dimethylaminopyridine (4-DMAP) were bought from Carl Roth (Karlsruhe, Germany). Adipic acid, 1,4-butanediol and a molecular sieve (4 Å) were obtained from Alfa Aesar (Kandel, Germany). A filament from polyethylene terephthalate glycol (PET-G) was purchased from FilamentWorld (Neu-Ulm, Germany). The ether-based thermoplastic polyurethane elastomer Desmopan® 9370AU was supplied by Covestro Deutschland AG (Leverkusen, Germany). The polymer is characterized by a Shore A hardness of 70 [60] and was used as a flexible component in our unit cell approaches.

Synthesis of Polyester Diol: 1,10-Decanediol and adipic acid were mixed at a molar ratio of 1.1:1 and heated in a three-necked round-bottomed flask, which was equipped with a mechanical stirrer, nitrogen gas inlet and distillation condenser. All reactants were molten at

about 150 °C while titanium(IV) isopropoxide was added under stirring. Adjacently, the mixture was heated to 190 °C. After a remarkable decrease in distillation temperature, the mixture was further heated to 210 °C, whereupon the pressure was reduced to approximately 20 mbar. After two hours of continuous stirring, the melt was poured into a can. The obtained poly(1,10-decylene adipate) diol (PDA) solidified and was analyzed before PEU synthesis was carried out.

Titration: Titration was used to determine both the acid value and hydroxyl value and thus the number average molecular weight M_n of PDA. Therefore, a TitroLine 7000 from SI Analytics (Mainz, Germany) was employed. The procedure was executed in compliance with DIN EN ISO 2114 and 4629-2 [61,62]. To determine the acid value, a sample of PDA was dissolved in a mixture of chloroform/methanol with a volume ratio of 5: 1. The solution was titrated against a potassium hydroxide solution in methanol, having a concentration of 0.1 mol^{-1}. For the determination of the hydroxyl value, another sample of PDA was dissolved in chloroform. After adding acetic anhydride diluted in 2-NMP as well as 4-DMAP diluted in 2- NMP, the solution was heated and kept under stirring at 60 °C for 15 min. Thereafter, deionized water was added. After 12 min, the sample solution was titrated against a potassium hydroxide solution in methanol, having a concentration of 0.5 mol^{-1}.

Synthesis of Polyester Urethane: A polyester urethane (PEU) was synthesized using the prepolymer method. In order to obtain a PEU with approximately 15% of hard segment content, the molar ratio of the reactants was set to 1:1.98:0.97with regard to PDA, 4,4'-MDI and 1,4-butanediol, respectively. The reaction was carried out with a slight excess of isocyanate (NCO/OH = 1.005). Overnight, PDA was dried in a glass reactor in a vacuum oven at 90 °C. The following day, it was heated under nitrogen flow and stirring to 120 °C. Adjacently, isocyanate was added, and the mixture was continuously stirred for 90 min. The obtained prepolymer was directly converted to PEU by adding 1,4-butanediol, serving as a chain extender. In parallel, the stirring speed was raised. As the viscosity increased significantly, the reaction was stopped, and the polymer melt was poured onto a plate covered with polytetrafluoroethylene. Finally, the PEU was cured in an oven for 120 min at 80 °C.

Fourier-Transform Infrared Spectroscopy: The synthesized PEU was investigated by Fourier-transform infrared (FT-IR) spectroscopy. The measurements were carried out with a Nicolet Nexus 470/670/870 FT-IR spectrometer from Thermo Fisher Scientific (Madison, WI, USA). The spectrometer was equipped with an attenuated total reflectance (ATR) device. In total, 40 scans with a spectral resolution of 2 cm^{-1} were averaged to give the spectrum from 4000 cm^{-1} to 650 cm^{-1}.

Extrusion: The synthesized PEU was ground with a cutting mill type M 50/80 from Hellweg Maschinenbau (Roetgen, Germany). The obtained flakes were dried at 110 °C for 150 min in a vacuum drying chamber VDL 53 from Binder GmbH (Tuttlingen, Germany). Subsequently, the flakes were fed into an extrusion line to produce filaments. A schematic drawing of the extrusion line is shown in **Figure 5.1.15**.

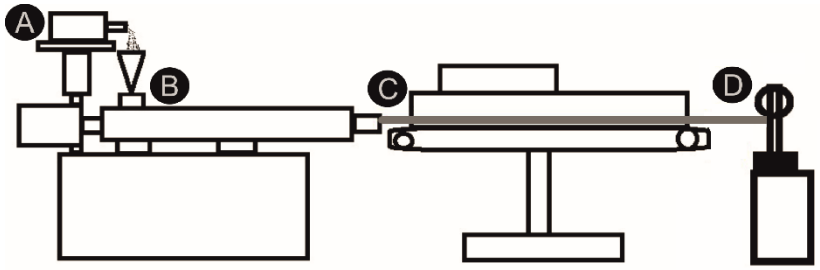

Figure 5.1.15. Technical drawing of an extrusion line as used for the production of PEU filaments: material feeding system (**A**), twin-screw extruder (**B**), conveyor belt (**C**) and filament winding machine (**D**). The extrudate is drawn in gray color.

The individual units of the extrusion line were put together in such a way that it included the volumetric material feeding system Color-exact 1000 from Plastic Recycling Machinery (Tranekær, Denmark), a Leistritz twin screw extruder MICRO 18 GL from Leistritz AG (Nürnberg, Germany), characterized by seven heating zones and a screw length of 600 mm, a conveyor belt, and a filament winder from Brabender GmbH and Co. KG (Duisburg, Germany). The temperatures of the individual heating zones of the extruder were 170 °C, 175 °C, 180 °C, 185 °C, 195 °C, 190 °C and 190 °C. To evaluate the quality of the filaments, the evolution in diameter was manually detected at regular intervals using a vernier caliper from Fowler High Precision (Newton, MA, USA).

Virtual Design and Fused Filament Fabrication: The online 3D modeling tinkercad.com [63], which is a web-based computer-aided design (CAD) program, was used for virtual construction. The developed CAD models were exported as standard triangle language (STL) files and later used for slicing.

After finalizing the designs of the tensile bar, actuator element, gripper and unit cells, Cura 3.6.1 [64] was used as a slicer program to generate numerically controlled codes, also denoted as G-codes. The 3D models were imported into the slicer program, and the models were sliced into layers according to the predefined printing parameters (**Table 5.1.1**).

Table 5.1.1. Printing parameters selected for additive manufacturing with different materials.

	PET-G	PEU	Desmopan® 9370AU
Diameter of the nozzle (µm)	400	400	400
Temperature of the nozzle (°C)	235	208	225
Speed of print head ($mm \cdot s^{-1}$)	50	15	25
Build platform temperature (°C)	85	75	60
Layer height (mm)	0.1	0.1	0.1

The specimens, as well as the actuator element for the gripper and for the different types of unit cells, were printed with the synthesized PDA-based PEU. Polyethylene terephthalate

glycol (PET-G) was used to produce the rigid parts of the robotic gripper and one of the unit cells, while the thermoplastic polyurethane elastomer Desmopan® 9370AU served as the elastic base material in both types of unit cells. The most relevant settings for additive manufacturing are listed in **Table 5.1.1**. To start additive manufacturing, the generated G-codes were transferred to the 3D printer. All 3D printed objects were produced by fused filament fabrication (FFF) using the commercially available 3D printer Ultimaker 3 from Ultimaker B.V. (Utrecht, The Netherlands).

Tensile Tests: The mechanical behavior of the synthesized PEU was investigated with the universal testing machine Criterion Model 43 from MTS (Eden Prairie, MN, USA). The device was equipped with a 500 N-load cell. The measurements were performed in compliance with DIN EN ISO 527 [43] by using dog-bone shaped tensile bars of type 5B as obtained from FFF. In the course of stretching, the velocity of 1%·min^{-1} was kept constant until a total strain of 5% was achieved before the specimen was further elongated with a velocity of 2000%·min^{-1} until rupture occurred. The Young's modulus, which is defined as the slope of stress-strain evolution between two stress-strain points during elastic loading, was determined by linear regression for strain values below 2%. Every tensile test was repeated three times at ambient temperature.

Characterization of Thermal Properties: The phase transition behavior of PDA was characterized by differential scanning calorimetry (DSC) using a Q100 DSC from TA Instruments (New Castle, DE, USA). The measurements were conducted both with the synthesized PDA and PEU. In the case of the latter, the center part of an additively manufactured type 5B tensile bar [43] was examined. In general, samples with a weight of 5 mg were investigated.

The synthesized PDA was initially cooled to −30 °C before it was heated to 110 °C and cooled back to–30 °C. The thermal cycle was repeated to finalize the measurement. In contrast, a sample of PEU was thermally cycled between −50 °C and 225 °C. For cooling and heating, a rate of 10 °C·min^{-1} was applied. The temperature holding time at the minimum and maximum temperatures were 2 min.

Characterization of Thermomechanical Properties: The thermomechanical properties of the PEU were studied by dynamic mechanical analysis (DMA). The experiments were carried out with a Q800 DMA from TA Instruments (New Castle, DE, USA) using film tension clamps on multi-frequency–strain mode. A frequency of 10 Hz, a static force of 0.1 N and an oscillating amplitude of 10 µm were selected to investigate the center part of an additively manufactured type 5B tensile bar [43]. At first, the sample was cooled to −80 °C and held there for 5 min, before it was heated to 100 °C with a rate of 3 °C·min^{-1}. In parallel, the evolution in storage modulus E' and loss factor $\tan \delta$ was determined.

Programming and Characterization of 2 W-SME: The programming of PEU samples was conducted with an MTS Criterion universal testing machine (model 43) from MTS Systems Corporation (Eden Prairie, MN, USA). The device was equipped with a 500 N-load cell and was operated with a temperature chamber, which was controlled by a Eurotherm temperature controller unit. Two heating elements were located at the back of the chamber. Liquid

nitrogen from a Dewar's vessel was fed into the chamber under a pressure of 1.3 bar as an essential prerequisite for cooling. At the beginning of thermomechanical treatment, the thermochamber was preheated to the deformation temperature T_d, which was either 75 °C or 85 °C, and the specimen was fixed in the pneumatic clamps of the universal testing machine using a clamping air pressure of 0.4 bar. After 20 min at T_d, the specimen was elongated to a maximum tensile strain of 700% using a rate of 300%·min^{-1}. In the next step, the heating elements of the temperature chamber were switched off, whereupon the specimen cooled down slowly to 23 °C while the clamping distance was kept constant. After unloading with a rate of 1 N·min^{-1}, the sample was removed from the clamps.

The Q800 DMA from TA Instruments (New Castle, DE, USA) was utilized to investigate the two-way shape memory properties of the PEU. For this purpose, a cuboid centerpiece of a specimen, which was thermomechanically treated as described above (T_d = 75 °C) and characterized by a dimensioning of 25 mm × 0.9 mm × 0.8 mm, was cut out and fixed in the film tension clamps of the DMA device. The actuation of the PEU was adjacently studied under stress-free conditions by cycling the temperature. Against this background, a first test series was run, in which the maximum temperature T_{max} was systematically varied, and a constant minimum temperature T_{min} of 15 °C was selected. For this purpose, a sample, which was thermomechanically treated as described above (T_d = 75 °C), was heated from 23 °C to T_{max} = 30 °C and held there for 15 min, before it was cooled to 15 °C, at which the temperature was kept for another 15 min. The heating and cooling were carried out three times. Afterward, the three cycles were repeated for each temperature T_{max} between 30 °C and 75 °C with an increment of 5 °C. Heating and cooling rates of 5 °C·min^{-1} were used for all experiments conducted.

In another approach, a cutout of a specimen, which was deformed at 85 °C, was investigated under the same conditions, but with maximum temperatures T_{max} between 30 °C and 90 °C.

In a durability experiment, a cutout of a thermomechanically treated PEU specimen (T_d = 75 °C) was studied under stress-free conditions by cycling the temperature between 15 °C and 64 °C. This time, actuation was investigated in 100 thermal cycles.

The reversible strain ε_{rev} is the key parameter when studying the actuation of polymers. It can be defined according to **Equation 5.1.1**):

$$\varepsilon_{rev}(N) = \frac{l_{low}(N) - l_{max}(N)}{l_{max}(N)} \times 100\% \qquad (\mathbf{5.1.1})$$

Herein, l_{low} *(N)* and l_{max} *(N)* are the lengths of the specimen in the N^{th} cycle of actuation at the respective temperatures T_{low} and T_{max}.

Demonstrator Development: Samples of PEU were additively manufactured by means of FFF, characterized by a size of 28 mm × 7 mm × 5 mm. Subsequently, they were thermomechanically treated with the procedure described in section 5.1.3.11 (T_d = 75 °C) to obtain the desired actuator elements. The actuation of the gripper was studied in the temperature chamber of our MTS Criterion universal testing machine (model 43) from MTS Systems Corporation (Eden Prairie, MN, USA). Solvent-free superglue from Pattex [65] was

used to attach the actuator elements to the unit cells. For functional testing, the unit cells were characterized similarly as the gripper in the temperature chamber of our universal testing machine. To better visualize actuation, the unit cells were placed on a platform, which was lined with centimeter paper. Both in case of the gripper and the unit cells, the temperature was cycled in between 23 °C and 64 °C with heating and cooling rates of 5 °C·min^{-1}.

5.1.4. Conclusions

A novel polyester urethane (PEU) was synthesized. After processing and thermomechanical treatment, thermoreversible shape changes could be witnessed. The PEU was used as an actuator element in a gripper, which was designed to precisely convert the comparatively small change in the shape of a few millimeters into a macroscopically well visible and technically relevant motion. The cautious gripping, holding and releasing of a hen's egg qualified the gripper for applications in soft robotics. Compared to grippers made entirely of shape memory polymer, the introduced concept has the advantage that the materials that come into contact with an object to be gripped can be freely selected according to the design of the gripper and that predefined movements can be carried out. Hence, in the end, a high degree of system control is possible. Future developments in gripper design are able to expand the range of possibilities, e.g., to grip even more challenging and bigger objects. The design space thus created allows the production of completely new systems with programmable gripping, holding and releasing properties.

Moreover, the implementation of the PEU actuator into macroscopic unit cells with elastic components led to programmable materials, which moved autonomously as a function of temperature. It is precisely this behavior that can initiate a paradigm shift in the future, in which the programming of material is understood as the programming of a functionality. The internal structure of materials is such that the material properties and behavior change reversibly according to a program. This is achieved by programming the reaction of the material to temperature signals into the material structure. In this way, completely new components with specific properties can be produced, which can be used in a wide variety of contexts. Considering that such concepts require neither control electronics nor cables or other technical devices, the self-sufficient material behavior is all the more promising.

Supplementary Materials: The following materials are available online, Videos: **s5.1.1.movie**: Actuation of the PEU-based gripper system (**Figure 5.1.10**) and **s5.1.2.movie**: Actuation of PEU to achieve unit cell morphing (**Figure 5.1.14**). Figure **S5.1.16**: FT-IR spectrum of PDA-based PEU.

Author Contributions: Conceptualization, T.P., D.C., and D.S.; methodology, D.S., D.C., F.W., and M.S.; validation, D.S. and D.C.; formal analysis, D.C. and D.S.; investigation, D.S. and D.C.;

writing—original draft preparation, D.S., D.C., F.W. and M.S.; writing—review and editing, T.P. and C.E.; visualization, D.C. and D.S.; supervision, T.P.; project administration, T.P. and C.E.

Funding: This research was funded by Fraunhofer Excellence Cluster "Programmable Materials", grant number 630500.

Acknowledgments: This work was supported as Fraunhofer Excellence Cluster "Programmable Materials" under project 630500. M.S. and C.E. acknowledge financial support from Cluster of Excellence *liv*MatS, University of Freiburg. T.P. wishes to thank the European Regional Development Fund for financing a large part of the laboratory equipment (project 85007031). Tobias Rümmler is kindly acknowledged for delivering his ideas for demonstrator development and carrying out the DMA measurements.

Conflicts of Interest: The authors declare no conflicts of interest.

Sample Availability: Samples of the compounds are provided by the authors in special cases.

5.1.5. References

1. Lee, J.-H.; Singer, J.P.; Thomas, E.L. Micro-/nanostructured mechanical metamaterials. *Adv. Mater. Weinheim.* **2012**, *24*, 4782–4810, doi:10.1002/adma.201201644.
2. Yu, X.; Zhou, J.; Liang, H.; Jiang, Z.; Wu, L. Mechanical metamaterials associated with stiffness, rigidity and compressibility: A brief review. *Progress in Materials Science* **2018**, *94*, 114–173, doi:10.1016/j.pmatsci.2017.12.003.
3. Berwind, M.F.; Kamas, A.; Eberl, C. A Hierarchical Programmable Mechanical Metamaterial Unit Cell Showing Metastable Shape Memory. *Adv. Eng. Mater.* **2018**, *20*, 1800771, doi:10.1002/adem.201800771.
4. Liu, C.; Qin, H.; Mather, P.T. Review of progress in shape-memory polymers. *J. Mater. Chem.* **2007**, *17*, 1543, doi:10.1039/b615954k.
5. J. Gough. A Description of a Property of Caoutchouc, or Indian Rubber; with some Reflections on the Cause of the Elasticity of this Substance. *Philos. Mag. Ser 1* **1806**, *24*, 39–43.
6. Huang, W.M.; Ding, Z.; Wang, C.C.; Wei, J.; Zhao, Y.; Purnawali, H. Shape memory materials. *Materials Today* **2010**, *13*, 54–61, doi:10.1016/S1369-7021(10)70128-0.
7. Small, W.; Singhal, P.; Wilson, T.S.; Maitland, D.J. Biomedical applications of thermally activated shape memory polymers. *J. Mater. Chem.* **2010**, *20*, 3356–3366, doi:10.1039/b923717h.
8. Pretsch, T. Review on the Functional Determinants and Durability of Shape Memory Polymers. *Polymers (Basel)* **2010**, *2*, 120–158, doi:10.3390/polym2030120.
9. Peponi, L.; Navarro-Baena, I.; Kenny, J.M. 7 - Shape memory polymers: properties, synthesis and applications. In *Smart polymers and their applications*; Aguilar, M.R., San Román, J., Eds.; Woodhead Publishing: Cambridge, 2014; pp 204–236, ISBN 978-0-85709-695-1.
10. Pilate, F.; Toncheva, A.; Dubois, P.; Raquez, J.-M. Shape-memory polymers for multiple applications in the materials world. *European Polymer Journal* **2016**, *80*, 268–294, doi:10.1016/j.eurpolymj.2016.05.004.
11. Karger-Kocsis, J.; Kéki, S. Review of Progress in Shape Memory Epoxies and Their Composites. *Polymers (Basel)* **2017**, *10*, doi:10.3390/polym10010034.
12. Sun, L.; Wang, T.X.; Chen, H.M.; Salvekar, A.V.; Naveen, B.S.; Xu, Q.; Weng, Y.; Guo, X.; Chen, Y.; Huang, W.M. A Brief Review of the Shape Memory Phenomena in Polymers and Their Typical Sensor Applications. *Polymers (Basel)* **2019**, *11*, doi:10.3390/polym11061049.
13. Cho, J.W.; Kim, J.W.; Jung, Y.C.; Goo, N.S. Electroactive Shape-Memory Polyurethane Composites Incorporating Carbon Nanotubes. *Macromol. Rapid Commun.* **2005**, *26*, 412–416, doi:10.1002/marc.200400492.

14. Leng, J.; Lan, X.; Liu, Y.; Du, S. Electroactive thermoset shape memory polymer nanocomposite filled with nanocarbon powders. *Smart Mater. Struct.* **2009**, *18*, 74003, doi:10.1088/0964-1726/18/7/074003.
15. Mohr, R.; Kratz, K.; Weigel, T.; Lucka-Gabor, M.; Moneke, M.; Lendlein, A. Initiation of shape-memory effect by inductive heating of magnetic nanoparticles in thermoplastic polymers. *PNAS* **2006**, *103*, 3540–3545, doi:10.1073/pnas.0600079103.
16. Schmidt, A.M. Electromagnetic Activation of Shape Memory Polymer Networks Containing Magnetic Nanoparticles. *Macromol. Rapid Commun.* **2006**, *27*, 1168–1172, doi:10.1002/marc.200600225.
17. Fang, T.; Cao, L.; Chen, S.; Fang, J.; Zhou, J.; Fang, L.; Lu, C.; Xu, Z. Preparation and assembly of five photoresponsive polymers to achieve complex light-induced shape deformations. *Materials & Design* **2018**, *144*, 129–139, doi:10.1016/j.matdes.2018.02.029.
18. Wang, H.; Fang, L.; Zhang, Z.; Epaarachchi, J.; Li, L.; Hu, X.; Lu, C.; Xu, Z. Light-induced rare earth organic complex/shape-memory polymer composites with high strength and luminescence based on hydrogen bonding. *Composites Part A: Applied Science and Manufacturing* **2019**, *125*, 105525, doi:10.1016/j.compositesa.2019.105525.
19. Chung, T.; Romo-Uribe, A.; Mather, P.T. Two-Way Reversible Shape Memory in a Semicrystalline Network. *Macromolecules* **2008**, *41*, 184–192, doi:10.1021/ma071517z.
20. Behl, M.; Kratz, K.; Zotzmann, J.; Nöchel, U.; Lendlein, A. Reversible bidirectional shape-memory polymers. *Adv. Mater. Weinheim.* **2013**, *25*, 4466–4469, doi:10.1002/adma.201300880.
21. Bothe, M.; Pretsch, T. Bidirectional actuation of a thermoplastic polyurethane elastomer. *J. Mater. Chem. A* **2013**, *1*, 14491–14497, doi:10.1039/C3TA13414H.
22. Meng, Y.; Jiang, J.; Anthamatten, M. Shape Actuation via Internal Stress-Induced Crystallization of Dual-Cure Networks. *ACS Macro Lett.* **2015**, *4*, 115–118, doi:10.1021/mz500773v.
23. Meng, Y.; Yang, J.-C.; Lewis, C.L.; Jiang, J.; Anthamatten, M. Photoinscription of Chain Anisotropy into Polymer Networks. *Macromolecules* **2016**, *49*, 9100–9107, doi:10.1021/acs.macromol.6b01990.
24. Bothe, M.; Pretsch, T. Two-Way Shape Changes of a Shape-Memory Poly(ester urethane). *Macromol. Chem. Phys.* **2012**, *213*, 2378–2385, doi:10.1002/macp.201200096.
25. Walter, M.; Friess, F.; Krus, M.; Zolanvari, S.M.H.; Grün, G.; Kröber, H.; Pretsch, T. Shape Memory Polymer Foam with Programmable Apertures. *Polymers (Basel)* **2020**, *12*, doi:10.3390/polym12091914.
26. Rus, D.; Tolley, M.T. Design, fabrication and control of soft robots. *Nature* **2015**, *521*, 467–475, doi:10.1038/nature14543.
27. Zolfagharian, A.; Kouzani, A.Z.; Khoo, S.Y.; Moghadam, A.A.A.; Gibson, I.; Kaynak, A. Evolution of 3D printed soft actuators. *Sensors and Actuators A: Physical* **2016**, *250*, 258–272, doi:10.1016/j.sna.2016.09.028.
28. Shintake, J.; Cacucciolo, V.; Floreano, D.; Shea, H. Soft Robotic Grippers. *Adv. Mater. Weinheim.* **2018**, e1707035, doi:10.1002/adma.201707035.
29. Chen, T.; Bilal, O.R.; Shea, K.; Daraio, C. Harnessing bistability for directional propulsion of soft, untethered robots. *PNAS* **2018**, *115*, 5698–5702, doi:10.1073/pnas.1800386115.
30. Ma, H.; Xiao, X.; Zhang, X.; Liu, K. Recent advances for phase-transition materials for actuators. *Journal of Applied Physics* **2020**, *128*, 101101, doi:10.1063/5.0020596.
31. Scalet, G. Two-Way and Multiple-Way Shape Memory Polymers for Soft Robotics: An Overview. *Actuators* **2020**, *9*, 10, doi:10.3390/act9010010.
32. Chen, Y.; Chen, C.; Rehman, H.U.; Zheng, X.; Li, H.; Liu, H.; Hedenqvist, M.S. Shape-Memory Polymeric Artificial Muscles: Mechanisms, Applications and Challenges. *Molecules* **2020**, *25*, doi:10.3390/molecules25184246.
33. Tolley, M.T.; Felton, S.M.; Miyashita, S.; Xu, L.; Shin, B.; Zhou, M.; Rus, D.; Wood, R.J. Self-folding shape memory laminates for automated fabrication. In *2013 IEEE/RSJ International Conference on Intelligent Robots and Systems.* 2013 IEEE/RSJ International Conference on Intelligent Robots and Systems (IROS 2013), Tokyo, 11/3/2013 - 11/7/2013; IEEE: [Place of publication not identified], 2013; pp 4931–4936, ISBN 978-1-4673-6358-7.
34. Ge, Q.; Sakhaei, A.H.; Lee, H.; Dunn, C.K.; Fang, N.X.; Dunn, M.L. Multimaterial 4D Printing with Tailorable Shape Memory Polymers. *Sci Rep* **2016**, *6*, 1–11, doi:10.1038/srep31110.
35. Yang, Y.; Chen, Y.; Li, Y.; Chen, M.Z.Q.; Wei, Y. Bioinspired Robotic Fingers Based on Pneumatic Actuator and 3D Printing of Smart Material. *Soft Robot.* **2017**, *4*, 147–162, doi:10.1089/soro.2016.0034.
36. Zhou, J.; Turner, S.A.; Brosnan, S.M.; Li, Q.; Carrillo, J.-M.Y.; Nykypanchuk, D.; Gang, O.; Ashby, V.S.; Dobrynin, A.V.; Sheiko, S.S. Shapeshifting: Reversible Shape Memory in Semicrystalline Elastomers. *Macromolecules* **2014**, *47*, 1768–1776, doi:10.1021/ma4023185.
37. Kadic, M.; Milton, G.W.; van Hecke, M.; Wegener, M. 3D metamaterials. *Nat Rev Phys* **2019**, *1*, 198–210, doi:10.1038/s42254-018-0018-y.

38. Vouyiouka, S.N.; Topakas, E.; Katsini, A.; Papaspyrides, C.D.; Christakopoulos, P. A Green Route for the Preparation of Aliphatic Polyesters via Lipase-catalyzed Prepolymerization and Low-temperature Postpolymerization. *Macromolecular Materials and Engineering* **2013**, *298*, 679–689, doi:10.1002/mame.201200188.
39. Kasprzyk, P.; Sadowska, E.; Datta, J. Investigation of Thermoplastic Polyurethanes Synthesized via Two Different Prepolymers. *J Polym Environ* **2019**, *27*, 2588–2599, doi:10.1007/s10924-019-01543-7.
40. Yilgör, I.; Yilgör, E.; Wilkes, G.L. Critical parameters in designing segmented polyurethanes and their effect on morphology and properties: A comprehensive review. *Polymer* **2015**, *58*, A1-A36, doi:10.1016/j.polymer.2014.12.014.
41. Kim, S.G.; Lee, D.S. Effect of polymerization procedure on thermal and mechanical properties of polyether based thermoplastic polyurethanes. *Macromolecular Research* **2002**, *10*, 365–368.
42. Chalissery, D.; Pretsch, T.; Staub, S.; Andrä, H. Additive Manufacturing of Information Carriers Based on Shape Memory Polyester Urethane. *Polymers (Basel)* **2019**, *11*, doi:10.3390/polym11061005.
43. DIN EN ISO 527-2 - 1996-07 - Beuth.de. Available online: https://www.beuth.de/en/standard/din-en-iso-527-2/2808009 (accessed on 26 November 2020).
44. Bothe, M.; Mya, K.Y.; Jie Lin, E.M.; Yeo, C.C.; Lu, X.; He, C.; Pretsch, T. Triple-shape properties of star-shaped POSS-polycaprolactone polyurethane networks. *Soft Matter* **2012**, *8*, 965–972, doi:10.1039/C1SM06474F.
45. Huang, W.M.; Lu, H.B.; Zhao, Y.; Ding, Z.; Wang, C.C.; Zhang, J.L.; Sun, L.; Fu, J.; Gao, X.Y. Instability/collapse of polymeric materials and their structures in stimulus-induced shape/surface morphology switching. *Materials & Design* **2014**, *59*, 176–192, doi:10.1016/j.matdes.2014.03.028.
46. Mirtschin, N.; Pretsch, T. Designing temperature-memory effects in semicrystalline polyurethane. *RSC Adv.* **2015**, *5*, 46307–46315, doi:10.1039/C5RA05492C.
47. van Horn, R.M.; Steffen, M.R.; O'Connor, D. Recent progress in block copolymer crystallization. *Polymer Crystallization* **2018**, *1*, doi:10.1002/pcr2.10039.
48. Li, F.; Hou, J.; Zhu, W.; Zhang, X.; Xu, M.; Luo, X.; Ma, D.; Kim, B.K. Crystallinity and morphology of segmented polyurethanes with different soft-segment length. *Journal of Applied Polymer Science* **1996**, *62*, 631–638, doi:10.1002/(SICI)1097-4628(19961024)62:4<631:AID-APP6>3.0.CO;2-U.
49. Bogdanov, B.; Toncheva, V.; Schacht, E.; Finelli, L.; Sarti, B.; Scandola, M. Physical properties of poly(ester-urethanes) prepared from different molar mass polycaprolactone-diols. *Polymer* **1999**, *40*, 3171–3182, doi:10.1016/S0032-3861(98)00552-7.
50. Chen, S.; Hu, J.; Liu, Y.; Liem, H.; Zhu, Y.; Meng, Q. Effect of molecular weight on shape memory behavior in polyurethane films. *Polymer International* **2007**, *56*, 1128–1134, doi:10.1002/pi.2248.
51. Chen, S.; Hu, J.; Liu, Y.; Liem, H.; Zhu, Y.; Liu, Y. Effect of SSL and HSC on morphology and properties of PHA based SMPU synthesized by bulk polymerization method. *Journal of Polymer Science Part B: Polymer Physics* **2007**, *45*, 444–454, doi:10.1002/polb.21046.
52. Bothe, M.; Emmerling, F.; Pretsch, T. Poly(ester urethane) with Varying Polyester Chain Length: Polymorphism and Shape-Memory Behavior. *Macromolecular Chemistry and Physics* **2013**, *214*, 2683–2693, doi:10.1002/macp.201300464.
53. Rocco, J.A.F.F.; Lima, J.E.S.; Lourenço, V.L.; Batista, N.L.; Botelho, E.C.; Iha, K. Dynamic mechanical properties for polyurethane elastomers applied in elastomeric mortar. *J. Appl. Polym. Sci.* **2012**, *126*, 1461–1467, doi:10.1002/app.36847.
54. Li, J.; Kan, Q.; Chen, K.; Liang, Z.; Kang, G. In Situ Observation on Rate-Dependent Strain Localization of Thermo-Induced Shape Memory Polyurethane. *Polymers (Basel)* **2019**, *11*, doi:10.3390/polym11060982.
55. Lu, L.; Cao, J.; Li, G. Giant reversible elongation upon cooling and contraction upon heating for a crosslinked cis poly(1,4-butadiene) system at temperatures below zero Celsius. *Sci Rep* **2018**, *8*, 14233, doi:10.1038/s41598-018-32436-9.
56. Gholaminezhad, I.; Jamali, A.; Assimi, H. Multi-objective reliability-based robust design optimization of robot gripper mechanism with probabilistically uncertain parameters. *Neural Comput & Applic* **2017**, *28*, 659–670, doi:10.1007/s00521-016-2392-7.
57. Latko-Durałek, P.; Dydek, K.; Boczkowska, A. Thermal, Rheological and Mechanical Properties of PETG/rPETG Blends. *J Polym Environ* **2019**, *27*, 2600–2606, doi:10.1007/s10924-019-01544-6.
58. Shan, S.; Kang, S.H.; Raney, J.R.; Wang, P.; Fang, L.; Candido, F.; Lewis, J.A.; Bertoldi, K. Multistable Architected Materials for Trapping Elastic Strain Energy. *Adv. Mater. Weinheim.* **2015**, *27*, 4296–4301, doi:10.1002/adma.201501708.
59. Specht, M.; Berwind, M.; Eberl, C. Adaptive Wettability of a Programmable Metasurface. *Adv. Eng. Mater.* **2021**, *23*, 2001037, doi:10.1002/adem.202001037.

60. M-Base Engineering + Software GmbH. CAMPUSplastics | Datenblatt Desmopan 9370A. Available online: https://www.campusplastics.com/campus/de/datasheet/Desmopan%C2%AE+9370A/Covestro+Deutschland+AG/22/15fed464 (accessed on 11 December 2020).
61. 2006. Deutsches Institut für Normung e.V. *Kunststoffe (Polyester) und Beschichtungsstoffe (Bindemittel) - Bestimmung der partiellen Säurezahl und der Gesamtsäurezahl;* Beuth Verlag GmbH: Berlin (2114).
62. 2016. Deutsches Institut für Normung e.V. *Bindemittel für Beschichtungsstoffe - Bestimmung der Hydroxylzahl - Teil 2: Titrimetrisches Verfahren mit Katalysator;* Beuth Verlag GmbH: Berlin (4629-2).
63. Dashboard | Tinkercad. Available online: https://www.tinkercad.com/dashboard (accessed on 26 November 2020).
64. Ultimaker Cura: Powerful, easy-to-use 3D printing software. Available online: https://ultimaker.com/software/ultimaker-cura (accessed on 26 November 2020).
65. Flüssig Mini Trio. Available online: https://www.pattex.de/de/products/klebstoff/sekundenkleber/fluessig_mini_trio.html (accessed on 26 November 2020).

5.1.6. Supplementary Material

5.1.6.1. Fourier-Transform Infrared (FT-IR) Spectroscopy

Normally, a distinct signal at about 2270 cm^{-1} occurs in the FT-IR spectrum of polyurethanes in case of an incomplete reaction as associated with freely available isocyanate groups [1,2]. In the present case, the reaction seemed to be almost complete because the signal at 2283 cm^{-1} was very weak, while at the same time, vibration modes were present as characteristic for the formation of a polyester urethane (**Figure S5.1.16**) [3].

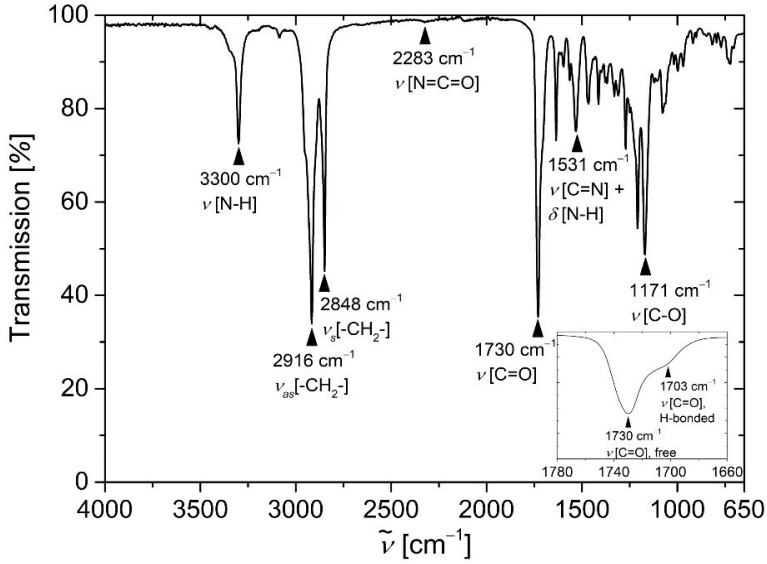

Figure S5.1.16. FT-IR spectrum of poly(1,10-decylene adipate) diol (PDA)-based polyester urethane (PEU), including the assignment of vibration modes and the specification of their wavenumbers. The inset highlights the carbonyl stretching vibration region.

In fact, a more detailed analysis of the FT-IR spectrum showed distinct absorbances at 2916 cm^{-1} and 2848 cm^{-1}, which can be assigned to the asymmetric and symmetric stretching vibrations of CH2 entities [2,4,5]. Two overlapping bands are present in the carbonyl stretching region – one dominating peak apparently centered at 1730 cm^{-1} and a broad shoulder at 1703 cm^{-1}. The two signals are ascribed to the stretching vibrations of free (non-

hydrogen-bonded) and hydrogen-bonded carbonyl, respectively [3,6–8]. The band at 1171 cm^{-1} was assigned to the corresponding *v*[C–O] stretching vibrations [4,9,10]. The stretching vibration *v*[N–H] at 3300 cm^{-1} and an amide peak (*v*[C=N] + *δ*[N–H]) at 1531 cm^{-1} were attributed to vibrations associated with the hard segments of the PEU [11,12].

5.1.6.2. References

1. Sáenz-Pérez, M.; Lizundia, E.; Laza, J.M.; García-Barrasa, J.; Vilas, J.L.; León, L.M. Methylene diphenyl diisocyanate (MDI) and toluene diisocyanate (TDI) based polyurethanes: thermal, shape-memory and mechanical behavior. *Rsc Adv.* 2016, *6*, 69094–69102, doi:10.1039/c6ra13492k.
2. Tan, C.; Tirri, T.; Wilen, C.-E. Investigation on the Influence of Chain Extenders on the Performance of OneComponent Moisture-Curable Polyurethane Adhesives. *Polym. (Basel)* 2017, *9*, doi:10.3390/polym9050184.
3. Pretsch, T.; Jakob, I.; Müller, W. Hydrolytic degradation and functional stability of a segmented shape memory poly(ester urethane). *Polym. Degrad. Stab.* 2009, *94*, 61–73, doi:10.1016/j.polymdegradstab.2008.10.012.
4. Panwiriyarat, W.; Tanrattanakul, V.; Pilard, J.-F.; Pasetto, P.; Khaokong, C. Effect of the diisocyanate structure and the molecular weight of diols on bio-based polyurethanes. *J. Appl. Polym. Sci.* 2013, *130*, 453–462, doi:10.1002/app.39170.
5. Lei, W.; Fang, C.; Zhou, X.; Cheng, Y.; Yang, R.; Liu, D. Morphology and thermal properties of polyurethane elastomer based on representative structural chain extenders. *Thermochim. Acta* 2017, *653*, 116–125, doi:10.1016/j.tca.2017.04.008.
6. Seymour, R.W.; Estes, G.M.; Cooper, S.L. Infrared Studies of Segmented Polyurethan Elastomers. I. Hydrogen Bonding. *Macromolecules* 1970, *3*, 579–583, doi:10.1021/ma60017a021.
7. Lee, H.S.; Wang, Y.K.; Hsu, S.L. Spectroscopic analysis of phase separation behavior of model polyurethanes. *Macromolecules* 1987, *20*, 2089–2095, doi:10.1021/ma00175a008.
8. Teo, L.-S.; Chen, C.-Y.; Kuo, J.-F. Fourier Transform Infrared Spectroscopy Study on Effects of Temperature on Hydrogen Bonding in Amine-Containing Polyurethanes and Poly(urethane−urea)s. *Macromolecules* 1997, *30*, 1793–1799, doi:10.1021/ma961035f.
9. Yen, M.-S.; Cheng, K.-L. Synthesis and physical properties of H 12 MDI-based polyurethane resins. *J Polym. Res.* 1996, *3*, 115–123, doi:10.1007/BF01492902.
10. Peruzzo, P.J.; Anbinder, P.S.; Pardini, O.R.; Vega, J.R.; Amalvy, J.I. Influence of diisocyanate structure on the morphology and properties of waterborne polyurethane-acrylates. *Polym. J.* 2012, *44*, 232–239, doi:10.1038/pj.2011.111.
11. Schoonover, J.R.; Thompson, D.G.; Osborn, J.C.; ORLER, E.B.; Wrobleski, D.A. Infrared linear dichroism study of a hydrolytically degraded poly(ester urethane). In *Polymer degradation and stability*, 2001; pp. 87–96, ISBN 01413910.
12. Schoonover, J.R.; Steckle, W.P.; Cox, J.D.; Johnston, C.T.; Wang, Y.; Gillikin, A.M.; Palmer, R.A. Humiditydependent dynamic infrared linear dichroism study of a poly(ester urethane). *Spectrochim. Acta Part A: Mol. Biomol. Spectrosc.* 2007, *67*, 208–213, doi:10.1016/j.saa.2006.07.015.

Chapter 5.2: Programmable Materials

Chapter 5.2: Programmable Materials

Abstract

Thermoresponsive programmable materials can perform sensory and actuator tasks as soon as their ambient temperature changes. Shape memory polymers (SMPs) are smart materials that are suitable as functional base materials for the development of thermoresponsive programmable materials. The examples considered herein include a gear-like object and a unit cell, which differ in their required thermomechanical treatment. Besides the comparable temperature guidance, in the case of the gear-like structure, a deformation by compression was followed, and a deformation applied by stretching was carried out in the case of the unit cell. The polymer used to design the programmable materials was a self-synthesized poly(1,10-decylene adipate) diol-based polyester urethane (PEU). After processing into filaments, programmable materials were additively manufactured by fused filament fabrication. Once thermomechanically treated, the unit cell actuated under a weak external stress of 0.01 N at temperatures between 23 °C and 58 °C. In the case of the “gear,” a maximum thermoreversible change in height $\Delta H/H_0$ of about 42% in relation to its external dimensions was detected. The object is a first step towards the development of systems for overheating protection or process regulation, which could allow the force transmission to be switched from "On" to "Off" and vice versa according to a temperature program. In terms of thermoreversible length changes $\Delta L/L_0$, the unit cell even proved to be slightly stronger in actuation with regard to linear motion.

5.2.1. Introduction

Shape memory polymers (SMPs) are smart materials that can fix a temporary shape after a thermomechanical treatment, also denoted as "programming." When applying a suitable stimulus, SMPs can almost completely recover the initial shape. In other words, the so-called "one-way (1W) shape memory effect (SME)" is triggered [1–6]. Shape recovery is an entropically driven process that is based on entropy elasticity according to the theory of rubber elasticity [7]. Among stimulus-responsive SMPs that have been investigated so far, thermoresponsive SMPs are the most widely investigated [8–10]. After triggering the 1W-SME, an SMP requires another thermomechanical treatment to become thermoresponsive again. By contrast, in the case of the so-called "two-way (2W) SME", an SMP is able to switch between two metastable states without the need for further programming steps [11–17]. For SMPs, the 2W-SME has been investigated on semicrystalline polymers since these materials fulfill the necessary morphological requirements [17,18]. Here, the main driving forces are caused by the crystallization of polymer chains and the melting of the associated crystallites, the same as entropy elasticity [12,19,20]. In particular, phase-segregated thermoplastic polyurethanes (TPUs), which are built up of hard and soft segments, have proven their

potential over other thermoplastic and chemically cross-linked SMPs [21–34], due to the capability of reprocessing and mechanical recycling. In the last decade, scientists unveiled how to implement the 2W-SME into physically cross-linked TPUs [11,20,31]. For instance, Schönfeld et al. developed a poly(1,10-decylene adipate) (PDA)-based polyester urethane (PEU) and processed the PEU via the additive manufacturing technique "fused filament fabrication" (FFF). As a result, objects could be obtained, which were programmed by significant tensile deformation at 75 °C, cooling to 23 °C while holding the elongated shape, followed by unloading. Adjacently, the object shrank on heating and expanded on cooling with a maximum thermoreversible strain of 16% [20]. A few years earlier, Bothe and Pretsch applied substantial tensile deformation to achieve deformation-induced crystallization in the soft segment phase of a commercially available PEU and witnessed a maximum actuation of 17% upon temperature cycling under free-strain conditions [14]. Likewise, in other contributions, an actuation of physically cross-linked PEUs with a maximum of 21% was verified [35–39].

Despite the steadily growing number of publications on 2W SMPs in the last few years, the question arises to what extent actuation can be realized by more complex motion sequences or even by the parallel motion of several parts within a single component. The answer is the design and construction of programmable materials from polymers and harnessing the 2W-SME with the adaption of thermomechanical treatment. Programmable materials are currently the subject of intensive research [20,40–46]. When material functionality meets structural design, new types of material behaviors can be realized. Advantageously, programmable materials are not dependent on a constant power supply. They are essentially characterized by self-sufficient material behavior. Thus, they entail an all-in-one sensor, actuator, and controlling unit functionality [45,47]. Here, it is presented how to take advantage of thermoresponsive programmable materials in the context of a gearbox. The idea behind is to provide one day overheating protection; in other words, the force transmission in gear units is switched from "On" to "Off" and vice versa as a result of heating and cooling. Taking a first step into this direction, the same PDA-based PEU, which was recently developed and characterized by promising actuation under stress-free conditions [20] was selected as the base material. After developing a gear-like design and rapid prototyping via FFF, the object was thermomechanically treated, and actuation was studied while systematically varying the temperature. Following the same idea of transferring a programmable material into bistable states by means of thermomechanical treatment, a second demonstrator was built, and its actuation behavior was investigated. In this context, it will be shown that the design of the programmable material leads to the realization of a considerably larger change in length compared to the pure base material in linear form.

5.2.2. Result and Discussion

For this work, a poly(1,10-decylene adipate) (PDA)-based polyester urethane (PEU) which was developed in our previous work [20] was selected as functional base material. In the

phase segregated PEU, the PDA served as the soft segment and exhibited a broad melting transition, ranging from 29 °C to 72 °C, with a maximum located at 65 °C, while a crystallization transition was found between 52 °C and 24 °C with a crystallization peak at 45 °C. Due to the verified actuation capability under stress-free actuation conditions [20], PEU in the form of filaments was selected as the base material for the production of demonstrators using fused filament fabrication (FFF).

Next, the model of an object characterized by a gear-like design (**Figure 5.2.1**) was developed.

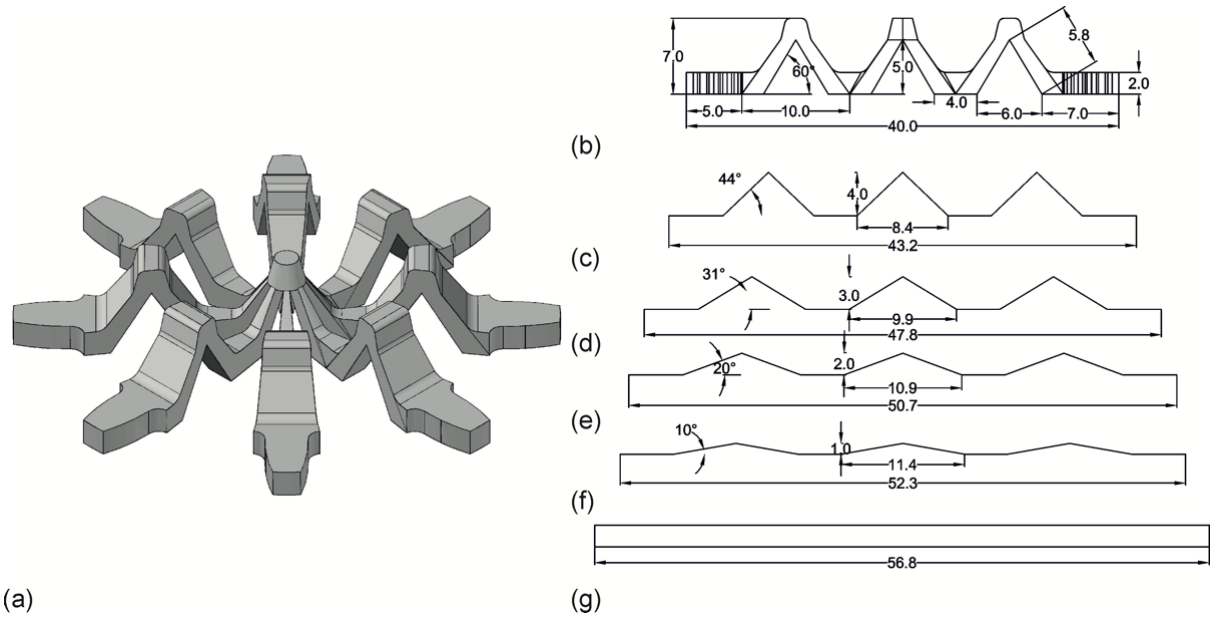

Figure 5.2.1. Technical drawing for a programmable gear in its (a) isometric view, (b) front view including the dimensions of the original shape, and (c-g) the potential shape modifications due to stepwise loading with regard to individual displacements (all the dimensions are in mm).

The object was designed in such a way that a compressive load applied during thermomechanical treatment would shift the out-of-plane parts resulting in an entirely flat structure (**Figure 5.2.1**). Specifically, the gear consisted of three inverted "V" shaped structures in each line (**Figure 5.2.1. b**). The structures were designed to translate any vertical motion directly into horizontal motion. When the gear was compressed from top to bottom, the "V"-shaped structures bent to form a flat shape, increasing the outer diameter of the gear (**Figure 5.2.1. b-g**). This change in diameter could possibly establish contact with similarly designed objects in a kind of force transmission system.

The next step was to develop a method for thermomechanically treatment, which later enabled the stress-free actuation of the gear. Here an approach of compression bending was followed by means of a dynamic mechanical analysis (DMA) device, which was also used to identify the ideal actuation conditions. It is noteworthy that this approach did not allow the characterization of length changes with regard to the diameter of the object. In detail, the thermomechanical treatment consisted of heating to 75 °C, applying a compressive force of 17 N, ensuring that only compression bending and no pressure crushing occurred, cooling to 15 °C, and holding the temperature constant for 30 min, followed by unloading. In response

to the applied compressive force, the height of the object was reduced from 7 mm to 2 mm, at which the latter corresponded to the thickness of the “gear tooth.” Upon temperature cycling, thermoreversible changes in shape and, in particular, the height of the object, also denoted as actuation could be detected in every single measurement cycle, even when the upper-temperature T_{max} was continuously increased from 55 °C to 70 °C while the lower temperature of 15 °C was left unchanged (**Figure 5.2.2a**). Here, actuation was enabled by heating-induced melting of the PDA soft segment, leading to a movement out of the plane of the flat gear and the cooling-induced crystallization of the PDA soft segment, resulting in the movement back into the plane of the flat gear, along the direction of the compressive force applied during thermomechanical treatment (**Figure 5.2.2b**).

Only a small quantity of crystallizable segments was present when selecting a lower maximum temperature T_{max} because a larger part of the PDA phase was still in a crystalline state [20], resulting in weak elongation on heating and weak contraction on cooling, as can be seen in the $\Delta H/H_0$—temperature diagram of **Figure 5.2.2c**, at which the ratio of $\Delta H/H_0$ describes the evolution of changes in the height of the object under a constant external load of 0.01 N. By contrast, the increase in T_{max} can be associated with an increase in the proportion of crystallizable segments because more PDA crystals were molten [20]. At 58 °C, the most pronounced actuation could be observed, characterized by a thermoreversible change in the height of 42% (averaged for three cycles), which can be seen in the associated $\Delta H/H_0$-temperature diagram (**Figure 5.2.2c**). The respective schematic bistable states of the object at 58 °C and 15 °C are illustrated in **Figures 5.2.2d and e**. During actuation, a change in vertical height of 1.5 mm was accompanied by a change in diameter of 4.4 mm. The further increase of T_{max} (> 58 °C) gave a decrease in actuation due to the systematic melting of PDA crystals [20], which resulted in the steady recovery of the original shape and thus a lower overall change in height $\Delta H/H_0$. In other words, the elongation at the beginning of each cooling step was gradually shifted to higher values and recovered large parts of the initial shape of the object. Obviously, under these conditions, stress-induced oriented PDA crystals serving as physical netpoints were molten and no longer available to support the structural integrity associated with the respective metastable states of the polymer. In this context, it will be shown that the design of the programmable material leads to the realization of a considerably larger change in length compared to the pure base material in linear form.

Conceptually, the object has its potential application to be used wherever the change in shape can assure or interrupt force transmission and thus, e.g., prevent systems from overheating.

To ensure that the developed compression-related programming method can also be used to obtain bistable states in other programmable materials and thus to verify distinct actuation, another programmable material was designed (**Figure 5.2.3a-d**). Additionally, a simulation was run on the actuator element to understand the shape change during compressive deformation in the course of thermomechanical treatment (**Figure 5.2.3e and f**).

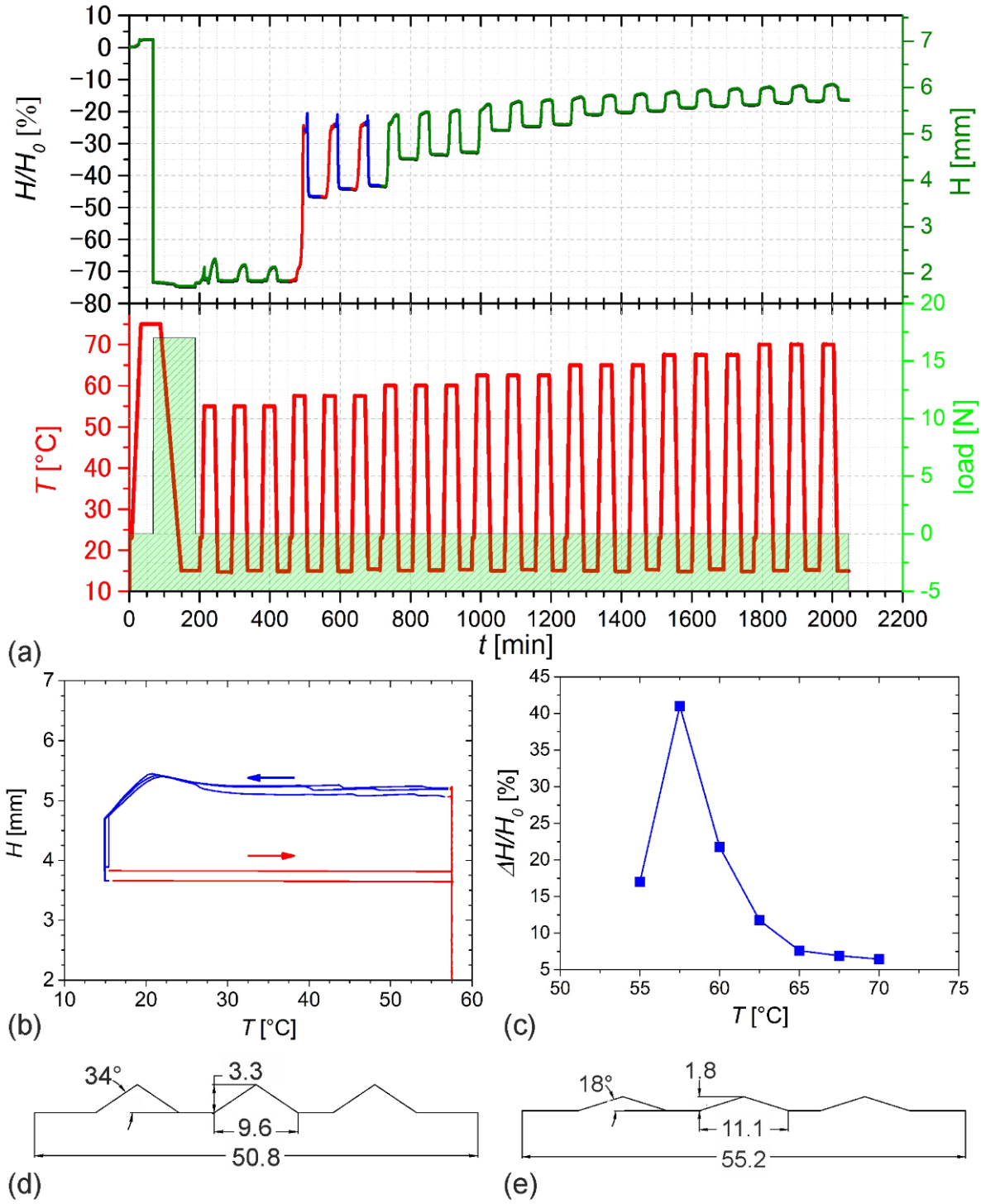

Figure 5.2.2. Influence of the selection of T_{max} on the actuation of a programmable gear made from PDA-based PEU. After thermomechanical treatment, a weak external load of 0.01 N was applied: Evolution of (a) changes in object heigth $\Delta H/H_0$, sample height H (red and blue color for heating and cooling, respectively) and temperature T (bottom graph) over measurement time t, (b) object height upon temperature cycling between 15 °C and 58 °C, and (c) $\Delta H/H_0$ depending on T_{max} (the values are averaged for the second and third thermal cycle). The corresponding bistable states of the gear in (d) its first bistable state characterized by a small outer diameter at T_{max} = 58 °C and (e) its second bistable and mostly expanded state, characterized by a maximum outer diameter at T_{low} = 15 °C (all the dimensions are in mm).

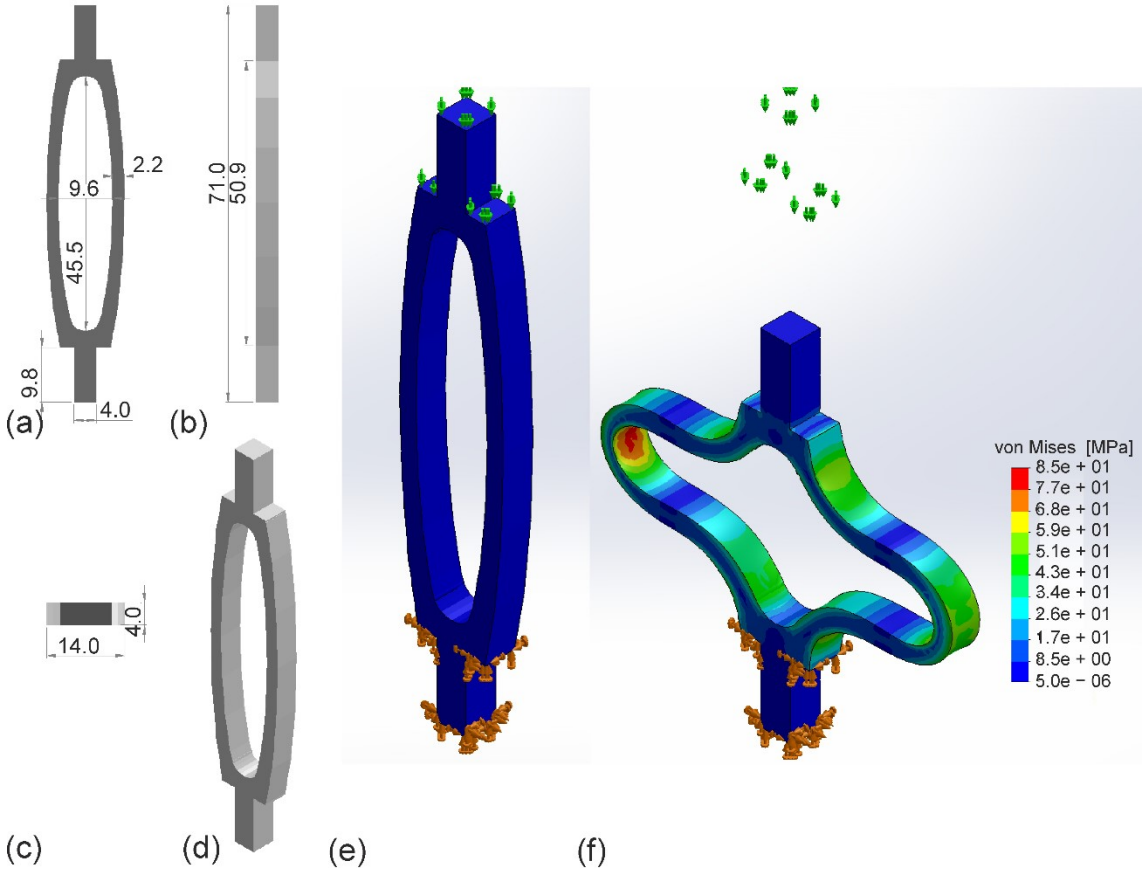

Figure 5.2.3. Technical drawing of an actuating element in the perspectives (a) front view, (b) right view, (c) top view and (d) isometric view. The von Mises stress distribution on (e) before and (f) after deformation (all dimensions are in mm).

The actuator element was conceptualized in such a way that the two opposite beams protrude slightly in the middle (**Figure 5.2.3 a-d**). Due to the slight protrusion, the beams pull out when the upper and lower parts of the actuation element are pressed and reach the maximum bending for each beam segment, as the simulation shows (**Figure 5.2.3e and f**).

After three-dimensional (3D) printing (**Figure 5.2.4a**), the actuator element was found to have excellent dimensional accuracy when compared to the CAD model (**Figure 5.2.3a**). Once programmed (**Figure 5.2.4b**), the new shape of the actuating element was stable at room temperature (23 °C) and showed an overall height of 23.8 mm. Subsequently, the 2W-SME was examined. On raising the temperature to 58 °C, the actuating element partially returned to its original shape to attain its second bistable state by expanding into the opposite direction of deformation, resulting in a total height of about 36 mm (**Figure 5.2.3c**). Thus, a change in length $\Delta L/L_0$ of about 51% was determined. Once cooled back to 23 °C, the initial bistable state was achieved due to contraction of the actuating element in the direction of deformation (**Figure 5.2.4d**). This resulted in a length of the bistable state of 24.6mm, corresponding to a change in $\Delta L/L_0$ of about 46%. The actuation was proven on repeating the heating and cooling cycle four more times (**Figure 5.2.4e and f**). This unveils that the actuation achieved through compression bending programming for both the programmable gear and the actuating element is almost identical and can be reproduced.

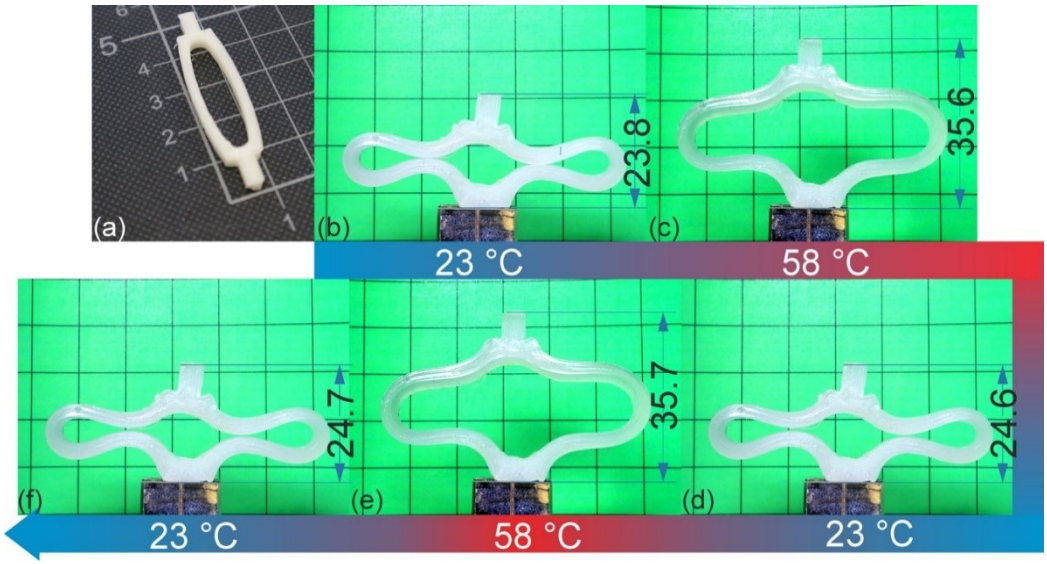

Figure 5.2.4. Actuating element made from PDA based PEU in its (a) permanent shape as obtained after fused filament fabrication, (b) programmed shape and (c-f) during switching between its bistable states when cycling *the* temperature. In the background centimeter paper can be seen (all the dimensions are in mm).

Thus, the path taken here leads to significantly higher actuation compared to solid materials, as the programmable materials approach combines the functionality of external structure with the molecular structure [11,20,31, 35–39]. More precisely, the pure solid material, programmed using tensile stretching in our previous work using the same PEU, showed a maximum actuation of about 16%.[20] Comparing the actuation from our previous literature with the current work, the added programmable material design for the same material largely increased the actuation to about 46%. In perspective, the higher actuating length from comparatively smaller-sized elements can open the door to other applications. Beyond that, the reduction in the size of the actuating element may contribute to reducing the complexity and size proportions of the previously presented actuating systems. For example, a PEU actuation element connected to a gripper, as presented in one of our previous works [20], could be produced in smaller sizes using programmable materials and also reliably actuate.

5.2.3. Conclusions

Using an in-house developed polyester urethane, two types of programmable materials were additively manufactured via fused filament fabrication. First of all, a gear-like object turned out as fruitful example for a programmable material, which after thermomechanical treatment was capable of actuating between two bistable states under almost stress-free conditions. In this regard, increases in the object's height were reliably transferred into decreases in the object's diameter and vice versa. Remarkably, an average thermoreversible change in height $\Delta H/H_0$ of 42% could be witnessed. Theoretically, the developed

programmable gear can be used to enable or disable a force transmission, which could protect a system from overheating. Transferring the thermomechanical treatment to a unit cell allowed witnessing almost identical thermoreversible changes in the object's length and/or height. In any case, the main driving forces of actuation were the melting and crystallization of the soft segment. Such programmable materials may replace earlier generations of actuating elements and could, for instance, reduce the complexity and size of grippers. This work thereby unveils that thermomechanically treated programmable materials are caplable of both drastic and complex shape changes, which cannot be witnessed when using classical design approaches for 2W-SMPs. In perspective, the unit cell can be incorporated with embedded wires for heating purposes. This could be done through adapted printing processes, as this creates possibilities for the local heating of polymers including complex motion and in addition control over mechanical properties and thereby even expand the existing potentials.

5.2.4. Experimental Section

Material: The same poly(1,10-decylene adipate) (PDA) based polyester urethane (PEU) which was synthesized recently [20], is again used as the base material for this work. The material was used in the form of filament for 3D printing. For more details about the thermal, mechanical and thermomechanical properties, the characterization details can be obtained from the previous literature [20].

Virtual Design and Fused Filament Fabrication: The AutoCAD software from Autodesk, Inc. (San Rafael, CA, USA) was used to design the programmable material in the form of a gear, while the programmable material in the form of an actuating element was designed and simulated using Solidworks from Dassault Systèmes (Vélizy-Villacoublay, Île-de-France, France). The developed CAD models were exported as standard triangle language (STL) files and later used for slicing. After finalizing the designs of the gear and actuating element, Cura 3.6.1 [48] was used as a slicer program to generate numerically controlled codes, also denoted as G-codes. The 3D models were imported into the slicer program, and the models were sliced into layers according to the predefined printing parameters (**Table 5.2.1**). The most relevant settings for additive manufacturing (AM) are listed in **Table 5.2.1**. To start AM, the generated G-codes were transferred to the 3D printer. All 3D printed objects were produced by fused filament fabrication (FFF) using the commercially available 3D printer Ultimaker 3 from Ultimaker B.V. (Utrecht, The Netherlands).

Table 5.2.1. Printing parameters selected for additive manufacturing.

Printing parameters	PEU
Diameter of the nozzle (µm)	400
Temperature of the nozzle (°C)	208
Speed of print head (mm × s^{-1})	15
Build platform temperature (°C)	75
Layer height (mm)	0.1

Programming and Characterization of 2W-SME: The programmable materials made from PDA-based PEU were both thermomechanically treated (programmed) and the actuation analyzed using a Q800 DMA from TA Instruments (New Castle, DE, USA). In order to characterize the 2W-SME, the gear-like object was initially placed between two compression clamps. The chamber was heated to 75 °C at the beginning of thermomechanical treatment. After holding the temperature at 75 °C constant for 30 min, the object was compressed with a force of 17 N using a loading rate of 1 N·min^{-1}. Then, the deformed object was cooled to 15 °C (T_{min}) while maintaining the compressive force. The temperature T_{min} was held isothermally for 30 min. Subsequently, the applied force was unloaded with a rate of 1 N·min^{-1}, and the object was heated to 23 °C and held at that temperature for another 5 min to mark the end of programming. The actuation of the programmable material was studied under a constant external load of 0.01 N by cycling the temperature. In detail, the sample was heated from 23 °C to T_{max} = 55 °C and held there for 30 min, before it was cooled to 15 °C, at which the temperature was kept for another 30 min. Heating and cooling were carried out three times. Afterward, T_{max} was increased from 55 °C to 70 °C with an increment of 2.5 °C and for each increment, the three temperature cycles were repeated. Heating and cooling rates of 5 °C·min^{-1} were used for the whole experiment.

In case of the unit cell serving as actuating element, the thermomechanical treatment of samples was conducted with an MTS Criterion universal testing machine (model 43) from MTS Systems Corporation (Eden Prairie, MN, USA). The device was equipped with a 500 N load cell and was operated with a temperature chamber, which was controlled by a Eurotherm temperature controller unit. Two heating elements were located at the back of the chamber. Liquid nitrogen from a Dewar's vessel was fed into the chamber under a pressure of 1.3 bar as an essential prerequisite for cooling. At the beginning of thermomechanical treatment, the thermochamber was preheated to 75 °C, and the unit cell was fixed in the pneumatic clamps of the universal testing machine using a clamping air pressure of 0.4 bar. After 30 min at 75 °C, the unit cell was compressed in such a way that the top part touched the bottom using a loading rate of 1 N·min^{-1}. In the next step, the temperature was brought to 15 °C and held there for 30 min to fix the new shape while maintaining the compressive load. Then, the unit cell was unloaded with a rate of 1 N·min^{-1}. The temperature was then heated to 23°C, and the unit cell was removed from the clamps. The 2W-SME of the programmable material was subsequently characterized by unclamping only from the upper clamp and cycling the temperature between 58 °C (T_{max}) and 23 °C (T_{min}).

The thermoreversible changes in height $\Delta H/H_0$ and length $\Delta L/L_0$ are key parameters when studying the actuation of polymers. They can be defined according to **Equation 5.2.1 and Equation 5.2.2**:

$$\frac{\Delta H}{H_0} = \frac{h_{min}(N) - h_{max}(N)}{h_{max}(N)} \times 100\% \qquad (\mathbf{5.2.1})$$

$$\frac{\Delta L}{L_0} = \frac{l_{min}(N) - l_{max}(N)}{l_{max}(N)} \times 100\% \qquad (\mathbf{5.2.2})$$

In the present case, $h_{min}(N)$ and $h_{max}(N)$ are the heights of a programmable material in the *N*th cycle of actuation at the respective temperatures T_{min} and T_{max}. While, $l_{min}(N)$ and $l_{max}(N)$ are the lengths of the programmable material in the *N*th cycle of actuation at the respective temperatures T_{min} and T_{max}.

Simulation: The simulation of the programmable material in the sense of the actuating element was conducted using Solidworks from Dassault Systèmes (Vélizy-Villacoublay, Île-de-France, France). After CAD modelling, the simulation was carried out using a nonlinear-static study, where the bottom part of the sample (orange arrows in **Figure 5.2.3e and f**) was fixed while a pressure of 10 N s^{-2} was applied on its top part (green arrows in **Figure 5.2.3e** and **f**). After simulation, the von Mises stresses were analyzed.

5.2.5. References

1. Liu, C.; Qin, H.; Mather, P.T. Review of progress in shape-memory polymers. *J. Mater. Chem.* **2007**, *17*, 1543, doi:10.1039/b615954k.
2. Dietsch, B.; Tong, T. A review-: Features and benefits of shape memory polymers (smps). *Journal of advanced materials* **2007**, *39*, 3–12.
3. Ratna, D.; Karger-Kocsis, J. Recent advances in shape memory polymers and composites: a review. *J Mater Sci* **2008**, *43*, 254–269, doi:10.1007/s10853-007-2176-7.
4. Pretsch, T. Review on the Functional Determinants and Durability of Shape Memory Polymers. *Polymers* **2010**, *2*, 120–158, doi:10.3390/polym2030120.
5. L. Sun; W.M. Huang; Z. Ding; Y. Zhao; C.C. Wang; H. Purnawali; C. Tang. Stimulus-responsive shape memory materials: A review. *Materials & Design* **2012**, *33*, 577–640, doi:10.1016/j.matdes.2011.04.065.
6. Chalissery, D.; Pretsch, T.; Staub, S.; Andrä, H. Additive Manufacturing of Information Carriers Based on Shape Memory Polyester Urethane. *Polymers* **2019**, *11*, doi:10.3390/polym11061005.
7. Holme. VII. A description of a property of caoutchouc, or indian rubber; with some reflections on the cause of the elasticity of this substance. In a letter to Dr.Holme. *The Philosophical Magazine* **1806**, *24*, 39–43, doi:10.1080/14786440608563329.
8. Kim, Y.-J.; Matsunaga, Y.T. Thermo-responsive polymers and their application as smart biomaterials. *J. Mater. Chem. B* **2017**, *5*, 4307–4321, doi:10.1039/c7tb00157f.
9. Hoffman, A.S. Stimuli-responsive polymers: biomedical applications and challenges for clinical translation. *Advanced Drug Delivery Reviews* **2013**, *65*, 10–16, doi:10.1016/j.addr.2012.11.004.
10. Yin, X.; Hoffman, A.S.; Stayton, P.S. Poly(N-isopropylacrylamide-co-propylacrylic acid) copolymers that respond sharply to temperature and pH. *Biomacromolecules* **2006**, *7*, 1381–1385, doi:10.1021/bm0507812.
11. Ke, D.; Chen, Z.; Momo, Z.Y.; Jiani, W.; Xuan, C.; Xiaojie, Y.; Xueliang, X. Recent advances of two-way shape memory polymers and four-dimensional printing under stress-free conditions. *Smart Mater. Struct.* **2020**, *29*, 23001, doi:10.1088/1361-665X/ab5e6d.
12. Zhao, Q.; Qi, H.J.; Xie, T. Recent progress in shape memory polymer: New behavior, enabling materials, and mechanistic understanding. *Progress in Polymer Science* **2015**, *49-50*, 79–120, doi:10.1016/j.progpolymsci.2015.04.001.
13. Hager, M.D.; Bode, S.; Weber, C.; Schubert, U.S. Shape memory polymers: Past, present and future developments. *Progress in Polymer Science* **2015**, *49-50*, 3–33, doi:10.1016/j.progpolymsci.2015.04.002.
14. Bothe, M.; Pretsch, T. Two-Way Shape Changes of a Shape-Memory Poly(ester urethane). *Macromol. Chem. Phys.* **2012**, *213*, 2378–2385, doi:10.1002/macp.201200096.
15. Chung, T.; Romo-Uribe, A.; Mather, P.T. Two-Way Reversible Shape Memory in a Semicrystalline Network. *Macromolecules* **2008**, *41*, 184–192, doi:10.1021/ma071517z.
16. Scalet, G. Two-Way and Multiple-Way Shape Memory Polymers for Soft Robotics: An Overview. *Actuators* **2020**, *9*, 10, doi:10.3390/act9010010.

17. Zare, M.; Prabhakaran, M.P.; Parvin, N.; Ramakrishna, S. Thermally-induced two-way shape memory polymers: Mechanisms, structures, and applications. *Chemical Engineering Journal* **2019**, *374*, 706–720, doi:10.1016/j.cej.2019.05.167.
18. Westbrook, K.K.; Mather, P.T.; Parakh, V.; Dunn, M.L.; Ge, Q.; Lee, B.M.; Qi, H.J. Two-way reversible shape memory effects in a free-standing polymer composite. *Smart Mater. Struct.* **2011**, *20*, 65010, doi:10.1088/0964-1726/20/6/065010.
19. Westbrook, K.K.; Mather, P.T.; Parakh, V.; Dunn, M.L.; Ge, Q.; Lee, B.M.; Qi, H.J. Two-way reversible shape memory effects in a free-standing polymer composite. *Smart Mater. Struct.* **2011**, *20*, 65010, doi:10.1088/0964-1726/20/6/065010.
20. Schönfeld, D.; Chalissery, D.; Wenz, F.; Specht, M.; Eberl, C.; Pretsch, T. Actuating Shape Memory Polymer for Thermoresponsive Soft Robotic Gripper and Programmable Materials. *Molecules* **2021**, *26*, doi:10.3390/molecules26030522.
21. Kim, B.K.; Lee, S.Y.; Xu, M. Polyurethanes having shape memory effects. *Polymer* **1996**, *37*, 5781–5793, doi:10.1016/S0032-3861(96)00442-9.
22. Li, F.; Zhang, X.; Hou, J.; Xu, M.; Luo, X.; Ma, D.; Kim, B.K. Studies on thermally stimulated shape memory effect of segmented polyurethanes. *J. Appl. Polym. Sci.* **1997**, *64*, 1511–1516, doi:10.1002/(SICI)1097-4628(19970523)64:8<1511:AID-APP8>3.0.CO;2-K.
23. Lee, B.S.; Chun, B.C.; Chung, Y.-C.; Sul, K.I.; Cho, J.W. Structure and Thermomechanical Properties of Polyurethane Block Copolymers with Shape Memory Effect. *Macromolecules* **2001**, *34*, 6431–6437, doi:10.1021/ma001842l.
24. Ji, F.L.; Hu, J.L.; Li, T.C.; Wong, Y.W. Morphology and shape memory effect of segmented polyurethanes. Part I: With crystalline reversible phase. *Polymer* **2007**, *48*, 5133–5145, doi:10.1016/j.polymer.2007.06.032.
25. Pereira, I.M.; Oréfice, R.L. The morphology and phase mixing studies on poly(ester–urethane) during shape memory cycle. *J Mater Sci* **2010**, *45*, 511–522, doi:10.1007/s10853-009-3969-7.
26. Huang, W.M.; Yang, B.; Zhao, Y.; Ding, Z. Thermo-moisture responsive polyurethane shape-memory polymer and composites: a review. *J. Mater. Chem.* **2010**, *20*, 3367, doi:10.1039/b922943d.
27. Wang, W.; Jin, Y.; Ping, P.; Chen, X.; Jing, X.; Su, Z. Structure Evolution in Segmented Poly(ester urethane) in Shape-Memory Process. *Macromolecules* **2010**, *43*, 2942–2947, doi:10.1021/ma902781e.
28. Pretsch, T.; Müller, W.W. Shape memory poly(ester urethane) with improved hydrolytic stability. *Polymer Degradation and Stability* **2010**, *95*, 880–888, doi:10.1016/j.polymdegradstab.2009.12.020.
29. Müller, W.W.; Pretsch, T. Hydrolytic aging of crystallizable shape memory poly(ester urethane): Effects on the thermo-mechanical properties and visco-elastic modeling. *European Polymer Journal* **2010**, *46*, 1745–1758, doi:10.1016/j.eurpolymj.2010.05.004.
30. Petchsuk, A.; Klinsukhon, W.; Sirikittikul, D.; Prahsarn, C. Parameters affecting transition temperatures of poly(lactic acid-co-polydiols) copolymer-based polyester urethanes and their shape memory behavior. *Polym. Adv. Technol.* **2012**, *23*, 1166–1173, doi:10.1002/pat.2017.
31. Bothe, M.; Emmerling, F.; Pretsch, T. Poly(ester urethane) with Varying Polyester Chain Length: Polymorphism and Shape-Memory Behavior. *Macromolecular Chemistry and Physics* **2013**, *214*, 2683–2693, doi:10.1002/macp.201300464.
32. Liu, W.; Zhang, R.; Huang, M.; Dong, X.; Xu, W.; Wang, Y.; Hu, G.-H.; Zhu, J. Synthesis and shape memory property of segmented poly(ester urethane) with poly(butylene 1,4-cyclohexanedicarboxylate) as the soft segment. *RSC Adv.* **2016**, *6*, 95527–95534, doi:10.1039/C6RA16325D.
33. Ren, H.; Mei, Z.; Chen, S.; Zhuo, H.; Chen, S.; Yang, H.; Zuo, J.; Ge, Z. A new strategy for designing multifunctional shape memory polymers with amine-containing polyurethanes. *J Mater Sci* **2016**, *51*, 9131–9144, doi:10.1007/s10853-016-0166-3.
34. Mirtschin, N.; Pretsch, T. Programming of One- and Two-Step Stress Recovery in a Poly(ester urethane). *Polymers* **2017**, *9*, doi:10.3390/polym9030098.
35. Behl, M.; Kratz, K.; Zotzmann, J.; Nöchel, U.; Lendlein, A. Reversible bidirectional shape-memory polymers. *Adv. Mater. Weinheim.* **2013**, *25*, 4466–4469, doi:10.1002/adma.201300880.
36. Fan, L.F.; Rong, M.Z.; Zhang, M.Q.; Chen, X.D. A Very Simple Strategy for Preparing External Stress-Free Two-Way Shape Memory Polymers by Making Use of Hydrogen Bonds. *Macromol. Rapid Commun.* **2018**, *39*, e1700714, doi:10.1002/marc.201700714.
37. Fan, L.F.; Rong, M.Z.; Zhang, M.Q.; Chen, X.D. A Facile Approach Toward Scalable Fabrication of Reversible Shape-Memory Polymers with Bonded Elastomer Microphases as Internal Stress Provider. *Macromol. Rapid Commun.* **2017**, *38*, doi:10.1002/marc.201700124.

38. Fan, L.F.; Rong, M.Z.; Zhang, M.Q.; Chen, X.D. Dynamic reversible bonds enable external stress-free two-way shape memory effect of a polymer network and the interrelated intrinsic self-healability of wider crack and recyclability. *J. Mater. Chem. A* **2018**, *6*, 16053–16063, doi:10.1039/C8TA05751F.
39. Fan, L.F.; Huang, Y.N.; Rong, M.Z.; Zhang, M.Q. A simple and universal strategy for preparing external stress-free two-way shape memory polymers by making use of the chemical crosslinkages derived from peroxide initiator. *Express Polym. Lett.* **2020**, *14*, 295–308, doi:10.3144/expresspolymlett.2020.26.
40. Fischer, S.C.L.; Hillen, L.; Eberl, C. Mechanical Metamaterials on the Way from Laboratory Scale to Industrial Applications: Challenges for Characterization and Scalability. *Materials (Basel)* **2020**, *13*, doi:10.3390/ma13163605.
41. Jin, L.; Forte, A.E.; Deng, B.; Rafsanjani, A.; Bertoldi, K. Kirigami-Inspired Inflatables with Programmable Shapes. *Adv. Mater. Weinheim.* **2020**, *32*, e2001863, doi:10.1002/adma.202001863.
42. Berwind, M.F.; Kamas, A.; Eberl, C. A Hierarchical Programmable Mechanical Metamaterial Unit Cell Showing Metastable Shape Memory. *Adv. Eng. Mater.* **2018**, *20*, 1800771, doi:10.1002/adem.201800771.
43. Restrepo, D.; Mankame, N.D.; Zavattieri, P.D. Programmable materials based on periodic cellular solids. Part I: Experiments. *International Journal of Solids and Structures* **2016**, *100-101*, 485–504, doi:10.1016/j.ijsolstr.2016.09.021.
44. Specht, M.; Berwind, M.; Eberl, C. Adaptive Wettability of a Programmable Metasurface. *Adv. Eng. Mater.* **2021**, *23*, 2001037, doi:10.1002/adem.202001037.
45. Zhang, X.; Pint, C.L.; Lee, M.H.; Schubert, B.E.; Jamshidi, A.; Takei, K.; Ko, H.; Gillies, A.; Bardhan, R.; Urban, J.J.; et al. Optically- and thermally-responsive programmable materials based on carbon nanotube-hydrogel polymer composites. *Nano Lett.* **2011**, *11*, 3239–3244, doi:10.1021/nl201503e.
46. Walter, M.; Friess, F.; Krus, M.; Zolanvari, S.M.H.; Grün, G.; Kröber, H.; Pretsch, T. Shape Memory Polymer Foam with Programmable Apertures. *Polymers* **2020**, *12*, doi:10.3390/polym12091914.
47. Takeuchi, N.; Nakajima, S.; Yoshida, K.; Kawano, R.; Hori, Y.; Onoe, H. Microfiber-Shaped Programmable Materials with Stimuli-Responsive Hydrogel. *Soft Robot.* **2022**, *9*, 89–97, doi:10.1089/soro.2020.0038.
48. Ultimaker Cura: Powerful, easy-to-use 3D printing software. Available online: https://ultimaker.com/software/ultimaker-cura (accessed on 19 January 2022).

Chapter 6: Fused Filament Fabrication of Actuating Objects

Chapter 6: Fused Filament Fabrication of Actuating Objects

The original article Chalissery, D., Schönfeld, D., Walter, M., Ziervogel, F., Pretsch, T., Fused Filament Fabrication of Actuating Objects. Macromol. Mater. Eng. 2022, 2200214 and graphical abstract are published in Wiley Macromolecular Materials and Engineering and available at https://doi.org/10.1002/mame.202200214.

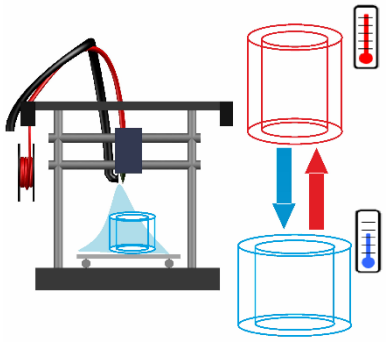

Figure 6.0.0 The table of content image of the article "Fused Filament Fabrication of Actuating Objects" is published in Wiley Macromolecular Materials and Engineering 2200214.

Contribution

My contribution: The concept idea of two-way four dimensional printing and its potential applications. The idea of the whole manuscript, design development, conducting experiments, formal analysis, investigation, methodology, validation, visualization, filament extrusion, 4D-printing, characterization: DSC and DMA, preparation of all the images (including table of content image and cover image), videos, writing—original draft and project lead.
Not included in my contribution: Polymer-synthesis.

Schönfeld, D.: Synthesis of polymer and carried out differential scanning calorimetry of synthesized polymer (**Figures 6.1a**).

Walter, M.: Developed the polymer.

Ziervogel, F.: Concept development of wire integration for future scope.

Pretsch, T.: Funding acquisition, project administration, supervision, writing—review and editing

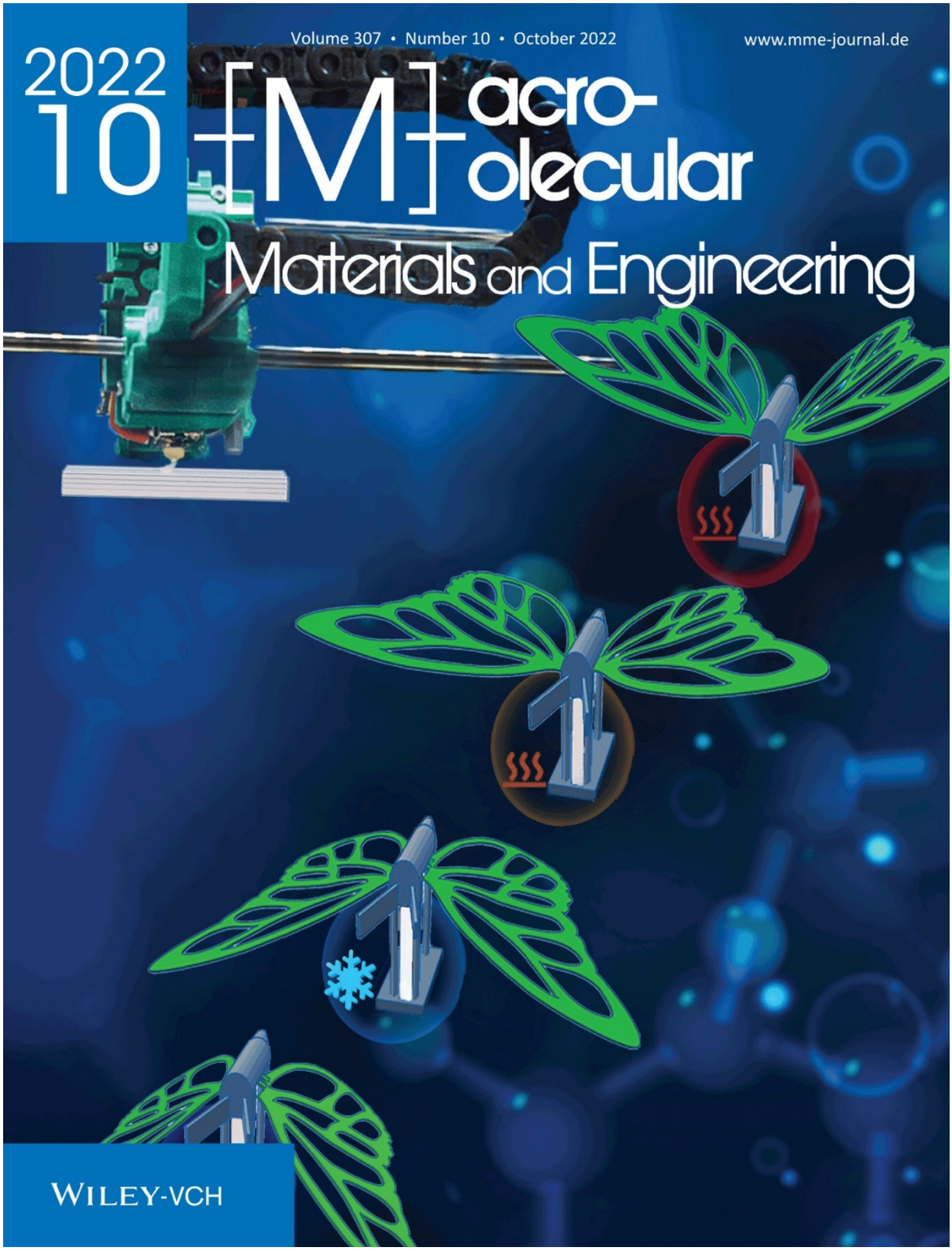

Figure 6.0.1. Cover image of "Fused Filament Fabrication of Actuating Objects" published in Wiley Macromolecular materials and engineering, Volume 307, Issue 10 October 202. © 2022 Chalissery et al. Macromolecular Materials and Engineering published by Wiley-VCH GmbH.

Chapter 6: Fused Filament Fabrication of Actuating Objects

Dilip Chalissery[1], Dennis Schönfeld[1], Mario Walter[1], Fabian Ziervogel[2], and Thorsten Pretsch[1]*

[1] Fraunhofer Institute for Applied Polymer Research IAP, Geiselbergstraße 69, Potsdam 14476, Germany E-mail: dilip.chalissery@iap.fraunhofer.de; thorsten.pretsch@iap.fraunhofer.de
[2] Fraunhofer Institute for Machine Tools and Forming Technology IWU, Nöthnitzer Straße 44, Dresden 01187, Germany
* Correspondence: thorsten.pretsch@iap.fraunhofer.de; Tel.: +49-(0)-331/568-1414

6.0. Abstract: Thermoresponsive objects can be manufactured from shape memory polymers (SMPs) via fused filament fabrication (FFF). Here a new technological approach to obtain thermally actuating objects using an in-house synthesized, phase segregated poly(ester urethane) (PEU) is introduced. Under almost stress-free conditions of a dynamic mechanical analysis, cuboid objects obtained from FFF shrank when heated to 62 °C and expanded when cooled to 15 °C with a maximum thermoreversible strain of 7.2%. Actuation can be traced back to the phenomena of melting-induced contraction and crystallization-induced elongation of the PEU's soft segment, supported by internal stresses as implemented in course of FFF. To translate small changes in shape to a next larger scale, an artificial butterfly is developed in which the movements of two actuator elements are transferred to the wings with the aid of a lever concept. Following a different approach, additive manufacturing of cylindrical samples implied application potential as a self-sufficient gripper, enabling a programmable material behavior in the sense of temperature-controlled gripping, transport, and release of exemplarily selected smooth surfaced objects in the form of vials.

Keywords: shape memory polymer, actuation, additive manufacturing, two-way 4D printing, gripper, programmable materials

6.1. Introduction

Shape memory polymers (SMPs) can maintain a temporary shape after a thermomechanical treatment, also known as “programming”. The temporary shape remains stable until the “one-way shape memory effect” (1W SME) is triggered,[1-6] whereupon the polymer returns into its almost permanent shape. Shape recovery is an entropically driven process; it is based on the theory of rubber elasticity.[7]

In the context of additive manufacturing (AM), the so-called “four-dimensional (4D)-printing” makes it possible to control the shape of an SMP both before and after heating above the material-specific switching temperature.[8] This means that in certain cases the classic programming of the 1W SME can be omitted. In other words, 4D-printed objects are thermoresponsive and thus available for immediate use. Today, there are only a few

contributions on 4D-printing primarily focusing on AM via fused filament fabrication (FFF), which makes it clear that the technology is still in its infancy. For instance, researchers carried out 4D-printing with "glass transition temperature-based" polymers like poly(ether urethanes),[9-11] polylactic acid (PLA),[12-16] acrylonitrile butadiene styrene (ABS),[13] and high impact polystyrene (HIPS).[13] Until recently, researchers focused on the implementation of thermoresponsiveness in objects with smaller layer heights (z < 5 mm), where the degree of shrinkage becomes weaker from layer to layer.[8, 14] In a recent study, some of us employed an amorphous poly(ether urethane) and PLA for 4D-printing and showed that the technological key to realize distinct shrinkage is keeping the difference between the nozzle temperature and the glass transition temperature (T_g) of the polymers to a minimum possible value. This allows a rapid vitrification of the polymers once deposited on a printing bed.[8] All these approaches have in common is that the underlying technique of 4D-printing can be controlled by appropriate AM parameters, ensuring that polymer relaxation is avoided as far as possible. For this reason, 4D-printing can be understood as an "in situ" programming technology, which does not necessitate a thermomechanical treatment in the aftermath of production.

In the last few years, researchers have learned how to program semicrystalline SMPs in order to transform them into metastable states, between which they can be switched back and forth by varying the temperature.[17-20] The underlying material behavior is the so-called "two-way shape memory effect" (2W-SME). Beyond entropy elasticity, the main driving forces are crystallization-induced elongation (CIE) and melting-induced contraction (MIC) as caused by the phase transitions in the polymer matrix.[20, 21] The fundamental understanding of the 2W-SME was originally developed for a semicrystalline polymer network by Chung et al., who investigated cross-linked poly(cyclooctene) films under constant external loads.[22] Later on, the same working principle and thus the general validity of the approach was verified for other semicrystalline polymers under externally imposed stresses including, i.e., poly(ethylene-co-vinyl acetate) cross-linked by dicumyl peroxide,[23] poly(ε-caprolactone)-based polymer systems,[24-26] phase segregated poly(ester urethanes) (PEUs) with crystallizable segments of poly(1,4-butylene adipate),[27] polymer networks with crystallizable segments of poly(ω-pentadecalactone),[28] poly(ε-caprolactone)-*co*-poly(ethylene glycol) foams [29] and polyester-based poly(urethane urea) foam.[30]

Conversely, stress-free actuation can be achieved for phase segregated, semicrystalline PEU by programming the 2W-SME. The essential steps include the application of relatively high strains at temperatures above the offset melting transition temperature of the soft segment, followed by cooling below the corresponding offset crystallization transition temperature while retaining the deformation and a final step of unloading.[31, 32] Although even other programming methods and concepts were applied to SMPs to realize stress-free bidirectional actuation, [33, 34] the necessary thermomechanical treatment is still a time-, energy-, and thus a cost-intensive process which stands in the way of economic exploitation.

The maturation of AM technology in recent years has led to the development of objects that actuate immediately after printing.[35] Today, two-way (2W) 4D-printing approaches can

be subdivided as follows: core-shell embedded structures and bilayer or gradient structures.[36] The first ones focused on the manufacturing of elastomeric material composites containing magnetic particles.[37-40] When applying a specific magnetic field, their shape can be changed in a controllable manner; as soon as the magnetic field is switched off, the initial shape is recovered due to the elastomeric properties of the matrix material. By contrast, the concept of bilayer or gradient structures is based on composite AM technology.[41-47] In this case, composite layers are fabricated consisting of a material with antagonistic properties, e.g. reversible physical properties associated with water absorption/desorption or temperature changes, to realize stimulus-governed shape changes. However, the main disadvantage is the need for two entirely different stimuli like water and heat. To make matters worse, the effort associated with recycling in the sense of a recovering the individual materials at the end of their life cycle is very high. One in all, there seem to be no technological approaches so far, considering a single material system, which exhibits bidirectional actuation immediately after AM.

Here we demonstrate how to obtain thermally actuating objects from a semicrystalline SMP by means of FFF. To gain the greatest possible control over material functionality, a poly(1,10-decylene adipate) (PDA)-based PEU was selected, as it was previously identified as a promising material with regard to 2W-SMEs under stress-free actuation conditions.[32] Exploiting a lever mechanism coupled with two PEU actuators turned out as an appropriate strategy to translate small changes in shape to a next larger scale. Beyond that, we describe how to design and manufacture structures, like cylindrical actuating elements which are able to grab, transport, and release smooth surfaced objects in the form of vials. In this way, we provide first examples to open a new design space for actuators made from programmable materials.[30, 32, 48-53]

6.2. Results and discussion

Poly(1,10-decylene adipate) diol (PDA) is an attractive building block in the chemistry of PEUs, which may exhibit pronounced two-way shape memory properties.[32] In order to synthesize the hydroxyl-terminated PDA oligoester, 1,10-decanediol and adipic acid were brought to reaction. Subsequent to this polycondensation, further reaction with 4,4'-diphenylmethane diisocyanate (4,4'-MDI) was carried out to build up an isocyanate-endcapped prepolymer, before 1,4-butanediol (BD), serving as a chain extender, was finally added. This led to the formation of the desired PEU.

After polymer synthesis, the PDA-based PEU was extruded into filament. The filament was characterized by a uniform diameter of 2.85 ± 0.05 mm. The thermal properties of the PEU raw material were analyzed by means of differential scanning calorimetry (DSC, **Figure 6.1a**). Thermomechanical investigations were carried out by dynamic mechanical analysis (DMA, **Figure 6.1b**) on a cuboid sample consisting of 20 individual layers with dimensions of 40 mm × 2 mm × 2 mm and fabricated by FFF ("3D-printing"; the underlying print settings are summarized in **Table 6.1**.).

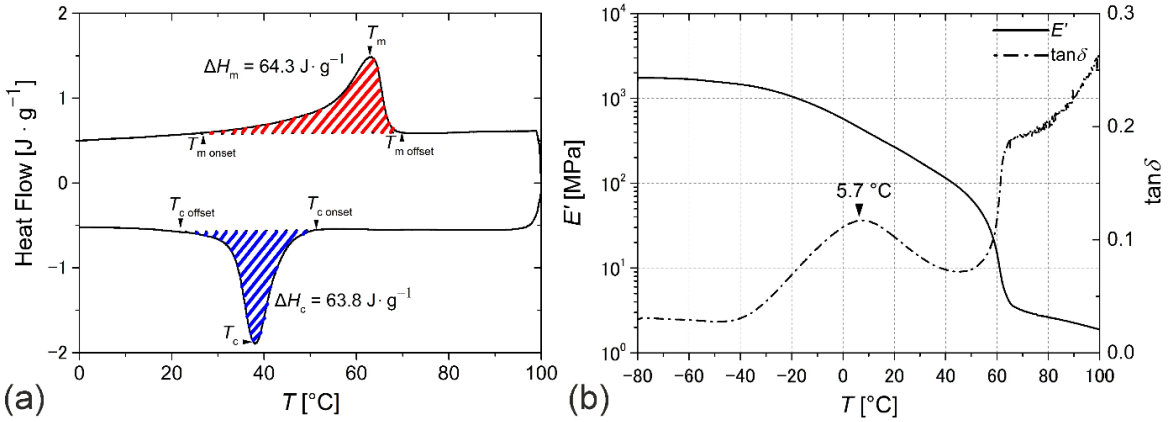

Figure 6.1. Thermal and thermomechanical properties of PDA-based PEU as determined by a) DSC subsequent to the synthesis, second heating and cooling with temperature rates of 10 °C x min^{-1}. The enthalpies of melting ΔH_m, red dashed area, and crystallization ΔH_c, blue dashed area, are included. b) DMA of a cuboid sample obtained after FFF exhibiting the temperature dependence of storage modulus E', and loss factor tan δ at a heating rate of 3 °C x min^{-1}.

The thermal properties of the PDA-based PEU were characterized by a broad melt transition temperature in between 30 and 71 °C with a maximum at about 63 °C, while the crystallization transition spread from 53 to 19 °C and exhibited a peak at 38 °C (**Figure 6.1a**). With regard to the DMA (**Figure 6.1b**) a similar evolution was detected for the storage modulus E' and tan δ curve as in our previous work.[32] In fact, the storage modulus E' declined upon heating in two steps as associated with the devitrification and melting of the PDA phase. At temperatures of about 71 °C and thus above the melting transition of the PDA phase, the hard segments of the PEU ensured that the polymer still had a sufficiently high degree of dimensional stability. The evolution of tan δ is often used to determine the glass transition temperature T_g in urethane-based polymers.[54-56] Here, the tan δ peak was located at ≈6 °C.

After characterizing the PEU, an FFF 4D-printing approach was followed in accordance with the above-studied thermal properties of the material. The approach is aimed at realizing a rapid vitrification. For this reason, the FFF printer was modified with a cooling unit, which continuously applied compressed nitrogen with a stream temperature (T_s) of about −5 °C as soon as the polymer strand left the nozzle (**Figure 6.2**).

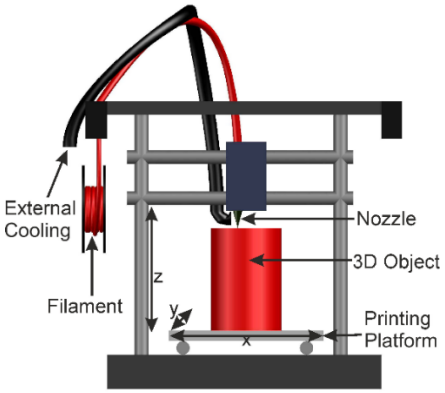

Figure 6.2. Schematic drawing of a fused filament fabrication printer modified with a hose to apply a cold stream of compressed nitrogen to polymer strands as soon as they left the nozzle.

In course of additive manufacturing, the efficiency of the cooling unit was verified by means of in situ thermal imaging for an exemplarily selected cuboid sample (**Figure 6.3**).

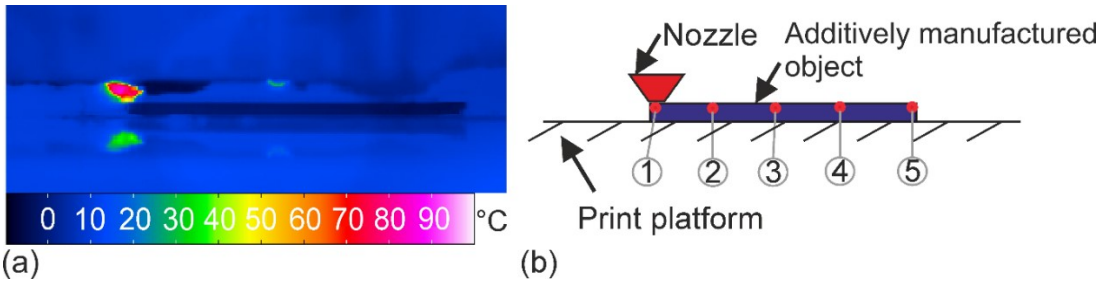

Figure 6.3. *In situ* thermal imaging to supervise the temperature distribution in PDA-based PEU a) during FFF and b) schematic representation of the process at five randomly selected measurement points in the top layer during strand deposition.

It was found that the temperature of each freshly deposited polymer strand fell quickly below 0 °C (**Figure 6.3a**). In any case, temperatures of 11 °C, −1 °C, −4 °C, −5 °C, and –5 °C were recorded at the individual measurement points 1 to 5 (**Figure 6.3b**). Taking into account the printing speed and the distance of the individual measurement points, it can be concluded that the use of the external cooling unit permitted the PEU to cool below its T_g in ≈150 ms. Most importantly, after leaving the nozzle the rapid cooling of polymer strands seemed to support a quick crystallization and vitrification of the PDA phase. The former is indicated by a whitish coloring of the cuboid sample while the latter is implied by the temperature distribution in the freshly deposited polymer strands (**Figure 6.3a**).

Further cuboid samples of PEU were fabricated via FFF with a printing speed S_P of 8 mm x s^{-1} and a nozzle temperature T_N of 170 °C under permanent exposure to a compressed nitrogen stream with a temperature T_S of about −5 °C. Hereafter it will be demonstrated that these objects exhibited both the so-called “one-way (1W) 4D effect” and the “two-way (2W) 4D effect”. In any case, the underlying print settings were the same and will be referred to as “2W 4D-printing” in the following (compare **Table 6.1**).

First, the print result and stability of another cuboid sample were investigated at 23 °C, before the responsiveness on heating to 75 °C was studied with respect to the 1W 4D effect to evaluate the efficiency of the printing process for the implementation and subsequent release of internal stresses (**Figure 6.4**).

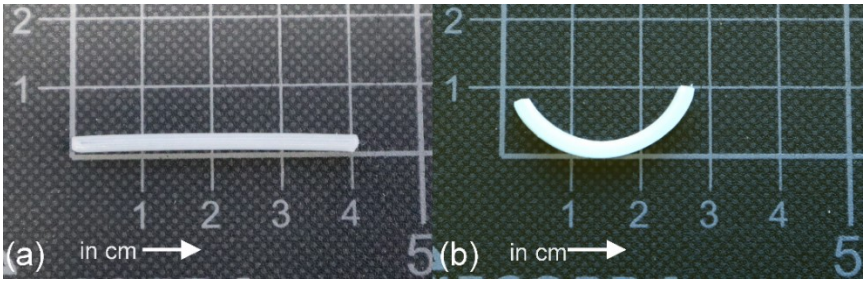

Figure 6.4. Cuboid sample of PDA-based PEU: a) Immediately after FFF using the method of 2W 4D-printing (**Table 6.1**), and b) after temperature conditioning for 5 min at 75 °C to trigger the 1W 4D effect (all the dimensions are in cm).

The sample remained stable after printing (**Figure 6.4a**) even when raising the temperature to 23 °C and thus above the glass transition temperature of the PEU (**Figure 6.1b**). Upon heating to 75 °C under stress-free conditions and holding that temperature for 5 min, significant shrinkage accompanied by a bending of the sample occurred. After shrinkage an arc length of 30.5 mm was measured; in parallel, an arc measure of 134.8° and a radius of curvature of 13 mm were verified (**Figure 6.4b**). The bending behavior of the sample can be explained by the fact that every single hot molten top layer favored the relaxation of the layer below in course of FFF. As a result, a gradient in stress distribution presumably formed. This phenomenon is well-known from other studies when utilizing the same printing method. For instance, similar shrinkage and bending behavior was observed after FFF 4D-printing of objects made of poly(ether urethanes),[9, 10] PLA,[13-16] and ABS.[13]

Subsequently, two types of cuboid samples of PEU were additively manufactured according to the object dimensions from **Figure 6.4a**. In the first case, the abovementioned 2W 4D-printing method (**Table 6.1**) was used again. In the other case, T_N was increased to 208 °C and T_S to 75 °C while S_P remained unchanged, using the print settings of "3D-printing" (**Table 6.1**). Later, the thermoresponsiveness of the samples was studied by means of DMA (**Figure 6.5**).

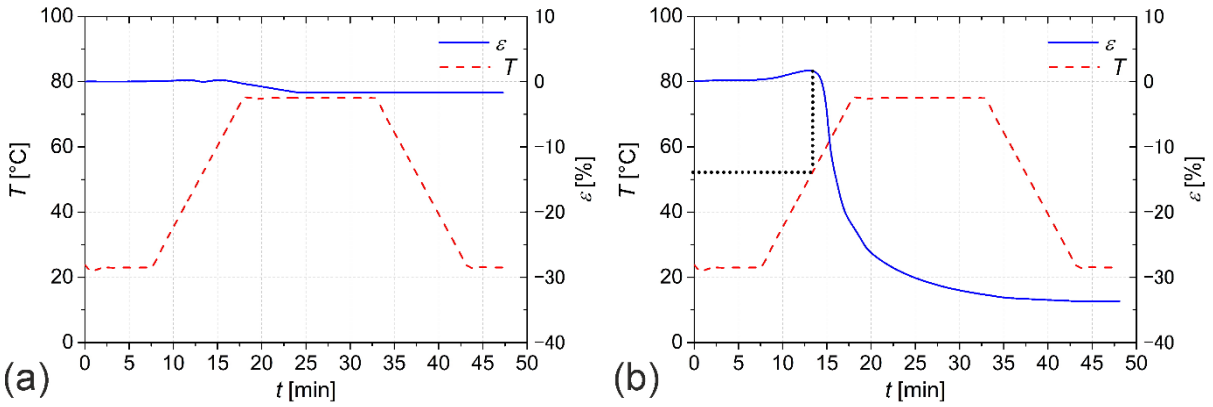

Figure 6.5. DMA measurement protocols of PDA-based PEU, exhibiting the evolution of strain ε (solid blue line) when varying the temperature T (dashed red line). The samples were obtained by FFF via a) 3D-printing and b) 2W 4D-printing (**Table 6.1**).

In contrast to the first study of thermoresponsiveness, in which no fixation of the sample was made (**Figure 6.4b**), this time the clamping conditions, where the distance between the clamping units of the DMA was 20 mm, ensured that no bending occurred during heating. In the case of the 3D-printed sample, heating to 75 °C and holding that temperature constant resulted in a slight decrease in strain of ≈1.6% (**Figure 6.5a**). By contrast, slight expansion followed by strong shrinkage of ≈34% occurred after 2W 4D-printing (**Figure 6.5b**). Here, the initial increase in sample length by 1.7% during heating from 23 to 53 °C can be associated with the recrystallization of the PDA phase, since some of the polymer chains may have vitrified as a consequence of the rapid cooling before, so that they did not have sufficient time to crystallize. Further heating initiated strong shrinkage and thus the 1W 4D effect. After cooling back to 23 °C, the shrunken sample remained almost stable.

In the next step, the focus of the investigations was directed away from 1W 4D effects and toward 2W 4D effects. From a conceptual point of view it was evident from **Figure 6.5b** that a too high maximum temperature, as selected with 75 °C, would lead to the complete melting of the PDA soft segment (compare **Figure 6.1a**) and thus no movement of the sample in the ensuing cooling contrary to the reduction of strain. For this reason, the maximum temperature was limited to a lower temperature value of 64 °C in the following DMA measurement. The measurement was carried out under almost stress-free conditions – only a weak load of 0.001 N was applied – on a 2W 4D-printed cuboid sample (**Figure 6.4a** and **Table 6.1**) to investigate both the actuation capability and identify the optimal temperature conditions. Again, the same clamping conditions as used for the other DMA were selected to avoid any bending in the first heating. The results are exhibited in (**Figure 6.6**).

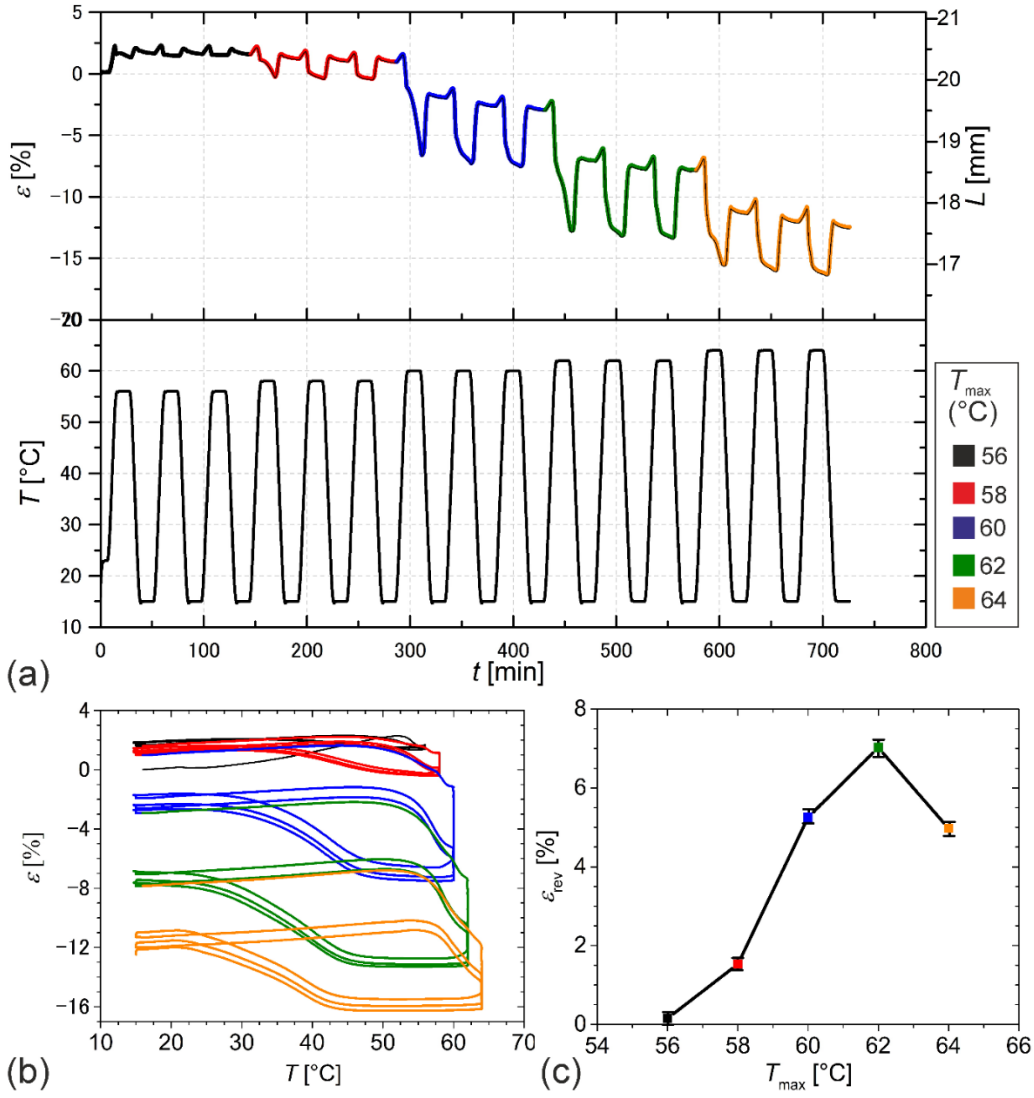

Figure 6.6. Actuation of a 2W 4D-printed sample of PDA-based PEU (**Figure 6.4a and Table 6.1**) under a weak load of 0.001 N: a) Evolution of strain ε and sample length L (differently colored according to the temperature intervals investigated) and temperature T with measuring time t; b) relationship between strain and temperature for the experiment shown in (a) using the same color codes and c) evolution of thermoreversible strain ε_{rev} depending on T_{max}, the values for ε_{rev} are averaged for the second and third cycle.

Remarkably, thermoreversible changes in strain could be verified in every single measurement cycle, even when continuously raising the upper temperature T_{max} from 56 to 64 °C, while keeping the lower temperature T_{min} at 15 °C (**Figure 6.6a,b**). As known from similar semicrystalline polymeric materials,[20, 32] the driving force for actuation is – beyond entropy elasticity – melting-induced contraction (MIC) and crystallization-induced elongation (CIE). When selecting a lower T_{max}, obviously only a small quantity of PDA crystals were molten, resulting in weak PDA crystallization and sample elongation on cooling and weak PDA melting and sample contraction on heating as can particularly be seen in the respective strain-temperature diagram in **Figure6. 6b** (black lines). By contrast, the steady increase in T_{max} enhanced polymer shrinkage in the first heating due to a more pronounced release of internal stress introduced in the course of additive manufacturing and stored by rapid cooling. With ongoing measurement, a directed crystallization of the PDA phase seemed to occur during cooling (**Figure 6.6b**); in parallel, the proportion of crystallizable segments increased, since more PDA crystals were melted in the previous heating, favoring more pronounced polymer expansion on cooling. At the same time, a hysteresis behavior was detected. Actuation substantially increased when selecting a T_{max} of 58 °C (**Figure 6.6b**, red color) and even got stronger at T_{max} = 60 °C (**Figure 6.6b**, blue color). Further increasing T_{max} to 62 °C culminated in the most pronounced actuation (**Figure 6.6b**, green color) with a maximum change in thermoreversible strain ε_{rev} of 7.2% and an average value for ε_{rev} of 7.0%. This becomes particularly clear in the associated ε_{rev} /T_{max} diagram (**Figure 6.6c**, green point). Interestingly, the value for T_{max} corresponded precisely with the melting peak temperature (second heating) of the FFF-printed PDA-based PEU in our DSC measurements (**Figure 6.1a**). Upon further increasing T_{max}, actuation decreased (**Figure 6.6b**, orange) since the systematic melting of PDA crystals resulted in strain recovery of the PEU and thus a lower overall strain as caused by a reduction of internal stresses implemented in course of additive manufacturing and stored by rapid cooling. In other words, the overall elongation at the beginning of each cooling step was gradually reduced. Above all, a new type of functional integration using 2W 4D-printing could be realized due to the thermoreversible shape changes detected. In comparison with our previous work on thermomechanically treated PDA-based PEU,[32] the values for ε_{rev} were found to be lower here. This is not surprising, as in the other scenario a strong deformation, measuring 700% in strain, was applied during programming to achieve strain-induced PDA crystallization. Advantageously, in our present approach, an actuator can be manufactured within a short time of 5 min. This is in sharp contrast to the other route of processing and programming, which roughly takes 245 min.[32]

The durability of almost stress-free actuation was investigated in another DMA measurement. A 2W 4D-printed cuboid sample of PEU (**Figure 6.4a** and **Table 6.1**) was subjected to 100 heating-cooling cycles with maximum and minimum temperatures of 62 °C and –15 °C, respectively (**Figure 6.7**).

In the beginning, a strong drop in strain was observed (**Figure 6.7a**). This was attributed to the melting of highly oriented PDA crystals and the associated release of internal stresses. In the first three cycles, actuation decreased (**Figure 6.7b**), which was presumably caused by the

rearrangement of polymer chains.[57] More stable actuation was detected after 20 cycles of heating and cooling. Apparently, the PDA-based PEU formed temperature-bistable states, differing in elongation. In the end, ε_{rev} approached an almost constant value of 5.7%, thus qualifying it as a reliable actuator. In addition, we would like to emphasize that the clamping conditions in the DMA assured once more that no bending effects were observed.

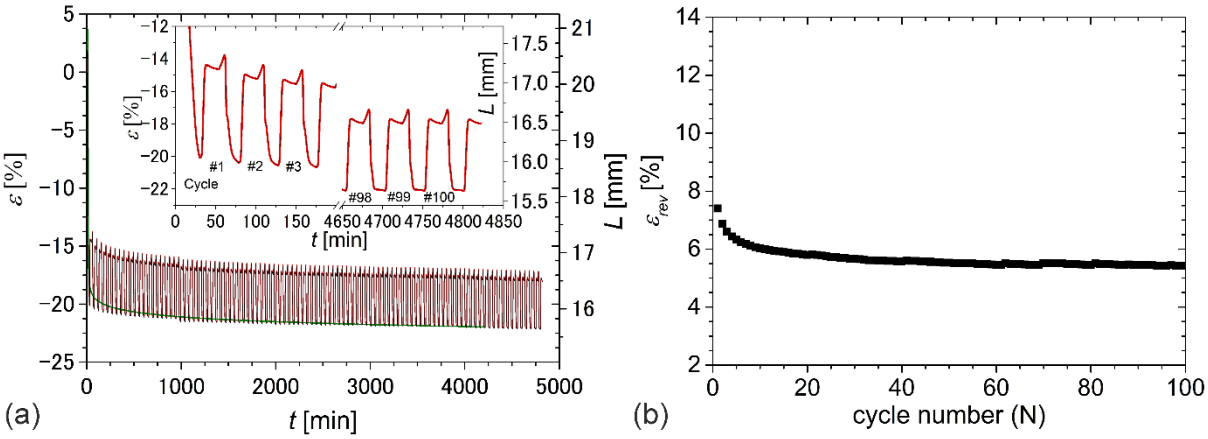

Figure 6.7. DMA measurement to determine the durability of actuation of 2W 4D-printed PEU (**Table 6.1**) under a weak load of 0.001 N: Evolution of a) nominal strain ε with time t in the actuation measurement (red) including the measurement protocol of an isothermal strain measurement (green) and b) thermoreversible strain ε_{rev} with cycle number N.

To closely examine the temperature resistance of 2W 4D-printed PEU (**Figure 6.4a** and **Table 6.1**), a final DMA measurement was conducted. This time, a cuboid sample was heated to 62 °C and kept there for 70 h without external load. In the course of the experiment, the strain of the sample decreased sharply at first and later gradually to a value of −22% (**Figure 6.7a**, green). It is noteworthy that the length of the sample largely coincided with the length of the sample from the actuation measurement at 62 °C (**Figure 6.7a**, red).

As the 2W 4D-printed PEU showed promising actuation even in multiple cycles, some potential applications were explored. For a start, a lever mechanism was developed for an artificial butterfly in order to transfer the actuation in a targeted manner to its wings. In this regard, the concept was inspired by our recently published work on a gripper system containing embedded actuating elements, whose linkage mechanism allowed to magnify the 2W-SME.[32] The underlying scalable vector graphics of the lever mechanism is shown together with the demonstrator in **Figure 6.8**.

After finalizing the design, the individual parts (**Figure 6.8a-p**) were laser cut from 5 mm thick poly(methyl methacrylate) sheets (parts in **Figure 6.8a–e,h–p**), while the left and right wing (**Figure 6.8f,g**) were laser cut from a thin, rigid sheet of paper. The design was such that one millimeter of actuation of the 2W 4D-printed cuboid sample (**Figure 6.4a** and **Table 6.1**) can cause a wing to rotate by 10°, resulting in lateral differences of 11 mm between its first and second position (**Figure 6.8q**). After cutting out the parts, the artificial butterfly was assembled (**Figure 6.9**).

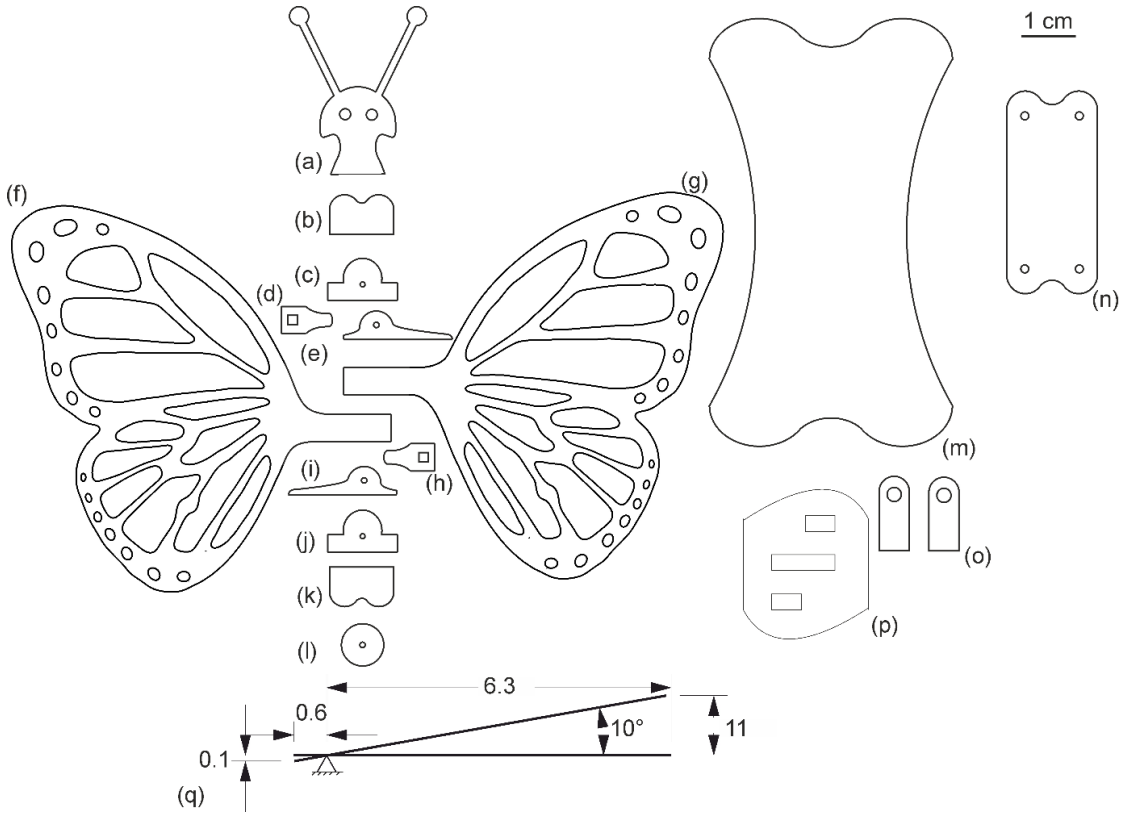

Figure 6.8. Technical drawing of the individual components of a butterfly: a) Head; b) front base; c) front alignment part; d) right wing actuator holder; e) right fulcrum; f) left wing; g) right wing; h) left wing actuator holder; i) left fulcrum; j) rear alignment part; k) rear base; l) tail; m) base; n) intermediate base; o) two base actuator fixing part and p) base actuator holder. q) Illustration of the leverage effect.

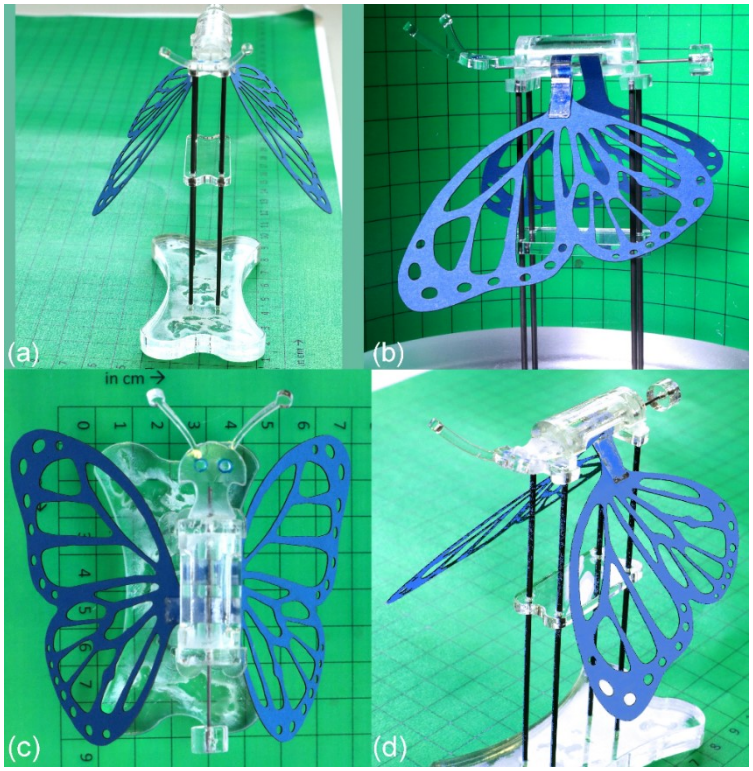

Figure 6.9. Butterfly demonstrator in the perspectives a) front view, b) right view, c) top view, and d) isometric view.

Two 2W 4D-printed actuators were then manually inserted, each responsible to move one wing, by gluing their ends in the upper area of the butterfly and fixing the other ends with the aid of two screws, whereupon the system was ready to use. Since the fixing length of every actuator was about 3 cm, a larger change in total length could be expected compared to the DMA measurement, in which the sample was clamped at a length of 2 cm (compare **Figure 6.6a**). For functional proof-of-principle, the temperature was cycled three times between 23 and 62 °C while the movements of the butterfly were followed (**Figure 6.10**, **s6.1.movie** in Supporting Information).

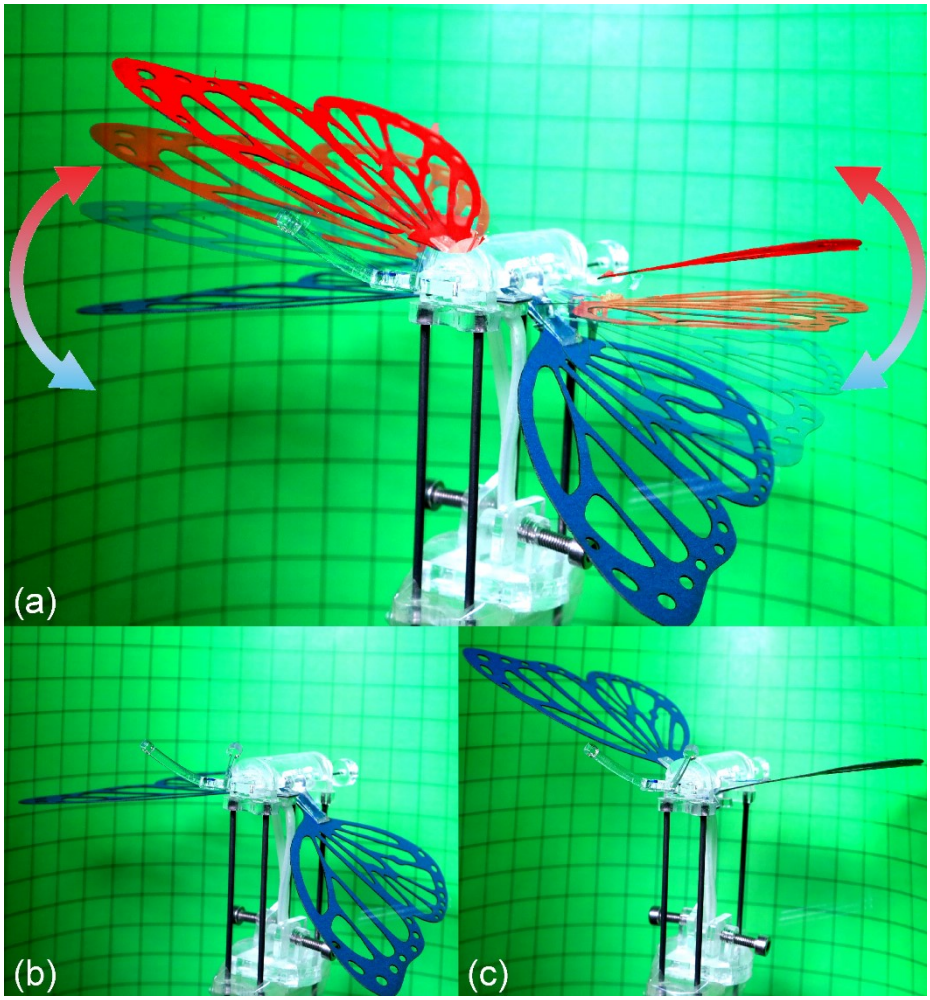

Figure 6.10. Artificially generated wing beat of a butterfly, enabled by two actuators from 2W 4D-printed PDA-based PEU: a) Four superimposed images of the setup during heating from 23 °C (blue) to 62 °C (red coloring was accomplished with an image editing software)[58]; b) shapes at 23 °C and c) at 62 °C.

Figure 6.10 proves that the actuation of the PEU of roughly 3 mm could be transferred to the butterfly's wings as verified by four superimposed images taken at different temperatures (**Figure 6.10a**). In fact, the wings of the butterfly hung down at first (**Figure 6.10b**), but when raising the temperature to 62 °C a slight expansion and an associated bending of the actuators occurred coupled with a slight lowering of the wings, followed by the contraction and straightening of the PEU. In this way, the longer sides of the wing actuator holders

(**Figures 6.8d,h**) were pulled, which in turn caused the shorter ends to be lifted pressing against the fulcrums (**Figures 6.8e,i**). The wings attached in between (**Figures 6.8f,g**) followed the movement of the fulcrums and were lifted (**Figure 6.10c**, **s6.1.movie** in Supporting Information). Thus, the thermoresponsive behavior of the two actuators during the first heating was in good agreement with the behavior determined in the DMA (**Figure 6.5b**). Upon cooling to 23 °C, the expansion of the actuators pushed the wing actuator holders (**Figures 6.8d,h**) upward, causing the fulcrums (**Figures 6.8e,i**) to lower while the actuators finally bend through. In parallel, the wings returned almost to their original position (**Figure 6.10b**, **s6.1.movie** in Supporting Information). The experiment was repeated twice, in which the actuation proved to be stable.

In a progressive approach, two hollow cylinders were 2W 4D-printed using the same printing equipment and parameters as selected before (**Table 6.1**) and their actuation capability was explored (**Figure 6.11, s6.2.movie and s6.3.movie** in supplementary material).

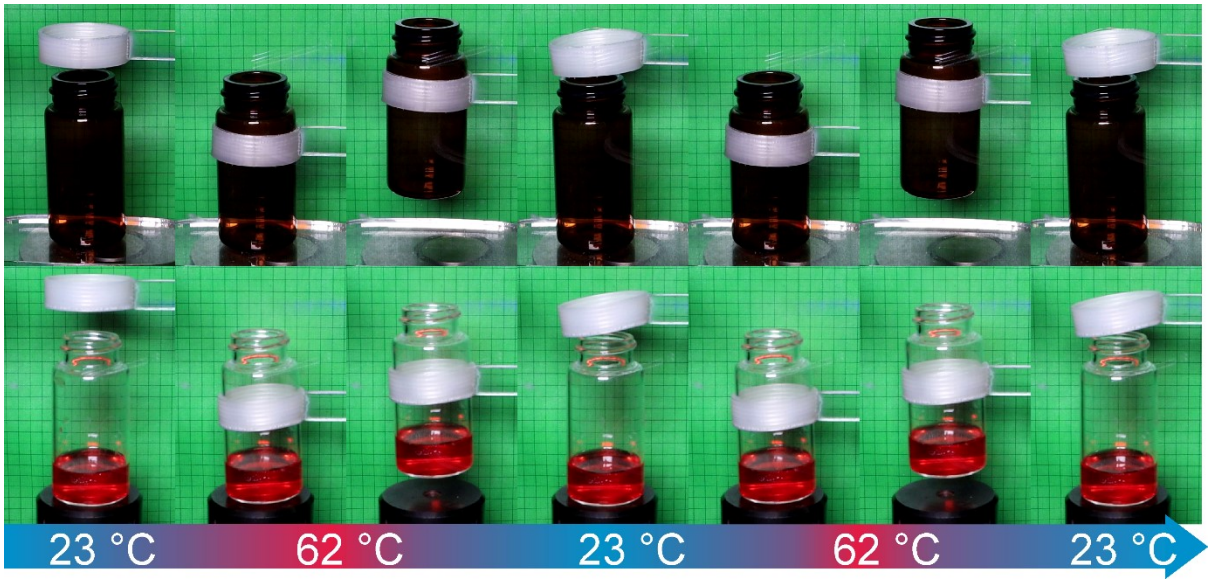

Figure 6.11. 2W 4D-printed cylindrical actuators of PDA-based PEU in operation: Gripping, lifting, releasing of (top row) an empty brownish vial (15 g in weight) and (bottom row) a transparent vial filled with red liquid (total weight of 30 g) in two consecutive thermal cycles.

The image series in **Figure 6.11** clearly show that the hollow cylinders actuated when cycling the temperature. At the beginning, the cylinders had an inner diameter ø of ≈30 mm and an inner circumference of 94.2 mm at 23 °C, thus exceeding the dimensions of both the brownish vial (outer ø of 27 mm and circumference of 86.4 mm) and the transparent vial (outer ø of 25 mm and circumference of 78.5 mm). As a result, the cylinders were able to slide over both vials. When raising the temperature to 62 °C, the PEU shrank and initiated the gripping. At this temperature, the degree of shrinkage was so pronounced that a lifting of each vial became possible. Cooling to 23 °C expanded the cylindrical elements, so that the vials could be released. The overall process was repeated ten times for both cases, thus demonstrating the reliable functionality of the actuators. It is obvious that a different bidirectional actuation behavior has been demonstrated than for the other actuator

elements (**Figure 6.11**). The reasons are that the actuators were not fixed at the beginning of the experiment and that the printing paths were different. Obviously selecting a circular printing path as done for 2W 4D-printing of the cylinders favored a more uniform distribution of internal stresses and thus a more homogenous shrinkage and expansion behavior of printed objects. Thus, the path of strand deposition can be understood as another key element to gain control over thermoresponsiveness of 2W 4D-printed objects. In a final experiment, the vials could be gripped one after the other with an actuator, which makes it clear that the actuator is even capable of adapting to different shapes.

6.3. Conclusions

Here we introduce a 2W 4D-printing approach based on FFF to obtain thermoresponsive actuators from an in-house synthesized PEU. The actuation could be attributed to the phenomena of melting-induced contraction and crystallization-induced elongation of the PEU's switching segment as supported by internal stresses implemented in the course of additive manufacturing. Beyond a 1W 4D effect, actuation could be witnessed under different conditions. The movements of the polymer followed a program in terms of shrinkage on heating and expansion on cooling under the clamped, but almost stress-free conditions of samples in the DMA. Similarly, straightening and contraction on heating and expansion and bending on cooling in the clamped situation of an artificial butterfly were witnessed. Following the concept of a gripper, contraction in the sense of circular shrinkage on heating and circular expansion corresponding to a widening on cooling could be achieved. All this makes it clear that the material behavior in the actuation depends on the prevailing test conditions or installation situation as well as on the sample geometry and the printing paths during additive manufacturing. Having this in mind, the introduced technology may pave the way for the production of actuators that enable even more complex system functionalities when taking into account design-related boundary conditions.

Most importantly, the introduced 2W 4D-printing approach may save time and costs when considering scenarios, where minor changes in sample size are desired. The reason is that a thermomechanical treatment of a shape memory polymer is no longer needed. Provided that no severe degradation has occurred, the thermoplastic nature of the PEU implies that even a mechanical recycling is possible at the end-of-life.

In the future, the printing technology can contribute to qualify programmable materials for new applications. In perspective, FFF printing of fiber-reinforced polymers can even expand the existing potentials, as this creates possibilities for the local heating of polymers including complex motion and in addition control over mechanical properties.[59-62] All this can further strengthen the potential of programmable materials and the underlying manufacturing technology.

6.4. Experimental Section

Materials: 1,10-Decanediol, 4,4'-methylene diphenyl diisocyanate (4,4'-MDI), and titanium(IV) isopropoxide (TTIP) were purchased from Fisher Scientific (Schwerte, Germany). For titration tests, acetic anhydride, methanol, and potassium hydroxide solution in methanol with concentrations of 0.5 mol^{-1} and 0.1 mol^{-1} were purchased from Merck (Darmstadt, Germany). N-Methyl-2-pyrrolidone (2-NMP), chloroform, and 4-dimethylaminopyridine (4-DMAP) were bought from Carl Roth (Karlsruhe, Germany). Adipic acid, 1,4-butanediol, and a molecular sieve (4 Å) were obtained from Alfa Aesar (Kandel, Germany).

Synthesis of polyester diol: 1,10-Decanediol and adipic acid were mixed at a molar ratio of 1.1:1 and heated in a three-necked round-bottomed flask, which was equipped with a mechanical stirrer, nitrogen gas inlet, and distillation condenser. All reactants were molten at about 150 °C while titanium(IV) isopropoxide was added under stirring. Adjacently, the mixture was heated to 190 °C. After a remarkable decrease in distillation temperature, the mixture was further heated to 210 °C, whereupon the pressure was reduced to approximately 20 mbar. After two hours of continuous stirring, the melt was poured into a can. The obtained poly(1,10-decylene adipate) diol (PDA) solidified and was analyzed prior to the synthesis of PEU.

Titration: Titration was used to determine both the acid value and hydroxyl value and thus the number average molecular weight M_n of PDA. Therefore, a TitroLine 7000 from SI Analytics (Mainz, Germany) was employed. The procedure was executed in compliance with DIN EN ISO 2114[63] and DIN EN ISO 4629-2.[64] To determine the acid value, a sample of PDA was dissolved in a mixture of chloroform/methanol with a volume ratio of 5:1. The solution was titrated against a potassium hydroxide solution in methanol, having a concentration of 0.1 mol^{-1}. For the determination of the hydroxyl value, another sample of PDA was dissolved in chloroform. After adding acetic anhydride diluted in 2-NMP as well as 4-DMAP diluted in 2-NMP, the solution was heated and kept under stirring at 60 °C for 15 min. Thereafter, deionized water was added. After 12 min, the sample solution was titrated against a potassium hydroxide solution in methanol, having a concentration of 0.5 mol^{-1}.

Synthesis of polyester urethane (PEU): A PEU was synthesized using the prepolymer method. In order to obtain a PDA-based PEU with approximately 15% of hard segment content, the molar ratio of the reactants was set to 1:1.98:0.97 with regard to PDA, 4,4'-MDI, and 1,4-butanediol, respectively. The reaction was carried out with a slight excess of isocyanate (NCO/OH = 1.005). Overnight, PDA was dried in a glass reactor in a vacuum oven at 90 °C. The following day, it was heated under nitrogen flow and stirred to 120 °C. Adjacently, isocyanate was added, and the mixture was continuously stirred for 90 min. The obtained prepolymer was directly converted to PEU by adding 1,4-butanediol, serving as a chain extender. In parallel, the stirring speed was raised. As the viscosity increased significantly, the reaction was stopped, and the polymer melt was poured onto a plate covered with polytetrafluoroethylene. Finally, the PDA-based PEU was cured in an oven for 120 min at 80 °C.

Extrusion: The synthesized PEU was ground with a cutting mill type M 50/80 from Hellweg Maschinenbau (Roetgen, Germany). The obtained flakes were dried at 110 °C for 150 min in a vacuum drying chamber VDL 53 from Binder GmbH (Tuttlingen, Germany). Subsequently, the flakes were fed into an extrusion line to produce filaments. The same extrusion line as previously used was employed in this work.[6, 8, 32] The individual units of the extrusion line were put together in such a way that it included the volumetric material feeding system Color-exact 1000 from Plastic Recycling Machinery (Tranekær, Denmark), a Leistritz twin screw extruder MICRO 18 GL from Leistritz AG (Nürnberg, Germany), characterized by seven heating zones and a screw length of 600 mm, a conveyor belt, and a filament winder from Brabender GmbH and Co. KG (Duisburg, Germany). The temperatures of the individual heating zones of the extruder were 170, 175, 180, 185, 195, 190, and 190 °C. To evaluate the quality of the filaments, the evolution in diameter was manually detected at regular intervals using a vernier caliper from Fowler High Precision (Newton, MA, USA).

Virtual design and fused filament fabrication: The AutoCAD from Autodesk, Inc. (San Rafael, CA, USA) was used for the virtual construction of 3D models, like cuboid sample with dimensions 40 mm × 2 mm × 2 mm and a hollow cylinder with an outer diameter of 30 mm, a height of 20 mm and a thickness of 1 mm. The developed CAD models were then exported as standard triangle language (STL) files and later used for slicing. After finalizing the designs, Cura 3.6.1[65] was used as a slicer program to generate numerically controlled codes, also denoted as G-codes. The 3D models were imported into the slicer program and were sliced into layers according to the predefined printing parameters (**Table 6.1**). The most relevant settings for 3D-printing and 2W 4D-printing via fused filament fabrication (FFF) are listed in **Table 6.1**. To start additive manufacturing, the generated G-codes were transferred to the 3D-printer. All printed objects were produced by FFF using the commercially available 3D-printer Ultimaker three from Ultimaker B.V. (Utrecht, The Netherlands). In the case of 2W 4D-printing with the PDA-based PEU, the air chiller system from TA Instruments (New Castle, DE, USA) featuring a multi-stage cascading compressor system was used to generate a cold stream of compressed nitrogen, which was brought to the print head of the 3D-printer using a Teflon tube, as shown in **Figure 6.2**. For 2W 4D-printing, the air chiller system was connected to a nitrogen gas system of the house, and the pressure was regulated to 1.5 bar. Additionally, the 3D-printer was equipped with a top cover and a door to restrict the escape of cold air.

Table 6.1. Selected printing equipment and parameters for additive manufacturing of objects from PDA-based PEU using 3D- and 2W 4D-printing

Printing parameters	3D-printing	4D-printing
Diameter of the nozzle (µm)	400	400
Temperature of the nozzle (T_N, °C)	208	170
Speed of print head (S_P, mm × s^{-1})	8	8
Nitrogen stream temperature (T_S,°C)	75	–5
Layer height (mm)	0.1	0.1

In-situ thermal imaging: In situ thermal imaging was applied during FFF using a Variocam HD from InfraTec GmbH (Dresden, Germany) to study the temperature distribution in freshly deposited polymer strands at five different measurement points (**Table 6.1**). In course of additive manufacturing the thermal images were recorded with a frequency of 15 Hz and evaluated with the software IRBIS 3.1[66] from InfraTec GmbH.

Characterization of thermal properties: The PEU was investigated with regard to the phase transition behavior of PDA by differential scanning calorimetry (DSC) using a Q100 DSC from TA Instruments (New Castle, DE, USA). The measurement was conducted on a freshly synthesized sample with a weight of 5 mg. The sample was thermally cycled between −70 and 100 °C. For cooling and heating, a rate of 10 °C x min^{-1} was applied. The temperature holding time at the minimum and maximum temperature was 2 min.

Characterization of thermomechanical properties: The thermomechanical properties of the PEU were studied by dynamic mechanical analysis (DMA). The experiments were carried out with a Q800 DMA from TA Instruments (New Castle, DE, USA) using film tension clamps on multi-frequency–strain mode. A frequency of 10 Hz, a static force of 0.1 N and an oscillating amplitude of 10 µm were selected to investigate the center part of a 3D-printed additively manufactured cuboid with dimensions of 40 mm × 2 mm × 2 mm (**Table 6.1**). At first, the sample was cooled to −80 °C and held there for 5 min, before it was heated to 100 °C with a rate of 3 °C x min^{-1}. In parallel, the evolution in storage modulus E' and loss factor tan δ was determined.

Characterization of actuation under stress-free conditions: The actuation of 2W 4D-printed cuboid samples made from PDA-based PEU (**Table 6.1**) was studied by means of DMA immediately after additive manufacturing. Against this background, a first test series was run, in which the maximum temperature T_{max} was systematically varied, and a constant minimum temperature T_{min} of 15 °C was selected. First, the sample was clamped with a distance of 20 mm in the holders of the DMA and a weak load of 0.001 N was applied, so that almost stress-free conditions prevailed. Adjacently, the sample was heated from 23 °C to T_{max} = 56 °C and held there for 15 min, before it was cooled to 15 °C, at which the temperature was kept for another 15 min. Heating and cooling were carried out three times. Afterwards, the three cycles were repeated for different temperatures T_{max} of 58, 60, 62, and 64 °C. Heating and cooling rates of 5 °C x min^{-1} were selected in all experiments conducted.

In a durability experiment, a cuboid sample of 4D-printed PDA-based PEU **(Figure 6.4a** and **Table 6.1**) was studied in the DMA under a weak load of 0.001 N by cycling the temperature between 15 and 62 °C. In the measurement, heating and cooling rates of 5 °C x min^{-1} were used. This time, actuation was investigated in 100 thermal cycles.

The thermoreversible strain ε_{rev} is the key parameter when studying the actuation of polymers. It can be defined according to **Equation 6.1**:

$$\varepsilon_{rev}(N) = \frac{l_{Tlow}(N) - l_{Tmax}(N)}{l_{Tmax}(N)} \times 100\% \qquad (6.1)$$

Herein, l_{Tlow} (N) and l_{Tmax} (N) are the lengths of the sample in the N^{th} cycle of actuation at the respective temperatures T_{low} and T_{max}.

In a temperature resistance measurement, a cuboid sample of 2W 4D-printed PDA-based PEU (**Figure 6.4a** and **Table 6.1**) was clamped in the DMA and heated to 62 °C with at a rate of 5 °C x min^{-1}. Adjacently, the temperature was held constant for 4200 min while the evolution of strain was recorded under stress-free conditions.

Demonstrator development: The actuation of a sample made from a 2W 4D-printed PDA-based PEU was examined with an MTS Criterion universal testing machine (UTM) (model 43) from MTS Systems Corporation (Eden Prairie, MN, USA). The device was operated with a temperature chamber, which was controlled by a Eurotherm temperature controller unit. Two heating elements were located at the back of the chamber. Liquid nitrogen from a Dewar's vessel was fed into the chamber under a pressure of 1.3 bar as an essential prerequisite for cooling. At first, the 2W 4D-printed hollow cylinder with an outer diameter of 30 mm, a height of 20 mm, and a thickness of 1 mm, was glued to a bar made of poly(methyl methacrylate) with dimensions 40 mm × 20 mm. The other end of the bar was then attached to an L-shaped bracket, and the bracket was attached to the top clamp of the UTM. To better visualize actuation, a brownish and a colorless bottle of which the latter was filled with a red liquid were placed on a platform, which was lined with centimeter paper. While, in the case of the artificial butterfly, individual parts were first laser cut using Epilog Zing 16 laser Engraver 30 W with suction exhaust from Epilog Laser United Kingdom (Kenn, Clevedon, United Kingdom). The parts and 2W 4D-printed cuboid PDA-based PEU samples (**Table 6.1**) were then assembled. Afterwards, the temperature was cycled in between 23 and 62 °C with heating and cooling rates of 10 °C x min^{-1}.

Supporting Information: Supporting Information is available from the Wiley Online Library or from the author.

Acknowledgements: This work was supported by the Fraunhofer Cluster of Excellence “Programmable Materials” under project PSP elements 40-01922-2500-00002 and 40-03420-2500-00003. The working group of Fraunhofer IAP wishes to thank the European Regional Development Fund for financing a large part of the laboratory equipment (project 85007031) and the Fraunhofer High-Performance Center “Integration of Biological and Physical-Chemical Material Functions” in Potsdam-Golm for the funding of some of the FFF printers (project 630505). Tobias Rümmler is kindly acknowledged for crafting the artificial butterfly and supporting DC during demonstrator filming.

Conflict of Interest: There are no conflicts to declare.

Data Availability Statement: The data that support the findings of this study are available from the corresponding author upon reasonable request.

Received: March 25, 2022; Revised: May 23, 2022
Published online: (First published: 13 July 2022)

6.5. References

1 Liu, C., Qin, H., and Mather, P.T., *J. Mater. Chem.*, Vol. 17, 1543, 2007.
2 Dietsch, B., and Tong, T.H., *J Adv Mater*, Vol. 39, 3–12, 2007.
3 Ratna, D., and Karger-Kocsis, J., *J Mater Sci*, Vol. 43, 254–269, 2008.
4 Pretsch, T., *Polymers*, Vol. 2, 120–158, 2010.
5 L. Sun, W.M. Huang, Z. Ding, Y. Zhao, C.C. Wang, H. Purnawali, and C. Tang, *Materials & Design*, Vol. 33, 577–640, 2012.
6 Chalissery, D., Pretsch, T., Staub, S., and Andrä, H., *Polymers*, Vol. 11, 1005, 2019.
7 Holme, *The Philosophical Magazine*, Vol. 24, 39–43, 1806.
8 Chalissery, D., Schönfeld, D., Walter, M., Shklyar, I., Andrae, H., Schwörer, C., Amann, T., Weisheit, L., and Pretsch, T., *Macromol Mater Eng*, Vol. 307, 2100619, 2022.
9 Hu, G.F., Damanpack, A.R., Bodaghi, M., and Liao, W.H., *Smart Mater. Struct.*, Vol. 26, 125023, 2017.
10 Bodaghi, M., Damanpack, A.R., and Liao, W.H., *Materials & Design*, Vol. 135, 26–36, 2017.
11 Bodaghi, M., Damanpack, A.R., and Liao, W.H., *Smart Mater. Struct.*, Vol. 27, 65010, 2018.
12 Zhang, Q., Yan, D., Zhang, K., and Hu, G., *Sci Rep*, Vol. 5, 8936, 2015.
13 Rajkumar, A.R., and Shanmugam, K., *J. Mater. Res.*, Vol. 33, 4362–4376, 2018.
14 van Manen, T., Janbaz, S., and Zadpoor, A.A., *Mater. Horiz.*, Vol. 4, 1064–1069, 2017.
15 Noroozi, R., Bodaghi, M., Jafari, H., Zolfagharian, A., and Fotouhi, M., *Polymers*, Vol. 12, 519, 2020.
16 Bodaghi, M., Noroozi, R., Zolfagharian, A., Fotouhi, M., and Norouzi, S., *Materials (Basel, Switzerland)*, Vol. 12, 1353, 2019.
17 Sun, L., Wang, T.X., Chen, H.M., Salvekar, A.V., Naveen, B.S., Xu, Q., Weng, Y., Guo, X., Chen, Y., and Huang, W.M., *Polymers*, Vol. 11, 1049, 2019.
18 Xia, Y., He, Y., Zhang, F., Liu, Y., and Leng, J., *Adv. Mater.*, Vol. 33, e2000713, 2021.
19 Scalet, G., *Actuators*, Vol. 9, 10, 2020.
20 Zhao, Q., Qi, H.J., and Xie, T., *Progress in Polymer Science*, Vol. 49-50, 79–120, 2015.
21 Westbrook, K.K., Mather, P.T., Parakh, V., Dunn, M.L., Ge, Q., Lee, B.M., and Qi, H.J., *Smart Mater. Struct.*, Vol. 20, 65010, 2011.
22 Chung, T., Romo-Uribe, A., and Mather, P.T., *Macromolecules*, Vol. 41, 184–192, 2008.
23 Li, J., Rodgers, W.R., and Xie, T., *Polymer*, Vol. 52, 5320–5325, 2011.
24 Pandini, S., Passera, S., Messori, M., Paderni, K., Toselli, M., Gianoncelli, A., Bontempi, E., and Riccò, T., *Polymer*, Vol. 53, 1915–1924, 2012.
25 Posada-Murcia, A., Uribe-Gomez, J.M., Förster, S., Sommer, J.-U., Dulle, M., and Ionov, L., *Macromolecules*, Vol. 55, 1680–1689, 2022.
26 Raquez, J.-M., Vanderstappen, S., Meyer, F., Verge, P., Alexandre, M., Thomassin, J.-M., Jérôme, C., and Dubois, P., *Chemistry (Weinheim an der Bergstrasse, Germany)*, Vol. 17, 10135–10143, 2011.
27 Bothe, M., and Pretsch, T., *Macromol. Chem. Phys.*, Vol. 213, 2378–2385, 2012.
28 Behl, M., Zotzmann, J., and Lendlein, A., *The International journal of artificial organs*, Vol. 34, 231–237, 2011.
29 Baker, R.M., Henderson, J.H., and Mather, P.T., *Journal of materials chemistry. B*, Vol. 1, 4916–4920, 2013.
30 Walter, M., Friess, F., Krus, M., Zolanvari, S.M.H., Grün, G., Kröber, H., and Pretsch, T., *Polymers*, Vol. 12, 1914, 2020.
31 Bothe, M., and Pretsch, T., *J. Mater. Chem. A*, Vol. 1, 14491–14497, 2013.
32 Schönfeld, D., Chalissery, D., Wenz, F., Specht, M., Eberl, C., and Pretsch, T., *Molecules (Basel, Switzerland)*, Vol. 26, 522, 2021.
33 Behl, M., Kratz, K., Noechel, U., Sauter, T., and Lendlein, A., *PNAS*, Vol. 110, 12555–12559, 2013.
34 Meng, Y., Jiang, J., and Anthamatten, M., *ACS Macro Lett.*, Vol. 4, 115–118, 2015.
35 Lee, A.Y., An, J., and Chua, C.K., *Engineering*, Vol. 3, 663–674, 2017.
36 Ke, D., Chen, Z., Momo, Z.Y., Jiani, W., Xuan, C., Xiaojie, Y., and Xueliang, X., *Smart Mater. Struct.*, Vol. 29, 23001, 2020.
37 Zhu, P., Yang, W., Wang, R., Gao, S., Li, B., and Li, Q., *ACS applied materials & interfaces*, Vol. 10, 36435–36442, 2018.
38 Kokkinis, D., Schaffner, M., and Studart, A.R., *Nature communications*, Vol. 6, 8643, 2015.
39 Kim, Y., Yuk, H., Zhao, R., Chester, S.A., and Zhao, X., *Nature*, Vol. 558, 274–279, 2018.
40 Xu, T., Zhang, J., Salehizadeh, M., Onaizah, O., and Diller, E., *Science robotics*, Vol. 4, 2019.

41 Mao, Y., Ding, Z., Yuan, C., Ai, S., Isakov, M., Wu, J., Wang, T., Dunn, M.L., and Qi, H.J., *Sci Rep*, Vol. 6, 24761, 2016.
42 Yuan, C., Roach, D.J., Dunn, C.K., Mu, Q., Kuang, X., Yakacki, C.M., Wang, T.J., Yu, K., and Qi, H.J., *Soft Matter*, Vol. 13, 5558–5568, 2017.
43 Shafranek, R.T., Millik, S.C., Smith, P.T., Lee, C.-U., Boydston, A.J., and Nelson, A., *Progress in Polymer Science*, Vol. 93, 36–67, 2019.
44 Momeni, F., and Ni, J., *Renewable Energy*, Vol. 122, 35–44, 2018.
45 Rastogi, P., and Kandasubramanian, B., *Chemical Engineering Journal*, Vol. 366, 264–304, 2019.
46 Baker, A.B., Bates, S.R.G., Llewellyn-Jones, T.M., Valori, L.P.B., Dicker, M.P.M., and Trask, R.S., *Materials & Design*, Vol. 163, 107544, 2019.
47 Zhang, H., Guo, X., Wu, J., Fang, D., and Zhang, Y., *Science advances*, Vol. 4, eaar8535, 2018.
48 Fischer, S.C.L., Hillen, L., and Eberl, C., *Materials (Basel, Switzerland)*, Vol. 13, 2020.
49 Jin, L., Forte, A.E., Deng, B., Rafsanjani, A., and Bertoldi, K., *Advanced materials (Deerfield Beach, Fla.)*, Vol. 32, e2001863, 2020.
50 Berwind, M.F., Kamas, A., and Eberl, C., *Adv. Eng. Mater.*, Vol. 20, 1800771, 2018.
51 Restrepo, D., Mankame, N.D., and Zavattieri, P.D., *International Journal of Solids and Structures*, Vol. 100-101, 485–504, 2016.
52 Specht, M., Berwind, M., and Eberl, C., *Adv. Eng. Mater.*, Vol. 23, 2001037, 2021.
53 Zhang, X., Pint, C.L., Lee, M.H., Schubert, B.E., Jamshidi, A., Takei, K., Ko, H., Gillies, A., Bardhan, R., Urban, J.J., Wu, M., Fearing, R., and Javey, A., *Nano letters*, Vol. 11, 3239–3244, 2011.
54 Fritzsche, N., and Pretsch, T., *Macromolecules*, Vol. 47, 5952–5959, 2014.
55 Rocco, J.A.F.F., Lima, J.E.S., Lourenço, V.L., Batista, N.L., Botelho, E.C., and Iha, K., *J. Appl. Polym. Sci.*, Vol. 126, 1461–1467, 2012.
56 Li, J., Kan, Q., Chen, K., Liang, Z., and Kang, G., *Polymers*, Vol. 11, 2019.
57 Lu, L., Cao, J., and Li, G., *Sci Rep*, Vol. 8, 14233, 2018.
58 Official Adobe Photoshop | Photo and design software, https://www.adobe.com/products/photoshop.html.
59 Ibrahim, Y., and Kempers, R., *Prog Addit Manuf*, 2022.
60 Y. Ibrahim, *3D Printing of Continuous Wire Polymer Composite for Mechanical and Thermal Applications.*, 2019.
61 Ziervogel, F., Boxberger, L., Bucht, A., and Drossel, W.-G., *IEEE Access*, Vol. 9, 43036–43049, 2021.
62 M. Saari, *Design and Control of Fiber Encapsulation Additive Manufacturing*, 2019.
63 DIN EN ISO 2114 - 2002-06 - Beuth.de, https://www.beuth.de/de/norm/din-en-iso-2114/34241036.
64 DIN EN ISO 4629-2 - 2016-12 - Beuth.de, https://www.beuth.de/de/norm/din-en-iso-4629-2/247719817.
65 Ultimaker Cura: Powerful, easy-to-use 3D printing software, https://ultimaker.com/software/ultimaker-cura.
66 IRBIS 3 Analysis Software, https://www.infratec.eu/thermography/thermographic-software/irbis3/.

Chapter 7:
Discussion

Chapter 7: Discussion

Before the beginning of this doctoral work in 2017, there were only a few scientific research works on fused filament fabrication (FFF) with thermoplastic polyurethanes (TPU) with shape memory properties [1–4]. This doctoral thesis focuses on processing TPU-based shape memory polymer (SMP) with commercially available FFF machines to reduce the complexity of additive manufacturing (AM) and ease the slicing of three-dimensional (3D) models using standard slicer software. The primary goal of this doctoral study is to utilize FFF 3D printers to manufacture TPU-SMP objects. For exhibiting shape memory properties on thermomechanical treatment ("*ex-situ*" programming) or even as a result of printing ("*in-situ*" programming).

In 2012, Pretsch and his group introduced quick response (QR) code carriers made from TPU with shape memory properties, which can be both employed as anti-counterfeiting technology [5] and for supervising cold chains [6]. However, the production of information carriers was labor-intensive, where, at first, the TPU-SMP plaques were produced using an injection molding technique. Surface-specific coloration via "guest diffusion" and engraving of two-dimensional computer-generated codes onto the surface of the polymer [5], or – as later introduced – applying coating and code engraving on the surface, punching or laser cutting [7,8]. In the first part of the doctoral study, information carriers using the QR code technique are manufactured via FFF from a dyed and a non-dyed TPU-SMP to establish a new production route [9]. The developed manufacturing process eases production and allows exchanging of QR codes with less effort. Since the codes can be easily imported into the slicer software, rapid prototyping is only associated with little effort. An essential understanding extracted from this approach is that using a 100 µm nozzle qualifies to manufacture information carriers with higher print quality in 25 min. Here, on employing a 100 µm nozzle, one of the small cuboidal elevations of the QR code was characterized using a microscope and found to have exceeded the virtual 3D model by just 40 µm, thereby revealing the high print resolution and less dimensional tolerance. On the other hand, using a 400 µm nozzle for FFF printing shows slightly compromised print quality. However, it permits to finalization of the manufacturing of machine-readable information carriers in 11 min and 30 s.

Furthermore, by reducing the substrate height of the information carriers from 180 µm to 9 µm, it is possible to significantly reduce the weight of the QR code from 340 mg to about 100 mg, which qualifies the manufacturing of lightweight QR codes. Most importantly, the shape memory properties of the QR codes reveal that the information carriers are durable and can be bent or rolled in a thermomechanical treatment step in contrast to the classical programming method, which includes tensile deformation, compressive deformation, or indentation [10]. In any case, the QR codes may recover their permanent shape in less than 10 s, proving the high sensitivity toward heating, primarily achieved using a thinner base substrate. The development presented here may be considered the first step toward mass production as this may reduce material costs, manufacturing time, and logistics costs. The

work also compares the build rate versus layer thickness of different AM techniques like fused filament fabrication (FFF), stereolithography (SLA), big area additive manufacturing (BAAM), multi-jet fusion (MJF), and selective laser sintering (SLS). Here it becomes clear that even though FFF has lower build rates than other AM methods, the FFF technique can control the layer thickness over a wide range, achieving the lowest value for Z (layer thickness) [11]. The excellent print resolution presented via FFF is also superior to the results from other working groups using extrusion-based AM techniques to process TPU with shape memory properties [1–4,12–15]. This good print quality was achieved primarily from the precise selection of printing parameters in the slicer software, such as lower printing speed and lower nozzle temperature, along with a smaller nozzle opening (100 µm). The extruded polymer strand could be precisely controlled during deposition with minor errors and stringing.

In a different approach, efforts are taken to control the printing pattern of objects made from TPU-SMP to understand how print-orientation in semicrystalline polyester urethanes (PEUs) affects the mechanical and shape memory properties. The study was conducted because few scientific publications have previously studied the influence of printing patterns of SMP 3D models manufactured via FFF. The studies were primarily carried out on amorphous SMPs [12,16]. Here, it was unknown how semicrystalline SMP properties vary using different printing patterns. Specifically when applying a tensile strain during thermomechanical treatment. This work observed that injection-molded tensile bars exhibit superior mechanical properties compared to 3D-printed samples [17–19]. Most importantly, the properties of the semicrystalline PEU are analogous to other thermoplastics, which are processed via FFF in horizontal and vertical orientations. The ultimate tensile strength was highest when the tensile strain acted parallel to the print orientation [18]. The other FFF thermoplastic materials that were used to perform similar studies are acrylonitrile butadiene styrene (ABS) [20,21], ABS-carbon nanotubes composite [22], polycarbonate-ABS blends [19], polypropylene [17,23,24], and polyethylene glycol diamines [25]. Astonishingly, the characterization reveals that the recovery strain remains unaffected for print orientation patterns or injection molded tensile bars. Nevertheless, when measuring the recovery stresses during the triggering of the shape memory effect (SME) under constant strain conditions, the injection-molded sample shows the highest recovery stress, followed by the horizontally printed and then vertically printed FFF-PEU sample. Comparing the results of the work to other scientific contributions, the evolution in recovery stresses is in line with the one verified by Villacres et al. [16], where it is deduced that the recovery stress and tensile strength are the highest once the load direction is parallel to the strand orientation for both semicrystalline and amorphous materials [18]. In this way, the print orientation of AM objects can be locally controlled to set the mechanical and shape memory properties. Without the need to restart the material or product development from the polymer synthesis or add additives during processing.

The ability to print high-resolution small cuboidal elevations as part of the QR codes atop a thin film of PEU using a 100 µm nozzle in the first part of the study (**Chapter 3.1**) has directly opened up the bridge to fabricate filigree structures of TPU-SMP with FFF. Here, exploring the

lowest printing limits of manufacturing filigree structures is of scientific interest to enable the manufacturing of miniature objects in high resolution using FFF. For this, Arial fonts of the letter “A” in sizes 3, 4, and 10 are printed using FFF with differently colored TPU-based SMP filaments. Closely studying the print quality under a microscope reveals the high-quality printability of filigree structures. The Arial font “A” in size three exceeded the longitudinal and transverse dimension of about 100 µm compared to its virtual design. It is also apparent at this point that the miniature printing exceeds the print resolution of the previous extrusion-based AM contributions [1–4,11–15], which was again attained due to the careful selection of printing parameters and printing setups, as explained earlier. Further, the Arial font size ten is used to print texts that can be read with the naked eye. The developed SMP letters have application potential as privacy etiquettes, security labels, text-based cold chain indicators, information carriers, admission tickets, or entry tickets. Additionally, smart keyboard keys were developed, where the fonts on the keys can change their shape and height from a non-legible to readable form when triggering the SME. The shape memory keyboard keys may be employed in bilingual keyboards such as Braille and QWERTY layouts.

Shape memory gears are one further example of filigree printing. They can activate or deactivate transmission systems on demand. This application of SMP has potential applicability in mechanical and automotive industries, where an overheating of a system can be prevented by triggering the shape memory effect and thus disconnecting the transmission. In turn, activating a transmission system can regulate the flow of fluids, e.g., in the coffee industry or biomedical applications.

The second part of the doctoral work focuses on four-dimensional (4D)-printing, where internal stresses are implemented in SMPs during AM to manufacture thermoresponsive objects [26–28]. The key benefit of this functional integration is that the objects do not require additional thermomechanical treatment. Thus, it is a crucial step to reduce the effort required to produce thermoresponsive objects. The concept of 4D-printing was introduced in a TED talk in 2013 by Skylar Tibbits on multi-material printing using a poly jet printer [29,30]. Later, 4D-printing was realized via FFF with a single material [26–28,31–37]. Until the first half of 2021, researchers focused on implementing thermoresponsiveness in objects with smaller layer heights ($z < 5$ mm), where the degree of shrinkage gets weaker from layer to layer [26,28,32,33,36,37]. Furthermore, there were only a few contributions to 4D-printing utilizing TPU-based SMP as functional base material [28].

This work aims at investigating new materials suitable for 4D-printing. In the first step, a novel polypropylene glycol (PPG)-based polyether urethane is investigated as 4D-printing material. Here, the work reveals that using a lower nozzle temperature and keeping the difference between the nozzle and glass transition temperature of the TPU-SMP to its minimum can effectively store internal stresses and supports strong “4D effects” in the sense of sample shrinkage upon heating. This allowed us to deduce the key for 4D-printing to avoid bending and enable uniform shrinkage, allowing us to build larger objects up to 32 mm on the z-axis without compromising the 4D shrinkage effect. From a processing point of view, it is advantageous when the glass transition temperature of the printing material exceeds

ambient temperature, which helps to store more significant internal stresses. The work further advances by demonstrating one of the highest 4D shrinkage effects achieved with FFF for a rectangular cuboid with a height and width of 2 mm and length of 40 mm, for which a strain shrinkage of about 63% is witnessed [26–28,31–37]. One of the successes of the work is transferring the know-how of 4D-printing to other materials like polylactic acid (PLA), where the ability to store maximum "4D effects" allowed to achieve the strongest 4D-shrinkage behavior, among other contributions [32,37,38]. Transferring the results to more complex objects is proven for a hollow cylinder and solid- and hollow cuboids with a total height of 32 mm. Finally, heat-shrinkable hands-free door openers are developed, whose design follows a lightweight construction and allows optimum distribution of stresses upon loading. The respective dimensions in the x-,y-, and z-axis are 105 mm × 18 mm × 30 mm and were able to change to about 55 mm × 9 mm × 48 mm after heating to 75 °C and thereby triggering the 4D effect. The uniform 4D shrinkage effect may help researchers develop new thermoresponsive products of even larger sizes. The design freedom of the thermoresponsiveness indicates that it will not always be necessary to change the material composition to address innovations in the field of 4D-printing. The 4D-printing technique is then used to develop demonstrators for active assembly that is directly programmed during the printing process. The active assembly concept was first introduced by Chiodo et al. in 1999 [39]. This way, active thermoresponsive fixtures, closures, connecting elements, and grippers can be produced without requiring further programming step.

Additionally, the proof-of-concept for active disassembly and end-of-life technologies is also shown, in which the separation of two and three-component systems is facilitated. The objects are capable of self-disassembling upon heating. The active assembly and disassembly of parts have application potential in parts for furniture or construction, manufacturing or production industries, or even inside space stations, space habitats, or environments where the human body has restricted access. For space habitats and technologies, it would be necessary to meet space material requirements by adjusting the material formulation as it is a preliminary requirement of materials to be used for space applications. Another application is an active-deactivating gear. Once the ambient temperature exceeds a critical value, power transmission can be switched off, thus interrupting the transmission system to reduce the risk of damaging any components or neighboring electronics. Such systems may be implemented in industrial safety systems to avoid overheating. Later, replacing the 4D-printed object with a new gear after reprocessing or reprogramming is a prerequisite to entering the next life cycle. Finally, the 4D-printing technique is used to develop programming tools for the thermomechanical treatment of other SMPs. The 4D-printed tools can also be used with foam to grip or hold objects during transport.

The objects programmed via classical one-way (1W) programming ("*ex-situ*") or 4D-printing ("*in-situ*") always require reprogramming or reprocessing to make them thermoresponsive again. To enable switching between two metastable states, scientists and researchers have learned how to attain with semicrystalline SMPs, where the shapes can be reversibly switched as often as desired by varying the stimuli. The so-called two-way (2W)

SME was first observed in 2008 for cross-linked poly(cyclooctene) films in the presence of an external load by Chung et al. [40]. The programming technology was later transferred to other polymer systems, so actuation in the stress-free state became possible [41–47]. Although scientists could transfer the 2W-SME to physically cross-linked TPU with shape memory properties under constant strain and stress-free conditions, their overall thermoreversible actuation was lower than their chemically cross-linked counterparts [41,48–52].

Additionally, SMPs were employed in soft robotics to demonstrate the thermoreversible actuation of grippers [53–56]. Although the contributions presented triggering of the 2W-SME could grab or lift smaller objects like screws and nuts [57], the scalability of the 2W-SME to transport larger seized objects remained unknown. Furthermore, it was unclear how to amplify the effect and combinate 2W-programmed SMP with other polymers to develop programmable materials. These points are addressed in the third part of this doctoral work using an in-house synthesized poly(1,10-decylene adipate) diol (PDA) based polyester urethane. After identifying a suitable programming method, a novel characterization technique is developed to identify the ideal actuation temperatures for the 2W-SME at which a maximum actuation occurs. Here, stable shrinkage on heating and expansion on cooling, exemplified by averaged strain changes of about 16%, is verified for a thermomechanically pretreated TPU-SMP. Combining a TPU-based SMP actuator with a mechanical linkage system allows for magnifying the 2W-SME. For instance, in a soft robotic gripper system, the 2W-SME of an actuator can transfer and increase its motion sixteen-fold for the gripper arms, thus achieving an opening and closing of the arms to grab and release bigger and more complex objects. On the other hand, coupling the SMP actuator with an elastic unit cell leads to the developing of novel programmable materials. In this way, the 2W-SME is directly transferred to the unit cell to achieve a thermoreversible shape switch, accompanied by the opening and closing of a hole in the surface. Unit cells with thermally switchable openings can potentially enable a programmable heat transfer. The self-sufficient material behavior is desirable for applications that do not require a power supply, control technology, or similar.

However, these studies show that the actuation of physically cross-linked PEUs could achieve a maximum of only 21% [41,58–62], and a significant actuation can be extracted from the SMP only with the combination of a mechanical linkage [47]. It is essential to understand if an SMP-based programmable material structure can exhibit bidirectional actuation, in which non-linear and more complex motion sequences characterize the movements. For this, efforts are taken to develop a 2W programmable gear. Once programmed and characterized, the results revealed that a reversible change in length $\Delta L/L_0$ of about 45% could be achieved. Since the programming procedure includes compressional bending, the results cannot be compared with those of other contributions because the deformation in the programming course was realized by tensile stretching.

Furthermore, an actuating element is developed to ensure that the strong 2W-SME achieved with the gear can be transferred and achieved for another actuating element when programmed similarly. After thermomechanically treating the actuating element similar to the 2W programmable gear, almost similar actuation is detected by varying the temperature

between 23 °C and 58 °C. Excellent actuation is achieved due to the employment of programmable materials as actuating elements, where the external and molecular structures are synergetically utilized during actuation. At the same time, previously presented contributions focused only on the molecular structure for 2W-SME.

From the previous section of this work, it becomes apparent that SMPs require a complex thermomechanical treatment that includes time-, energy-, and cost-intensive steps. Here, the maturation of AM technology in recent years has led to the development of objects that actuate immediately after AM [63]. Up to 2022, the 2W-4D printing technique was attained either by using core-shell embedded structures or bilayer or gradient structures.[46] The core-shell embedded structures utilized the manufacturing of elastomeric material composites containing magnetic particles[64–67]. Under an external magnetic field, the material composite could change its shape controllably. Once the magnetic field was turned off, the original shape was recovered due to the elastomeric properties of the matrix material. In contrast, the bilayer or gradient structures were based on composite AM technology.[68–74], where composite layers were selected with antagonistic or reversible physical properties, e.g., associated with water absorption/desorption or temperature changes, to realize stimulus-governed shape changes. Nevertheless, the main drawback of such systems is the need for two entirely different stimuli, like water and heat. Moreover, the effort to recover and recycle individual materials at the end of their life cycle was very high. In short, there were no technological approaches for a single material system that exhibited bidirectional actuation immediately after AM. Motivated by this, the heart of the work is to develop a novel additive manufacturing technique for semicrystalline SMPs, which allows programming the 2W-SME using a single material. To pursue this, a TPU-SMP, which was built up from soft segments of poly(1,10-decylene adipate) diol (PDA) and hard segments of 4,4'-diphenylmethane diisocyanate (4,4'-MDI) and 1,4-butanediol (BD) were selected. For attaining 4D-printing and, thereby, functional integration. For this, an external cooling unit is combined with the lower nozzle temperature, allowing the SMP to store internal stresses in its oriented state. Modifying a standard printer with an external cooling air unit ensures the polymer quickly cools below its glass transition temperature, thereby achieving rapid vitrification of the switching segment. The work thereby shows one of the first attempts to 4D-print a bidirectionally actuating semicrystalline SMP utilizing FFF. After a temperature screening and extrapolating the ideal actuation temperature range for attaining the most pronounced 2W-SME, it is observed that the polymer can arbitrarily actuate between two shapes under stress-free conditions. This way, new generations of programmable materials or actuating elements can be manufactured without needing a subsequent thermomechanical treatment.

The work further shows an actuating hollow cylinder fabricated via the "*in-situ*" 2W-4D printing technique. After printing, the developed cylinder could contract and expand its circumference on heating and cooling. The actuation is strong enough to lift smooth surfaced objects and release them on demand. Such actuating elements can play a role in soft robotics, e.g., in grippers for transportation or even in smart etiquettes, which can actively assemble

or disassemble at the end of life. Assuming that the high material requirements in space technologies are met, the extent of actuation may be leveraged by specific mechanisms to qualify such systems for space-deployable structures.

References

1. Raasch, J.; Ivey, M.; Aldrich, D.; Nobes, D.S.; Ayranci, C. Characterization of polyurethane shape memory polymer processed by material extrusion additive manufacturing. *Additive Manufacturing* **2015**, *8*, 132–141, doi:10.1016/j.addma.2015.09.004.
2. Yang, Y.; Chen, Y.; Wei, Y.; Li, Y. 3D printing of shape memory polymer for functional part fabrication. *Int J Adv Manuf Technol* **2016**, *84*, 2079–2095, doi:10.1007/s00170-015-7843-2.
3. Hendrikson, W.J.; Rouwkema, J.; Clementi, F.; van Blitterswijk, C.A.; Farè, S.; Moroni, L. Towards 4D printed scaffolds for tissue engineering: exploiting 3D shape memory polymers to deliver time-controlled stimulus on cultured cells. *Biofabrication* **2017**, *9*, 31001, doi:10.1088/1758-5090/aa8114.
4. Monzón, M.D.; Paz, R.; Pei, E.; Ortega, F.; Suárez, L.A.; Ortega, Z.; Alemán, M.E.; Plucinski, T.; Clow, N. 4D printing: processability and measurement of recovery force in shape memory polymers. *Int J Adv Manuf Technol* **2017**, *89*, 1827–1836, doi:10.1007/s00170-016-9233-9.
5. Pretsch, T.; Ecker, M.; Schildhauer, M.; Maskos, M. Switchable information carriers based on shape memory polymer. *J. Mater. Chem.* **2012**, *22*, 7757, doi:10.1039/c2jm16204k.
6. Fritzsche, N.; Pretsch, T. Programming of Temperature-Memory Onsets in a Semicrystalline Polyurethane Elastomer. *Macromolecules* **2014**, *47*, 5952–5959, doi:10.1021/ma501171p.
7. Ecker, M.; Pretsch, T. Multifunctional poly(ester urethane) laminates with encoded information. *RSC Adv* **2014**, *4*, 286–292, doi:10.1039/C3RA45651J.
8. Ecker, M.; Pretsch, T. Novel design approaches for multifunctional information carriers. *RSC Adv* **2014**, *4*, 46680–46688, doi:10.1039/C4RA08977D.
9. Chalissery, D.; Pretsch, T.; Staub, S.; Andrä, H. Additive Manufacturing of Information Carriers Based on Shape Memory Polyester Urethane. *Polymers* **2019**, *11*, doi:10.3390/polym11061005.
10. Ecker, M.; Pretsch, T. Freely configurable Functionalization Tool for switchable Information Carriers. In *Materials challenges and testing for manufacturing, mobility, biomedical applications and climate*; Udomkichdecha, W., Böllinghaus, T., Manonukul, A., Lexow, J., Eds.; Springer: New York, 2014; pp 25–35, ISBN 978-3-319-11339-5.
11. Quinlan, H.E.; Hasan, T.; Jaddou, J.; Hart, A.J. Industrial and Consumer Uses of Additive Manufacturing: A Discussion of Capabilities, Trajectories, and Challenges. *Journal of Industrial Ecology* **2017**, *21*, S15-S20, doi:10.1111/jiec.12609.
12. Villacres, J.; Nobes, D.; Ayranci, C. Additive manufacturing of shape memory polymers: effects of print orientation and infill percentage on mechanical properties. *RPJ* **2018**, *24*, 744–751, doi:10.1108/RPJ-03-2017-0043.
13. Jung, Y.C.; Cho, J.W. Application of shape memory polyurethane in orthodontic. *J Mater Sci: Mater Med* **2010**, *21*, 2881–2886, doi:10.1007/s10856-008-3538-7.
14. Kashyap, D.; Kishore Kumar, P.; Kanagaraj, S. 4D printed porous radiopaque shape memory polyurethane for endovascular embolization. *Additive Manufacturing* **2018**, *24*, 687–695, doi:10.1016/j.addma.2018.04.009.
15. Berwind, M.F.; Kamas, A.; Eberl, C. A Hierarchical Programmable Mechanical Metamaterial Unit Cell Showing Metastable Shape Memory. *Adv. Eng. Mater.* **2018**, *20*, 1800771, doi:10.1002/adem.201800771.
16. Villacres, J.; Nobes, D.; Ayranci, C. Additive manufacturing of shape memory polymers: effects of print orientation and infill percentage on shape memory recovery properties. *RPJ* **2020**, *26*, 1593–1602, doi:10.1108/RPJ-09-2019-0239.
17. Saroia, J.; Wang, Y.; Wei, Q.; Lei, M.; Li, X.; Guo, Y.; Zhang, K. A review on 3D printed matrix polymer composites: its potential and future challenges. *Int J Adv Manuf Technol* **2020**, *106*, 1695–1721, doi:10.1007/s00170-019-04534-z.
18. Syrlybayev, D.; Zharylkassyn, B.; Seisekulova, A.; Akhmetov, M.; Perveen, A.; Talamona, D. Optimisation of Strength Properties of FDM Printed Parts-A Critical Review. *Polymers* **2021**, *13*, doi:10.3390/polym13101587.

19. Zhou, Y.-G.; Zou, J.-R.; Wu, H.-H.; Xu, B.-P. Balance between bonding and deposition during fused deposition modeling of polycarbonate and acrylonitrile-butadiene-styrene composites. *Polym. Compos.* **2020**, *41*, 60–72, doi:10.1002/pc.25345.
20. Ahn, S.-H.; Montero, M.; Odell, D.; Roundy, S.; Wright, P.K. Anisotropic material properties of fused deposition modeling ABS. *RPJ* **2002**, *8*, 248–257, doi:10.1108/13552540210441166.
21. Durgun, I.; Ertan, R. Experimental investigation of FDM process for improvement of mechanical properties and production cost. *RPJ* **2014**, *20*, 228–235, doi:10.1108/RPJ-10-2012-0091.
22. Dul, S.; Fambri, L.; Pegoretti, A. Filaments Production and Fused Deposition Modelling of ABS/Carbon Nanotubes Composites. *Nanomaterials (Basel)* **2018**, *8*, doi:10.3390/nano8010049.
23. Zhou, Y.-G.; Su, B.; Turng, L.-S. Deposition-induced effects of isotactic polypropylene and polycarbonate composites during fused deposition modeling. *RPJ* **2017**, *23*, 869–880, doi:10.1108/RPJ-12-2015-0189.
24. Carneiro, O.S.; Silva, A.F.; Gomes, R. Fused deposition modeling with polypropylene. *Materials & Design* **2015**, *83*, 768–776, doi:10.1016/j.matdes.2015.06.053.
25. Jin, M.; Stihl, M.; Giesa, R.; Neuber, C.; Schmidt, H.-W. (AB) n Segmented Copolyetherimides for 4D Printing. *Macro Materials & Eng* **2021**, *306*, 2000473, doi:10.1002/mame.202000473.
26. Bodaghi, M.; Damanpack, A.R.; Liao, W.H. Adaptive metamaterials by functionally graded 4D printing. *Materials & Design* **2017**, *135*, 26–36, doi:10.1016/j.matdes.2017.08.069.
27. Bodaghi, M.; Damanpack, A.R.; Liao, W.H. Triple shape memory polymers by 4D printing. *Smart Mater. Struct.* **2018**, *27*, 65010, doi:10.1088/1361-665X/aabc2a.
28. Chalissery, D.; Schönfeld, D.; Walter, M.; Shklyar, I.; Andrae, H.; Schwörer, C.; Amann, T.; Weisheit, L.; Pretsch, T. Highly Shrinkable Objects as Obtained from 4D Printing. *Macro Materials & Eng* **2022**, *307*, 2100619, doi:10.1002/mame.202100619.
29. Tibbits, S. Skylar Tibbits: The emergence of "4D printing". Available online: https://www.ted.com/talks/skylar_tibbits_the_emergence_of_4d_printing (accessed on 20 January 2022).
30. Tibbits, S. 4D Printing: Multi-Material Shape Change. *Archit Design* **2014**, *84*, 116–121, doi:10.1002/ad.1710.
31. Zhang, Y.; Qi, Y.-h.; Zhang, Z.-p. The influence of 2,4-toluene diisocyanate content on the intrinsic self-healing performance of polyurethane at room-temperature. *J Polym Res* **2015**, *22*, doi:10.1007/s10965-015-0744-0.
32. van Manen, T.; Janbaz, S.; Zadpoor, A.A. Programming 2D/3D shape-shifting with hobbyist 3D printers. *Mater. Horiz.* **2017**, *4*, 1064–1069, doi:10.1039/c7mh00269f.
33. Hu, G.F.; Damanpack, A.R.; Bodaghi, M.; Liao, W.H. Increasing dimension of structures by 4D printing shape memory polymers via fused deposition modeling. *Smart Mater. Struct.* **2017**, *26*, 125023, doi:10.1088/1361-665X/aa95ec.
34. Noroozi, R.; Bodaghi, M.; Jafari, H.; Zolfagharian, A.; Fotouhi, M. Shape-Adaptive Metastructures with Variable Bandgap Regions by 4D Printing. *Polymers* **2020**, *12*, doi:10.3390/polym12030519.
35. Bodaghi, M.; Noroozi, R.; Zolfagharian, A.; Fotouhi, M.; Norouzi, S. 4D Printing Self-Morphing Structures. *Materials (Basel)* **2019**, *12*, doi:10.3390/ma12081353.
36. Nezhad, I.S.; Golzar, M.; Behravesh, A.; Zare, S. *Comprehensive Study on Shape Shifting Behaviors of Thermally Activated Hinges in FDM-based 4D Printing*, 2021.
37. Rajkumar, A.R.; Shanmugam, K. Additive manufacturing-enabled shape transformations via FFF 4D printing. *J. Mater. Res.* **2018**, *33*, 4362–4376, doi:10.1557/jmr.2018.397.
38. Zhang, Q.; Yan, D.; Zhang, K.; Hu, G. Pattern transformation of heat-shrinkable polymer by three-dimensional (3D) printing technique. *Sci Rep* **2015**, *5*, 8936, doi:10.1038/srep08936.
39. Chiodo, J.D.; Billett, E.H.; Harrison, D.J. Preliminary investigations of active disassembly using shape memory polymers. In *First international symposium on environmentally conscious design and inverse manufacturing*, February 1-3, 1999, Tokyo, Japan / edited by Hiroyuki Yoshikawa … [et al.]. Proceedings First International Symposium on Environmentally Conscious Design and Inverse Manufacturing, Tokyo, Japan, 2/3/1999 - 2/3/1999; Yoshikawa, H., Ed.; IEEE Computer Society: Los Alamitos, CA, 1999; pp 590–596, ISBN 0-7695-0007-2.
40. Chung, T.; Romo-Uribe, A.; Mather, P.T. Two-Way Reversible Shape Memory in a Semicrystalline Network. *Macromolecules* **2008**, *41*, 184–192, doi:10.1021/ma071517z.
41. Behl, M.; Kratz, K.; Zotzmann, J.; Nöchel, U.; Lendlein, A. Reversible bidirectional shape-memory polymers. *Adv. Mater. Weinheim.* **2013**, *25*, 4466–4469, doi:10.1002/adma.201300880.
42. Bothe, M.; Pretsch, T. Bidirectional actuation of a thermoplastic polyurethane elastomer. *J. Mater. Chem. A* **2013**, *1*, 14491–14497, doi:10.1039/C3TA13414H.

43. Meng, Y.; Jiang, J.; Anthamatten, M. Shape Actuation via Internal Stress-Induced Crystallization of Dual-Cure Networks. *ACS Macro Lett.* **2015**, *4*, 115–118, doi:10.1021/mz500773v.
44. Meng, Y.; Yang, J.-C.; Lewis, C.L.; Jiang, J.; Anthamatten, M. Photoinscription of Chain Anisotropy into Polymer Networks. *Macromolecules* **2016**, *49*, 9100–9107, doi:10.1021/acs.macromol.6b01990.
45. Walter, M.; Friess, F.; Krus, M.; Zolanvari, S.M.H.; Grün, G.; Kröber, H.; Pretsch, T. Shape Memory Polymer Foam with Programmable Apertures. *Polymers* **2020**, *12*, doi:10.3390/polym12091914.
46. Ke, D.; Chen, Z.; Momo, Z.Y.; Jiani, W.; Xuan, C.; Xiaojie, Y.; Xueliang, X. Recent advances of two-way shape memory polymers and four-dimensional printing under stress-free conditions. *Smart Mater. Struct.* **2020**, *29*, 23001, doi:10.1088/1361-665X/ab5e6d.
47. Schönfeld, D.; Chalissery, D.; Wenz, F.; Specht, M.; Eberl, C.; Pretsch, T. Actuating Shape Memory Polymer for Thermoresponsive Soft Robotic Gripper and Programmable Materials. *Molecules* **2021**, *26*, doi:10.3390/molecules26030522.
48. Pilate, F.; Stoclet, G.; Mincheva, R.; Dubois, P.; Raquez, J.-M. Poly(ε-caprolactone) and Poly(ω-pentadecalactone)-Based Networks with Two-Way Shape-Memory Effect through [2+2] Cycloaddition Reactions. *Macromol. Chem. Phys.* **2018**, *219*, 1700345, doi:10.1002/macp.201700345.
49. Zhou, J.; Turner, S.A.; Brosnan, S.M.; Li, Q.; Carrillo, J.-M.Y.; Nykypanchuk, D.; Gang, O.; Ashby, V.S.; Dobrynin, A.V.; Sheiko, S.S. Shapeshifting: Reversible Shape Memory in Semicrystalline Elastomers. *Macromolecules* **2014**, *47*, 1768–1776, doi:10.1021/ma4023185.
50. Basit, A.; L'Hostis, G.; Durand, B. Multi-shape memory effect in shape memory polymer composites. *Materials Letters* **2012**, *74*, 220–222, doi:10.1016/j.matlet.2012.01.113.
51. Basit, A.; L'Hostis, G.; Pac, M.J.; Durand, B. Thermally Activated Composite with Two-Way and Multi-Shape Memory Effects. *Materials (Basel)* **2013**, *6*, 4031–4045, doi:10.3390/ma6094031.
52. Wu, Y.; Hu, J.; Han, J.; Zhu, Y.; Huang, H.; Li, J.; Tang, B. Two-way shape memory polymer with "switch–spring" composition by interpenetrating polymer network. *J. Mater. Chem. A* **2014**, *2*, 18816–18822, doi:10.1039/C4TA03640A.
53. Chen, T.; Bilal, O.R.; Shea, K.; Daraio, C. Harnessing bistability for directional propulsion of soft, untethered robots. *PNAS* **2018**, *115*, 5698–5702, doi:10.1073/pnas.1800386115.
54. Ma, H.; Xiao, X.; Zhang, X.; Liu, K. Recent advances for phase-transition materials for actuators. *Journal of Applied Physics* **2020**, *128*, 101101, doi:10.1063/5.0020596.
55. Scalet, G. Two-Way and Multiple-Way Shape Memory Polymers for Soft Robotics: An Overview. *Actuators* **2020**, *9*, 10, doi:10.3390/act9010010.
56. Chen, Y.; Chen, C.; Rehman, H.U.; Zheng, X.; Li, H.; Liu, H.; Hedenqvist, M.S. Shape-Memory Polymeric Artificial Muscles: Mechanisms, Applications and Challenges. *Molecules* **2020**, *25*, doi:10.3390/molecules25184246.
57. Ge, Q.; Sakhaei, A.H.; Lee, H.; Dunn, C.K.; Fang, N.X.; Dunn, M.L. Multimaterial 4D Printing with Tailorable Shape Memory Polymers. *Sci Rep* **2016**, *6*, 1–11, doi:10.1038/srep31110.
58. Fan, L.F.; Rong, M.Z.; Zhang, M.Q.; Chen, X.D. A Very Simple Strategy for Preparing External Stress-Free Two-Way Shape Memory Polymers by Making Use of Hydrogen Bonds. *Macromol. Rapid Commun.* **2018**, *39*, e1700714, doi:10.1002/marc.201700714.
59. Fan, L.F.; Rong, M.Z.; Zhang, M.Q.; Chen, X.D. A Facile Approach Toward Scalable Fabrication of Reversible Shape-Memory Polymers with Bonded Elastomer Microphases as Internal Stress Provider. *Macromol. Rapid Commun.* **2017**, *38*, doi:10.1002/marc.201700124.
60. Fan, L.F.; Rong, M.Z.; Zhang, M.Q.; Chen, X.D. Dynamic reversible bonds enable external stress-free two-way shape memory effect of a polymer network and the interrelated intrinsic self-healability of wider crack and recyclability. *J. Mater. Chem. A* **2018**, *6*, 16053–16063, doi:10.1039/C8TA05751F.
61. Fan, L.F.; Huang, Y.N.; Rong, M.Z.; Zhang, M.Q. A simple and universal strategy for preparing external stress-free two-way shape memory polymers by making use of the chemical crosslinkages derived from peroxide initiator. *Express Polym. Lett.* **2020**, *14*, 295–308, doi:10.3144/expresspolymlett.2020.26.
62. Bothe, M.; Pretsch, T. Two-Way Shape Changes of a Shape-Memory Poly(ester urethane). *Macromol. Chem. Phys.* **2012**, *213*, 2378–2385, doi:10.1002/macp.201200096.
63. Lee, A.Y.; An, J.; Chua, C.K. Two-Way 4D Printing: A Review on the Reversibility of 3D-Printed Shape Memory Materials. *Engineering* **2017**, *3*, 663–674, doi:10.1016/J.ENG.2017.05.014.
64. Zhu, P.; Yang, W.; Wang, R.; Gao, S.; Li, B.; Li, Q. 4D Printing of Complex Structures with a Fast Response Time to Magnetic Stimulus. *ACS Appl. Mater. Interfaces* **2018**, *10*, 36435–36442, doi:10.1021/acsami.8b12853.
65. Kokkinis, D.; Schaffner, M.; Studart, A.R. Multimaterial magnetically assisted 3D printing of composite materials. *Nat. Commun.* **2015**, *6*, 8643, doi:10.1038/ncomms9643.

66. Kim, Y.; Yuk, H.; Zhao, R.; Chester, S.A.; Zhao, X. Printing ferromagnetic domains for untethered fast-transforming soft materials. *Nature* **2018**, *558*, 274–279, doi:10.1038/s41586-018-0185-0.
67. Xu, T.; Zhang, J.; Salehizadeh, M.; Onaizah, O.; Diller, E. Millimeter-scale flexible robots with programmable three-dimensional magnetization and motions. *Sci. Robot.* **2019**, *4*, doi:10.1126/scirobotics.aav4494.
68. Mao, Y.; Ding, Z.; Yuan, C.; Ai, S.; Isakov, M.; Wu, J.; Wang, T.; Dunn, M.L.; Qi, H.J. 3D Printed Reversible Shape Changing Components with Stimuli Responsive Materials. *Sci Rep* **2016**, *6*, 24761, doi:10.1038/srep24761.
69. Yuan, C.; Roach, D.J.; Dunn, C.K.; Mu, Q.; Kuang, X.; Yakacki, C.M.; Wang, T.J.; Yu, K.; Qi, H.J. 3D printed reversible shape changing soft actuators assisted by liquid crystal elastomers. *Soft Matter* **2017**, *13*, 5558–5568, doi:10.1039/c7sm00759k.
70. Shafranek, R.T.; Millik, S.C.; Smith, P.T.; Lee, C.-U.; Boydston, A.J.; Nelson, A. Stimuli-responsive materials in additive manufacturing. *Progress in Polymer Science* **2019**, *93*, 36–67, doi:10.1016/j.progpolymsci.2019.03.002.
71. Momeni, F.; Ni, J. Nature-inspired smart solar concentrators by 4D printing. *Renewable Energy* **2018**, *122*, 35–44, doi:10.1016/j.renene.2018.01.062.
72. Rastogi, P.; Kandasubramanian, B. Breakthrough in the printing tactics for stimuli-responsive materials: 4D printing. *Chemical Engineering Journal* **2019**, *366*, 264–304, doi:10.1016/j.cej.2019.02.085.
73. Baker, A.B.; Bates, S.R.G.; Llewellyn-Jones, T.M.; Valori, L.P.B.; Dicker, M.P.M.; Trask, R.S. 4D printing with robust thermoplastic polyurethane hydrogel-elastomer trilayers. *Materials & Design* **2019**, *163*, 107544, doi:10.1016/j.matdes.2018.107544.
74. Zhang, H.; Guo, X.; Wu, J.; Fang, D.; Zhang, Y. Soft mechanical metamaterials with unusual swelling behavior and tunable stress-strain curves. *Sci. Adv.* **2018**, *4*, eaar8535, doi:10.1126/sciadv.aar8535.

Chapter 8: Conclusion and Outlook

Chapter 8: Conclusion and Outlook

This dissertation aims at utilizing fused filament fabrication (FFF) to enable various shape memory effects (SMEs) for shape memory polymers (SMPs), making it a powerful tool to qualify both commercial and novel shape memory polyurethanes for new applications.

The doctoral work shows the processing of SMPs as differently colored filaments to build up high-contrast three-dimensional (3D) objects. By using different-sized nozzles, it is experimentally proven that the print resolution in the XY- plane and Z-direction concerning the layer height can be controlled by the experimental setup same as by the print instructions. Most importantly, additively manufactured quick response (QR) codes are characterized by distinct shape memory properties after thermomechanical treatment. The primary advantages of the developed additive manufacturing (AM) process are the quick availability of QR codes, control over the print resolution, the possibility to fabricate QR codes even with substrate thicknesses below 10 µm, and avoiding using solvents during production.

Further understanding of the ability to manipulate the print orientation helps to control the mechanical and shape memory properties of SMPs. This is particularly important when tuning or adjusting the material properties of specific parts of an object without changing the material itself by modifying the polymer synthesis. Extending the filigree FFF printing approach to the fabrication of miniature objects like letters with Arial font sizes 3, 4, and 10 allows for identifying the lower boundaries of FFF, which helps to expand the application platform for FFF 3D printers. The development of filigree printing demonstrated shape memory keyboard keys, which may be employed in bilingual keyboards like Braille and those with QWERTY layout. Here, for better applicability of smart keyboard keys, the one-way (1W) SME of font scripts has to be later extended to a two-way (2W) SME to transfer them into two metastable states. The introduction of heating and cooling elements for the SMP letters can further trigger the 2W-SME on command. Further, developing SMP gears for activating or deactivating a transmission gear is a significant step towards addressing potential applications in many industries and mechanical systems to activate or deactivate transmission systems on demand.

Taking a step further, FFF is first utilized to achieve "*in-situ*" programming and thus the implementation of the one-way SME. Such one-way four-dimensional (4D)-printed objects exhibit thermoresponsive behavior directly after printing. Here, the challenges were to enable uniform shrinkage of objects and to build up homogenous and thermoresponsive objects of larger size. This is achieved when printing with a lower nozzle temperature, thereby keeping the difference between the nozzle and glass transition temperature of the SMP as small as possible. Transferring the know-how to polylactic acid (PLA) material shows that the findings can be transferred to other thermoplastics is possible. The understanding of the work enables the development of novel applications for 4D-printing, including active assembly, disassembly, deactivating gear, and programming devices that can program other SMPs or for holding or gripping complex objects.

The work further shows the processing of a semicrystalline poly(1,10-decylene adipate) diol (PDA) based polyester urethane via FFF and its thermomechanical treatment to achieve 2W-SME. The novel temperature screening characterization method allows us to identify the optimum actuation range and conditions. Further, it is noteworthy to mention that the combination of actuating elements with a mechanical linkage system allows multiplying the actuation by about sixteen-fold of the materials 2W-SME. This permitted the development of grippers, especially for soft robotics. Moreover, the combination of actuating elements with deformable structures allows new approaches in the field of thermoresponsive programmable materials.

Furthermore, the work put effort into combining programmable materials with SMPs, where the former is manufactured using the latter. Once thermomechanically treated and investigated in a stress-free state by varying temperatures, thermoreversible length changes $\Delta L/L_0$ of about 45% were witnessed. The developed programmable gear can actively engage and/or disengage a force transmission system at specific temperatures. The work further shows that other actuator designs can obtain more complex motion sequences. The more significant reversible length change $\Delta L/L_0$ was achieved from a relatively smaller actuating element to be used as an alternative actuating element for the previously presented actuation grippers.

Last but not least, the ability to process the same semicrystalline PDA-based SMP permits the accomplishment of two-way 4D-printing, where objects actuate directly after AM when changing the temperature. This is particularly beneficial because no further thermomechanical treatment is necessary. This approach creates many opportunities in the future for the mechanical, aerospace, and biomedical industries, where moving parts can be manufactured with fewer parts, thereby reducing the probability of failures. Even though the thermoreversible actuation was comparatively lower than in the case of "*ex-situ*" 2W-programmed samples, the extent of actuation may be large enough to address new applications, e.g., as temperature-surface morphing, biomedical grippers, or sensory applications.

In the future, one-way 4D-printing using FFF could turn out as a seminal technology for SMPs in fields like the counterfeit-proof marking of goods at risk of plagiarism or the supervision of cold chains. Future challenges include shortening the production time without compromising on resolution. In the case of 2W-4D printing, the material platform will have to be drastically expanded to eliminate the need for an external cooling unit. This would open up a wide variety of applications, including sustainable energy objects or parts that may contribute to the introduction of a circular plastics/materials economy, where one metastable state allows active assembly and the other active disassembly. This permits the parts to be recovered separately for effective recycling for the next life cycle. The improvement of the future 3D printers would be to include multi-extrusion heads that work parallelly in a single-build platform to realize large-scale manufacturing. Artificial intelligence and monitoring devices could be used to observe real-time printing conditions and forecast and adapt the printing parameter to achieve failure-free printed parts. In the case of slicer

software, the software should be improved to implement user-friendly options, e.g., the printing patterns or print orientation can be easily modified for each or selected layer during the slicing. In addition, it can run a simulation study to understand the thermal, mechanical, and thermomechanical behavior and predict and optimize the printing parameter to achieve desired 4D-shape changes on appropriate stimulus. Another critical step is evaluating how similar results can be achieved using other AM techniques. A further significant technological step forward would be the transfer of the 2W-4D printing to other melt-based processing methods like injection molding to realize mass production of thermoresponsive objects.

Appendix

Appendix

Journals

1. **Chalissery, D**.; Pretsch, T.; Staub, S.; Andrä, H. Additive Manufacturing of Information Carriers Based on Shape Memory Polyester Urethane. Polymers 2019, 11, 1005. https://doi.org/10.3390/polym11061005
2. **Chalissery, D**; Pretsch, T; Staub, S; Kasack, K; Andrä, H; 3D-Druck von QR-Codes mit Formgedächtniseigenschaften. In Druckspiegel (Nr.11-12), pp. 34–37.
3. Schönfeld, D.; **Chalissery, D.**; Wenz, F.; Specht, M.; Eberl, C.; Pretsch, T. Actuating Shape Memory Polymer for Thermoresponsive Soft Robotic Gripper and Programmable Materials. Molecules 2021, 26, 522. https://doi.org/10.3390/molecules26030522
4. **Chalissery, D**., Schönfeld, D., Walter, M., Shklyar, I., Andrae, H., Schwörer, C., Amann, T., Weisheit, L. and Pretsch, T. (2022), Highly Shrinkable Objects as Obtained from 4D-printing. Macromol. Mater. Eng., 307: 2100619. https://doi.org/10.1002/mame.202100619
5. **Chalissery, D.**, Schönfeld, D., Walter, M., Ziervogel, F., Pretsch, T., Fused Filament Fabrication of Actuating Objects. *Macromol. Mater. Eng.* 2022, 2200214. https://doi.org/10.1002/mame.202200214.

Patents

1. DE102018003273A1 Verfahren zur Herstellung von komplexen Strukturen aus thermoplastischen Polymeren und Polymer-Formteile mit solchermaßen hergestellten, komplexen Strukturen; Pretsch, Thorsten; **Chalissery, Dilip**
2. DE102019007939A1 Verfahren zur Herstellung von Polymer-Formteilen aus thermoplastischen Polymeren mit Formgedächtniseigenschaften und/oder mit thermoresponsiven Eigenschaften, insbesondere mittels 4D-Druck, sowie solchermaßen hergestelltes Polymer-Formteil; Walter, Mario; Pretsch, Thorsten; **Chalissery, Dilip**; Frieß, Fabian; Rümmler, Tobias; Schönfeld, Dennis
3. DE102022124851.8 Verfahren zur Programmierung von Polymer-Formteilen aus Polymeren mit Formgedächtniseigenschaften oder mit thermoresponsiven Eigenschaften; Pretsch, Thorsten; **Chalissery, Dilip**; Ziervogel, Fabian
4. DE102022126382.7 Lagenförmiges Verbundmaterial mit Formgedächtnispolymeren und Verfahren zu seiner Herstellung; Pretsch, Thorsten; **Chalissery, Dilip**; Ziervogel, Fabian

Presentations

1. Thermoresponsive Programmable Materials, International Conference on Programmable Materials, 12.7.2022, **Dilip Chalissery**, Dennis Schönfeld, Mario Walter, Heiko Andrae, Franziska Wenz, Chris Eberl, Linda Weisheit, Fabian Ziervogel, Sarah C. L. Fischer, Thorsten Pretsch, Berlin (Deutschland)
2. Formgedächtnispolymere – neue Möglichkeiten mit 4D-Druck, KeyNote Lecture, 9. Mitteldeutsches Forum 3D-Druck in der Anwendung, 29.6.2022, **Dilip Chalissery**, Dennis Schönfeld, Mario Walter, Inga Shklyar, Heiko Andrä, Christoph Schwörer, Tobias Amann, Linda Weisheit, Thorsten Pretsch, Jena (Deutschland)
3. Recognizing the Potential of 4D-Printing, 2nd Edition of International Conference on Materials Science and Engineering, 28.3.2022, **Dilip Chalissery**, Dennis Schönfeld, Mario Walter, Inga Shklyar, Heiko Andrä, Christoph Schwörer, Tobias Amann, Linda Weisheit, Thorsten Pretsch, Virtuelle Veranstaltung (Indien)
4. Additive Manufacturing of thermoresponsive Objects, KeyNote Lecture, Global Scientific Guild Conference: Global Webinar on 3D Printing and Addtive Modeling 25.2.2022, **Dilip Chalissery**, Dennis Schönfeld, Mario Walter, Inga Shklyar, Heiko Andrä, Christoph Schwörer, Tobias Amann, Linda Weisheit, Thorsten Pretsch, Virtuelle Veranstaltung (Indien)
5. Funktionsintegration mit Additiver Fertigung, 4. Veranstaltung - Virtuelles Werkstattgespräch, 19.01.2022, **Dilip Chalissery**, Dennis Schönfeld, Mario Walter, Inga Shklyar, Heiko Andrä, Christoph Schwörer, Tobias Amann, Linda Weisheit, Thorsten Pretsch, Virtuelle Veranstaltung (Deutschland)
6. Presentation titled “Addive Manufacturing of thermoresponsive Objects” at Global Scientific Guild Conference on 18-20 March 2022 (Online-event); **Chalissery, Dilip**; Schönfeld, Dennis; Walter, Mario; Shkylar, Inga; Andrä, Heiko; Schwörer, Christoph; Amann, Tobias; Weisheit, Linda; Pretsch, Thorsten
7. Presentation titled “Funktionsintegration mit Additiver Fertigung“ at 4th Virtual Workshop “Additive Fertigung” on 19 Januar 2022; Pretsch, Thorsten; **Chalissery, Dilip**; Schönfeld, Dennis; Walter, Mario; Shklyar, Inga; Andrä, Heiko; Schwörer, Christoph; Amann, Tobias; Weisheit, Linda
8. Presentation titled “Additive Fertigung mit Formgedächtnispolymeren” at 4th Status-Workshop of Fraunhofer High-Performance Center for Functional Integration in Materials, Phase III & KickOff zum Joint Lab BioF, 30. September 2021, (Online event); Pretsch, Thorsten; **Chalissery, Dilip**; Schönfeld, Dennis; Walter, Mario; Shkylar, Inga; Andrä, Heiko; Schwörer, Christoph; Amann, Tobias; Weisheit, Linda
9. Presentation titled “Shape Memory Polymers in Transition to Programmable Materials” at 2nd Advanced Chemistry World Congress - Latest Global Innovations and Market Insights in Chemistry, 14-15 June 2021, Berlin, Germany; Pretsch, Thorsten; Schönfeld, Dennis; **Chalissery, Dilip**; Walter, Mario; Köbler, Jonathan; Andrä, Heiko; Wenz, Franziska; Eberl, Chris

10. Presentation titled “Design for Recycling mit Formgedächtnispolymeren” at VDI - Arbeitskreis Kunststofftechnik, 25. November 2020; Pretsch, Thorsten; **Chalissery, Dilip**; Schönfeld, Dennis; Walter, Mario; Wafzig, Florian
11. Presentation titled “Formgedächtnispolymere für Soft Robotics” at WerkstoffWoche 2019, Symposium “Soft Robotik, mechanische und funktionalisierte Materialien”, 18.-20. September 2019, Dresden; Walter, Mario; Frieß, Fabian; Rümmler, Tobias; **Chalissery, Dilip**; Pretsch, Thorsten
12. Presentation titled “Additive Fertigung von Informationsträgern mit Formgedächtniseigenschaften” at WerkstoffWoche 2019, Symposium “Additive Fertigung”, 18.-20. September 2019, Dresden; **Chalissery, Dilip**; Rümmler, Tobias; Pretsch, Thorsten
13. Presentation titled “Additive Manufacturing of complex filigree-structured Objects based on Shape-Memory Polymer” at Elmia Subcontractor Trade Show, 13.–16. November 2018, Jönköping/Sweden; Pretsch, Thorsten; **Chalissery, Dilip**
14. Industry Workshop: High-Performance Center »Integration of Biological and Physical-Chemical Material Functions« 3D-Printing of Shape-Memory Polymers; 17 July 2018; **Dilip Chalissery**, Dr. Thorsten Pretsch
15. Bericht zum Status des Projektes LIM-5: Formgedächtnispolymere für den 3D-Druck; 17 May 2018; Dr. Thorsten Pretsch, **Dilip Chalissery**, Dennis Schönfeld
16. Bericht zum Status des Projektes LIM-5: Integration von Formgedächtnisfunktionalitäten in polymere 3D-Druckmaterialien; 20 November 2018; Dr. Thorsten Pretsch, **Dilip Chalissery**, Harish Babu Eppa, Dr. Mario Walter, Dr. Fabian Frieß, Tobias Rümmler
17. Vorstellung der Projektskizze: Funktionsintegration durch Additive Fertigung von Objekten mit Formgedächtniseigenschaften; 16 May 2019; Dr. Thorsten Pretsch, **Dilip Chalissery**, Dr. Mario Walter, Dennis Schönfeld
18. AMBER - AM Cluster Berlin-Brandenburg Kickoff meeting and virtuell industry Workshop on 28 May 2020 and 10 June 2020, respectively; Prof. Dr. Aleksander Gurlo, Dr. Stephan Schröder, Dr. Siegfried Behrendt, Dr. Jens Kurreck, Ben Jastram, Dr. Dietmar Göhlich, Dr. Mario Birkholz, Dr. Jens Günster, Dr. Dietmar Stephan, Dr. Mathias Czasny, David Karl, Dr. Thorsten Pretsch, **Dilip Chalissery**

Permanent Database:

https://publica.fraunhofer.de/entities/person/ab790674-007c-41bf-8b52-aca0a75b0f10/publications

List of Abbreviations and Symbols

List of Abbreviations and Symbols

1W	One-way
2W	Two-way
2-NMP	*N*-Methyl-2-pyrrolidone
2PL	Two-photon lithography
3D	Three-dimensional
4D	Four-dimensional
ABS	Acrylonitrile butadiene styrene
AM	Additive manufacturing
AMF	Additive manufacturing file
BAAM	Big area additive manufacturing
BD	Butanediol
CAD	Computer-aided design
CIE	Crystallization-induced elongation
CNC	Computer numerical controlled
CTM	Cyclic thermo-mechanical measurements
DMA	Dynamic mechanical analysis
DSC	Differential scanning calorimetry
FFF	Fused filament fabrication
FGE	Formgedächtniseffekt
FGP	Formgedächtnispolymere
FTIR	Fourier-transform infrared spectroscopy
HIPS	High impact polystyrene
MDI	Methylene diphenyl diisocyanate
MIC	Melting-induced contraction
MJF	Multi-jet fusion
PBA	Poly(butylene adipate)
PDA	Poly(decylene adipate)
PET-G	Polyethylene terephthalate glycol
PEU	Poly ester/ether urethane
PEUU	Polyester urethane urea
PLA	Polylactic acid
PMMA	Poly(methyl methacrylate)
PPG	Polypropylene glycol
QR	Quick response
SLA	Stereolithography
SLS	Selective laser sintering
SME	Shape memory effect
SMP	Shape memory polymer
STL	Standard triangle language
TPU	Thermoplastic polyurethane
TTIP	Titanium(IV) isopropoxide
X-ray	X-radiation
E'	Storage modulus
E''	Loss modulus
L	Length
S_P	Speed of print head
T	Temperature
T_c	Crystallization transition temperature
T_d	Deformation temperature
T_{fix}	Fixation temperature
T_g	Glass transition temperature
T_m	Melt transition temperature
T_{max}	Maximum actuation temperature
T_N	Nozzle temperature
T_P	Print platform temperature
T_{perm}	Melt temperature
T_{trans}	Phase transition temperature
ΔH_c	Crystallization enthalpy
ΔH_m	Melting enthalphy
ε	Strain
σ	Stress
ρ	Density